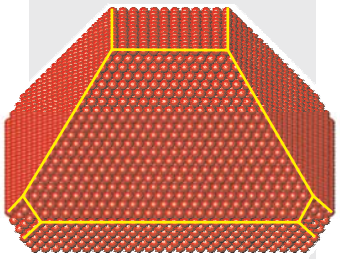

In situ Oxidation Study of Supported Rh and Pd Nanoparticles

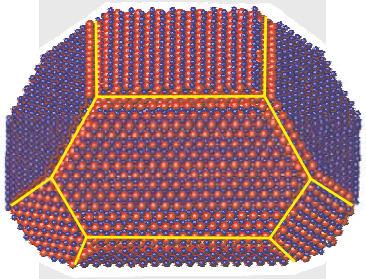

Philipp Nolte

2009

Max Planck Institute
for Metals Research

and

Institute for Theoretical
and Applied Physics
University of Stuttgart

In situ
Oxidation Study of Supported
Rh and Pd Nanoparticles

Von der Fakultät Mathematik und Physik der Universität Stuttgart
zur Erlangung der Würde eines Doktors der
Naturwissenschaften (Dr. rer. nat.) genehmigte Abhandlung

Vorgelegt von
Philipp Georg Nolte
aus Nagold

Hauptberichter:	Prof. Dr. H. Dosch
Mitberichter:	Prof. Dr. P. Michler

Tag der mündlichen Prüfung: 20. 03. 2009

Max-Planck-Institut für Metallforschung
und
Institut für Theoretische und Angewandte Physik
der Universität Stuttgart

2009

Contents

Zusammenfassung

Motivation

Schätzungsweise 90% der weltweiten Produktion in der chemischen Industrie erfolgt unter Einsatz von Katalysatoren [1]. Neben der Möglichkeit zur gezielten Synthese von Substanzen steht insbesondere die Energieersparnis im Vordergrund, wenn durch Katalysatoren Reaktionen bei erniedrigten Temperaturen ablaufen können. Typische Materialien in der heterogenen Katalyse sind Partikel aus Rhodium, Palladium, Platin oder Ruthenium, die auf feinsten Oxidpulvern aufgebracht sind.

Palladium zeigt eine hohe katalytische Aktivität für viele industriell bedeutende chemische Reaktionen. Hierzu zählen beispielsweise die Hydrierung von Acetylen und die Oxidation von Methan [2, 3]. Außerdem ist es Bestandteil von Dreiwegekatalysatoren in Kraftfahrzeugen zur Oxidation und Reduktion giftiger Abgasbestandteile wie CO und NO_x. In diesem Bereich spielt Rhodium ebenfalls eine bedeutende Rolle [4]. Derartige Anwendungen von Palladium und Rhodium sowie der übrigen 4d-Übergangsmetalle haben den Bedarf ausgelöst, einen detaillierten Einblick in die katalytischen Eigenschaften und die beteiligten chemischen Reaktionen auf atomarer Ebene zu gewinnen. Der Zusammenhang zwischen der Struktur und den katalytischen Eigenschaften ist von besonderem Interesse, damit für eine gewünschte chemische Reaktion entsprechende Katalysatoren gezielt verbessert werden können. Solche Verbesserungen betreffen die Erhöhung der chemischen Umsatzraten, eine höhere Selektivität der chemischen Reaktion und eine verlängerte Lebensdauer.

Im Fall von Oxidationsreaktionen, bei denen die Metalle als Katalysator eingesetzt werden, ist nicht allgemein geklärt, ob chemisorbierter Sauerstoff, ultradünne Oberflächenoxidfilme oder die Volumenoxidphasen die höchste katalytische Aktivität aufweisen. Unter Volumenoxiden versteht man solche Oxide, deren Struktur dem Metalloxid entspricht, wie es auch in makroskpischen Mengen vorkommt. Als Oberflächenoxide werden geordnete ultradünne Filme mit einer wohldefinierten Dicke bezeichnet, deren atomare Struktur sich von denen der Volumenoxide unterscheiden. Beispielsweise wächst auf der Rh(111)-Oberfläche ein dünner Oxidfilm auf, der aus einer dreiatomigen O-Rh-O-Schicht besteht. Die Beteiligung von chemisorbiertem Sauerstoff führt zu einem Langmuir-Hin-

shelwood-Mechanismus, die Beteiligung von Volumenoxid zu einem Mars-van-Krevelen-Mechanismus [5, 6, 7]. Beim Langmuir-Hinshelwood-Mechanismus werden die Edukte (z.B. CO) an der Oberfläche adsorbiert, und die Adsorbate reagieren auf der Oberfläche zum Produkt, welches anschließend desorbiert. Ein bekanntes Beispiel hierfür ist auch die CO-Oxidation auf Pt(110). Beim Mars-van-Krevelen-Mechanismus wird ein Edukt zunächst adsorbiert. Die weitere Oxidationsreaktion erfolgt jedoch nicht unmittelbar mit chemisorbiertem Sauerstoff aus der umgebenden Gasphase, sondern mit chemisch gebundenem Sauerstoff aus dem Katalysatormaterial. Nach der Desorption des oxidierten Produkts wird der Katalysator durch Sauerstoff aus der Umgebung reoxidiert, so dass der Ausgangszustand wieder erreicht ist.

Viele Erkenntnisse, die über Katalysatoren auf atomarer Skala gewonnen wurden, stammen von Einkristalloberflächen unter kontrollierten Bedingungen. Ein bekanntes Beispiel sind die Experimente von G. Ertl[1] zur Oxidation von Kohlenmonoxid auf Platinoberflächen sowie die Erklärung der katalytischen Eigenschaften von Eisen beim Haber-Bosch-Verfahren zur Ammoniaksynthese [8, 9]. Allerdings sind reale Katalysatormaterialien aus Nanopartikeln erheblich komplizierter aufgebaut und ihre Form, Größe und atomare Struktur der Oberfläche kann sich während einer chemischen Reaktion verändern. Nanopartikel werden typischerweise von niedrigindizierten Kristallebenen begrenzt. Untersuchungen an entsprechend orientierten Einkristalloberflächen geben einen Einblick in die Strukturen von Relaxationen und Rekonstruktionen, die durch den Einfluss von Adsorbaten entstehen. Auch die Form von Nanopartikeln ist wichtig für ihre katalytischen Aktivität. Zum einen bestimmt sie den Anteil der verschiedenen kristallographischen Oberflächen an einem Nanopartikel, die sich in ihrer Reaktivität unterscheiden können. Zweitens wird durch die Form eines Partikels auch die Art und Gestalt seiner Kanten bestimmt, die ebenfalls eine Rolle für die katalytische Aktivität spielen können. Dies wurde am Beispiel der Hydrierung von Aldehydgruppen an Goldpartikeln gezeigt [10]. Auf die Vorgänge an den Kanten von Partikeln kann durch die Untersuchung von vicinalen Kristalloberflächen geschlossen werden. Trotzdem stellt sich bei einfachen Modellsystemen die Frage, inwiefern sich ihre Eigenschaften auf die in technischen Anwendungen tatsächlich ablaufenden Vorgänge übertragen lassen können. Die Reaktionseigenschaften von Nanopartikeln können sich durch ihre Größe und den Einfluss des Substrates von den Einkristalloberflächen unterscheiden. Die entsprechende Unkenntnis, ob man von den Eigenschaften einfacher Modellsysteme Schlussfolgerungen über die Eigenschaften der Nanomaterialien treffen kann, wird als *Materials Gap* bezeichnet. Desweiteren laufen im technischen Maßstab Reaktionen in Druckbereichen ab, die erheblich über dem Atmosphärendruck liegen können.

Dies stellt eine Herausforderung für oberflächenempfindliche *in situ* Messungen dar, d.h. der Beobachtung eines Systems in derselben Umgebung, in der die

[1] ausgezeichnet mit dem Nobelpreis für Chemie 2007

chemische Reaktion abläuft. Werden beispielsweise Elektronen als oberflächenempfindliche Sonden eingesetzt, ist man auf Drücke im Hochvakuumbereich beschränkt. Man bezeichnet entsprechend die Unkenntnis, ob die im Hochvakuumbereich ablaufenden Prozesse auch bei atmosphärischen Drücken stattfinden, als *Pressure Gap*. Diese Lücken können beseitigt werden, wenn die Vorgänge unmittelbar auf den Oberflächen von Nanopartikeln untersucht und *in situ* Methoden verwendet werden, die mit technisch relevanten Druck- und Temperaturbedingungen kompatibel sind. Es gibt inzwischen instrumentelle Verbesserungen bei den elektronenbasierten Methoden, die auch XPS- und TEM-Messungen bei höheren Drücken erlauben. Gerade im Druckbereich liegt ein entscheidender Vorteil der Röntgenbeugung, die als wesentliche experimentelle Methode in dieser Arbeit verwendet wurde.

Zielsetzung und Methoden

Im Rahmen dieser Arbeit wurde die Oxidation von Rhodium und Palladiumpartikeln auf den Trägermaterialien MgO(001) und α-Al_2O_3(0001) untersucht. Die Zielsetzung besteht in der Feststellung und Klärung folgender Punkte:

- Bestimmung der Form von Nanoteilchen unter in situ Bedingungen und quantitative Beschreibung der Formänderung unter dem Einfluss von Sauerstoff
- Auffinden von geordneten Strukturen auf den Facetten von Nanopartikeln
- Kinetische Barrieren bei der Volumenoxidbildung im Vergleich mit den Einkristalloberflächen
- Einfluss der Partikelgröße auf das Oxidationsverhalten
- Struktur von Nanoteilchen während technisch relevanter chemischer Reaktionen

Die Nanopartikel wurden im Ultrahochvakuum mit Elektronenstrahlverdampfern hergestellt. Die in situ Experimente zum Wachstum und zur Oxidation wurden mit oberflächenempfindlicher Röntgenstreuung an Synchrotronstrahlungsquellen (Europäische Synchrotronstrahlungsquelle ESRF in Grenoble, Angströmquelle Karlsruhe ANKA) durchgeführt. Mit dieser Methode sind der Druck- und Temperaturbereich im Prinzip beliebig und werden nur durch die Eigenschaften der verwendeten Oxidationskammer beschränkt. Durch Position und Linienbreite von Braggreflexen lassen sich Phasen identifizieren und die Größe von Nanoteilchen bestimmen. Als bisher nicht konventionell verwendete Methode wurden Intensitätsverteilungen entlang von Ebenen im reziproken Raum aufgenommen. Hierbei wurde in der Umgebung der Bragg-Reflexe das Crystal Truncation Rod

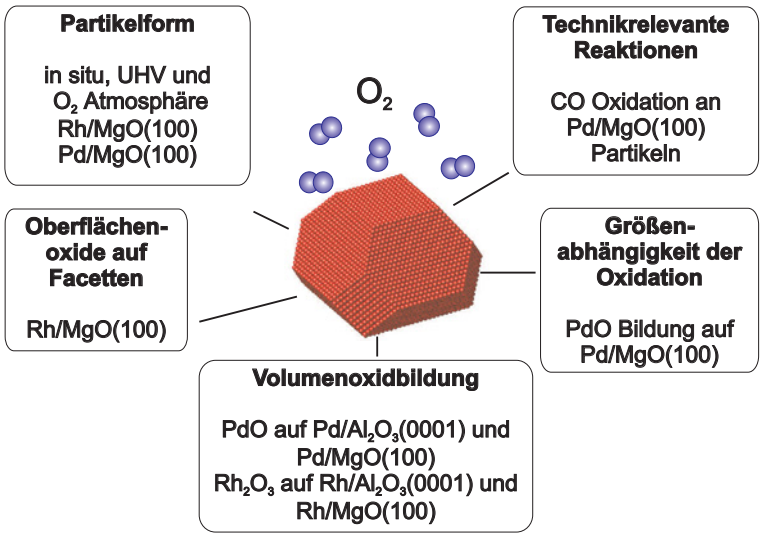

Abb. 1: Im Rahmen dieser Arbeit behandelte Fragestellungen.

Signal aufgezeichnet, einem Interferenzeffekt, der von der Röntgendiffraktion an definierten Kristalloberflächen bekannt ist. Eine unabdingbare experimentelle Voraussetzung ist das epitaktische Wachstum der Teilchen, damit das Streusignal aller Partikel in die gleiche Richtung führt. Die Intensitätsverteilung lässt unmittelbar qualitative Rückschlüsse auf die Form von Nanoteilchen zu. Zur quantitativen Formanalyse wurden Simulationen der Intensitätsverteilungen in der entsprechenden Ebene im reziproken Raum zur Formbestimmung der Nanoteilchen entwickelt.

Ergebnisse

Formempfindliche Röntgenbeugungsmessungen an Nanopartikeln

Von Einkristallen mit einer wohldefinierten Oberfläche ist bekannt, dass auch zwischen Braggreflexen ein Röntgenbeugungssignal beobachtet werden kann. Dieses Signal ist entlang von Crystal Truncation Rods (CTR = Oberflächenabbruch-Gitterstäbe) verteilt, deren Richtung der Impulsübertragskomponente senkrecht zur Oberfläche entspricht. Die Oberfläche eines facettierten Kristalls besteht aus verschiedenen terminierenden Flächen, von denen jede zu einem CTR-Signal beiträgt. In der Umgebung eines Braggreflexes in geeignete Richtungen kann dieses Signal ausgemessen werden, wie in Abb. 2 für einen Rh Nanopartikel auf MgO(100) dargestellt ist. In der abgebildeten Ebene um den Rh(111)-Reflex liegen die CTR-Signale entlang der (001)- sowie von (111)-artigen Richtungen. Dadurch kann auf die Form des Partikels geschlossen werden, die einem an

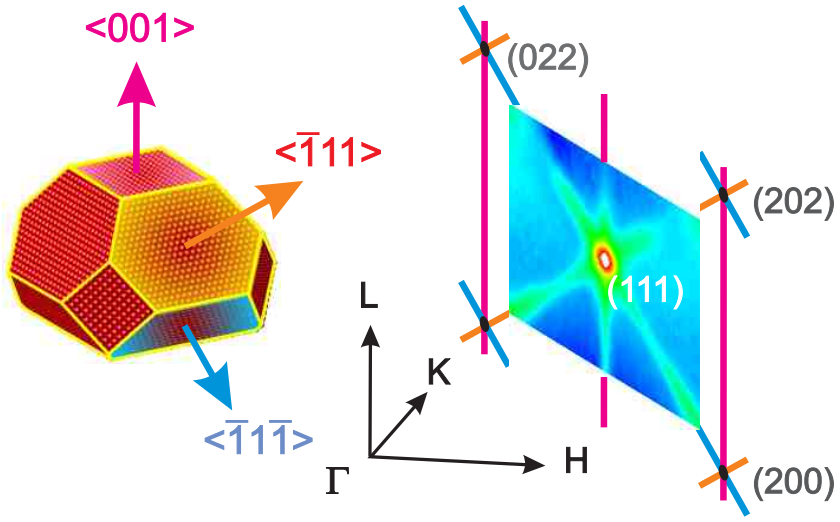

Abb. 2: Information über die Form von Partikeln kann aus Intensitätsverteilungen entlang von Ebenen im reziproken Raum erhalten werden.

den Spitzen abgeschnittenen Oktaeder entspricht. Mit dieser Methode wurde die sauerstoffbedingte Formänderung von Rh- und Pd-Teilchen auf MgO(100)-Substraten bestimmt.

Formänderung von Rh/MgO(100)-Partikeln

Die Oxidation von Rh/MgO(100)-Teilchen wurde in Röntgenbeugungsexperimenten mit Synchrotronstrahlung an Partikeln mit einem mittleren Durchmesser von 8 bzw. 9 Nanometern studiert. Es wurden formempfindliche Messungen durch Aufzeichnung der Intensitätsverteilung in einer Ebene im reziproken Raum gewonnen, womit sich (111)- und (001)-äquivalente Oberflächen nachweisen ließen. In einer Sauerstoffatmosphäre von $3{\cdot}10^{-5}$ mbar wurde eine Abnahme des Signals in die (111)-äquivalenten Richtungen beobachtet und eine Zunahme des Signals in (001)-Richtung (siehe Abb. 3 a). Dies deutet unmittelbar auf eine Verkleinerung der (111) Facetten und eine Vergrößerung der (001)-Facetten auf der Ober- oder Unterseite der Partikel hin. Bei der quantitativen Analyse stellte sich heraus, dass sich die (001)-Facetten auf der Oberseite der Partikel sowie auch die (100) Facetten an den Seiten der Partikel vergrößern (Abb. 3 b). Bei den Partikeln mit 9 nm Durchmesser konnte außerdem die sauerstoffinduzierte Bildung von (110)-Facetten nachgewiesen werden.

Die Formänderung konnte auf die Adsorption des Sauerstoffs auf der Partikeloberfläche zurückgeführt werden. Zu Beginn der Oxidation findet die Bildung einer instabilen (3×1)-Überstruktur auf der Rh(001)-Facette statt. Als Endzustand konnten die Oberflächenoxide, die bisher nur von den Rh(111) und Rh(100) Einkristalloberflächen bekannt waren, nachgewiesen werden. Diese Oberflächen-

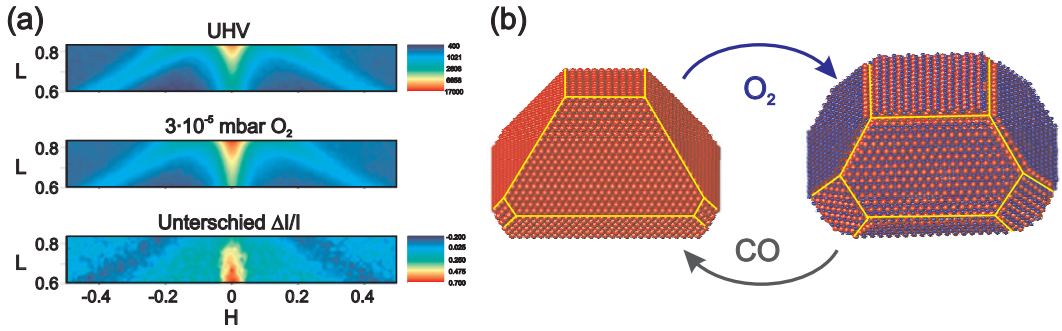

Abb. 3: Aus der quantitativen Analyse von Flächen im reziproken Raum konnte die Formänderung der Rhodiumteilchen unter dem Einfluss von Sauerstoff ermittelt werden. Es vergrößern sich die (100)-artigen Facetten, dabei bildet sich eine drei Atomlagen dünne O-Rh-O-Oxidhülle.

oxide bestehen aus einer O-Rh-O-Dreifachlage mit einer hexagonalen Struktur [11, 12]. Dieser Oxidfilm kann in einer reduzierenden CO-Atmosphäre wieder entfernt werden. Neben den in situ Röntgenmessungen erfolgte der Nachweis der Oberflächenoxide unter ex situ Bedingungen mit hochaufgelöster Transmissionselektronenmikroskopie [13]. Es konnte ferner an den 9 nm Teilchen gezeigt werden, dass sich die Volumenoxidphase Rh_2O_3 durch die Anwesenheit des Oberflächenoxids nicht unter den theoretisch vorhergesagten Bedingungen bildet, sondern erst bei deutlich erhöhtem Sauerstoffdruck. Diese Beobachtung entspricht der Erkenntnis von Einkristalloberflächen, bei denen das Oberflächenoxid eine kinetische Barriere für das Wachstum der Volumenoxidphase darstellt [11, 12].

Formänderung von Pd/MgO(100)-Partikeln

In analoger Vorgehensweise wurden die Form von Pd/MgO(100)-Partikel mit einem Durchmesser von 8 nm unter dem Einfluss von Sauerstoff untersucht. Die Form der Pd-Teilchen entspricht wie bei Rh abgeschnittenen Oktaedern. Auch hier wurde das Streusignal von den (111)- und (001)-Facetten entlang einer Ebene im reziproken Raum aufgezeichnet. Durch Sauerstoffexposition im Bereich von 10^{-5} mbar verringert sich das Streusignal dieser Facetten, was eine Verkleinerung der entsprechenden Oberflächen bedeutet. Anders als bei Rh entstehen zusätzliche (112) Facetten. Eine quantitative Abschätzung ergibt, dass etwa vier Atomlagen auf der Oberseite der Partikel an der Facettierung beteiligt sind. Diese Formänderung wird nur durch die Anwesenheit von Sauerstoff stabilisiert und kann nur durch Abpumpen des Sauerstoffes oder auch durch eine reduzierende CO-Atmosphäre rückgängig gemacht werden.

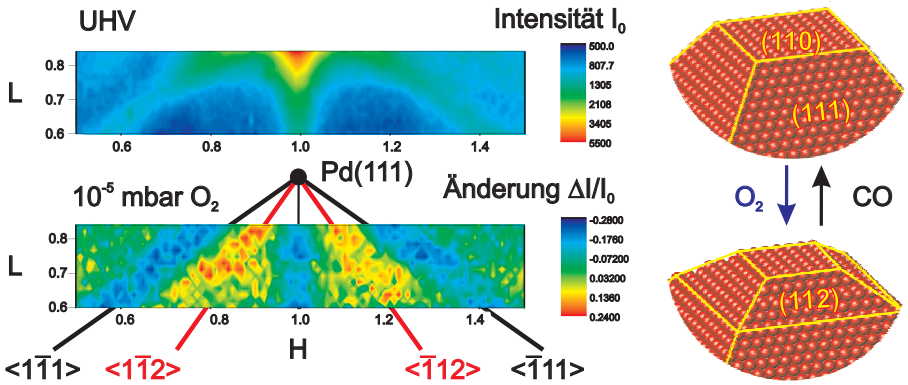

Abb. 4: Bei T = 570 K und einem Sauerstoffdruck von 10^{-5} mbar bilden sich bei 8 nm Pd/MgO(100) Partikeln (112)-Facetten an der Kante zwischen (001)- und den (111)-Facetten aus.

Oxidation von Pd/MgO(100)-Partikeln in Abhängigkeit der Teilchengröße

Die Reaktivität von Nanopartikeln in chemischen Reaktionen hat sich in Verschiedenen Kombinationen von Metallen und Trägermaterialien als stark abhängig von der Teilchengröße herausgestellt [14, 15, 16, 17]. Für hinreichend große Teilchen kann man erwarten, dass sie im Hinblick auf ihre Oxidationseigenschaften den Einkristalloberflächen ähneln. Für hinreichend kleine Partikel ist von einer erhöhten Reaktivität auszugehen. Es gilt zu klären, auf welcher Größenskala sich große und kleine Teilchen in ihren Oxidationseigenschaften voneinander unterscheiden.

Bei Pd/MgO(100)-Teilchen mit einem Durchmesser zwischen 4 nm und 24 nm wurde das PdO-Wachstum in einem kombinierten Experiment untersucht. Um eine identische Behandlung der Teilchen mit verschiedenen Durchmessern zu gewährleisten, wurde eine Streugeometrie mit Hochenergieröntgenbeugung verwendet. Zu diesem Zweck wurde eine Probe hergestellt, bei der auf das MgO-Substrat Streifen mit verschiedener mittlerer Pd-Dicke aufgedampft wurden, was entsprechend zu verschiedenen durchschnittlichen Teilchendurchmessern führt. Durch Rastern der Probe mit dem Röntgenstrahl konnte von der gewünschten Teilchengröße das Beugungssignal gewählt werden. Durch Analyse des Pd(111)-Reflexes wurde die Teilchengröße ermittelt. Bei der verwendeten Photonenenergie von 85 keV ist es nicht notwendig, die Probe zu drehen, um das Profil des Braggreflexes entlang einer hochsymmetrischen Richtung im reziproken Raum abzufahren. Bei der für oberflächenempfindliche Röntgenmessungen üblichen Strahlung im Bereich von 10 keV wäre bei einer vergleichbaren kombinierten Probe nicht gewährleistet, dass mit dem Röntgenstrahl nur eine definierte mitt-

lere Teilchengröße abgetastet wird.

Die Oxidation wurde in zwei Schritten mit einem Sauerstoffdruck von 0.3 mbar und 56 mbar durchgeführt. Es hat sich herausgestellt, dass es drei Bereiche von Teilchendurchmessern gibt, die sich in ihrem Oxidationsverhalten unterscheiden. Es kommt darauf an, ob die Teilchen kleiner als 5 nm oder größer als 9 nm sind (Abb. 5). Bei allen Teilchengrößen bildet sich PdO im ersten Oxidationsschritt. Jedoch sieht man bei den großen Teilchen mit D $>$ 9 nm eine deutliche Verkleinerung des metallischen fcc-Kerns, während sich die durchschnittliche Größe bei den kleinen und mittleren Teilchen kaum ändert. Ein anderes Verhalten tritt jedoch im zweiten Oxidationsschritt bei 56 mbar auf. Bei den großen Teilchen ist keine weitere Veränderung der Teilchengröße zu beobachten. Die mittleren Teilchen zeigen eine deutliche Abnahme in ihrer Größe, während die kleinsten Teilchen mit D $<$ 5 nm vollständig oxidiert werden. Ein weiterer Unterschied zeigt sich in der Orientierung des PdO. Bei kleinen und mittleren Teilchen ist der PdO(101)-Reflex so orientiert, wie es für epitaktisch orientieres PdO/MgO(100) nach [18] für 6 nm große Pd-Teilchen zu erwarten ist. Bei den großen Teilchen mit einem Durchmesser über 9 nm beobachtet man neben dem epitaktischen Oxid auch Debye-Scherrer-Ringe, die sich polykristallinem PdO zuordnen lassen.

Bei kleinen und mittleren Teilchen erfolgt die PdO-Bildung in Zusammenhang mit einer Verkleinerung der Pd Partikel. Bei den großen Pd Partikeln wächst das Oxid jedoch unmittelbar als polykristalline Schicht auf den Partikeln, die als passivierende Barriere gegen die weitere Oxidation des Partikels wirkt.

Oxidation von Rh- und Pd-Teilchen auf α-Al_2O_3(0001)

Um die Oxidationseigenschaften von Rh und Pd Teilchen in weiteren Kristallorientierungen zu untersuchen, wurde die α-Al_2O_3(0001)-Oberfläche als Träger gewählt. Die Teilchen wachsen in (111)-Orientierung mit einer $\left(\sqrt{3} \times \sqrt{3}\right) R30°$-Beziehung zum Substrat auf. Zusätzlich wurden (110)-orientierte epitaktische Teilchen beobachtet.

Die Palladiumteilchen hatten einen Durchmesser von 4 nm und eine Höhe von 3 nm. Das Verhalten der Teilchen in einer Sauerstoffatmosphäre wurde bei 570 K und 670 K untersucht. Bei Sauerstoffdrücken oberhalb von 10^{-7} mbar wurde eine Abnahme der Intensität des Pd Bragg-Reflexes festgestellt. Die Absenkung des Pd-Signals konnte auf zwei Arten rückgängig gemacht werden. Durch Abpumpen des Sauerstoffs konnte das ursprüngliche Signal zurückerhalten werden. Eine deutlich beschleunigte Rückbildung erfolgte durch den Einlass von Kohlenmonoxid. Es ist davon auszugehen, dass sich unter den experimentellen Bedingungen chemisorbierter Sauerstoff bildet, der zu einer Auslenkung der Metallatome an der Oberfläche aus ihren fcc-Positionen führt und somit die Intensitätsabsenkung auslöst. Bei T = 670 K wurde auch eine geringe Verbreiterung der Braggreflexe festgestellt, was ebenfalls mit einer Verkleinerung des fcc-Kerns

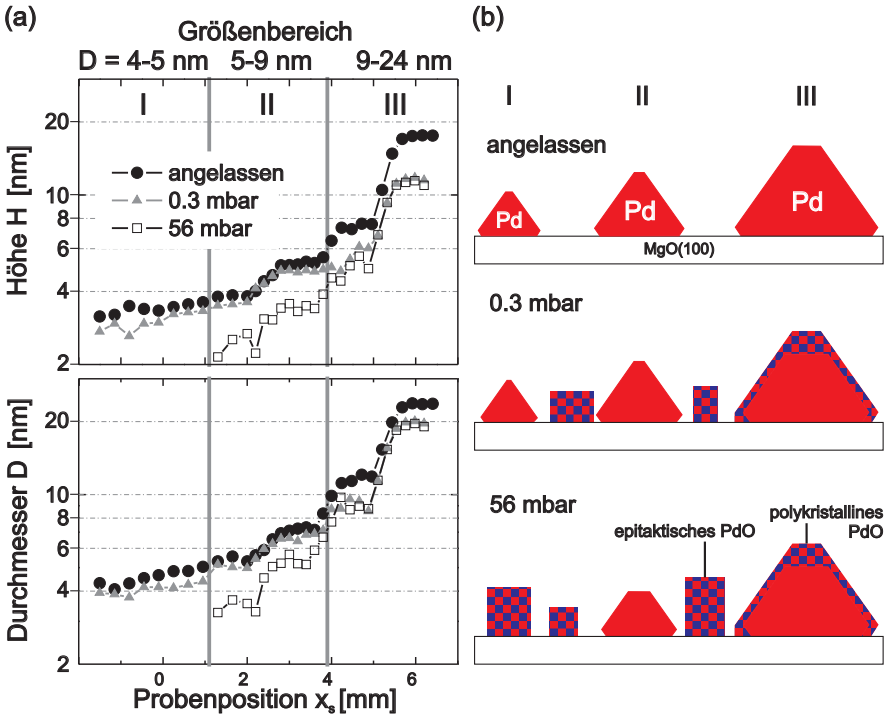

Abb. 5: Größenabhängigkeit der Oxidationsmechanismen von Pd Partikeln. (a) Anfangsgröße der Teilchen und bei zunehmendem Sauerstoffdruck. (b) Kleine Teilchen werden vollständig oxidiert und epitaxtisches PdO wächst, große Partikel werden von einer polykristallinen Oxidhülle umgeben.

der Teilchen zu erklären ist. Bei einem Sauerstoffdruck von 5 mbar nahm das Pd-Signal deutlich ab und ist bei 18 mbar vollständig verschwunden. Das dabei entstandene PdO wächst epitaktisch in (001)- und (100)-Orientierung auf. Der für die PdO-Bildung notwendige Sauerstoffdruck ist erheblich höher als aus dem theoretischen Phasendiagramm zu für die PdO-Bildung zu erwarten ist. Unter entsprechenden Bedingungen wäre auf den Einkristalloberflächen mit den Oberflächenoxiden zu rechnen, die das Wachstum von Volumenoxid verhindern. Es ist davon auszugehen, dass auch auf den Pd-Teilchen die Oberfläche von chemisorbiertem Sauerstoff belegt wird, der als kinetische Barriere das Wachstum des PdO-Volumenoxidphase erschwert.

Die (111)-orientierten Rh-Teilchen auf Saphir hatten einen Durchmesser von 5 nm und eine Höhe von 3 nm und somit eine zwar ähnliche Größe wie die Pd-Teilchen, aber eine flachere Form. Das Volumenoxid Rh_2O_3 wächst bei einer Temperatur von 670 K und einem Sauerstoffdruck von 10^{-4} mbar auf. Dieser Wert ist in Übereinstimmung mit dem theoretischen Phasendiagramm für die Bildung von Rhodiumoxid auf Rhodiumoberflächen. Rh_2O_3 hat wie Saphir eine Korundstruktur und wächst mit paralleler Orientierung seiner Kristallachsen auf dem Saphirsubstrat auf, darüberhinaus gibt es Domänen, die um 30° gedreht sind. Um einen möglichen Einblick in die Struktur katalytisch aktiver Teilchen zu gewinnen, die Oxidations- und Reduktionszyklen durchlaufen, wurde die Probe anschließend mit Kohlenmonoxid reduziert. Es konnte beobachtet werden, dass neben dem epitaktischen Rh auch polykristallines Rh mit einer etwa doppelten Teilchengröße als die anfänglichen epitaktischen Rh-Teilchen gebildet wurde. Bei einer erneuten Oxidation wurden die Teilchen wieder vollständig oxidiert, was zu polykristallinem Rh_2O_3 führte. Dies ist ein Hinweis darauf, dass das Rh_2O_3 unmittelbar auf den Rh-Partikeln wächst, und die Nukleation von Rhodiumoxid nicht oder nicht ausschließlich auf dem Substrat stattfindet und dass sich bei Zyklen aus Reduktion-Oxidation die Oberflächenmorphologie erheblich verändert.

Oxidation von Pd/MgO(100) Partikeln O_2/CO-Gemischen

Es wurde das Oxidationsverhalten von Pd/MgO(001)-Teilchen mit einem Durchmesser von 9 nm in Gemischen von CO/O_2 bei T = 570 K und Drücken im Bereich von 100 mbar untersucht. Für die in situ Beobachtung wurde oberflächenempfindliche Röntengbeugung angewandt, zusätzlich wurde die Probe nach den Oxidationsexperimenten mit TEM und verschiedenen spektroskopischen Methoden untersucht. Es konnte gezeigt werden, dass sich in den Gasgemischen eine neue Phase bildet, die durch den Einbau von Kohlenstoffatomen in die Pd-Teilchen entsteht. Dieser Kohlenstoffeinbau führt zu einer Vergrößerung der Netzebenenabstände auf die Werte von MgO. Gleichzeitig bildet sich eine etwa 100 nm dicke Abdeckschicht aus, die Magnesium, Sauerstoff und Kohlenstoff enthält (Abb. 6). Diese Abdeckschicht führt zu einer Deaktivierung der Teilchen. Eine

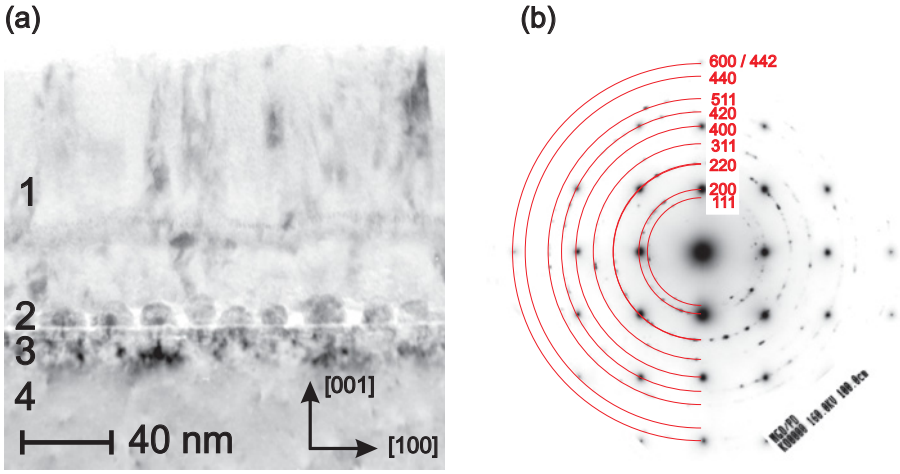

Abb. 6: Durch die Oxidation von Pd-Teilchen in einer 1:1 O_2/CO-Mischung bildet sich eine ≈ 100 nm dicke Abdeckschicht aus (1). Dabei nehmen die Pd-Teilchen (2) C-Atome auf, die zur Anpassung des Gitters an das MgO-Substrat führen (3, 4). Im Elektronenbeugungsbild (b) lassen sich alle Netzebenenabstände denen von MgO zuordnen. An der Grenzfläche zwischen Pd-Teilchen und Substrat liegt MgO in kleinen Kristalliten vor (3).

wichtige Erkenntnis aus diesen Experimenten ist, dass durch Beteiligung des Substrates unter atmospährennahen Drücken neue Reaktionspfade ermöglicht werden, mit denen weder aus UHV-nahen Studien von Nanopartikeln noch aus den Eigenschaften der Einkristalloberflächen zu rechnen war. Dies untermauert, wie wichtig es ist, Modellkatalysatoren auch unter atmosphärennahen Druckbedingungen zu untersuchen.

Chapter 1

Introduction

1.1 Oxidation of Nanoparticles

The world market for the production of chemicals is estimated today to be around 1,300 billion Euros per year. More than 90% of these chemicals are produced via a catalytic process [1]. The challenge for fundamental research is to experimentally access and understand the microscopic processes which take place in catalytic reactions. Oxide-supported metal nanoparticles are the building blocks of heterogeneous catalysts that are used in chemical reactions in industry and in catalytic converters in car exhausts. Among the many catalytically active materials are the 4d transition metals Ru, Rh, Pd and Ag which are applied for a number of important chemical reactions. For example, Palladium is used for the hydrogenation of ethylene or methane oxidation. Furthermore, it is a constituent of three-way catalytic converters in automotives for the oxidation and reduction of harmful exhaust gases like CO or NO_x [2, 3]. Rhodium also plays an important role in this field [4]. These key applications of Rh and Pd have triggered a demand for a detailed insight into the catalytic properties and the involved chemical reactions on an atomic scale. An understanding of the relationship between structure and catalytic properties aims on the development of tailor-made future catalysts with an enhanced performance with respect to an increase of turnover frequencies, an increased catalyst lifetime and a higher reaction selectivity. For oxidation reactions it has not been generally solved whether the chemisorbed oxygen, ultrathin surfaxce oxide films or the bulk oxides are the catalytically most active phases. In this context, its worth discussing metal oxide phases. The term bulk oxide denotes such oxygen compounds with the same atomic structure as oxides occurring on macroscopic scales. The *surface oxides* are ultrathin films with a well-defined thickness and an atomic structure different from the bulk oxides. An example for such a surface oxide is the O-Rh-O trilayer which can be grown on the Rh(111) surface upon oxygen exposure [11]. The involvement of chemisorbed oxygen leads to a Langmuir-Hinshelwood mechanism, while the involvement of

bulk oxides leads to a Mars-van-Krevelen reaction mechanism [5, 6, 7]. In the first case, the reactants (including oxygen) are adsorbed on the surface where they react to the product, which finally desorbs from the surface. A very well known example is the CO oxidation on Pt(110). In the latter case, the reactant is firstly adsorbed. The proceeding oxidation reaction is not mediated by oxygen from the gas atmosphere, but from chemically bound oxygen within the carrier material. After desorption of the oxidized reactant, the carrier is finally reoxidized from oxygen stemming from the gas phase.

Much fundamental insight into catalysis on an atomic scale has come from studies of single crystals under controlled conditions. Very well-known examples of these works are the results by G. Ertl[1] on the oxidation of carbon monoxide on the Pt(110) surface as well as the explanation of the catalysis within the Haber-Bosch process of ammonia synthesis [8, 9]. Real catalysts consisting of nanoparticles are more complex. During a chemical reaction, their shape, size and atomic structure of the surface may change. Typically, crystalline nanoparticles are limited by low-index crystal surfaces. Studies of the corresponding single-crystal surfaces give insight into the structure of relaxations and reconstructions stemming from the influence of adsorbates. The shape of nanocrystals is important for their catalytic activity. It determines to which amount the different crystallographic surfaces are present, of which each may have a different chemical reactivity. Furthermore, the shape of the particles determines its edges which can also play a role for the catalytic activity, as was shown for the hydrogenation of aldehydes on gold nano crystals [10]. Suitable model systems to understand the processes occurring on the edges of particles are vicinal surfaces. Still, in case of simple model systems, it is not generally clear whether the properties of the model systems also hold for technical catalysts. The enhanced catalytic activity of nanoparticles is assigned to the following differences from the corresponding low index single crystal surfaces:

- On nanoparticles, there co-exist several low-indexed surfaces whose size may change during a chemical reaction.
- The coordination of nanoparticles is reduced at the corners and edges of the facets.
- Due to the reduced dimensions and influence of the support, the electronic properties may be changed.
- At the metal-support interface, chemically more active sites may be created, or even the support may participate in the chemical reaction.

The lack of knowledge to which amount the properties of single crystal surfaces are also valid for supported nanocrystals is denoted the *materials gap* in

[1] laureate of the Nobel prize in chemistry 2007

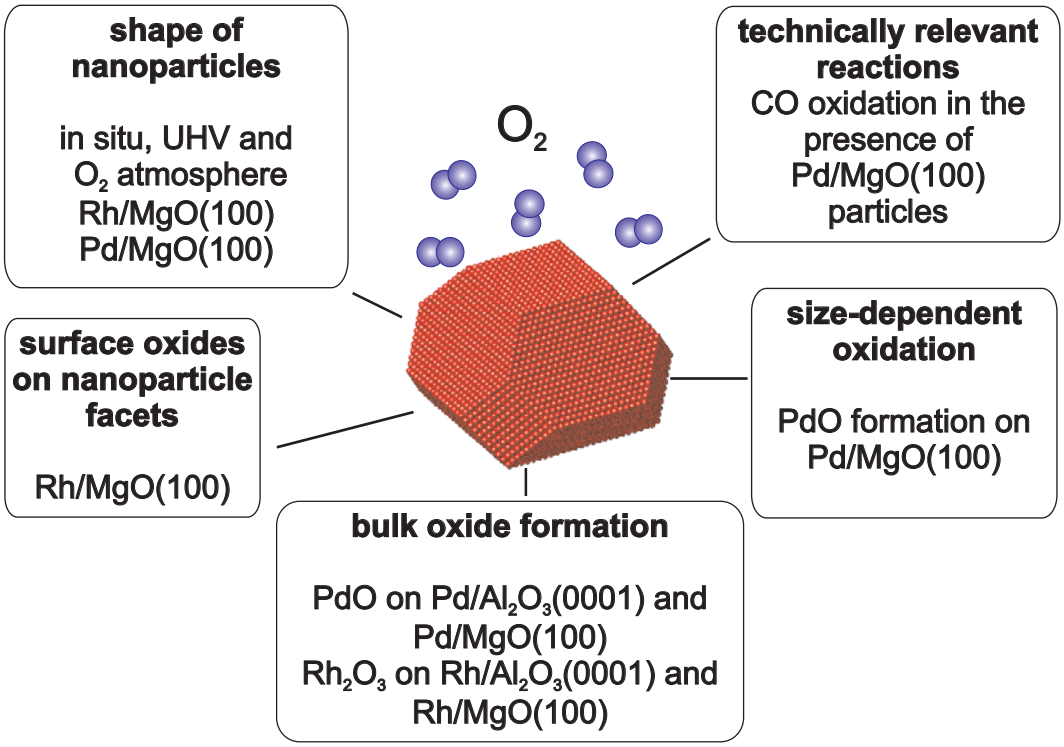

Fig. 1.1: Strategy followed in this work to approach chemical reactions under technically relevant conditions.

surface science. Another aspect is the pressure range under which the oxidation properties of particles are studied. In technical applications, the pressure may exceed several atmospheres which is a big challenge for the application of *in situ* surface analysis methods, this means the studies of a system in the same environment where the chemical reaction takes place. Prior to the advent of high pressure XPS, STM and TEM, the applicable pressure range was restricted to high vacuum for electrons as surface sensitive probes. The according lack of knowledge if the results obtained in high vacuum also hold for the technical processes is denoted the *pressure gap*.

These gaps can be closed if the processes are directly studied on the surfaces of nanoparticles on oxide supports and by applying in situ methods which are compatible with technologically relevant pressure and temperature conditions. A suitable experimental method for in situ studies is x-ray diffraction which has no intrinsic limitation of the applied gas pressures and was therefore used as the main technique within this work.

1.2 Key Questions

Even though the catalytic behavior of single crystal and vicinal surfaces has been well investigated today [9, 8, 19, 20, 21], much less has been known and understood about the atomic scale structure of catalytically active nanoparticles during the reaction. The following key questions on the oxidation properties of nanoparticles were studied within this thesis:

Particle Shape

It was observed by in situ and ex situ transmission electron microscopy, that metal nanoparticles undergo shape changes as a function of the gas composition [22, 23, 24]. Shape changes of unsupported Pd and Rh nanoparticles were investigated by density functional theory as a function of the oxygen chemical potential using the Wulff construction [25]. For Rh, it is predicted at chemical potentials close to bulk oxide formation that surface oxides stabilize the low index (100), (110) and (111) facets, resulting in a rounding of the particles. A complete microscopic understanding of the behavior of the catalytically active nanoparticle can only be achieved if the shape change of the nanoparticle can directly be related with the oxidation process itself. This implies that one is able to follow quantitatively the change of the facets of the nanoparticle simultaneously with the structural changes which take place at the facets themselves and at the interface to the oxide support.

Surface Oxides on Particles

Theoretical and experimental studies on the oxidation of of 4d transition metal single crystal surfaces [26, 27, 11, 28] suggest that the catalytic activity is related to an ultrathin metal oxide film on the surface. It has not been clear yet if these surface oxides form on nanoparticles, and if they are stable under the conditions of industrial catalysis.

Bulk Oxide Formation

It has been found experimentally for single crystal surfaces that the surface oxides can act as a kinetic barrier for the formation of bulk oxides and that a higher oxygen chemical potential needs to be applied than predicted by thermodynamics for the single crystal surfaces [29, 11]. Studies of bulk oxide formation on nanoparticles and a comparison with the theoretical phase diagrams of the single crystal surfaces can reveal if such barriers also exist for the nanoparticles or if bulk oxide formation is facilitated. In addition, from the epitaxial relationship between the oxide, the metallic nanoparticles and the support, conclusions can be made whether the oxide nucleation occurs on the support material or directly on the nanoparticle [18].

Size Dependent Oxidation

The activity of nanoparticles toward chemical reactions is observed to show a high size dependence for different metal/support combinations [14, 15, 16, 17]. For sufficiently large particles, one may expect oxidation properties comparable to single crystal surfaces and for sufficiently small particles, an enhanced reactivity is expected. It needs to be understood on which size scale distinct oxidation mechanisms exist.

Structure of Nanoparticles During CO Oxidizing Conditions

The previous points had the focus on the oxidation properties of the nanoparticles in pure oxygen atmospheres. However, for a definite identification of the catalytic active phases, the structure of the nanoparticles has to be studied during the chemical reaction and needs to be related with the formation of reaction products. Due to its high technical relevance and the simple feasibility of the experiment, the CO conversion into CO_2 was chosen as a model reaction.

These key questions are not completely independent, but have many cross connections. It will be shown that the shape changes are directly related with the formation of surface oxides, the surface oxides can act as kinetic barriers for the bulk oxide formation, the bulk oxide formation mechanism depends on the particle size, bulk oxides form under CO oxidation conditions etc.

1.3 Experimental Strategy

Within the research of this thesis, the oxidation properties of Rhodium and Palladium particles supported by MgO(001) and $\alpha-Al_2O_3(0001)$ were studied. Thereby, the substrate determines the orientation of the particles. The in situ oxidation studies were performed with synchrotron x-ray diffraction, which offers the following advantages, as compared to microscopy methods. A wide pressure and temperature range is applicable that is only limited to the capabilities of the applied vacuum chambers, which is important to overcome the pressure gap. The diffraction signal is averaged over an area of several mm^2 of the sample and therefore represents the typical statistically relevant behavior of the studied system. Diffraction can be applied as a shape sensitive method, as for epitaxially grown particles, the shape can be identified from the intensity distribution of maps in reciprocal space. This reciprocal space mapping is sensitive towards slight changes on the particle shape which are induced by an oxygen atmosphere. For a quantitative description of these shape sensitive measurements, an intensity simulation tool was developed by using straightforward kinematic diffraction theory. As a prerequisite for such shape sensitive diffraction experiments, growth conditions had to be found under which the particles grow epitaxially. Selected

samples were not only subject of in situ x-ray diffraction experiments, but were also studied under ex situ conditions with high-resolution transmission electron microscopy and spectroscopy techniques.

Basically, five key questions were studied with four metal/support combinations, which motivated a voluminous number of possible pertinent experiments. The choice of the metal/support combination to answer each key question was inspired by the following arguments. Firstly, the bulk oxide formation of Pd/MgO(100) particles had already been well understood [18] at the beginning of this research. Secondly, the studies should be as comprehensive to bear similarities and differences between the Rh and Pd particles. Finally, the studies should allow a comparison of the oxidation properties of the nanoparticles with the corresponding single crystal surfaces. Figure 1.1 gives an overview of the key questions and the choice of material systems for which according in situ oxidation experiments were performed.

1.4 Outline of the Thesis

The above mentioned key questions are the leitmotif of the thesis. In chapter 2, the basic properties of the relevant material systems are described, concerning the growth of nanoparticles and the oxidation properties of the Rh and Pd low index surfaces. An overview of the applied experimental methods is given in chapter 3, where the focus is set on shape sensitive x-ray diffraction. Further experimental techniques that were applied for a characterization of the samples are described in chapter 4. It is followed by the chapters of the experimental results.

Chapter 2

Growth of Nanoparticles and Oxidation of Rh and Pd Single Crystal Surfaces

In this chapter, the general properties on the growth and shape of nanoparticles are depicted that are excerpted from review articles concerning the growth of model catalysts [30, 31, 32, 33]. These articles also contain more details about distinct metal/support combinations of model catalysts. It is followed by a delineation of the oxidation properties of the low-index Rh and Pd single crystal surfaces, e.g. the formation and structure of the surface oxide and bulk oxide phases. Finally, the crystal structures of the support materials MgO and α-Al_2O_3 are described.

2.1 Growth and Shape of Nanoparticles

In technical applications of catalysis, the transition metals are dispersed over a suitable support in order to increase the surface area of the active phase. Several approaches have been applied for the growth of model catalysts. As supports, polycrystalline or amorphous oxide substrates can be used, which are close to the systems applied in technical catalysis. A second implementation is to use oxide thin films which can be grown by thermal oxidation from pure metal or metal alloy single crystals. As electrical conductivity is maintained, oxide thin films as support of metal nanoparticles are suitable for scanning electron microscopy studies. A compendium of such thin oxide films is given in ref. [31]. However, the applied temperature and pressure conditions to oxidize the metal nanoparticles may lead to a destabilization of the thin oxide film. This can be overcome, though on the cost of electric conductivity, by using oxide single crystals as a support for the metal nanoparticles. These model catalysts are suitable e.g. for x-ray diffraction, atomic force microscopy and transmission electron microscopy. A

review of different metals on various single crystal supports can be found in ref. [30]. There are different preparation methods of how the metal is deposited on the support. One possibility is the impregnation in solution which is a method related closely with technical catalysts. Alternatively, vapor deposition of metals can be applied, which is the deposition method for all samples prepared within the research for this work.

2.1.1 Principles of Nucleation and Particle Growth

The initial step of a growing particle is the adsorption of metal atoms on the surface, with a net sticking coefficient typically close to one. Subsequently, the atoms diffuse on the surface. For the actual growth process of a nanoparticle, two distinct mechanisms exist, either heterogeneous or homogeneous nucleation. In the first case, a diffusing metal atom may be trapped by a defect of the support. This trapped adatom serves as a nucleation center for the other diffusing metal atoms. In the case of homogeneous nucleation, several adatoms aggregate on regular sites. For thermodynamic reasons, a critical cluster size is necessary for the stability of this nucleus. If the particle has reached this minimum size, further diffusing metal atoms may be trapped which leads to the ongoing growth of the particle, otherwise, islands below this size can dissolve again [31]. In case of homogeneous nucleation, there exists a critical density of nuclei $N \propto \left(\frac{F}{D}\right)^{\frac{1}{3}}$, which depends on the deposition rate F and the diffusion coefficient D. After reaching saturation density, no further nuclei form and all diffusing metal atoms are captured by the existing nuclei.

Whether the growth of the deposited material occurs as islands or as a wetting film follows from the surface energies of the metal and the support and the interfacial energy. The surface energy γ is defined as the energy required to increase the surface of a material, which can be understood as the evaded energy that would have been gained to form bonds within the material with a smaller surface. Accordingly, the interfacial energy γ_{int} describes the energy per area that is gained when bonds between two materials are formed. For the growth of a two-dimensional film (Frank-van-der-Merwe growth), the equation $\gamma_{int} + \gamma_{metal} < \gamma_{substr}$ is fulfilled. Otherwise, the three-dimensional Vollmer-Weber growth mode takes place. Usually, $\gamma_{metal} > \gamma_{oxide}$ and three-dimensional island growth occurs for metal on oxide supports.

2.1.2 Equilibrium Shape of Crystals

To understand the shape of a nanoparticle, one may first consider the equilibrium shape of a crystal. The equilibrium shape of a crystal is described by the Wulff-theorem, which is the minimization of the total surface free energy of a crystal at a given volume and temperature. If the surface energy of a material is isotropic as

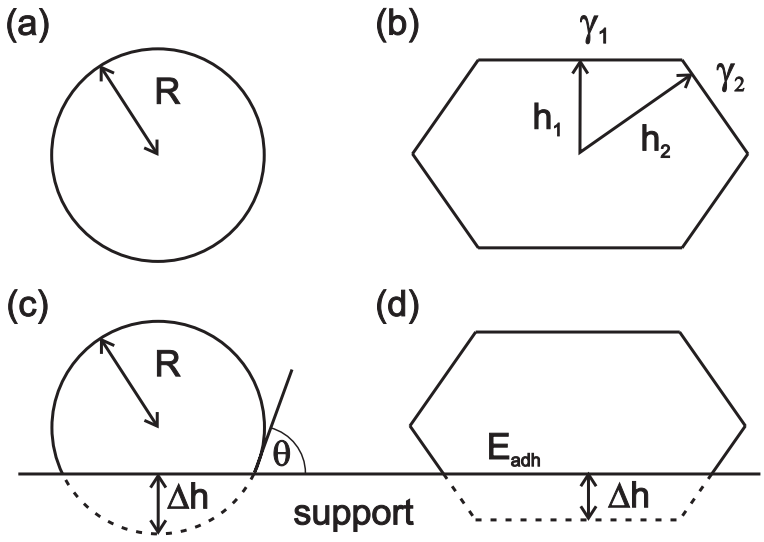

Fig. 2.1: Equilibrium shape of an unsupported medium with isotropic surface energy (a), anisotropic surface energies (b) and accordingly truncated on the bottom due to the influence of the support (c, d).

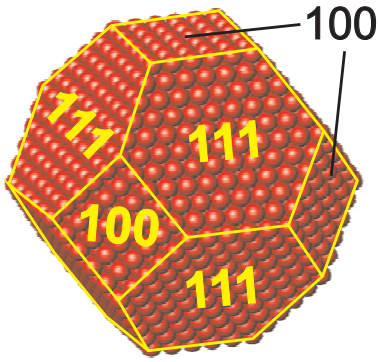

Fig. 2.2: Unsupported fcc-crystal with $\frac{h_{100}}{h_{111}} = \frac{2}{\sqrt{3}}$.

for liquids, the according equilibrium shape is a sphere (fig. 2.1 a). In crystalline solids, the surface energy is anisotropic. The according distance of the limiting planes from the center of the crystal belonging to the lowest possible surface energy are described by the Wulff theorem. It is given by the equation

$$\frac{\gamma_i}{h_i} = const. \tag{2.1}$$

The according shape of the crystal is denoted as the Wulff shape. Thereby, γ_i is the surface free energy of a facet and h_i its distance from the center of the nanoparticle (fig. 2.1 b).

The influence of the support on the shape of a liquid droplet leads to a truncation at the interface. The associated wetting angle θ is described by the Young equation $\cos\theta = \frac{\gamma_s - \gamma_{int}}{\gamma_l}$. This angle is usually considered as a measure of the adhesion of the droplet on the support. Equivalently, the adhesion can be quantified by the truncation Δh of the sphere $\Delta h/R = \gamma_{adh}/\gamma_s$. In analogy, a crystal on a support has a truncated shape in comparison with the unsupported crystal in equilibrium (fig. 2.1 b, d). This truncation Δh is considered in the Wulff-

Kaischiew-theorem and is quantified as

$$\Delta h/h_i = E_{adh}/\gamma_i. \tag{2.2}$$

Note, that the wetting angle of a droplet may not be applied for the angle between a particle facet and the surface. This latter angle is only determined from the crystallographic orientations of the facets. A variation of the adhesion energy changes only how strongly the particle is truncated on the bottom side by Δh, but the "contact angle" remains unaffected.

For an fcc crystal, the shape is limited by eight (111) facets and six (100) facets if only nearest neighbor interaction is taken into account in energy considerations. The anisotropy of the surface energy is $\frac{\gamma_{(100)}}{\gamma_{(111)}} = \frac{2}{\sqrt{3}} \approx 1.15$. An according crystal is sketched in (fig. 2.2). However, for nanoparticles the macroscopic Wulff-shape may be valid only restrictedly. In the Wulff-construction, the lower coordination of the atoms on the edges is not taken into account. It can be shown [34] that for small particles, the fraction of (100) facets drops when the particle size decreases, which leads to octahedra terminated only by (111) facets. Finally, for very small particles (clusters), arrangements of the atoms different from the bulk crystal structure occur, e.g. an icosahedral or dodecahedral arrangement of the atoms can be more stable [35, 36, 37].

2.1.3 Shape of a Nanoparticle in a Gas Atmosphere

The shape of a nanoparticle is determined by the surface energies of the facets. During chemical reactions, when the particle is exposed to a gas atmosphere, the influence of the ambient media (e.g. oxygen) on the surface energies needs to be considered. The according surface energy changes can be described [33] by $d\gamma = -\sum_i \Gamma_i d\mu_i$, where μ_i is the chemical potential of the ith species and Γ_i is its concentration. For a single gas species, the variation of the surface energy as a response to the pressure is $d\gamma = -k_B T \Gamma_g(P) dP/P$. An example for Pd particles is given in ref. [24], where an increase of the (100) facets is calculated upon oxygen exposure of the particle. In a more recent study [25] on the morphology of mesoscopic Rh and Pd particles, the adsorption of oxygen on the low index surfaces (111), (110) and (100) as well as on the stepped surfaces (311), (211) and (331) was calculated. At pressures below experimentally realistic UHV conditions, the (111) and (100) facets are dominating the shape of a Rh particle, but also a fraction of the considered stepped surfaces exists. At experimentally realistic UHV conditions, the stepped surfaces of Rh do not play a decisive role. Upon oxidation, the (110) and (100) facets become more pronounced on the cost of (111) facets. In contrast, for Pd particles, under experimentally realistic UHV conditions, there is a significant contribution of (110) and (311) facets, whereas at chemical potentials of oxygen closely below -1eV, (331) facets grow on cost of the (110) facets. At higher chemical potential of oxygen, the particle shape is

dominated by (111) and (100) facets, whereas the fraction of (110) facets is only small.

2.1.4 Kinetic Shape of Nanoparticles

The morphology of a nanoparticle can deviate from its equilibrium shape. One aspect is the possible different growth velocities at different faces. Secondly, the environment may be anisotropic, e.g. from an anisotropic diffusion of the metal atoms one can expect an anisotropy of the growth of the emerging particle. There are further arguments why the shape may differ from equilibrium shape. There may be different activation energies for the up stepping and down stepping of the diffusing metal atoms. Due to the preferred adsorption of the adatoms on the edge of an island, there may be a net effect of down stepping than with up stepping. On the other hand, for sufficiently large islands, the net down stepping may be overcome, if homogeneous nucleation takes place on the island. It has been reported that islands may thicken, even after the evaporation process has been stopped, which is denoted as self-thickening [31]. An important aspect of deviations from the equilibrium shape is the coalescence of the particles. If two particles touch each other during growth, this will lead to an anisotropic shape. Only due to an increased surface diffusion at more elevated temperature, the atoms can rearrange to a regular particle shape [33].

2.2 Concepts of Oxidation

For the growth of oxide layers on metal surfaces, several models exist that describe successfully the experimentally observed properties [38]. For example, the thickness of a growing oxide layer can be described by the formation of oxide and meal ions at the interfaces between the metal, the oxide layer and the oxygen atmosphere. The growth proceeds via the diffusion of the ions in the oxide layer. As soon as a stable oxide layer has formed, the transport of the ions can be described via a diffusion equation of the ions in an electric field [39]:

$$J_i(x,t) = -D_i \frac{dC_i(x,t)}{dx} + \mu_i E C_i(x,t) \tag{2.3}$$

Thereby, D_i is the diffusion coefficient, μ_i the mobility and $C_i(x,t)$ the concentration of an ion species i. Within the Mott-Cabrera-model, an Ohmic law is used for the ionic currents which leads to a parabolic growth law for the oxide thickness $d(t) \propto \sqrt{t}$. Oxidation is a process composited of several stages. Firstly, there must exist mechanisms for the creation of ions. The use of a diffusion equation to describe oxide growth is valid, if diffusion is the limiting step within the chain of single mechanisms. Oxidation may also be limited by the electron transport through the oxide layer, which leads to other time dependencies of the oxide

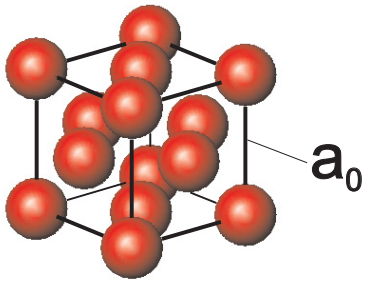

Fig. 2.3: Face centered cubic structure (fcc) of Rh (a_0 = 3.80 Å) and Pd (a_0 = 3.89 Å).

thicknesses. Details can be found in [38, 39]. In these descriptions, the initial state of oxide growth is not included, which is not sufficient for an understanding of oxidation on an atomic scale. More sophisticated and more suitable theoretical descriptions of the structures of oxides and phase diagrams that will be reviewed in the following sections were achieved by ab-initio density functional theory.

2.3 Oxidation of Rhodium Single Crystal Surfaces

In the following sections, an overview on the oxidation properties of the Rh and Pd single crystal surfaces is given. Rhodium is a 4d-transition fcc-metal with Z = 45 (fig. 2.3). Its lattice constant a_0 equals 3.80 Å. Rhodium has a density of $12.45\frac{g}{cm^3}$ and a melting temperature of 2237 K. Rhodium is frequently used in exhaust catalysts (pure or alloyed with Pt) and is also used as a coating material for x-ray mirrors, mirrors for visible light and finally as a coating material for jewelery. The electronic structure of Rh, concerning the band structure, density of states, Fermi surface, Compton profiles and x-ray form factors can be found in ref. [40]. Rh_2O_3 is the bulk oxide phase of Rhodium which occurs in a corundum structure. The unit cell is displayed in fig. 2.4. This structure corresponds to an hcp stacking of oxygen anions along the c-axis, with a slight displacement due to the Rh cations in two thirds of the oxygen interstices. Upon heating above 1020 K, it can be transformed into an orthorhombic form [41]. Another bulk oxide phase of Rh is RhO_2 with a rutile structure [42]. Its lattice constants are a = b = 4.4862 Å, c = 3.0884 Å, $\alpha = \beta = \gamma = 90°$.

2.3.1 Oxidation of the Rh(111) Surface

On Rh(111), several chemisorbed phases are reported. One phase is a p(2×2) structure with a coverage $\theta = 0.25$ and another p(2×2) structure at $\theta = 0.5$. For both types of reconstructions, the oxygen atoms are located at three-fold fcc-sites. Another structure of chemisorbed oxygen is reported in ref. [43]. It forms a $\left(2\sqrt{3} \times 2\sqrt{3}\right) R30°$-structure, but is thermodynamically instable. Besides these chemisorbed phases, an ultra thin oxide film can be grown on Rh(111) [11]. The

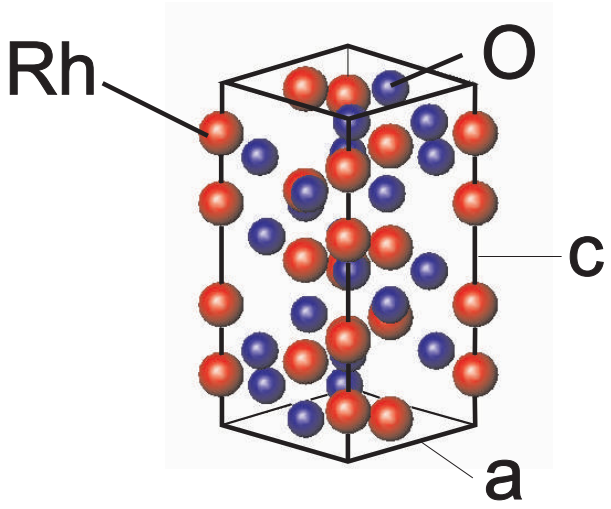

Fig. 2.4: Hexagonal unit cell of Rh_2O_3 with a = 5.127 Å and c = 13.853 Å [41].

structure of this film is plotted in fig. 2.6. This surface oxide consists of an O-Rh-O trilayer, with an hexagonal arrangement of the Rh atoms. As confirmed experimentally, this film forms a (8×8) on (9×9) super lattice with respect to the Rh(111) surface (as it is described in ref. [11], a very similar (7×7) on (8×8) structure would be slightly more stable, which is related to the lattice constants used in the DFT calculations). An interesting feature can be seen from the calculated phase diagram (fig. 2.5 a), with the values from ref. [43]. It shows the surface energy of the oxygen-adsorbed phases as a function of the chemical potential of the oxygen. The thermodynamically stable phase in such a plot is determined by the lowest surface energy at a given chemical potential. Interestingly, the O-Rh-O trilayer would only be stable if the bulk oxide phase did not exist. A pressure-temperature plot (fig. 2.5 a) can be obtained from the chemical potential of the metal/oxygen phases in equilibrium by applying the ideal gas equation $\mu_O(T,p) = \mu_O(T,p_O^0) + 1/2 k_B T \ln(p/p_O^0)$ for oxygen. It is found experimentally [11] that at T = 800 K and an oxygen pressure of 0.1 mbar the surface oxide forms even though the bulk oxide Rh_2O_3 is already thermodynamically stable. A pressure of 10 mbar is necessary to form Rh_2O_3, and the surface oxide acts as a kinetic barrier for bulk oxide formation.

2.3.2 Oxidation of the Rh(100) Surface

Several studies deal with oxygen-induced reconstructions on the Rh(100) surface. There exists a $p(2\times2)$ structure with a coverage $\theta = 1/4$ and a $c(2\times2)$ structure for $1/4 < \theta < 1/2$. A $p(2\times2)$-structure at $\theta = 1/2$ is known as the clock reconstruction [44, 45, 46, 47]. In a very early study [48], a (2×8) structure and another structure with $\theta = 1/3$ were reported, a (3×1)-structure also in ref. [49]. It is believed that the latter structure is identical to the $p(3\times1)$ phase observed on the $Pt_{25}Rh_{75}(100)$ surface [50]. The (2×8) phase from the early study turned

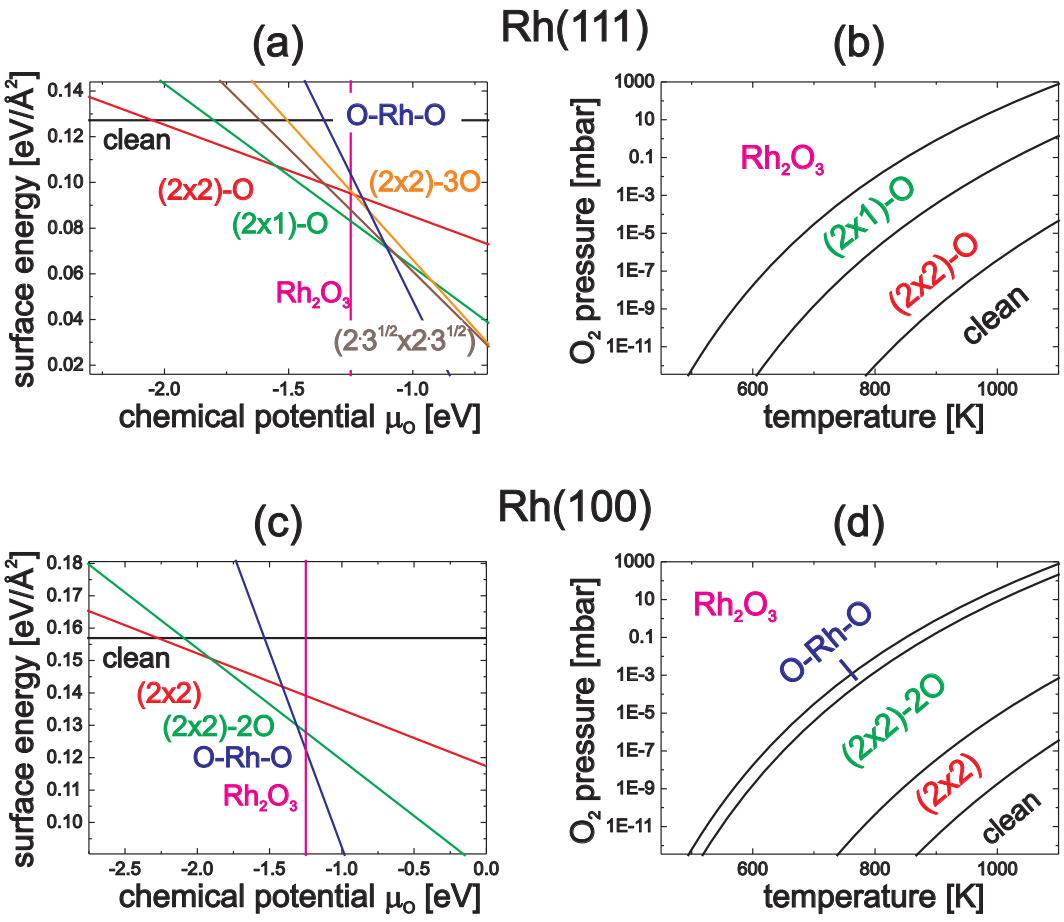

Fig. 2.5: Phase diagrams for the oxidation of Rh (111) and Rh(100) surface, determined by DFT calculations (adapted from refs. [43, 12]). The pressure-temperature diagrams (b, d) were obtained from the chemical potentials at the equilibrium points and by applying the ideal gas equation for oxygen.

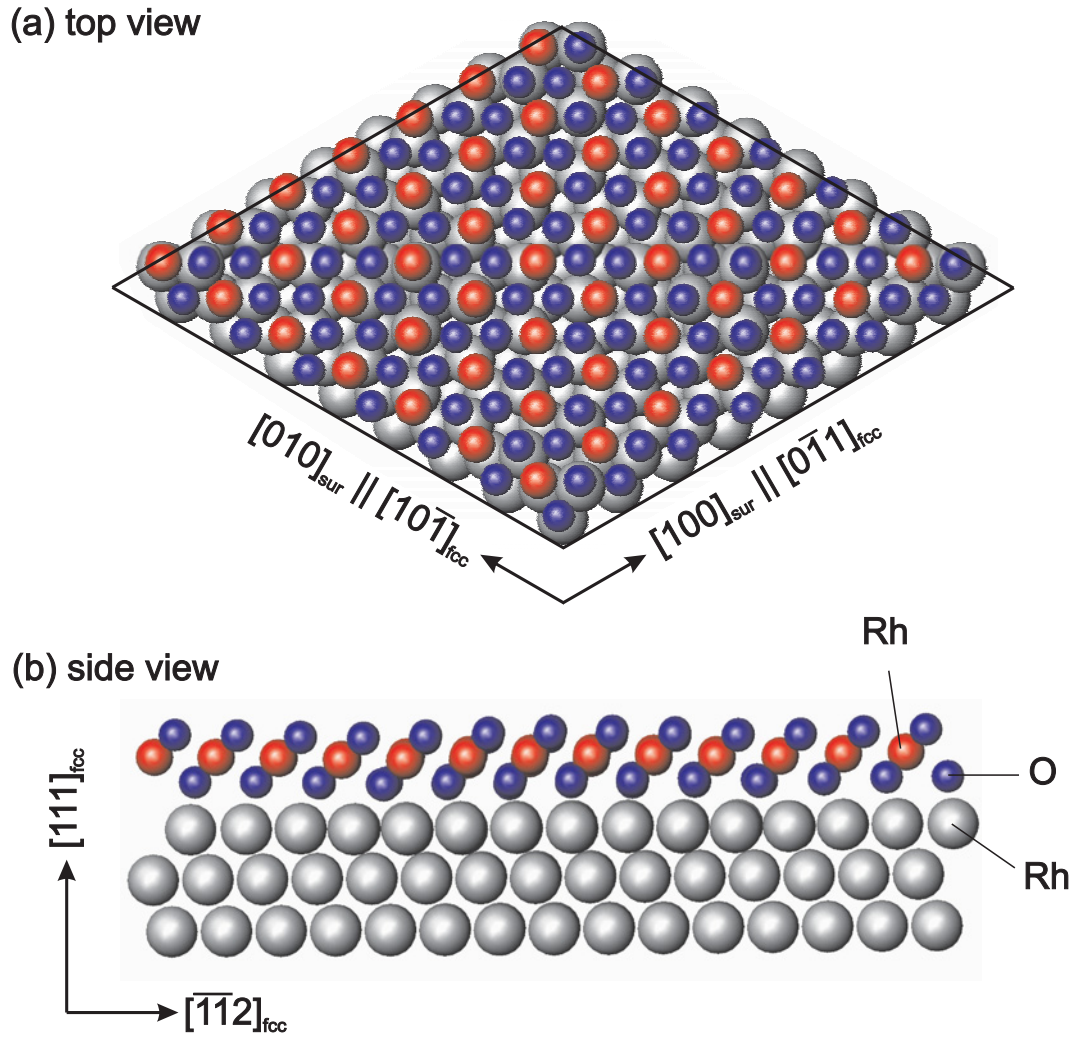

Fig. 2.6: Surface oxide on Rh(111). The atoms are arranged in a O-Rh-O trilayer. The plotted structure is the (7×7)/(8×8) reconstruction (coordinates provided by G. Kresse, TU Vienna) which is thermodynamically slightly more stable than the experimentally observed $(8 \times 8)/(9 \times 9)$ structure [11].

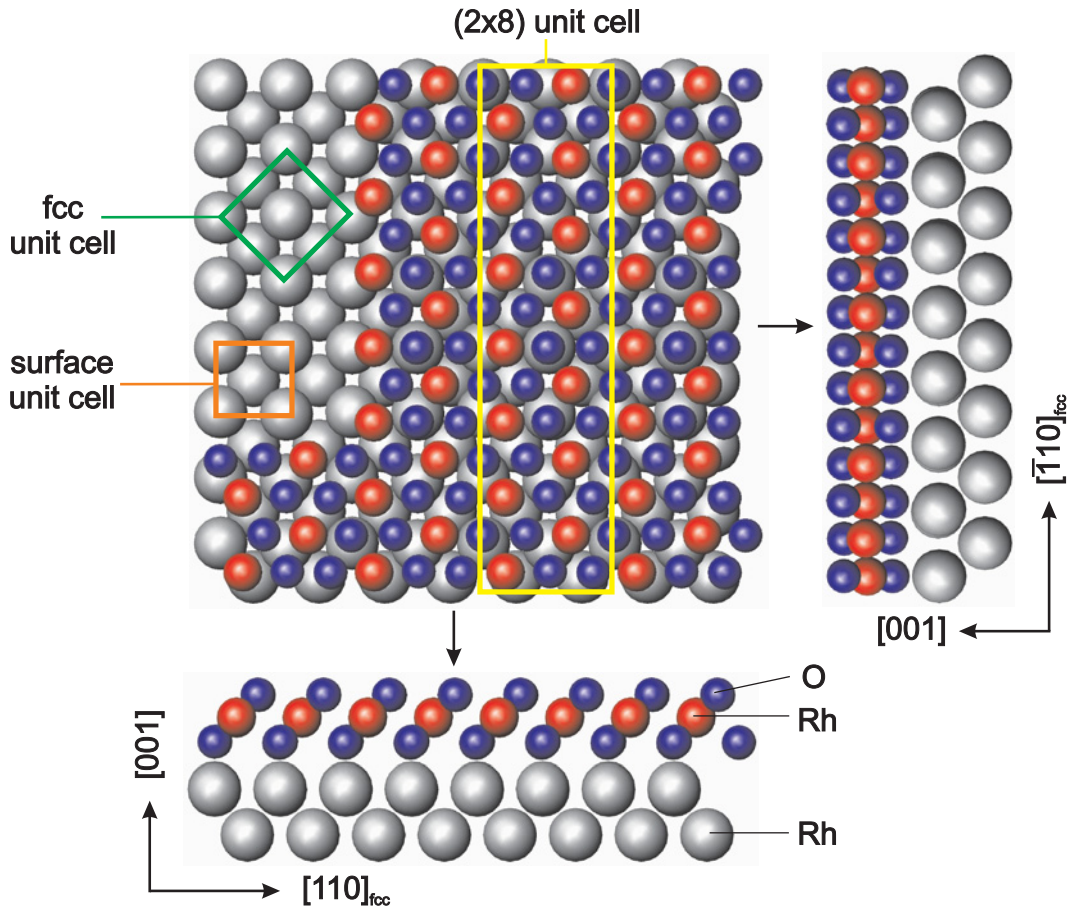

Fig. 2.7: The $c(2 \times 8)$ surface oxide on Rh(100) with the O-Rh-O trilayer structure. The atoms of the layer are arranged nearly in a hexagonal lattice. The green and the orange square show the orientation of the underlying Rh metal in standard fcc and surface coordinates respectively.

out to be a surface oxide with a $c(2 \times 8)$ structure forming an O-Rh-O-trilayer. The atomic arrangement within this phase was determined in a combined STM, HRCLS, SXRD and DFT study [12]. The structure of this film is plotted in fig. 2.7. It is formally $c(2 \times 8)$ structure, the atoms are arranged in such a way that it appears as an almost hexagonal structure. The phase diagram of oxygen on Rh(100) is plotted in fig. 2.5 (c, d). There exists a narrow stability region of 50 meV for Rh(100), where the surface oxide is stable, in contrast to Rh(111), where the surface oxide is thermodynamically not the most stable phase within the whole T-range. It is also reported that the core level spectra for the surface oxide on Rh(100) shows a high similarity with that on Rh(111) [11].

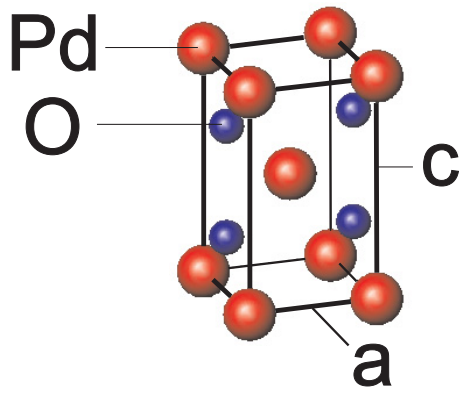

Fig. 2.8: Tetragonal unit cell of PdO with a = 3.03 Å and c = 5.33 Å [53].

2.3.3 Oxidation of the Rh(110) Surface

The initial oxidation of Rh(110) was studied by STM, core level spectroscopy and DFT [51]. It could be shown that a quasi hexagonal trilayer of O-Rh-O establishes which has a high similarity to the surface oxides on Rh(100) and Rh(111). The surface oxide on Rh(110) has a c(2×4) structure and was found experimentally at T = 750 K and p(O_2) = 10^{-4} mbar, or by using atomic oxygen at T ≈ 550 K in the 10^{-6} mbar range. The DFT calculations show that this structure is only metastable. Further chemisorbed structures are reported in ref. [52].

2.4 Oxidation of Palladium Single Crystal Surfaces

Palladium (Z=46) is a neighbor of Rhodium in the periodic table of elements. Its fcc-lattice constant a_0 equals 3.89 Å. Palladium has a density of 12.023 $\frac{g}{cm^3}$ and a melting temperature of 1828 K. Palladium can be found in Ni- and Cu-ores. Besides its applications in catalysis, Pd is used for jewelery in alloys with gold. An important technical application is hydrogen storage. The crystal structure of its bulk oxide phase PdO is displayed in fig. 2.8. It can be described by a tetragonal unit cell with two Palladium atoms located at $(0,0,0)$ and $\left(\frac{1}{2},\frac{1}{2},\frac{1}{2}\right)$ and two O atoms at $\left(\frac{1}{2},0,\frac{1}{4}\right)$ and $\left(\frac{1}{2},0,\frac{3}{4}\right)$ respectively.

2.4.1 Oxidation of the Pd(111) Surface

The oxidation of the Pd(111) surface is subject of a high number of experimental and theoretical studies studies [56, 57, 58, 59, 60] including DFT, LEED, STM and XPS. The thermodynamically stable phases of adsorbed oxygen are a $p(2\times2)$-structure of chemisorbed oxygen with θ=0.25, and the surface oxide phase Pd_5O_4. The atomic structure of the surface oxide is reported in [56] and is shown in fig. 2.10. It consists of a square unit cell with a lattice parameter $\sqrt{6}$ times the unit cell length $\frac{a_0}{\sqrt{2}}$ of the underlying Pd surface. Along one diagonal of the square unit

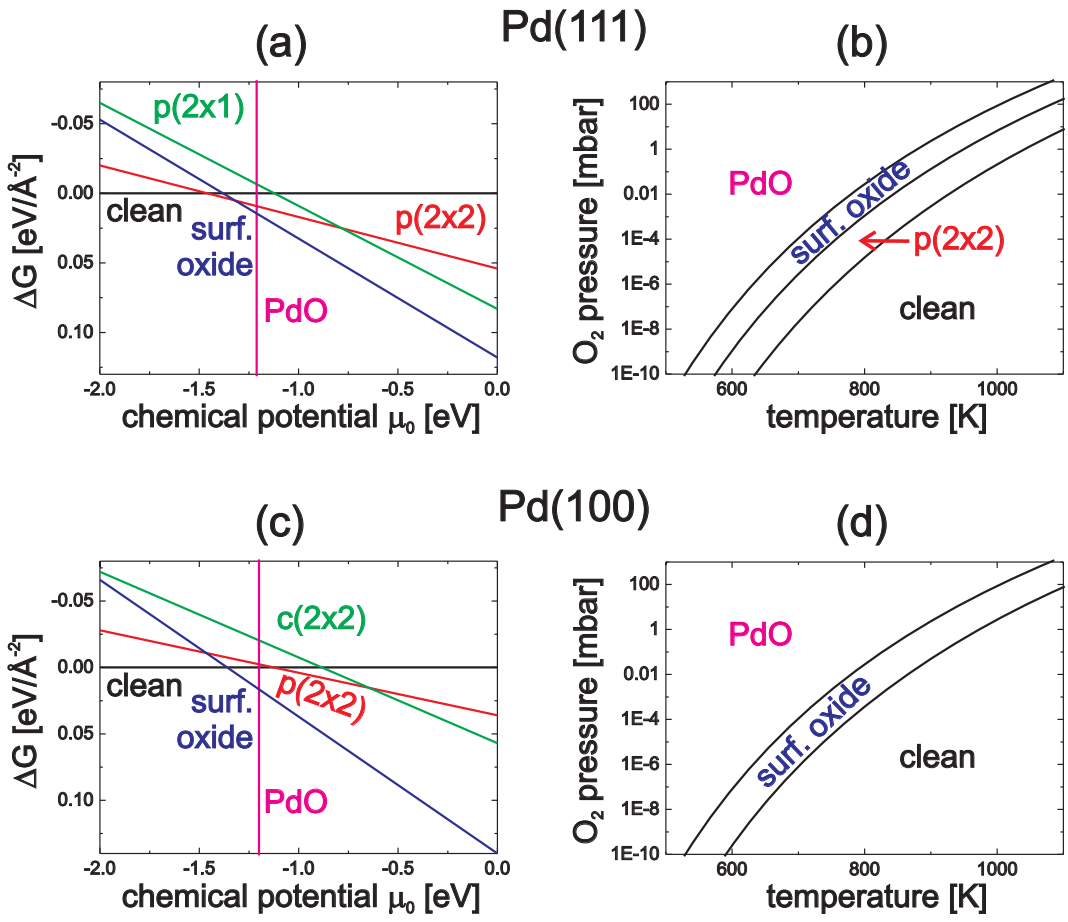

Fig. 2.9: Phase diagram for oxygen on Pd(111) and Pd(100). The values for the adsorption phases (a),(c) were taken from [54], the chemical potential for PdO was derived from ref. [55]. The pressure-temperature diagrams were obtained from the chemical potentials via the ideal gas equation.

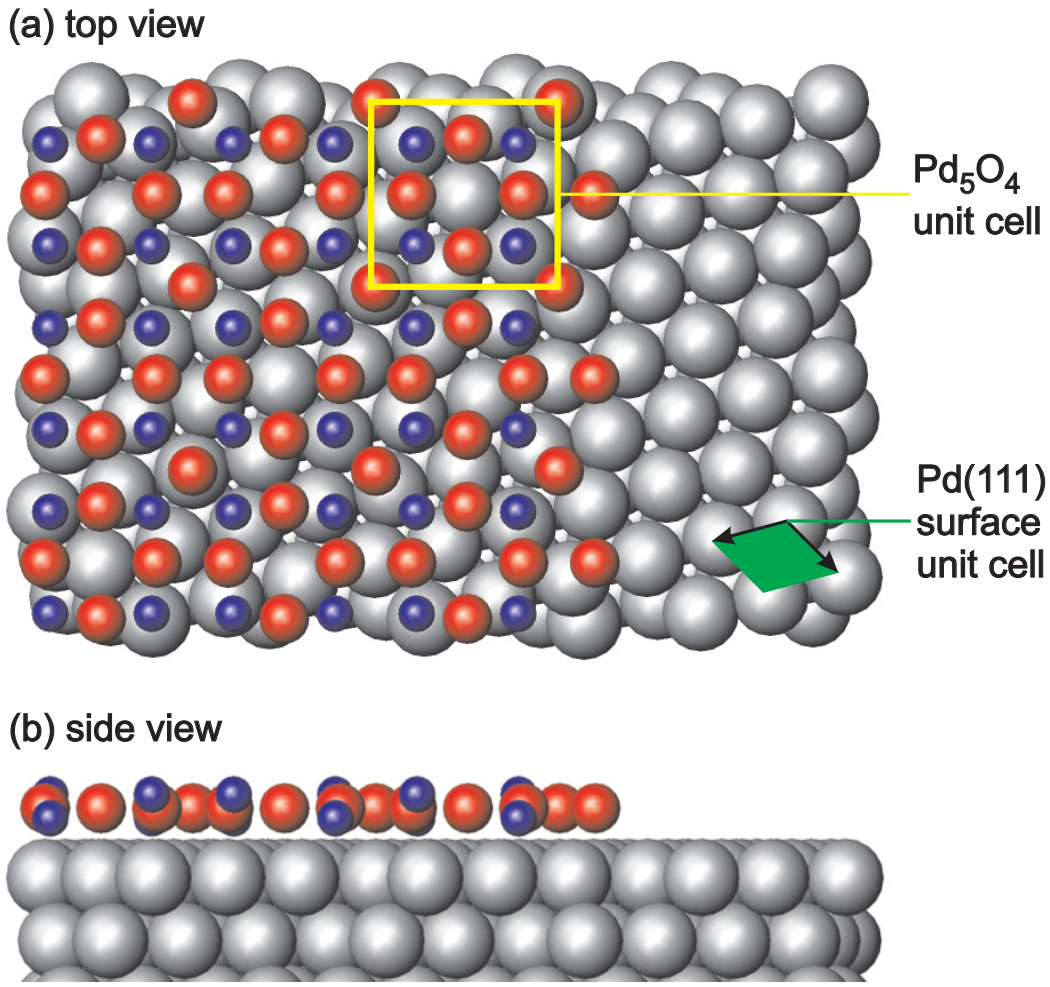

Fig. 2.10: Structure of the Pd_5O_4 surface oxide on Pd(111) (following ref. [56]). The yellow square is a unit cell of the surface oxide, the green quadrangle shows the orientation of the underlying Pd(111) surface unit cell.

cell, the surface oxide is commensurate with the substrate, into perpendicular direction it is incommensurate. The phase diagram for oxygen on Pd(111) is plotted in fig. 2.9 (a, b). Still, the oxidation properties seem rather complex. During growth and composition of Pd_5O_4, an intermediate phase was detected with a $\left(\sqrt{67} \times \sqrt{67}\right) R12°$ structure [61, 59]. In a combined STM and DFT study [62], it was shown that a high number of metastable surface oxides exists, with an almost 1:1 stoichiometry of Pd and O, for example Pd_9O_8 or $Pd_{19}O_{18}$.

2.4.2 Oxidation of the Pd(100) Surface

For the Pd(100) surface exposed exposed to oxygen under UHV-near conditions, several superstructures of chemisorbed oxygen are reported, namely the $p(2 \times 2)$,

$c(2 \times 2)$, and $p(5 \times 5)$ reconstructions [63, 64]. At a higher oxygen coverage, there exists a $\left(\sqrt{5} \times \sqrt{5}\right) R27°$ surface oxide phase. The structure of this phase is plotted in fig. 2.11. The coordinates were taken from ref. [63], which is an improved model of that previously suggested in ref. [65]. The structure shows high resemblance to an PdO(101) bulk oxide film which is strained and rumpled. Note, however, that even though this resemblance, the surface oxide is not an early stage of bulk oxide growth on the surface, as the bulk oxide phase PdO grows in (001) orientation on the Pd(100) surface upon oxygen exposure. The phase diagram obtained by DFT calculations [54] is plotted in fig. 2.9 (c). As was shown in an SXRD study [29] that was performed in a high pressure and temperature range, there are differences to the theoretical phase diagram. The chemisorbed $p(2 \times 2)$-phase which is according to theory never thermodynamically stable, was observed experimentally at 775 K and an oxygen pressure of 10^{-3} mbar. Here the surface oxide was anticipated, and kinetic barriers hinder the growth of surface oxide. For temperatures below 600 K, even at ambient pressures, the surface oxide is present, even though the bulk oxide is the stable phase. The surface oxide is considered as a kinetic barrier to the formation of the bulk oxide as it passivates the surface and no further oxygen molecules are dissociated. As underlying mechanisms, it was suspected that the bulk oxide formation requires activation due to the massive restructuring at the surface [66]. This massive restructuring during PdO growth can also be inferred from the enhanced roughness of the underlying Pd surface.

2.5 Structure of the Support Single Crystal Surfaces

Sapphire and MgO single crystals are standard materials for metal deposition. The crystallographic orientation of the deposited material is determined by the structure of the support material. The MgO(001) surface is used in this work to grow Rh and Pd nanoparticles in (001)-orientation. MgO has a NaCl structure, i.e. an fcc Bravais lattice, with a two atomic base consisting of Mg at (0, 0, 0) and O at (0.5, 0, 0). The unit cell of the crystal is plotted in fig. 2.12.

In order to obtain (111)-oriented Rh and Pd particles, the $\alpha{-}Al_2O_3(0001)$ surface can be utilized as a substrate. The atomic configuration of $\alpha{-}Al_2O_3$ is known as the corundum structure. Each unit cell contains six unities of Al_2O_3. The O atoms of each layer are at the same position along c, whereas the Al atoms are slightly displaced. According to theoretical and experimental studies [67, 68, 69], the (0001)-surface is single Al-terminated. The air-exposed surface is hydroxylated, i.e. it is terminated by OH groups [70]. Examples for metals deposited on the MgO and sapphire are reviewed in ref. [30].

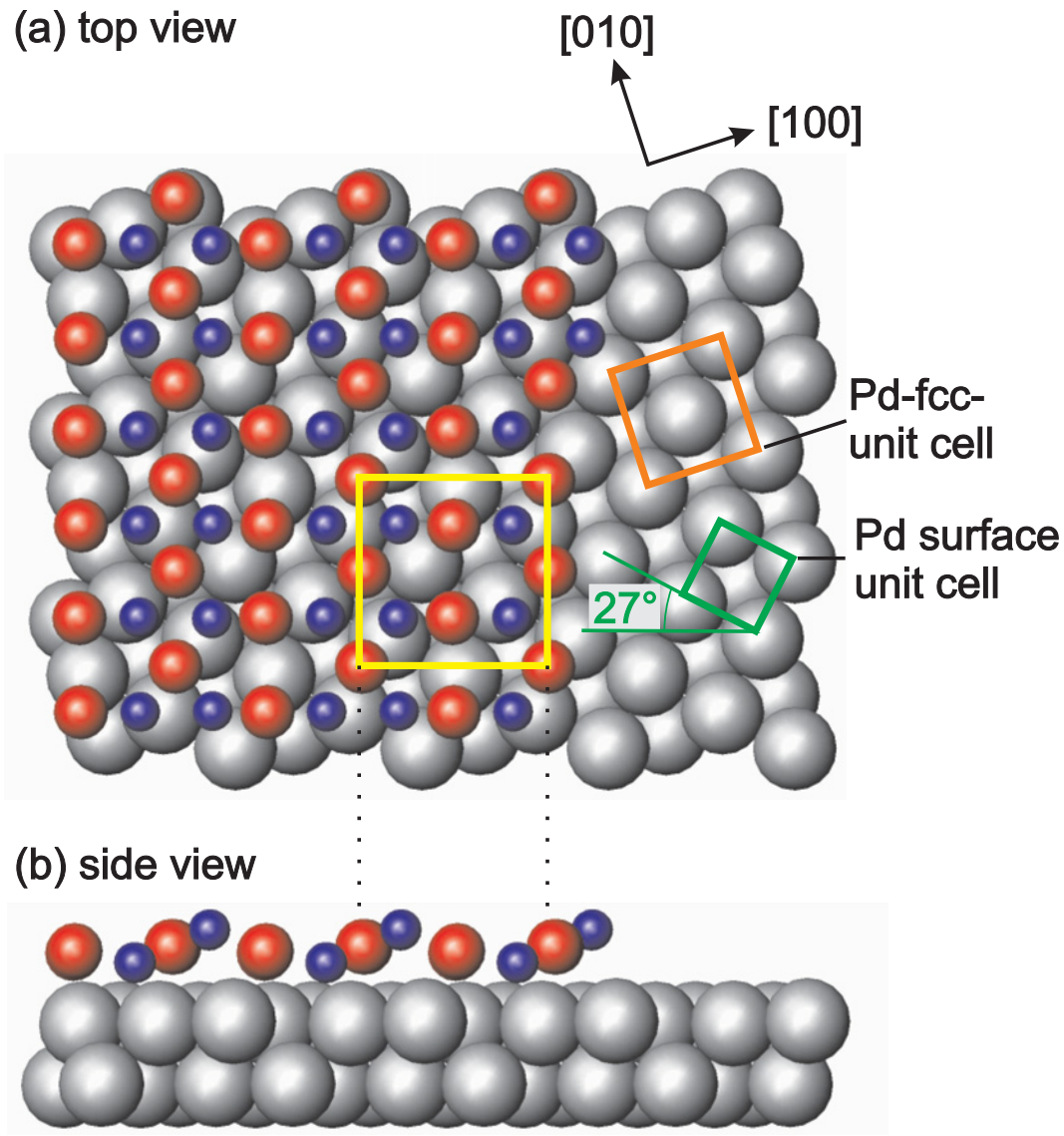

Fig. 2.11: Structure of the Pd(100)-$\left(\sqrt{5} \times \sqrt{5}\right) R27°$-O surface oxide with coordinates from the combined LEED/DFT-study reported in ref. [63]. The yellow square is a unit cell of the surface oxide, the green and the orange square show the orientation of the underlying Pd lattice.

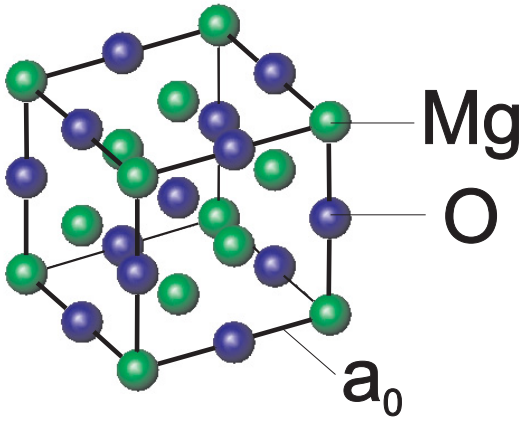

Fig. 2.12: Unit cell of MgO with $a_0 = 4.20$ Å.

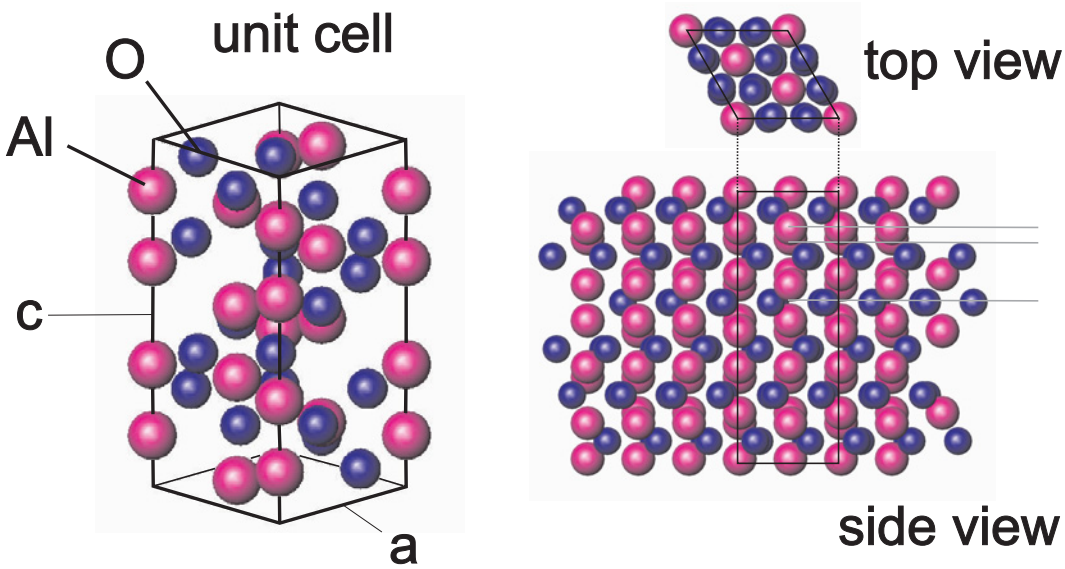

Fig. 2.13: The lattice parameters of the hexagonal $\alpha-Al_2O_3$ unit cell are a = 4.75 Å and c = 12.99 Å. The horizontal lines in the side view underline the oxygen atoms at equivalent vertical positions, whereas the Al-atoms form a double layer.

Chapter 3

X-ray Diffraction from Materials in Reduced Dimensions

This chapter starts with surface x-ray diffraction as it is used for structure analysis of two-dimensional systems. It is followed by an overview of x-ray techniques to obtain shape-sensitive information about nanoparticles. It will be discussed in more detail the analysis of reciprocal space maps that was applied and further developed for the shape analysis of the particles as described in the later chapters about the experimental results. More comprehensive descriptions of x-ray diffraction, especially at surfaces can be found in references [71, 72, 73, 74].

3.1 Kinematic X-ray Diffraction

Following the laws of classical electrodynamics, the ratio of amplitudes between an incident plane wave scattered by an electron and the elastically scattered spherical wave is given by $\frac{E_{scatter}}{E_{in}} = \frac{r_0}{R} e^{ikR} \cos(\psi)$, with the classic radius of the electron $r_0 = \frac{e^2}{4\pi\epsilon_0 m_e c^2}$, a polarization correction $\cos(\psi)$ and the distance R between electron and detector. In the kinematic approximation, the scattering at a system of electrons is given as the complex sum of contributions of each electron which leads to the following expression for the form factor of the system:

$$F(\boldsymbol{q}) = \int_V \rho(\boldsymbol{r}) e^{i\boldsymbol{q}\cdot\boldsymbol{r}} d^3\boldsymbol{r} \tag{3.1}$$

This is obviously the Fourier transform of the electron density distribution $\rho(\boldsymbol{r})$. The vector $\boldsymbol{q} = \boldsymbol{k_{out}} - \boldsymbol{k_{in}}$ denotes the momentum transfer between incident and scattered beam. The intensity is proportional to the squared modulus of the structure factor:

$$I \propto |F(\boldsymbol{q})|^2$$

This consideration holds for an arbitrary distribution of electron density within kinematic theory as long as multiple scattering effects can be neglected. For the

x-ray scattering at an atom, equation (3.1) can be straightforwardly applied. The atomic form factor is given by $f^0(\boldsymbol{q}) = \int_V \rho(\boldsymbol{r}) e^{i\boldsymbol{q}\cdot\boldsymbol{r}} d^3\boldsymbol{r}$. For radially symmetric distributions, this is typically approximated as $f^0(\boldsymbol{q}) = \sum_{j=1}^{4} a_j e^{-b_j(q/4\pi)^2} + c$ [74]. The effects of absorption and dispersion are included in energy dependent correction terms $f'(\omega) + \imath f''(\omega)$, which are not momentum transfer dependent.

3.1.1 Kinematic Diffraction at an Ideal Crystal

A crystal consists of a regular array of unit cells. The crystal lattice is defined via the linear combination of lattice vectors:

$$R_{(n_1,n_2,n_3)} = \sum_{i=1}^{3} n_i \boldsymbol{a_i}, n_i \in \mathbb{Z}, \tag{3.2}$$

at which the unit cell of the crystal is repeated. The structure factor of a unit cell

$$F_{UC}(\boldsymbol{q}) = \sum_j f_j(\boldsymbol{q}) e^{\imath \boldsymbol{q}\cdot\boldsymbol{r_j}} \tag{3.3}$$

is the sum of the form factors of all types of atoms, including a phase shift according to the position $\boldsymbol{r_j}$ within the unit cell. Thus, the structure factor of a finite crystal is given by

$$F_{crystal}(\boldsymbol{q}) = F_{UC}(\boldsymbol{q}) \cdot \sum_j e^{\imath \boldsymbol{q}\cdot\boldsymbol{r_j}}, \tag{3.4}$$

and the lattice sum needs to be performed for all unit cells j within the crystal. If the crystal has the shape of a rhomboid consisting of $N_1 \times N_2 \times N_3$ unit cells, this can be summed up as:

$$F_{crystal}(\boldsymbol{q}) = F_{UC}(\boldsymbol{q}) \prod_{i=1}^{3} \frac{e^{\imath N_i \boldsymbol{q}\cdot\boldsymbol{a_i}} - 1}{e^{\imath \boldsymbol{q}\cdot\boldsymbol{a_i}} - 1}, \tag{3.5}$$

which is obviously a product of N-slit interference functions leading to an intensity:

$$I(\boldsymbol{q}) \propto |F_{UC}(\boldsymbol{q})|^2 \prod_{i=1}^{3} \frac{\sin^2(\frac{N_i}{2}\boldsymbol{q}\cdot\boldsymbol{a_i})}{\sin^2(\frac{\boldsymbol{q}\cdot\boldsymbol{a_i}}{2})} \tag{3.6}$$

Bragg reflections are observed for $e^{\boldsymbol{q}\cdot\boldsymbol{R_n}} = 1$, or, equivalently, if the Laue-condition $\boldsymbol{q} = \boldsymbol{G}$ is fulfilled. $\boldsymbol{G} = h\boldsymbol{b_1} + k\boldsymbol{b_2} + l\boldsymbol{b_3}$ is a reciprocal lattice vector, whereas the integer numbers h, k, l are the Miller indices and the basis vectors of $\boldsymbol{b_j}$ of the reciprocal lattice are defined via the crystal basis lattice vectors $\boldsymbol{a_i} \cdot \boldsymbol{b_j} = 2\pi\delta_{ij}$. Independently of the shape of the crystal, if the object is sufficiently large in all dimensions ($N_i \to \infty$), this product of N-slit interference functions converges to a 3d-array of δ-functions.

3.1.2 Asymptotic Bragg Scattering

Semi-infinite Crystal

It can be shown that for a well defined surface of an ideal crystal ("semi-infinite crystal"), there is a non-zero structure factor contribution not only at the Bragg position, but also along the Crystal Truncation Rods (CTR). A crystal truncation rod is defined as a line interconnecting Bragg reflections, with a direction perpendicular to the sample surface. The structure factor is given as:

$$F_{CTR}(\boldsymbol{q}) = \frac{F_{uc}(\boldsymbol{q})}{1 - e^{-i\boldsymbol{q}_\perp \cdot \boldsymbol{a_3}}} \sum_{\boldsymbol{G}_\parallel} \delta(\boldsymbol{q}_\parallel - \boldsymbol{G}_\parallel) \tag{3.7}$$

$\boldsymbol{G}_\parallel$ is a reciprocal lattice vector according to the 2-dimensional lattice of the sample surface. The momentum transfer perpendicular to the sample surface is denoted as $\boldsymbol{q}_\perp$. This is sketched in the left part of fig. 3.1 (a), which is a top view on a Rh(100) surface[1]. The red dots in fig. 3.1 (b) are at the positions of the Bragg reflections. The violet lines interconnecting the Bragg reflections are the CTRs. The structure factor modulation along the CTRs is plotted in fig. 3.2.

The structure of a real surface may deviate from the structure of a truncated bulk crystal. For example, the topmost layers may show relaxations, or a reduced occupancy of the lattice sites, or even reconstructions may form, i.e. ordered structures of the surface with different surface lattice parameters than the surface of the truncated bulk system. The intensity distribution along the Crystal Truncation Rods is sensitive to such deviations of the atomic arrangement with respect to the bulk structure.

Scattering at a Two-dimensional System

The right part of fig. 3.1 (a) shows the trilayer surface oxide on Rh(100). The green rectangle shows the unit cell of this c(2×8)-superstructure. For the structure factor calculation of such a two-dimensional system, only two Laue-equations $\boldsymbol{q} \cdot \boldsymbol{a_1} = 2\pi h$, $\boldsymbol{q} \cdot \boldsymbol{a_2} = 2\pi k$ must be fulfilled as no summation of phase factors perpendicular to the surface is performed.

$$F_{2dlayer}(\boldsymbol{q}) = F_{2dUC}(\boldsymbol{q}) \cdot \sum_j e^{\imath \boldsymbol{q} \cdot \boldsymbol{r_j}} = F_{2dUC}(\boldsymbol{q}) \sum_{\boldsymbol{G}_\parallel} \delta(\boldsymbol{q}_\parallel - \boldsymbol{G}_\parallel) \tag{3.8}$$

$F_{2dUC}(\boldsymbol{q})$ denotes the structure factor of a unit cell of the two-dimensional system. As for the semi-infinite crystal, this defines a two-dimensional array of rods in reciprocal space. For the c(2×8)-structure, the green grid within fig. 3.1 (b) marks the position of the rods at a $q_\perp$=const.-plane. Along each rod, the variation of intensity depends on the structure factor of the unit cell $F_{2dUC}(\boldsymbol{q})$.

[1] The coordinates are given in surface coordinates. For details, cf. sec. B.1

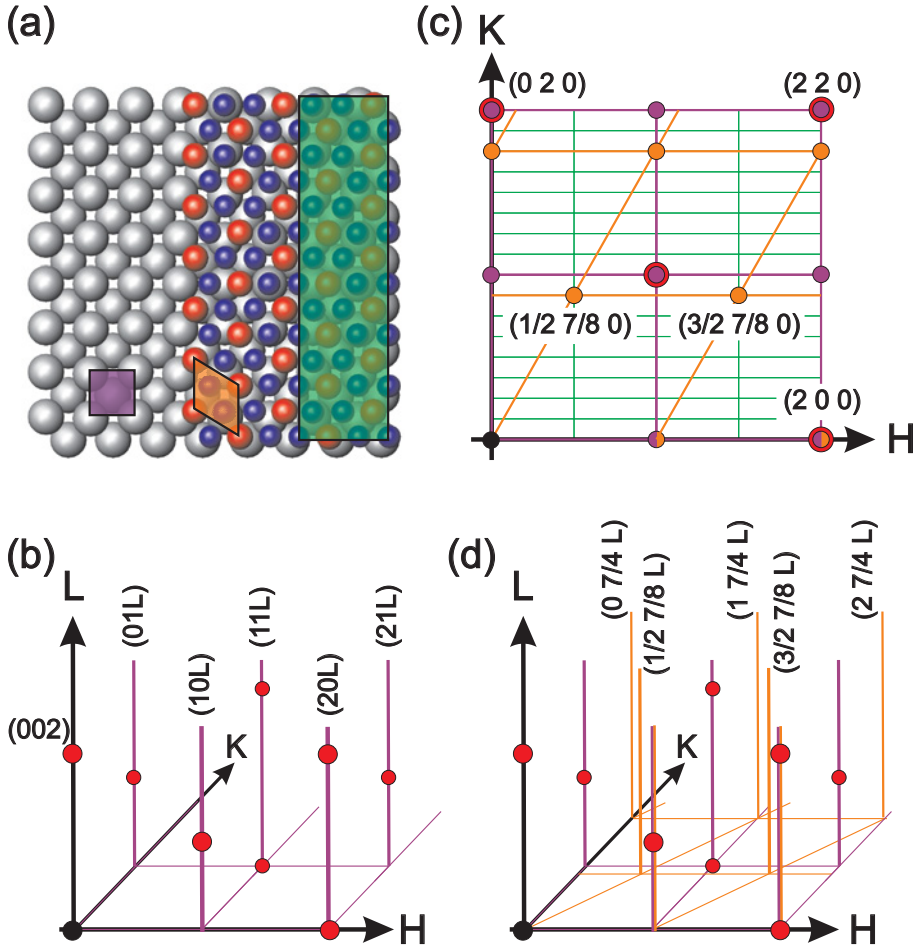

Fig. 3.1: (a): Sketch of the surface lattice of a semi-infinite crystal and a covering superstructure. (b): The according crystal truncation rods with their typical intensity profile and superstructure rods (c, d). The coordinates refer to the Rh(100) surface lattice, as explained in App. B.1.

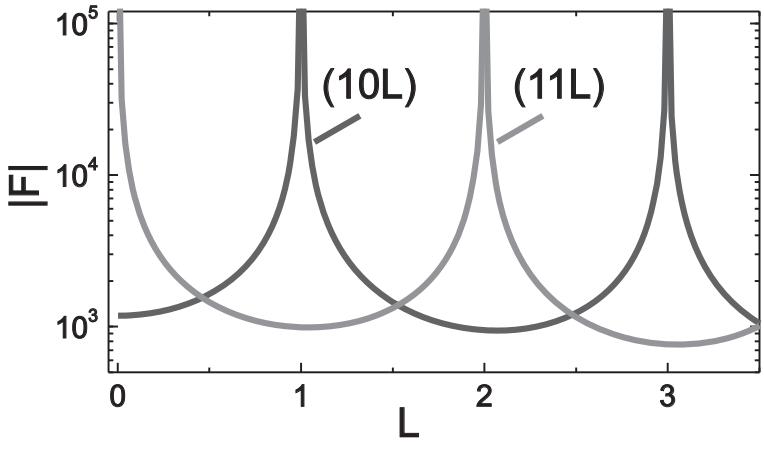

Fig. 3.2: Structure factor of a Rh(001) CTR along (10L) and (11L), given in surface coordinates of Rh(100).

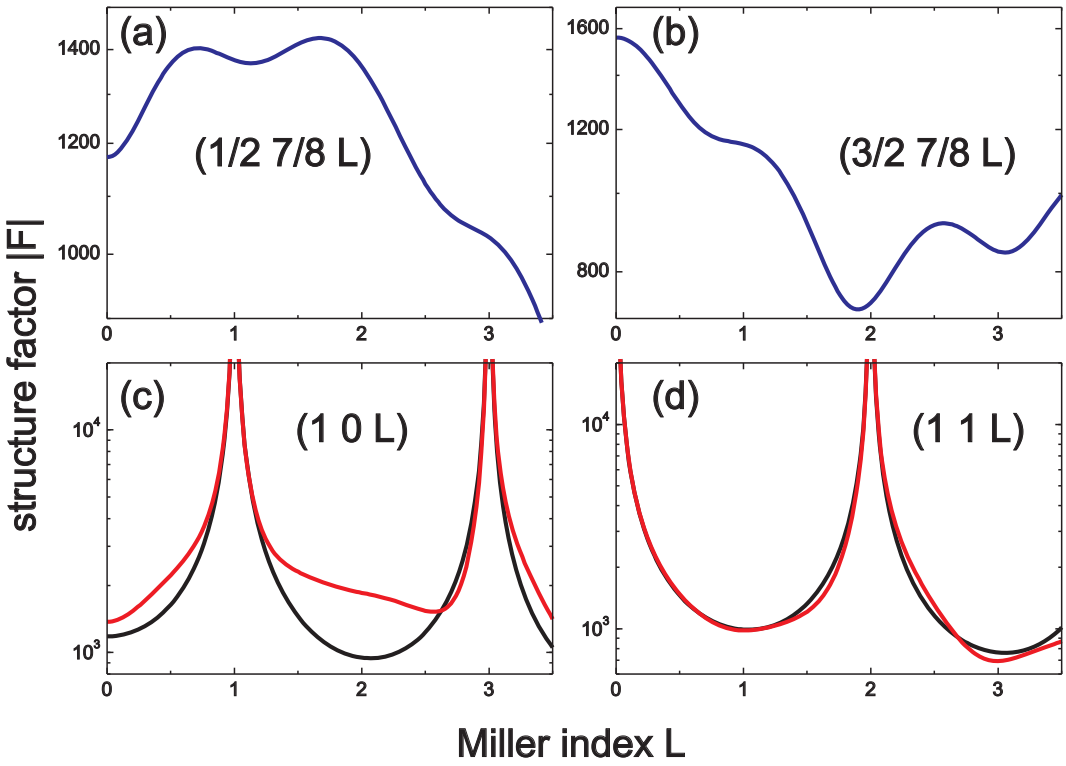

Fig. 3.3: (a, b): Structure factor modulation along the superstructure rods of the surface oxide layer. (c, d): Structure factors along fundamental rods for oxide-covered surface (red lines) in comparison with those of truncated bulk Rh(100) (black lines). The coordinates refer to the surface lattice of Rh(100).

This variation is displayed in fig. 3.3 (a, b) for the (1/2, 7/8, L) and (3/2, 7/8, L) rod. In the special case of the Rh(100) surface oxide, $F_{2dUC}(\boldsymbol{q})$ equals zero at most of the c(2×8) rods. This can be explained due to the hexagonal arrangement of the unit cell, which can also be well-described by a hexagonal unit cell, which is marked as the orange diamond in fig. 3.1 (a). The corresponding orange grid in fig. 3.1 (c) displays the position of the rods which are exactly the rods of the c(2×8) rods with a non-zero structure factor.

As can be seen in the same figures, there is an overlap of some of the rods of the oxide film with some of the crystal truncation rods. Along them, the structure factor $F_{total}(\boldsymbol{q})$ is given as the complex sum of contributions from the two-dimensional film and the CTR:

$$F_{total}(\boldsymbol{q}) = F_{2dlayer}(\boldsymbol{q}) + F_{CTR}(\boldsymbol{q}) \tag{3.9}$$

The superstructure rods, i.e. those rods of the two-dimensional film which are not overlapping with the CTRs are only sensitive to the internal crystalline structure of the film. The fundamental rods of the overlapping CTR and the rods of the two-dimensional film is sensitive to the registry of the film with the substrate. Such an overlap only exists for commensurate structures, this means the ratio of the surface lattice constants of the semi-infinite crystal and of the two-dimensional film must be rational numbers. Fig. 3.3 (c, d) shows the structure factor of the fundamental rods for the crystal covered with the c(2×8) surface oxide in comparison with the CTRs of the truncated-bulk structure.

For a real crystal surface, one has to take into account that the atomic arrangement may deviate from the ideal truncated bulk structure, even if no reconstruction is present. For example, the topmost atoms may show relaxations or the atomic sites are only partially occupied. The structure factor of such a surface can be calculated following equation (3.9) by treating the system as an ideal semi-infinite crystal, on which a two-dimensional film with a (1×1) periodicity is placed, and the effects of relaxations etc. are included into $F_{2dlayer}(\boldsymbol{q})$.

Finally, rotational domains may exist, e.g. in multiples of 90° for the trilayer surface oxide on Rh(100), which were included for the rods (10L) and (11L) in fig. 3.3 (c,d).

3.1.3 Optical Effects

As electromagnetic waves, x-rays obey the laws of electrodynamics. A beam hitting a surface splits up into a transmitted and a reflected fraction. The relationship between the amplitudes of the field strength of the incident, transmitted and reflected wave are described by the Fresnel equations. For x-rays, the complex index of refraction is given as:

$$n = 1 - \delta - \imath\beta \tag{3.10}$$

with a real part smaller than one. The values of δ and β can be related to the atomic form factors by the following: $\delta = \frac{\lambda^2}{2\pi} r_e \rho_e \frac{f'(E)}{Z} \approx \frac{\lambda^2}{2\pi} r_e \rho_e$ (the right parts holds far away from an absorption edge), and $\beta = \frac{\lambda^2}{2\pi} r_e \rho_e \frac{f''(E)}{Z} = \frac{\lambda^2}{4\pi} r_e \mu$, which shows the relation to the linear absorption coefficient μ.

As has been known from light optics, total reflection occurs at the transition from an optically more dense to the less dense medium, if the incident angle[2] is smaller than the critical angle for total external reflection $\alpha_c \approx \sqrt{2\delta}$. The electric field penetrates the medium with an exponential decay, which is denoted as an evanescent wave. Within the Distorted Wave Born Approximation (DWBA), the intensity distribution of the diffracted wave at a surface is given by:

$$I(q_x, q_y, q_z(\lambda, \alpha_i, \alpha_f)) = |t_i(\lambda, \alpha_i, \alpha_f)|^2 \cdot |t_f(\lambda, \alpha_i, \alpha_f)|^2 \cdot |F(\boldsymbol{q})|^2$$

Here, t_i and t_f denote the transmission functions of the incoming and detected exiting wave. A comprehensive description of the theory of grazing angle scattering which leads to the above term is given in ref. [73].

If surface sensitive x-ray diffraction experiments are performed under grazing incidence close to the critical angle, one can obtain a better signal to noise ratio. The scattering depth Λ is the depth of the sample which contributes to the diffracted signal:

$$\Lambda = \frac{\lambda}{2\pi(l_i + l_f)},$$

with $l_{i/f} = \frac{1}{\sqrt{2}}\{(2\delta - \sin^2\alpha_{i/f}) - [(\sin^2\alpha_{i/f} - 2\delta)^2 + 4\beta^2]^{1/2}\}^{1/2}$. This scattering depth depends symmetrically on the incident angle and the exit angle of the diffracted wave. This can be exploited to obtain depth-sensitive information [73].

3.2 X-ray Reflectivity

X-ray reflectivity can be used to characterize films and multilayers with respect to their thickness, electron density and roughness. The reflectivity exploits the contrast of different electron densities perpendicular to a surface. For the light reflected and transmitted at each interface, the Fresnel formulas from classical optics can be applied. For an incident angle below the critical angle for total external reflection, the reflection coefficient is one. For a smooth uncovered substrate, above the critical angle for total external reflection, the intensity profile is follows a q^{-4} dependence. For systems consisting of more than one interface, multiple scattering needs to be taken into account. This is done within the Parrat formalism, which connects iteratively the Fresnel coefficients at each interface [74]. As long as multiple scattering can be neglected (far above the critical angle),

[2]For x-rays, the incident angle refers to the surface plane and not to the surface normal as for light optics.

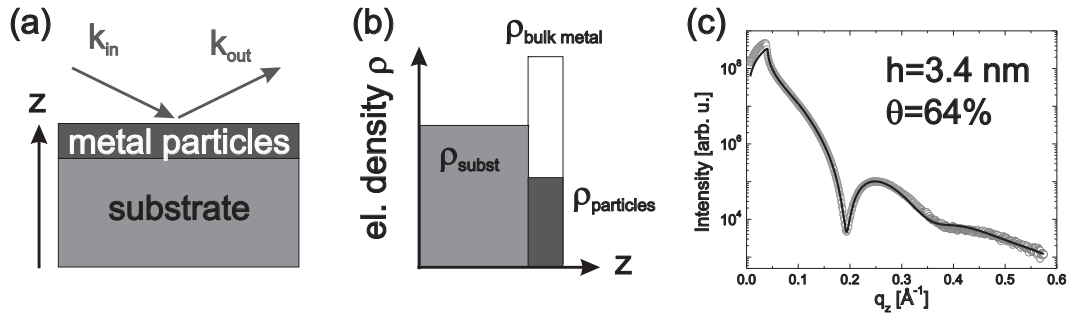

Fig. 3.4: (a) scattering geometry for reflection, (b) box model with different electron densities, (c) reflectivity curve of a Rh/α-Al_2O_3(0001) sample. The roughness of the substrate is 1.7 Å, the roughness of the film 6.3 Å.

the reflectivity of a substrate covered by a material with electron density profile $\rho(z)$ can be also be described by the master formula:

$$\begin{aligned} R^2(q) &= R_F^2(q)\,|F(q)|^2 \\ F(q) &= \frac{1}{\rho_{-\infty}-\rho_{\infty}}\int_{-\infty}^{\infty}\frac{d\rho(z)}{dz}e^{iqz} \end{aligned}$$

Here $\rho_{-\infty}$ and ρ_{∞} describe the electron density of the support material and the ambient medium and R_F is the Fresnel reflectivity of the underlying material. Furthermore, the intensity profiles depend on the interfacial roughness. X-ray reflectivity only requires a contrast of electron density, therefore no crystallinity of the studied sample is necessary.

The samples discussed in this work are metal nanoparticles on oxide supports. X-ray reflectivity was used to estimate the height of the nanoparticles. For the data analysis, a simple box model was assumed (fig. 3.4 b), i.e. a single layer on a substrate. As fit parameters, the height, electron density, absorption and roughness were fitted, apart from the roughness of the substrate. The ratio of electron density between the film and the tabulated value for the bulk metal was used as a measure for the coverage of the particles. The experimental profile and the obtained fit are displayed in fig. 3.4 (c). This method was previously applied for Pd/MgO(100) nanoparticles in ref. [18] and showed a good agreement with auxiliary measurements performed with AFM and TEM.

3.3 Shape Sensitive X-ray Methods

There exists no standard method to derive the atomic structure of nanoscale objects [75]. For studies with x-rays, no direct inversion from the diffracted intensity to the crystal structure or to the shape of an object can be performed due to the phase problem. This denotes the loss of information that occurs as only the magnitude of the scattering amplitude and not its complex quantity

is experimentally accessible. Thus, a suitable modeling of the intensity and a modification of the shape model is required. The structure factor of an object is nothing else than the complex lattice sum $\sum_j f_j(q)e^{i\boldsymbol{q}\cdot\boldsymbol{r}}$, including the position and the form factor for each atom. From the coordinates of all atoms within an object, the intensity distribution follows straightforwardly from the above formula. In the following sections, methods are described to infer the shape of nanoparticles from x-ray scattering data. The analysis of reciprocal space maps is described more comprehensively, as it was applied and further developed for the analysis of the experimental data within this work.

3.3.1 Modeling of Powder Data

The structure of nanoparticles can be extracted from powder diffraction data as described in refs. [76] and [77], where the structural characterization of ZnS, CdS and ZnO particles with a size below 5 nm is reported. The starting situation is a structural model (including the shape) of the nanoparticle with a list of all atomic coordinates. The powder diffraction pattern can be calculated by using the Debye formula

$$I(\boldsymbol{q}) = \sum_m \sum_n f_m(q) f_n(q) \frac{\sin(q \cdot r_{mn})}{q \cdot r_{mn}},$$

thereby summing up all possible combinations of interatomic distances r_{mn} and taking into account the atomic form factor of each type of atom $f_n(q)$. Equivalently, a histogram of all interatomic distances can be calculated, and its Fourier transform leads to the same diffraction pattern. A detailed modeling may include parameters e.g. for the size of the particle, the structure of the unit cell, relaxations of the atoms at the surface, stacking faults etc. For any of these parameters, a distribution can be considered, above which ensemble averaging is performed. There are basically two limitations for this method for metallic nanocrystals on oxide supports as studied in this work. It was explained in sec. (2.1.2) that the equilibrium shape of a supported crystal shows a truncation to the interface with the support in comparison with an unsupported crystal. Therefore, the shape of the supported crystal depends on its crystallographic orientation with respect to the support surface. In principle, this effect could be included into the structure factor modeling. However, the direction-averaged structure factor cannot be extracted from the experiment with a simple 2θ or $\theta - 2\theta$ scan. Rather, an extended 3-dimensional $\boldsymbol{q}$-mapping would be necessary experimentally, of which the data is subsequently directionally averaged for each $|\boldsymbol{q}|$-value.

3.3.2 GISAXS

Grazing incidence small angle x-ray scattering (GISAXS) is a method to characterize nano objects. Similar to reflectivity, small angle x-ray scattering does

not depend on their crystallinity. The scattering signal within a range of a few degrees around the direct beam is regarded, which illuminates the sample under grazing incidence. The structure factor depends on the average shape of the nano objects, and secondly how the positions of the objects are correlated which each other. For the latter case, not only the mean distance plays a role, but also if the objects are arranged regularly or irregularly. Within the Distorted Wave Born Approximation and the Local Monodisperse Approximation (LMA), the intensity can be written as [78]:

$$I(\boldsymbol{q}) = S(\boldsymbol{q}) \times \overline{|F(\boldsymbol{q})|^2} \tag{3.11}$$

Thereby, it is assumed that neighboring islands have the same shape and size over the coherent area of the x-ray beam. The function $S(\boldsymbol{q})$ is the total interference function, which is the Fourier transform of the island-island pair-correlation function. $F(\boldsymbol{q})$ is the Fourier transform of the electron density of an island, the averaged value on size-distributions is given as $\overline{|F(\boldsymbol{q})|^2}$. As GISAXS is performed with the incident angle close to the critical angle of total external reflection, different scattering events have to be summed up coherently to obtain the structure factor

$$\begin{aligned} F_{total}(\boldsymbol{q}) &= F(\boldsymbol{q}_{\parallel}, q_z) + R(\alpha_f)F(\boldsymbol{q}_{\parallel}, -(k_z^f + k_z^i)) + R(\alpha_i)F(\boldsymbol{q}_{\parallel}, k_z^f + k_z^i) \\ &\quad + R(\alpha_i)R(\alpha_f)F(\boldsymbol{q}_{\parallel}, -q_z) \end{aligned}$$

The terms describe that the beam is either scattered directly, or first reflected at the substrate and then scattered, or scattered and then reflected, or as a last possibility, first reflected at the substrate, scattered at the object and again reflected. To calculate an intensity pattern, a suitable model of the island shape is required, and also knowledge about the correlation between the particles, in order to obtain the interference function. GISAXS is size and shape sensitive, as it can contain a distinct signal from the facets of a particle. Technical details about the simulation of GISAXS patterns can be found in ref. [79]. Examples, where GISAXS was applied to describe the growth of Pd/MgO(100) particles with a size from a few nanometers up to 35 nm can be found in refs. [80, 78].

3.3.3 Coherent X-ray Diffraction Microscopy

In spite of the phase problem, methods have been developed to retrieve the shape of a nano or micro object. With coherent diffraction imaging, an object is illuminated with a coherent[3] beam . In the surrounding of a Bragg reflection, a region in reciprocal space is monitored with a sufficient density of points. With phase retrieving algorithms, it is possible to obtain the structure of the nano

[3]The term *coherent* is explicitly used in literature about x-ray diffraction microscopy, but actually requires the same coherency as 'usual' diffraction experiments.

object [81]. For example, the shape of a gold crystal with a size of a few microns was reported in ref. [82], and the shape of a 750 nm Pb nanoparticle could be reconstructed, with a resolution of 40 nm [83]. The decisive advantage of this method is that the shape of an object can be retrieved without any assumption of a model shape. Not only the shape of the object can be obtained, but also strain distributions within the object. In practice, its use is challenging, as for the scattering of a single particle the intensity is very low and therefore very high counting times are required. However, an exposure time of ten minutes was sufficient in a very recent study to reconstruct the shape of a 100 nm gold nanoparticle with a spatial resolution of 5 nm [84]. This was achieved by the focusing the available coherent flux onto the sample. Therefore, a signal within a high q-range could be recorded though the q^{-4} intensity decrease.

3.3.4 Bragg Peak Analysis of Epitaxial Particles with Well-defined Shape

The influence of the particle shape on the Bragg reflection was described in ref. [18]. The FWHM of Bragg reflections along high-symmetry directions was calculated for epitaxial (001)-oriented fcc-particles that are terminated by (111) and (001)-equivalent facets. The lattice sum

$$S(\mathbf{q}) = \sum_j e^{i\mathbf{q}\cdot\mathbf{R_j}} \tag{3.12}$$

has to be calculated by performing the summation via the positions $\boldsymbol{R_j}$ of all atoms j within the particle. The position of all atoms has to be follow from a shape model, which is the same approach as the starting point of the calculation of powder diffraction data as described in section 3.3.1. However, there are two aspects facilitating the calculation. Firstly, no directional averaging for each $|\boldsymbol{q}|$-value needs to be performed, but only the FWHMS along a few $\boldsymbol{q}$-directions (e.g. along $\langle 111\rangle$, $\langle 001\rangle$, $\langle 200\rangle$, $\langle 220\rangle$). Secondly, as was shown in ref. [18], no explicit list of atomic positions needs to be given if one assumes that all atoms are located at regular positions of the fcc lattice. With an explicit list of atomic positions (a 10 nm particle consists of several 10000 atoms) high calculations times would be necessary (especially if size dispersion and mosaicity are included, as will be described in the next sections). Furthermore, the numerical calculation for adding up several 10000 of phase factors might lead to an accumulation of rounding errors. Instead, the structure factor of a particle can be calculated by nested analytical expressions, which depend only on four natural numbers $\{N_P, N_E, N_T, N_B\}$ describing the nanoparticle shape. The meaning of these parameters is sketched in fig. 5.2 (a-d). The parameter N_P determines uniquely a pyramid with a squared (001) surface on its bottom and terminated by four (111) equivalent surfaces. If the pyramid is truncated on its top there

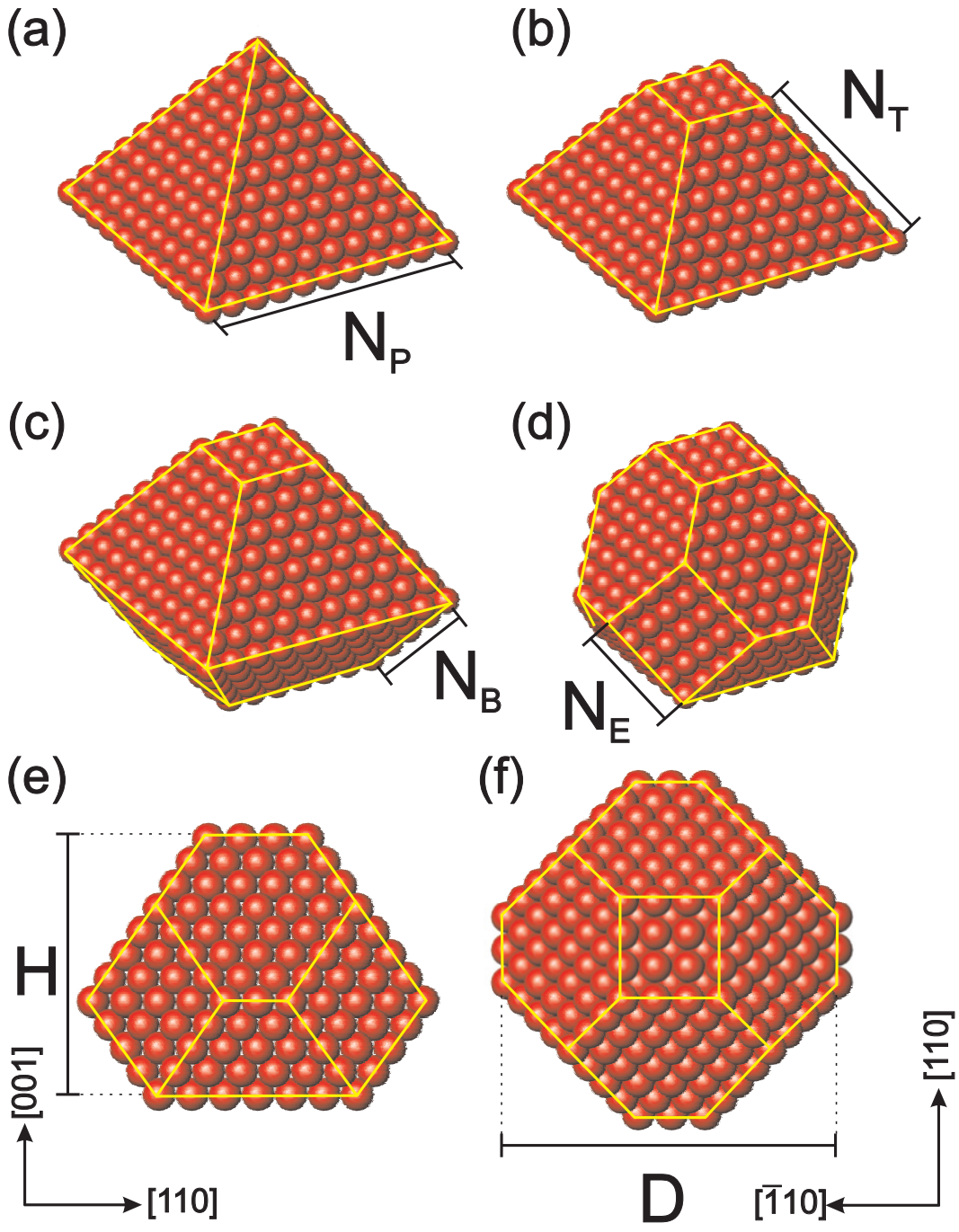

Fig. 3.5: (a)-(d) Scheme to construct a supported (001)-oriented fcc nanoparticle terminated by (111) and (100) equivalent facets with four parameters $\{N_P, N_E, N_T, N_B\}$ $= \{10, 4, 7, 4\}$. (e) The height of the particle is given by $H = \frac{N_T+N_B}{2} \cdot a_0$. (f) The diameter D along the (110) direction is $D = N_P \cdot \frac{a_0}{\sqrt{2}}$.

occurs a (001) facet. This can be characterized by the parameter N_T, which is the number of atomic layers above the base square. As the missing atoms would have formed a smaller pyramid, one just needs to subtract the accordingly phase-shifted structure factor of this missing smaller pyramid from the original pyramid. Four additional (111) facets are formed, if an inverted truncated pyramid is attached on the bottom, which is characterized by the parameter N_B. Finally, (100)-equivalent facets form on the particle by removing N_E layers starting from the corners of the particle. This approach eventually leads to the structure factor of a single particle. To take into account a size distribution, a corresponding averaging of the structure factor needs to be performed. For systems without lateral correlation between individual particles, this averaging can be done in an incoherent approximation[4]. This leads to a mean squared structure factor

$$\overline{|S(\boldsymbol{q})|^2} = \sum_{N_P,\ldots,N_B} D\left(N_P, N_E, N_T, N_B, \mathbf{q}\right) \cdot \left|S\left(N_P, N_E, N_T, N_B, \mathbf{q}\right)\right|^2 \quad (3.13)$$

whereupon a dispersion function $D\left(N_P, N_E, N_T, N_B\right)$ describes the frequency of occurence of each possible particle. The calculated FWHMs of the Bragg reflections along several directions can be used for a determination of the four particle parameters and therefore as a quantitative shape analysis.

An advantage of this Bragg peak analysis is that one is only sensitive to nanoparticles with a particular crystal structure and orientation. In contrast, e.g. misoriented crystals or amorphous particles would contribute to the GISAXS signal. Only in case there are particles with the same crystal structure, but with a shape different from the assumed model shape (as it is the case for coalesced particles), they would also contribute to the intensity at the same Bragg reflection. Furthermore, it cannot be extracted from the anisotropy of the Bragg FWHMs whether the particle surface has actually well-defined facets. This is why it is desirable to have a measurement method that gives a more direct evidence for the shape of the particle.

3.3.5 Analysis of Reciprocal Space Maps

In section 3.1.2, it was described that for x-ray diffraction at a well-defined surface, there occurs an intensity at positions in reciprocal space interconnecting the Bragg reflections that are perpendicular to the surface (CTR). One must consider that a nanoparticle is terminated by several surfaces with different orientations. One can therefore expect, that each of the surfaces gives rise to a diffraction signal, similar as a CTR. This kind of signal can indeed be observed experimentally. Fig. 3.6 shows the intensity distribution along the (H+K=2)-plane (in

[4]This is the case for the Rh and Pd nanoparticles on MgO, as their lattice constant does not match commensurately with the support surface. This is why the scattering signal from different particles is not in phase.

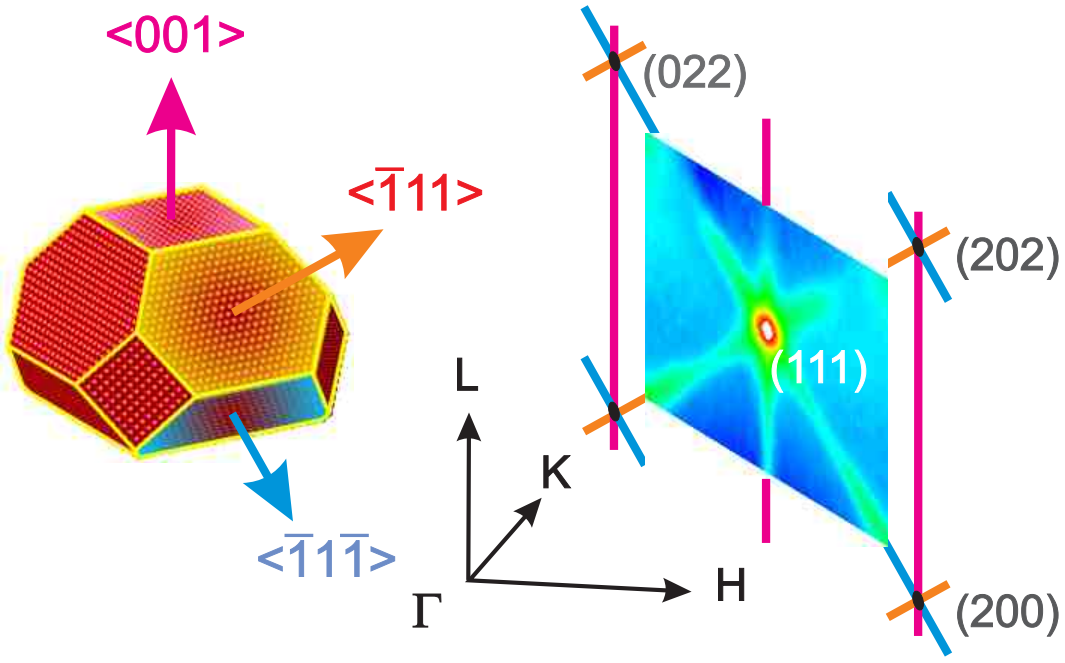

Fig. 3.6: Model shape of a fcc nanoparticle terminated by (111) and (100) equivalent facets. The experimental reciprocal space map was recorded at beamline BM32 (ESRF) from Rh particles with 8 nm in diameter, which will be described extensively in chapter 5. It shows characteristic rods in directions perpendicular to the terminating surfaces.

fcc-coordinates) in reciprocal space. It was recorded for Rh/MgO(100) nanoparticles with an average diameter of 8 nm at beamline BM 32 at the European Synchrotron Radiation Facility. It is centered at the Rh(111) Bragg reflection, and it shows streaks along the $\langle 001 \rangle$, $\langle \bar{1}11 \rangle$ and $\langle 1\bar{1}1 \rangle$ directions which emanate from the associated facets. As a consequence, one can infer the particle shape as a truncated octahedron. Note, that the rod signal of the (100) facets on the side of the particles is not included in this plane. In chapter 5, cuts of such a map will be used for a quantitative analysis on the particle shape and oxygen induced shape changes. The calculation of the structure factor follows the identical formula $S\left(N_P, N_E, N_T, N_B, \mathbf{q}\right) = \sum_j e^{i\mathbf{q}\cdot\mathbf{R_j}}$ as described in the previous section for the FWHM calculation. To take into account size-distributions, equation (3.13) has to be applied. Note, that in the following, the parameters N_P, N_E, N_T, N_B have the meaning of average parameters according to the size distribution function D, while in the the previous formulas, these parameters were used for the individual particle.

In addition, the mosaicity of the particles needs to be taken into account, as the particles are not perfectly aligned with the substrate, but usually show an angular distribution which smears out the experimentally accessible scattering signal. In fig. 3.7 (c), the azimuthal orientation of particles is indicated by a distribution function $A(\omega)$. This affects the structure factor by the following. The crystal coordinate system is defined with respect to the particles in the center of the angular distribution which are well-aligned with the substrate. On a position $\boldsymbol{q} = (q_x, q_y, q_z) = \left(\boldsymbol{q}_{\|}, q_z\right) = \left(|\boldsymbol{q}_{\|}| \cdot \cos(\omega_0), |\boldsymbol{q}_{\|}| \cdot \sin(\omega_0), q_z\right)$, the contribution of the well-aligned particles is

$$|S_0(N_P, N_E, N_T, N_B, \boldsymbol{q})|^2 := \overline{|S|^2}\left(|\boldsymbol{q}_{\|}| \cdot \cos(\omega_0), |\boldsymbol{q}_{\|}| \cdot \sin(\omega_0), q_z\right)$$

If the particles are tilted azimuthally with an angle ω_1, they contribute at the same experimental $\boldsymbol{q}$-position their structure factor of the correspondingly tilted $\mathbf{q}$-Vector:

$$|S_{\omega_0}(N_P, N_E, N_T, N_B, \boldsymbol{q})|^2 := \overline{|S|^2}\left(|\boldsymbol{q}_{\|}| \cdot \cos(\omega_0 + \omega_1), |\boldsymbol{q}_{\|}| \cdot \sin(\omega_0 + \omega_1), q_z\right).$$

For a given azimuthal distribution function $A\left(\omega\right)$, this argument leads to the formula

$$\overline{|S|^2_{A(\omega)}}\left(N_P, N_E, N_T, N_B, \boldsymbol{q}\right) :=$$

$$\int \overline{|S|^2}\left(N_P, ..., N_B, |\boldsymbol{q}_{\|}| \cdot \cos(\omega_0 + \omega), |\boldsymbol{q}_{\|}| \sin(\omega_0 + \omega), q_z\right) \cdot A(\omega) d\omega. \quad (3.14)$$

The effects of size dispersion and mosaicity on the intensity distribution is sketched in fig. 3.7 for an fcc particle with the parameters N_P=31, N_E=3, N_T=20, N_B=5. As a size dispersion function, a Gaussian distribution around the given particle parameters with a relative FWHM of 30% was applied, thereby fixing

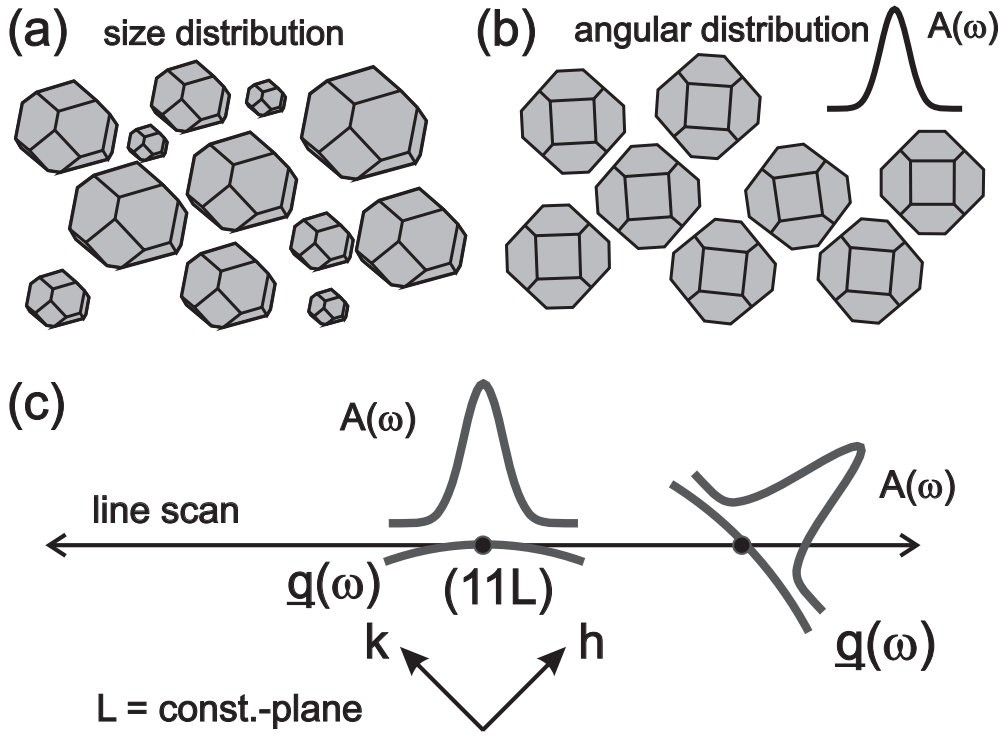

Fig. 3.7: Sketch of (a) the size distribution of the particles and (b) the angular distribution. (c) The arc sections show the region in reciprocal space above which the integral in equation (3.14) is calculated for each sampling point on the line scan.

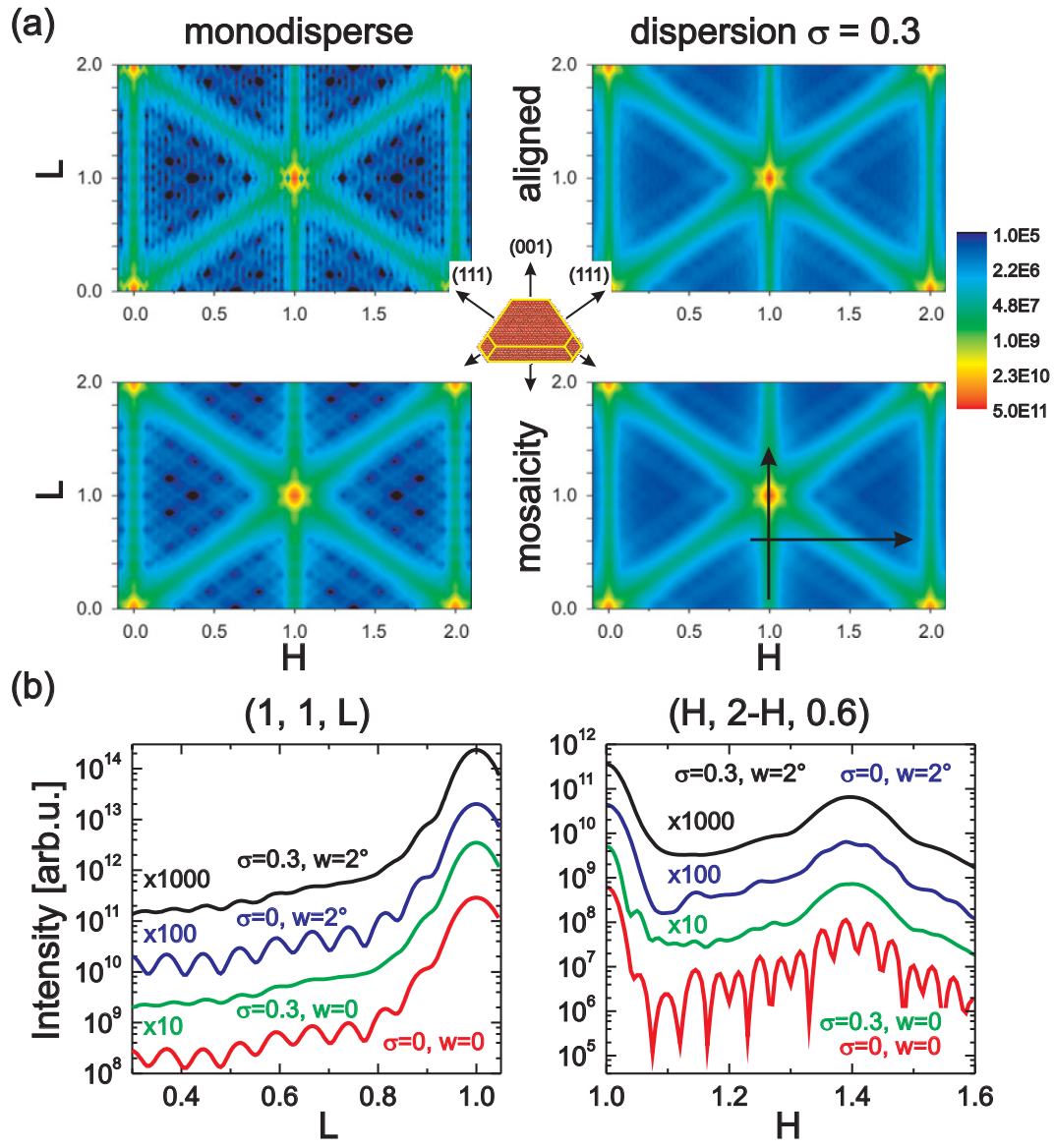

Fig. 3.8: Effects of size dispersion and azimuthal distribution for a particle with the parameters N_P=31, N_E=3, N_T=20, N_B=5. (a) Calculated Intensity in the (H+K=2)-plane. Left: monodisperse particles, right: particles with a Gaussian size distribution (with fixed ratio of the parameters N_P ... N_B) with a relative FWHM of 30%. Up: perfect alignment, down: Gaussian distribution of the azimuthal alignment with a FWHM of 2°. (b) Line scans for the different mosaicity/alignment combinations along the directions indicated with arrows in (a).

the ratio of $N_P : N_E : N_T : N_B$ within the distribution function. A Gaussian distribution with a FWHM of 2° was used as a function for the azimuthal distribution. The upper left part of fig. 3.8 (a) shows the intensity profile in the (H+K=2)-plane of a single particle (or, equivalently, on an ensemble of monodisperse particles with parallel alignment). The CTR-like signal according to the particle facets is clearly visible. In addition, the diffraction pattern shows characteristic Laue-oscillations. These characteristic oscillations are smeared out as an effect of the size dispersion of the particles and their mosaicity. Line scans along (11L) and (H, 2-H, 0.6) are plotted in fig. 3.8 (b) for the different mosaicity / dispersion combinations. The red line is the intensity profile of a single particle, containing characteristic oscillations. For the scan at constant L = 0.6, each of the distribution functions for size and mosaicity leads to a smearing out of the oscillations. When both functions are combined, no more waviness is present. Along the (11L) rod, only the size dispersion leads to a smearing out of the intensity oscillations, while no strong effect is delivered by mosaicity. This is related to the fact that mosaicity was only modeled as an azimuthal distribution function.

3.4 Details on the Quantitative Shape Analysis

3.4.1 Intensity Calculation for FCC Particles with Truncated Octahedral Shape

The goal of quantitative analysis of reciprocal space maps is to determine the average particle shape from an experimentally recorded intensity distribution in **q** including the rod-like signal stemming from the facets. As will be shown in chapters 5 and 6, high resolution reciprocal space maps will be used for quantitative analysis. Line scans were recorded starting from $(0.5, 1.5, L)$ to $(1.5, 0.5, L)$. For Rh, line scans 15 equidistant L-Values between 0.6 and 0.84 with a total amount of 1515 data points were recorded. The reciprocal space map is displayed in fig. 3.9. For Pd, 14 line scans were recorded with 1414 data points altogether. The reciprocal space area close above the Bragg peaks cannot be used, as the signal from internal twinning at $\frac{1}{3}$(4, 2, 4) and $\frac{1}{3}$(2, 4, 4) is lying on the (111)-like rods (cf. app. B.3). For the same reasons, lower values for q_z were not used due to the reflections at $\frac{1}{3}$(5, 1, 1) and $\frac{1}{3}$(1, 5, 1).

A computer program (C) was developed for the intensity calculation of particles with the shape of truncated octahedra. For the experimentally given **q**-positions, the structure factor $\overline{|S(\boldsymbol{q})|^2}$ was calculated. A wide range of average values $\{N_P, N_E, N_T, N_B\}$ for the particle size and shape was considered. For each parameter set, an incoherent averaging over a Gaussian size distribution with a FWHM of 30% of the average values was performed, thereby fixing the ratio of $N_P : N_E : N_T : N_E$ within the distribution. Furthermore, the effect of mosaicity

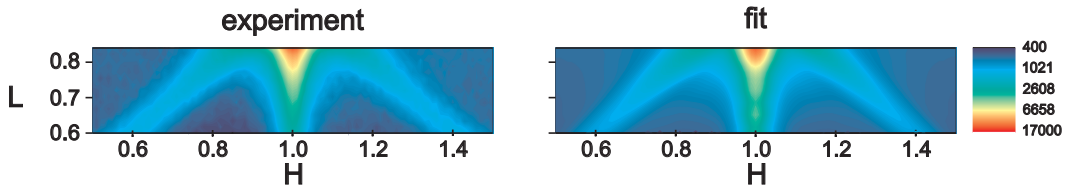

Fig. 3.9: Experimental and simulated high-resolution reciprocal space maps of Rh/MgO as obtained in the experiments described in chapter 5.

was considered. As was described in the previous section on azimuthal distribution, for each experimental $\boldsymbol{q_i}(\omega)$-position, an integral has to be calculated, of which the sampling points $\boldsymbol{q_i}(\omega_j)$ are outlying the actual line scan position. Hereby, it is important to keep in mind, that the mosaicity of the particles is not only azimuthal, but may also have a polar component. On the other hand, due to geometric constraints in the diffraction experiment, the total angular distribution is unknown. As an approximation for the unknown distribution function, a q_z-dependent profile of the angular distribution function was applied. Thereby, the rocking profile of the (220) and (111) reflections of Rh and Pd were fitted with Pseudo-Voigt functions[5] and their q_z-dependent linear combination was used as angular function $A(\omega, q_z)$. Furthermore, the atomic form factor $|f(q)|^2$ of Rh and Pd respectively and geometric correction factors $C_{geo}(\boldsymbol{q})$ were taken into account for the intensity:

$$\tilde{I}_{calc}(N_P, ..., N_B, \boldsymbol{q}) = |f(q)|^2 \cdot C_{geo}(\boldsymbol{q}) \cdot \overline{|S|^2_{A(\omega)}}(N_P, ..., N_B, \boldsymbol{q}) \tag{3.15}$$

As geometrical correction factors, effects of the diffractometer geometries need to be included. In the work presented here, surface diffractometers in z-axis mode were used. This kind of diffractometer allows a high q-accession (except for the vicinity of the specular rod) while keeping the incident angle of the beam with respect to the sample surface constant. Details on the scattering geometries can be found in references [85, 86, 87]. In the analysis, the effects of polarization, active sample surface and absorption of the beryllium window were considered. Furthermore, the detector slit integration interval $\Delta q_{\|}$ was included[6]. However, due to the small angular range of the diffractometer angles δ, γ, all the applied corrections are small and could also be neglected. However, they would play a

[5] A Pseudo-Voigt function is defined as the superposition of a Gaussian with a Lorentzian profile: $A(\omega) = a_0 \cdot \left(\mu \cdot \frac{2}{\pi} \cdot \frac{w}{4 \cdot (\omega - \omega_0)^2 + w^2} + (1 - \mu) \cdot \frac{\sqrt{4 \ln(2)}}{\sqrt{\pi} w} e^{-\frac{4 \ln(2)}{w^2} \cdot (\omega - \omega_0)^2} \right)$.

[6] Considering the slit settings as a multiplicative factor correction corresponds to a zero-order expansion of the intensity profile. This is valid as long as the structure factor varies only slowly between two sampling points, which is the case for the q-range mapped in this work. If the q-maps also contain Bragg-reflections, higher orders of the structure factor variation need to be considered for the integration within the detector slit interval.

decisive role, if an extended q-range would be used (e.g. the simultaneous analysis of a plane with varying q_z and an in-plane mesh with $q_z \approx 0$).

For a comparison with the experimental values, a scaling factor s and a linear background $b(q_z)$ were introduced for the calculated intensity:

$$I_{calc}\left(N_P, N_E, N_T, N_B, \boldsymbol{q}\right) = s \cdot \tilde{I}_{calc}\left(N_P, N_E, N_T, N_B, \boldsymbol{q}\right) + b(q_z)$$

For a given set of particle parameters $\{N_P, N_E, N_T, N_B\}$, describing the average size and shape of the particles, s and $b(q_z)$ were optimized to minimize the cost function

$$\chi^2 = \sum_i \frac{\left(I_{exp}\left(\boldsymbol{q}_i\right) - I_{calc}\left(\boldsymbol{q}_i\right)\right)^2}{I_{exp}\left(\boldsymbol{q}_i\right)}. \tag{3.16}$$

The combination of parameters $\{N_i\}$ with the least χ^2 leads in principle to the particle shape. However, as will be explained in chapter 5 for the analysis of Rh/MgO(001) particles, due to the mosaicity, the maps did not show a high sensitivity to the diameter parameter N_P. Therefore, the value of N_P was estimated with an additional comparison of the FWHMs of the Bragg reflections.

3.4.2 Inclusion of the Surface Oxide on the Top Facet for Rh Particles

As it will be shown in chapter 5, the ultrathin surface oxide grows on the Rh particles under oxidizing conditions. On the top (001) facet, there grows the $c\,(2 \times 8)$-structure. The structure of this film is given in figs. 2.7 and 3.1 (a).

As it was shown in section 3.1.2 and displayed in fig. 3.3 (c, d), this structure delivers an intensity contribution along (11L). For this reason, this oxide layer needs to be included in the structure factor calculation of the particles under oxidizing conditions. Two key aspects must be considered. Firstly, the top facet of the nanoparticle does not necessarily have the size of an integer multiple of the $c\,(2 \times 8)$-unit cell. This means the oxide unit cell must be properly truncated at the edge of the top facet (fig. 3.10 c). Secondly, and also related to the finite size of the top facet, there exist 7×2 different position defining the registry of the oxide with the underlying metal atoms. The mentioned finite size effects can be strongly simplified by using an unrelaxed structure of the surface oxide. For the unrelaxed model, the elementary building blocks for both oxygen layers and the Rhodium layer are face centered rectangles with $a_1 = \frac{8}{7} \cdot a_{top}$ and $a_2 = 2 \cdot a_{top}$. As z-coordinates, the z-values of the center of mass of each layer as given in ref. [12] were used. The first oxygen layer starts with one oxygen atom above a metal atom. The overlying Rhodium layer is shifted by a value of $\frac{2}{3}a_{top}$ along the y-direction, the topmost oxygen layer is shifted by another $\frac{2}{3}a_{top}$ along the $[010]_{top}$-direction (fig. 3.10 b). The underlying metal atoms are fixed at the bulk position, unlike in the exact model, where the first substrate-Rhodium layer has relaxations

along and perpendicular to the surface and the second and third layer are slightly relaxed perpendicular to the surface. To check for accuracy, the structure factors were calculated for a single crystal surface for the relaxed and unrelaxed model (cf. fig. 3.11). On the superstructure rods, there exist obvious differences between the relaxed model and the simplified unrelaxed model. However, both models show rather good agreement on the $(10L)_{top}$ rod (green and red lines in fig. 3.11 (c)) between L = 0.6 and 0.84, which the relevant q-range for the quantitative analysis of reciprocal space maps. One can see that there is a significant intensity difference present for the clean and the oxidized Rh(100) single crystal surface. Note that this difference is much less distinct for the nanoparticles, as the $(10L)_{top}$ rod considers simultaneously information on the top and bottom (001) surfaces (in contrast to the single crystal surface), and only the top (001) surface gets oxidized.

For the structure factor calculation of the oxidized surface, it was further assumed that the (001) facet is completely covered by a single oxide domain (fig. 3.10 c). Still, there is a degree of freedom to describe accurately the registry of the oxide with respect to the finite size (001) surface. The reference position is determined by that position, where an oxygen atom of the surface oxide is directly above a substrate Rh atom. This leads to 14 different configurations for a given top facet. For each set of particle parameters $\{N_P, N_E, N_T, N_B\}$, the reference position was chosen by random numbers. Finally, 90° rotational domains of the oxide where taken into account.

3.4.3 Modeling of Additional Facets

The shape sensitive intensity distribution discussed in the previous sections was modeled for particles that consist only of (111) and (100) equivalent facets. It will be shown in the experimental chapters for Rh and Pd on MgO(001) that upon oxidation additional facets can be formed. In the case of Pd, the intensity was modeled by additionally taking into account the contribution of (112) facets. More details will be described in chapter 6.

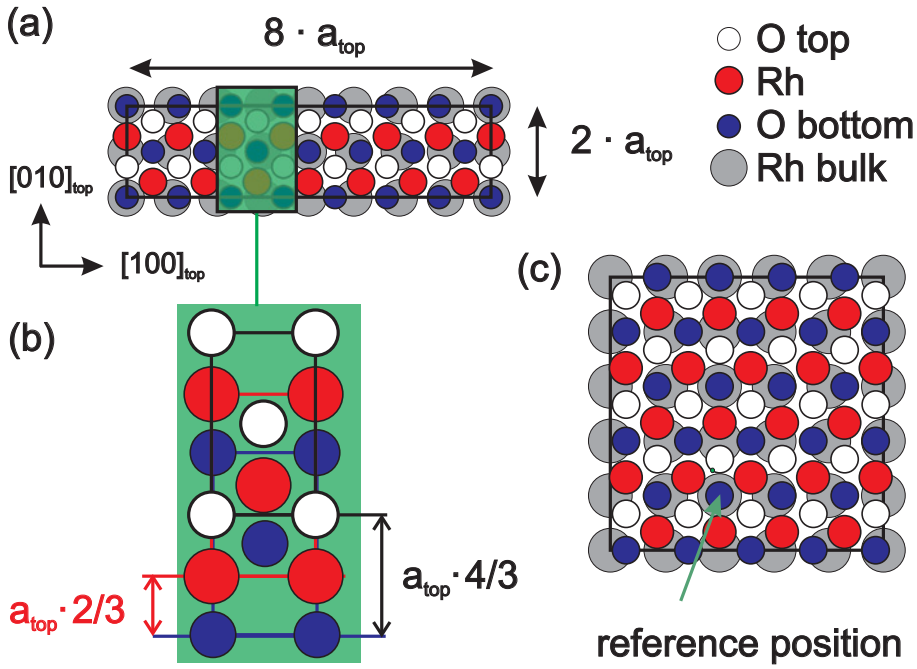

Fig. 3.10: (a) For the structure factor simulation, an unrelaxed model of the c (2× 8) surface oxide was used. (b) Its elementary building blocks for each atomic layer are face centered rectangles. (c) Placement of the surface oxide onto a finite square of Rh(001). The registry is determined by the position of the bottom O atom which is exactly above a Rh atom.

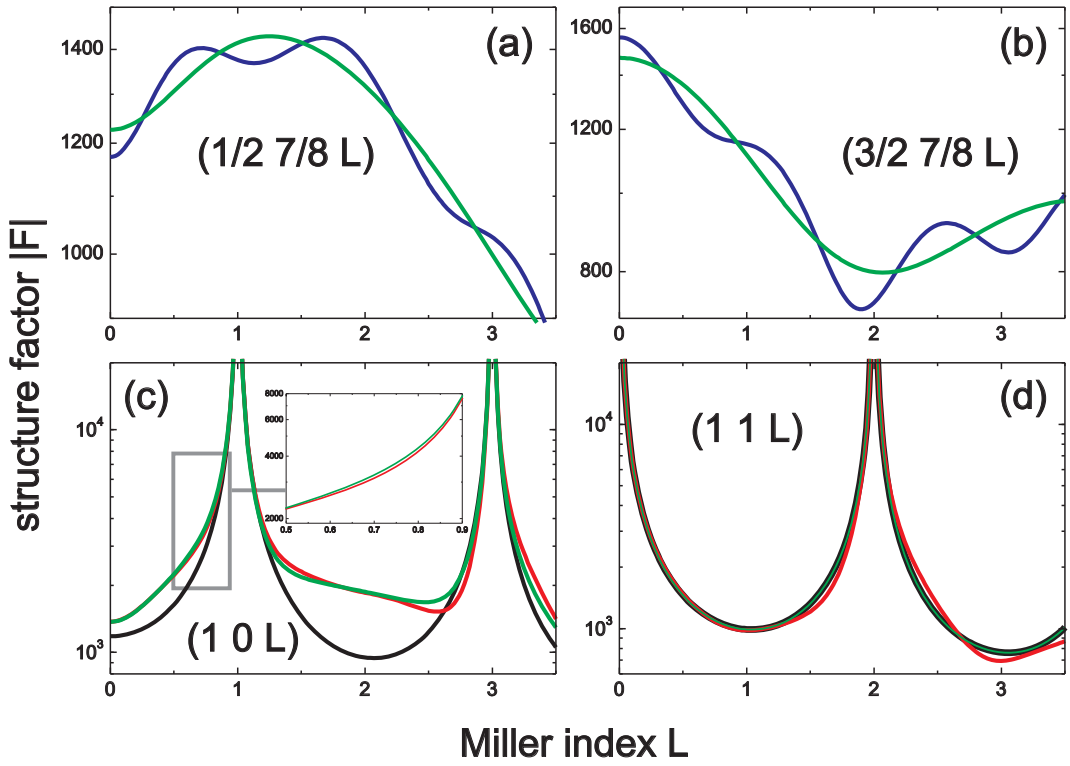

Fig. 3.11: Structure factors of the simplified structure model (green lines) and the precise model of the c(2×8) surface oxide on Rh(100). (a, b): Superstructure rods.(c, d): On the fundamental rods, there is rather good agreement with the precise model (red lines). The inset shows a detailed range for $(10L)_{top}$ between L = 0.6 and L = 0.84 which was used for the intensity calculations for the nanoparticles. Black lines: CTR profiles for bulk-terminated Rh(100).

Chapter 4

Further Analysis Methods and Experimental Details

This chapter deals with a description of the applied laboratory instruments and details of the sample preparation procedure. First, a description of the vacuum chambers is given that were used for the preparation of the supported nanoparticle specimens and for the oxidation of the particles. It is followed by a description of the end stations for x-ray diffraction and reflectivity analysis. A brief description is given about the applied electron based surface analysis methods. Finally, the typical substrate preparation process will be described.

4.1 Ultra High Vacuum Chambers

4.1.1 Stationary Growth and Preparation Chamber

Most of the samples that were used for the oxidation experiments described in this thesis were grown in a stationary UHV chamber in the home lab. The main part of this instrument is a vessel with a volume of ≈ 1 m^3, where a base pressure of $1{\cdot}10^{-10}$ mbar can be achieved. As a pumping system, a turbo molecular pump and a ion getter pump are used. Secondly, there is a load-lock chamber which is separated from the main vessel by a gate valve. Vacuum is created by a turbo molecular pump. This load-lock chamber is vented when samples are inserted or removed from the chamber. As no bake out is performed for this load-lock chamber, a pressure of typically 10^{-8} mbar can be achieved, typically within half a day. The pressure in the load-lock chamber and in the main vessel is measured via cold cathodes. For an analysis of the residual gas in the main chamber, a quadrupole mass spectrometer is used. All sample crystals are mounted on special sample holders, and can be transported via magnetically coupled transfer rods between the load-lock chamber and the main chamber. The main chamber is equipped with a heating station that allows annealing of the samples either purely

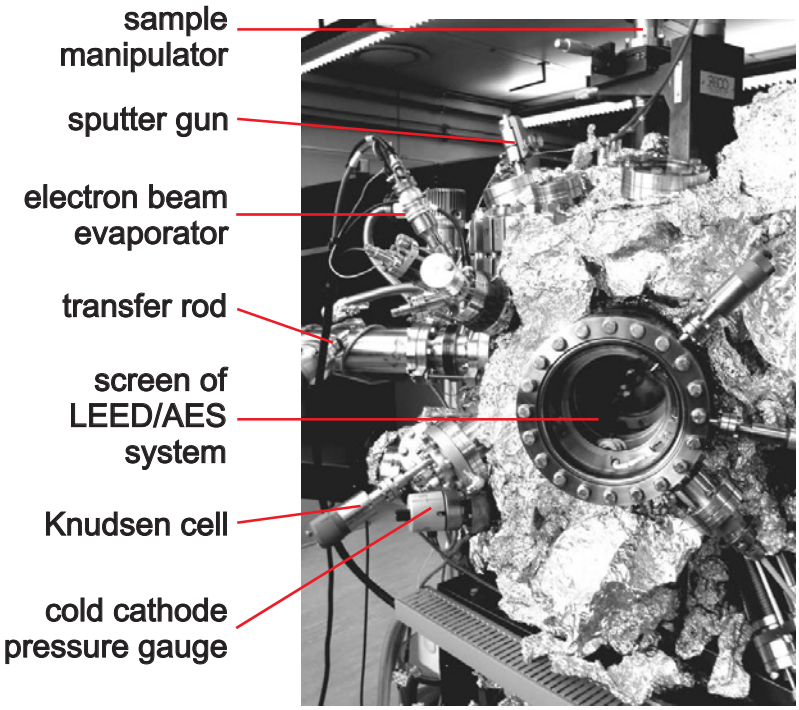

Fig. 4.1: Stationary preparation chamber which is used for the sample manufacturing including substrate processing, metal deposition and surface analysis.

by a filament or additionally by an electron beam which allows temperatures above 1000 K. A combined Auger/LEED system can be used to analyze the chemical composition of the surface as well as to check the crystalline order of the surface. The substrate surfaces can be cleaned by argon ion sputtering. Oxygen can also be dosed into the chamber. The upper limit of gas pressure is in the range of 10^{-5} mbar. The chamber is equipped with up to two electron beam evaporators, used either to deposit Rh or Pd. A readily prepared sample can not only be transferred out of vacuum via the load-lock-chamber. Furthermore, there exists a flange, separated by a gate valve, where the mobile vacuum chamber (sec. 4.1.2) can be attached and the sample can be transferred under remaining ultra high vacuum conditions.

4.1.2 Mobile Oxidation X-ray Chamber

There are two almost identical vacuum chambers to be used for the oxidation experiments under x-ray control (fig. 4.2). The most decisive part is a standing beryllium cylinder, which is used as a window for the x-rays. One of the chambers has a Be cylinder with a wall thickness of 0.5 mm, the second has a wall thickness of 2 mm. In addition, to avoid undesired precipitates on the walls of the Be windows, they are masked inside with a renewable thin aluminum foil. The vacuum is created with a turbo pump and optionally with an ion getter pump. A membrane pump creates the necessary vacuum to operate the turbo molecular pump. The chamber can be equipped with dosing valves in order to

apply gases (O_2, CO, Ar). The gas lines are also connected with the membrane pump. With valves, it can be switched between pumping either the gas lines or creating the vacuum for the turbo pump. When a gas atmosphere below 10^{-4} mbar is applied, gas is dosed while pumping the system with the turbo molecular pump. The pressure is then measured with a cold cathode. When higher pressures are applied, the connection between the main vessel and the turbo pump is closed by a valve, and the gas is filled stationarily into the chamber. The pressure is measured by capacitive high pressure gauges. Two kinds of heating stations can be used. One of them is a high temperature electron beam heating allowing sample temperatures even above 1300 K. Due to the material properties of the filament, it is not compatible with oxygen pressures in the mbar regime. For this reason, a high pressure compatible heating station can be mounted, where the filament is embedded into an Al_2O_3 ceramic and allows temperatures up to $\approx$ 900 K. The exact configuration of the chamber (number of dosing valves for the gas inlet, type of heating station, use of a quadrupole mass spectrometer etc.) is not stationary, but can be adapted to the needs of each experiment. Samples can be transferred under in situ conditions into this chamber by attaching it to the stationary vacuum chamber as described in the previous section. Otherwise, the chamber is loaded with a sample starting from ambient conditions. In the latter case, optionally a sputter gun or an electron beam evaporator can be mounted on the chamber. A pressure in the low 10^{-9} mbar range can be achieved after a bake out of 1-3 days. Fig. 4.2 shows the mobile oxidation chamber on the surface diffractometer at the MPI MF beamline at the synchrotron Angströmquelle Karlsruhe (sec. 4.3). Here, the chamber is equipped with an electron beam evaporator and allows the deposition of metal particles under x-ray control.

4.2 Generation of X-ray Radiation

X-ray radiation created from electrons decelerated by a metal anode has a spectrum consisting of two features. Firstly, it is the Bremsstrahlung with a continuous spectrum that has a maximum energy according to the high voltage that is used to accelerate the electrons. Secondly, there is the characteristic radiation of the anode material. Its spectral lines have a high intensity in comparison with the Bremsstrahlung radiation. Thereby, an incident electron removes an electron of the inner shell of the anode material. The relaxation of an outer shell electron filling the vacancy can be accompanied by the emission of an x-ray photon. For the creation of monochromatic x-ray radiation in laboratory sources, it is therefore efficient to use the wavelength of the characteristic radiation. It is separated from the Bremsstrahlung by a monochromator. The maximum power of water cooled standing anodes is in the range of 2 kW. For higher power, water cooled rotating anodes are used [74].

The highest available intensity of x-rays can be achieved with synchrotrons.

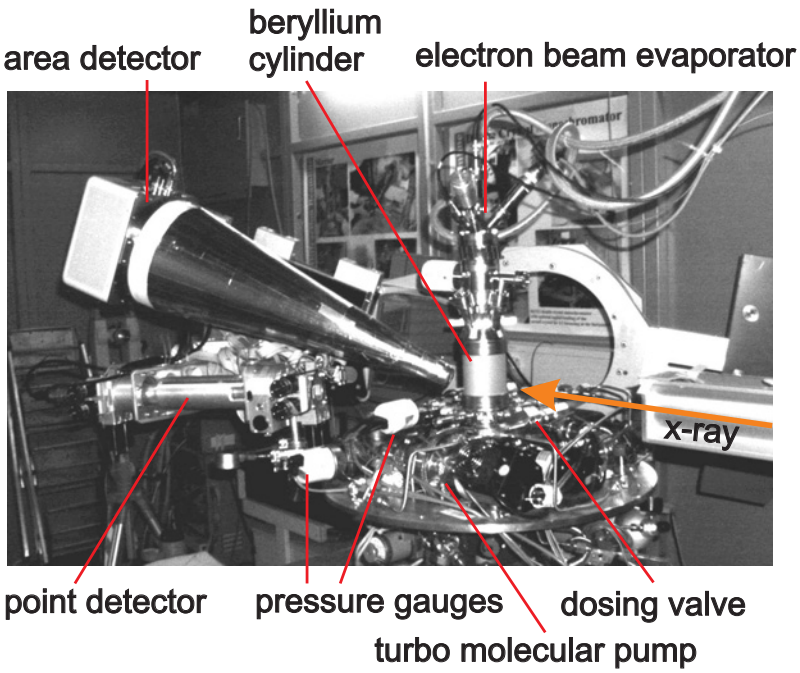

Fig. 4.2: The mobile high-pressure compatible oxidation x-ray chamber on the surface diffractometer at the MPI-MF beamline at the synchrotron radiation facility ANKA.

In a synchrotron radiation facility, an electron current with an energy in the GeV range is running in a storage ring[1]. Bending magnets are used to drive the electrons on a closed orbit. Due to the perpendicular acceleration of the electrons in the magnetic field, they emit radiation, which due to the relativistic energies is confined in a cone oriented in tangential direction to the electron beam. Between the circular arc segments, there are straight sections in the storage rings. Here, insertion devices can be installed, called wigglers and undulators. Wigglers consist of a periodically arranged sequence of magnets with their field pointing alternately in diametric directions and perpendicular to the trajectory of the electron. This arrangement forces the electrons on an oscillatory trajectory, which leads to an enhancement of the radiation power with increasing number of N periods of the magnets in the insertion device by a factor of $2N$. This can be optimized in the undulators with increasing the magnetic period and the magnetic field strength. The deflection of the electron perpendicular to its forward direction becomes negligible in comparison with the angular with of radiation. This leads to an almost coherent superposition of the contributions obtained for each oscillation. This means that not the intensities, but the amplitudes are added up coherently for each magnetic period within the wiggler and leads to an intensity scaling of N^2. As the electron beam in the storage ring loses energy after passing the insertion devices and arc elements, the electrons are reaccelerated with high frequency cavities. The unique properties of synchrotron radiation are its wide spectrum reaching from far infrared up to hard x-ray radiation, the high intensities, linear polarization and a directional beam with a typical divergence

[1] At the Storage Ring DORIS, positrons are used, cf. sec. 4.3.3.

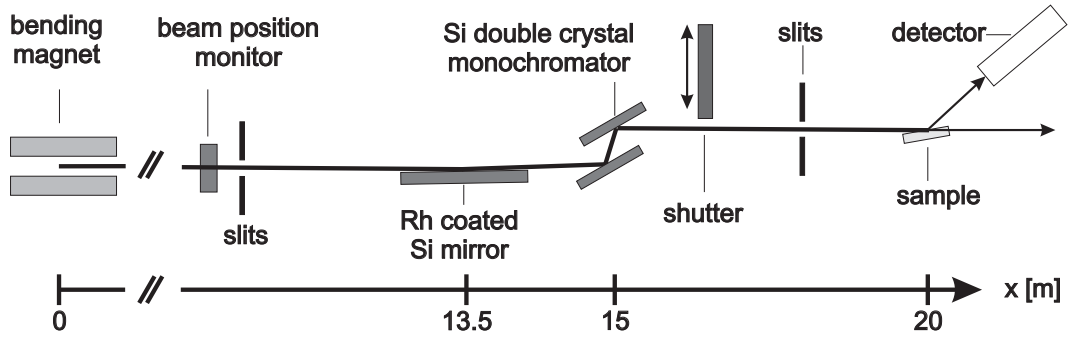

Fig. 4.3: Setup of the MPI-MF beamline at the Angstroemquelle Karlsruhe.

in the millirad range. As electron bunches are present in the storage ring, the emitted synchrotron radiation is accordingly pulsed. This allows for example time resolved experiments triggered with the x-ray pulse. In optical hutches of synchrotron beamlines, the created beam can be focused and monochromized to the desired photon energy with mirrors and crystal monochromators according to the requirements of the experimental end station.

4.3 Experimental Stations for X-ray Diffraction

4.3.1 MPI MF Surface Diffraction Beamline at the Angstromquelle Karlsruhe

The MPI-MF Surface Diffraction Beamline is located at the Angstromquelle Karlsruhe (ANKA), which is an electron synchrotron radiation facility at the Research Center of Karlsruhe. The electron energy in the storage ring is 2.5 GeV, the circumference is 110 m. The beamline is dedicated for the in situ investigations of surfaces, interfaces and thin films [88]. The radiation for the beamline is produced with a bending magnet. Its set up is sketched in fig. 4.3. Via a Rh coated silicon mirror, the high energies are cut off and the beam is focussed vertically. The photon energy can be adjusted with a Si-double crystal monochromator. The experimental end station is a (2+3) surface diffractometer, with a modified vertical geometry towards a usual z-axis diffractometer. It therefore allows to load heavy set-ups. X-ray photons with an energy from 6-20 keV can be provided. For the experiments described in this thesis, a photon energy of 10 and 10.5 keV respectively was used.

4.3.2 Beamlines BM 32, ID 15, ID 03 at the ESRF

The European Synchrotron Radiation Facility (ESRF) in Grenoble (France) is a third generation synchrotron source. The storage ring has a circumference of

844 m and the electrons have an energy of 6 GeV. The ring current is up to 200 mA and can be operated in different filling modes, i.e. different temporal structures of the inserted electron bunch. More than 40 beamlines are installed, mainly at insertion devices. The following sections describe the main features of the beamlines used for the experiments presented here.

BM 32

Beamline BM32 at the ESRF is operated by the *Centre National de la Recherche Scientifique* (CNRS) and the *Commisariat à l'Energie Atomique* (CEA). The bending magnet beamline is dedicated to studies of surfaces and interfaces. The white beam is reflected at a vertically collimating mirror, passes a Si(111) double crystal monochromator in reflection geometry that allows horizontal focusing and is reflected at a second Ir-mirror for vertical focusing. The spectral range of the x-ray light is from 7–30 keV. The SUV station (*S*urface under *U*ltra-high *V*acuum) is a surface preparation chamber which is stationarily installed on a z-axis surface diffractometer, with the sample surface normal oriented horizontally. By tilting the whole chamber, the incident angle can be adjusted with respect to the sample surface. The sample alignment is realized with a goniometric head, which allows tilts and translations of the sample inside vacuum. The azimuthal orientation of the sample is obtained by rocking of the goniometric head with a differentially pumped rotary feedthrough. The chamber is equipped with UHV preparation and analysis tools such as electron beam evaporators, reflection high energy electron diffraction, Auger electron analysis, ion sputtering, quartz microbalance and a high-temperature heating station. Via a load lock chamber and an intermediate chamber, a quick sample introduction is possible.

A photon energy of 11.04 eV was applied in the experiments described in this work. Wide-angle x-ray diffraction was performed with a point detector, in addition the GISAXS-signal was recorded with a CCD-camera. This camera was placed 1.4 m downstream of the sample. An adjustable beam stop protected the camera from the direct beam. The scattering scheme is described in ref. [80].

ID 15A

The high energy scattering beamline ID 15A is optimized for x-rays in the photon energy range range between 40 keV and 300 keV. The optical path is sketched in fig. 4.4. The x-rays are generated in a wiggler. The white beam is monochromized with a double crystal monochromator in Laue geometry. The High Energy Micro Diffraction (HEMD) setup is installed in the experimental hutch of beamline ID 15 A. To reduce the size of the footprint of the sample at small incident angles, the beam is focused with a compound refractive lens system, consisting of a stack of 232 Beryllium lenses, resulting to a beam size of 4×24 μm. The HEMD diffractometer has the degrees of freedom of a six-circle diffractometer,

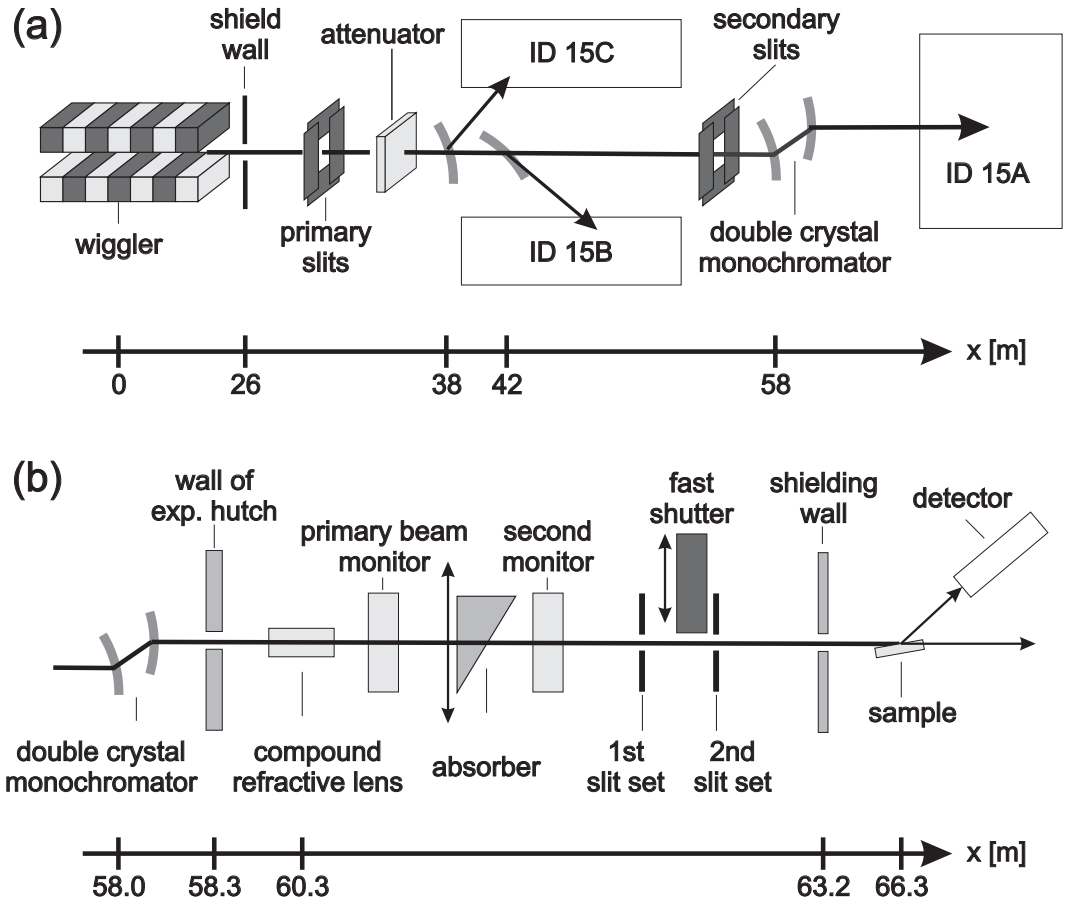

Fig. 4.4: (a) Layout of the high-energy beamline ID 15A. (b) Optical elements and beamline set up [89].

but with the motions of the detector realized by a combination of linear motions, in contrast to conventional x-ray diffractometers and therefore providing a very high precision. The sample is positioned on a Huber tower allowing an alignment of the optical sample surface and rocking the sample around its surface normal. This tower is mounted on a circle that allows an adjustment of the incident angle. A scintillation detector, a photo diode as well as a CCD camera can be used for data collection. An additional feature of the setup is a pair of monochromators in front of the sample tower, which allows tilting the incident x-ray beam. These monochromators were not applied for the experiment described in this work, but they serve e.g. for reflectivity studies at liquid surfaces. The previous prototype instrument is described in ref. [90], and a more detailed description of the HEMD setup is given in ref. [89].

ID 03

The source of beamline ID03 is a set of three undulators that provide radiation in the energy range from 5-24 keV. A channel-cut Si(111) monochromator is used which does not allow focusing of the beam. The beam size at the sample position can be configured by a mirror system. One mirror is a cylindrical piece of Si which is mounted on a bender. A second flat mirror is used to put back the x-ray beam into horizontal direction. Both mirrors are coated with Pd, its absorption edge at 24.35 keV leads to the high energy cut-off. The first experimental hutch downstream of the optics hutch is equipped with a surface diffractometer in vertical geometry. For the x-ray diffraction experiment described in chapter 9, a photon energy of 14 keV was used.

4.3.3 BW2 at HASYLAB

The storage ring DORIS III (Double Ring Store) is operated by the Hamburg Synchrotron Laboratory HASYLAB. It is located at the research center DESY (Deutsches Elektronen-Synchrotron). It was originally build as an electron-positron collider for high-energy physics in 1974, and since 1993 it has been operated as a dedicated source for synchrotron radiation. The ring stores a positron current of 140 mA at an energy of 4.5 GeV. It contains nine insertion devices and operates 36 experimental stations, including dipole beamlines. The x-ray source of beamline BW2 is a wiggler, with a spectrum from 2 keV to 33 keV. To cut off the high-energy part of the spectrum, a Au/SiC/C-plane mirror is used. A carbon foil serves as a window between storage ring and the monochromator entrance window to allow transmission of low-energy x-rays. The double crystal monochromator consists of two Si(111) crystals. Downstream, an Au-coated mirror focuses the monochromatic beam in the experimental hutch. The end station is a horizontal[2]

[2]with respect to the sample surface normal

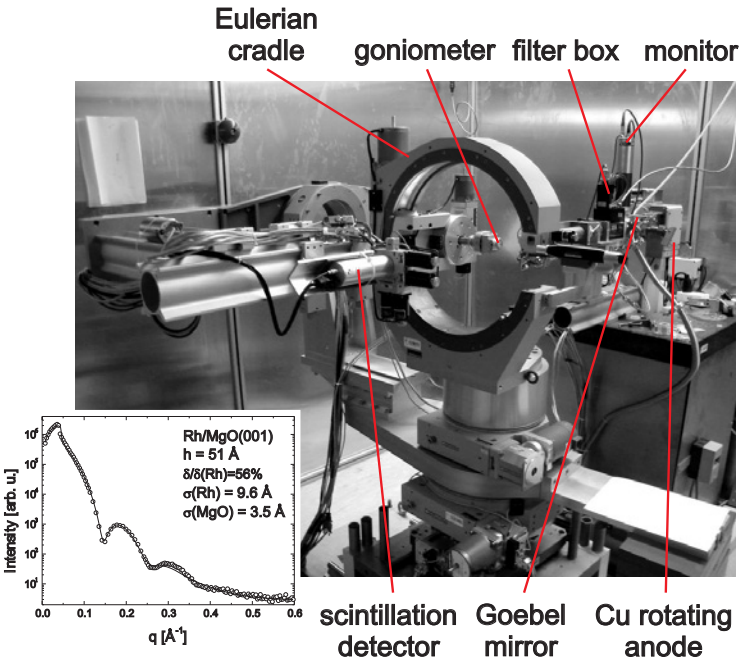

Fig. 4.5: The diffractometer at the Cu rotating anode was used mainly for x-ray reflectivity, but also for in-plane and out-of plane diffraction to study epitaxial relationships. The inset shows a reflectivity curve for Rh/MgO(100) nanoparticles.

z-axis diffractometer. A more detailed description of the beamline optics can be found in [91], the diffractometer is described in ref. [87].

4.3.4 High Power Rotating Anode

A Cu rotating anode with a power of 5.4 kW served for an ex situ characterization of the samples in the home lab (fig. 4.5). The basic set-up is a z-axis diffractometer in vertical geometry. Either a Eulerian cradle or a Huber tower can be mounted. The setup allows x-ray reflectivity measurements and diffraction analysis in θ-2θ-geometry (specular and in-plane) to determine the crystalline orientation of the deposited metal of the samples. The x-ray reflectivity measurements were of special importance to determine the deposited amount of metal on a substrate in order to calibrate the flux of the electron beam evaporator in the stationary growth chamber (sec. 4.1.1). The inset in the figure shows an x-ray reflectivity curve obtained for a Rh/MgO(100) sample.

4.4 Electron Based Sample Analysis

4.4.1 Auger Electron Spectroscopy

Auger electron spectroscopy can be used to analyze the elemental composition at a surface [92]. The method exploits the emission of Auger electrons when an atom is ionized by a primary electron beam, with a typical energy of 3 keV or a

photon beam with sufficiently high energy. The emitted Auger electrons have an energy distribution characteristic for each element.

The most important application of Auger electron spectroscopy in this work is to check the substrate crystal surfaces for contamination before the deposition of the metal. A further application of Auger electron spectroscopy was to obtain depth-resolved information on the chemical composition of the sample. As will be described in chapter 9, this can be achieved by repeated sputtering of a spot on a sample surface and subsequent recording of an Auger spectrum.

4.4.2 Transmission Electron Microscopy

Transmission Electron microscopy allows the mapping of structures with a spatial resolution in the Angstrom-range [93]. Here, the wave properties of the electrons are exploited. An acceleration voltage of several hundred keV is used to achieve a sufficiently small De-Broglie wave length of the electrons. Secondly, a high energy of the electrons is required in order to yield the transmission through the sample. In analogy to light microscopy, the electrons illuminate the sample section uniformly which is achieved by a condensor lens system. Downstream of the sample, there is an objective lens, an objective aperture, an intermediate lens and a projective lens. By the setting an aperture into the focal plane of the objective lens, either bright field or dark field TEM can be performed. At bright field imaging conditions, only the direct beam can pass. This allows a mass-thickness contrast. In the dark field imaging, the direct beam is blocked. For high resolution TEM, the phase contrast is exploited.

Scanning TEM can be used for a chemical analysis with a high spatial resolution. Energy dispersive x-ray spectroscopy (EDX) exploits the emission of element-specific x-ray radiation after ionization of an inner shell of an atom. With electron energy loss spectroscopy (EELS), the spectrum of the change of the kinetic energy of the monoenergetic electron beam is measured after transmitting the sample. During transmission, the electrons are scattered inelastically within the sample due to the Coulomb interaction with the electrons. An EELS spectrum consists of core edges occurring at the binding energy of the electrons, but may contain additional features. Firstly, the electron may also create plasmons. Secondly, for transition metals, a transition of the electrons of a p into an unoccupied d-state may occur, which leads to broad features in the spectrum. The typical energy range of EELS is from 0-3 keV. A description of the instrumentation and examples of different classes of materials are given in ref. [94].

For TEM, a high preparative expenditure of the specimens is required. For a sufficient thinning of the material, the sample has to be grounded mechanically, and subsequently treated with ion milling.

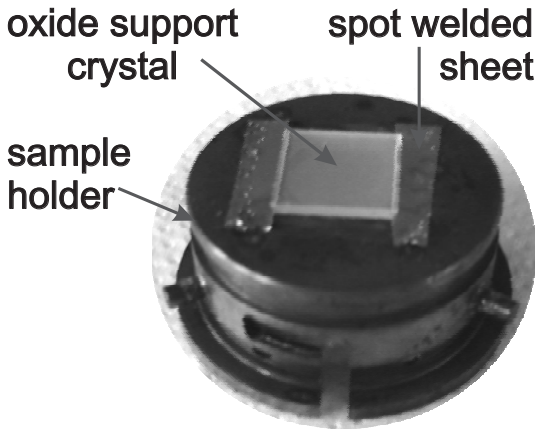

Fig. 4.6: The support crystals (size: 10 mm × 10 mm × 1 mm) had two slits on their sides and were clamped between two metal sheets that were spot-welded on the sample holder. For the oxidation studies, inconel sample holders and sheets were used. If no high pressure oxidation was applied, alternatively a molybdenum sample holder was used with tantalum metal sheets.

4.4.3 X-ray Photon Spectroscopy

X-ray photon spectroscopy (XPS) exploits the photoemission of electrons [92]. The analysis of the energy spectrum of the emitted electrons allows an identification of the chemical elements. The measured quantity is the kinetic energy E_k of the electrons. The relation to the binding energy E_B is

$$E_B = h\nu - E_k - W, \tag{4.1}$$

where $h\nu$ is the photon energy and W is the work function of the spectrometer. As a source for the x-ray radiation, typically Al or Mg K_α-radiation is used. The use of synchrotron radiation offers the advantage of tunable photon energy and therefore different information depth. Due to the limited free paths of electrons in a solid, the method is surface sensitive. By using hard x-rays, also buried structures within a sample can be probed. XPS does not only allow an identification of the chemical elements. The detailed core-level binding energies depend on the chemical state of the atom. An according chemical shift can be used to identify elements in different chemical compounds.

4.5 Details on the Sample Preparation

The nanoparticle samples were prepared by metal deposition on oxide single crystals in ultrahigh vacuum. For using the sample in the oxidation x-ray chamber and the stationary preparation chamber, they were mounted on an inconel sample holder which is a high-temperature oxygen resistant Ni alloy. Inconel plates were clamping the support crystal in two slits on diametric sides. The plates were spot-welded on the sample holder (see fig. 4.6).

For all samples, the Rh and Pd nanoparticles were deposited by electron beam evaporation. Before oxidation studies on the systems Rh/MgO(100) and Rh/α-Al_2O_3(0001) could be accomplished, prestudies on the control of epitaxial growth and the possibility to obtain a shape-sensitive diffraction signal from

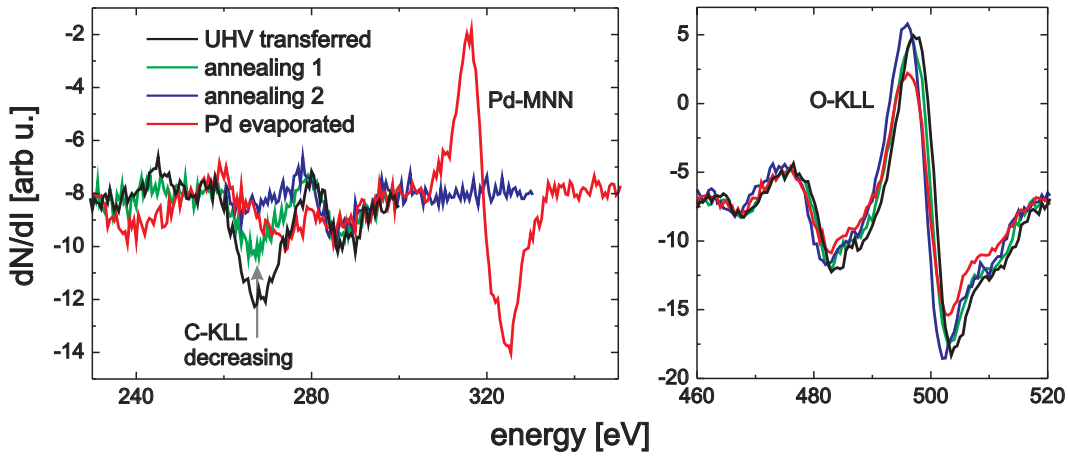

Fig. 4.7: Evolution of Auger spectra of α-Al_2O_3(0001) in UHV prior to processing (black lines) after 1 hour UHV annealing 1200K (green lines), 1 hour UHV annealing and 10 minutes O_2 exposure (10^{-5} mbar) at 1350 K (blue lines) and Pd deposition (red lines).

the particles were transacted. These first samples were grown with different nominal thickness and at different substrate temperatures by the staff of the central scientific facility *Thin Film Growth Laboratory* at the MPI MF. The later samples that were used for the oxidation were either grown in the described stationary growth and preparation chamber (sec. 4.1.1) , in the mobile oxidation x-ray chamber (sec. 4.1.2) or in the SUV-chamber at BM32 at the ESRF (sec. 4.3.2).

The support crystals were commercially available α-Al_2O_3(0001) and MgO(100) single crystals (CrysTec GmbH Berlin), with a miscut $< 0.1°$.

In the beginning of this research work, the as-bought α-Al_2O_3(0001) crystal was directly transferred into the preparation chamber and the oxidation chamber, later on, the crystals were cleaned for 10 minutes with acetone in an ultrasonic bath and subsequently for 10 minutes with ethanol prior to transferring them into the preparation chamber. For the growth of Pd/Al_2O_3 as described in chapter 8, the ultrasonically cleaned sapphire was transfered into the preparation chamber. The Auger spectra displayed in fig. 4.7 show a contamination of carbon. First, the sample was UHV-annealed at 1200 K for one hour, which lead to a decrease of the carbon signal. Further UHV annealing at a temperature of 1350 K for one hour and applying 10^{-5} mbar of oxygen for 10 minutes lead to a remarkable decrease of the C-signal. Finally, Pd was deposited at T = 570 K.

For the Rh/Al_2O_3samples prepared in the *Thin Film Growth Laboratory*, a 10 minutes Ar-ion sputtering at low energy (200 eV) was applied between two cycles of UHV annealing for the acetone/ethanol cleaned crystals.

Prior to mounting MgO(001) crystals on the a sample holder, they were first

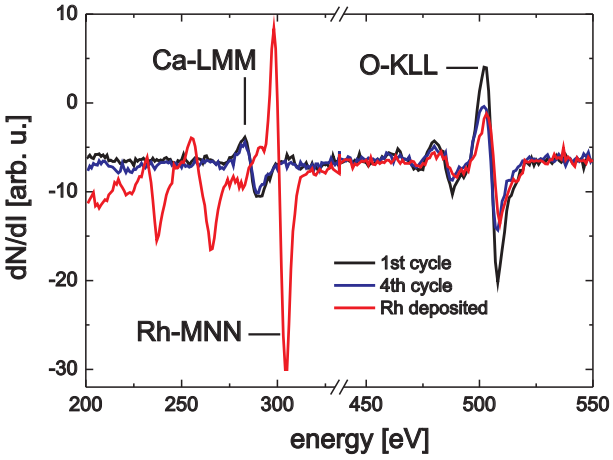

Fig. 4.8: Auger spectra of MgO(100) after cycles of sputter/annealing and after Rh deposition.

annealed in air at a temperature of 1670 K for one hour, with a heating rate of 20 K/minute. This procedure serves to segregate subsurface contaminants to the crystal surface (typically Ca), and secondly for an enlargement of the terraces. After transferring the crystal into UHV, cycles of argon ion sputtering with energies between 600 eV and 1500 eV for typically 1 hour were applied, subsequently the crystals were annealed in an oxygen atmosphere of around 10^{-5} mbar. The composition of the surface was checked with Auger electron spectroscopy, and the sputtering/oxidation cycles were repeated until no further progress in the removal of Ca could be achieved. Fig. 4.8 shows an Auger spectrum during the preparation process and after deposition of rhodium.

4.6 Overview of the Samples Studied with Synchrotron Radiation

Table (4.1) shows a summary of the samples of Rh and Pd on MgO and α-Al_2O_3 that were studied at synchrotron radiation facilities with x-ray diffraction. Additional samples were grown e.g. with the purpose of evaporator calibration or as backup samples for the synchrotron beamtimes.

Material	growth station	beamline	remark
Rh/Al_2O_3, Rh/MgO	Central Scientific Facility Thin-Film Laboratory	BW2 (HASYLAB)	ex situ prestudies on epitaxy and particle shape, TEM
Rh/MgO	SUV station, particle growth under x-ray control	BM32 (ESRF)	cf. chapter 5, TEM
Rh/MgO	stationary preparation chamber, in situ transfer into mobile chamber	MPI MF (ANKA)	cf. chapter 5
Pd/MgO	SUV station, particle growth under x-ray control	BM32 (ESRF)	cf. chapter 6, TEM
Pd/MgO	stationary preparation chamber, in situ transfer into mobile chamber	ID15A (ESRF)	cf. chapter 7
Pd/Al_2O_3	stationary preparation chamber, ambient transfer into mobile chamber	MPI MF (ANKA)	cf. chapter 8
Rh/Al_2O_3	mobile chamber, Rh growth under x-ray control	MPI MF (ANKA)	cf. chapter 8
Pd/MgO	stationary preparation chamber, ambient transfer into mobile chamber	ID03 (ESRF)	cf. chapter 9, TEM

Table 4.1: Synchrotron x-ray diffraction studies exhibited in this work. For selected samples, also TEM studies were performed after the x-ray experiments.

Chapter 5

Oxygen Induced Shape Changes of Rh/MgO(001) Particles and Microscopic Origin

This chapter deals with shape sensitive oxidation experiments under in situ conditions of Rh/MgO(001) particles with mean diameters of 8 and 9 nm. The oxidation of the 8 nm particles in the 10^{-5} mbar range at T = 600 K leads to a change of the particle shape which is accompanied by the formation of the surface oxide phase which has been known from Rh(100) and Rh(111) single crystal surfaces. The shape change is given by an increase of the (100)-equivalent facets of the particles. On the 9 nm particles, in addition the formation of (110) facets could be detected. As for the Rh(111) and Rh(100) single crystal surfaces, the surface oxide forms a kinetic barrier for the bulk oxide formation.

The shape analysis was performed with kinematic x-ray scattering as described in section (3.3.5). As for the quantitative analysis, many details had to be considered, the results of the ready analysis will be given in the consecutive text. The details of the analysis will be described in the appendix of this chapter.

5.1 Preparation of the Rhodium Nanoparticles

Two in situ oxidation experiments were performed on the MgO(001) supported Rhodium particles. The manufactured specimens will be denoted sample A and sample B in the following. The preparation of the MgO(100) crystals was described in sec. 4.5.

For sample A, Rh was evaporated in the SUV chamber at beamline BM32 at the European Synchrotron Radiation Facility (cf. sec. 4.3) under x-ray control. A photon energy of 11.04 keV was used and the incident angle was set to the critical angle of total external reflection of MgO, which is 0.20°. Rh was evaporated from an Omicron EFM3 electron beam evaporator with a substrate temperature of

670 K. The effective growth rate was 1 Å per minute, as estimated from a quartz microbalance and the flux monitor on the evaporator. The growth was monitored by in-plane XRD scans through the Rh(200) reflection. Oxidation experiments were performed in the temperature range between 500 K and 600 K and oxygen pressures in the range of 1-3·10^{-5} mbar. Simultaneous to wide angle diffraction, the grazing incidence small angle scattering (GISAXS) signal was recorded with a CCD camera (MAR 240). The camera was placed 1.4 m downstream of the sample. Beam stops inside the SUV chamber suppressed the background from the specular and direct beam as well as the background from the Be windows. Further details on GISAXS at BM32 that were previously obtained for Pd/MgO(001) can be found in [80]. The susceptibility of the GISAXS patterns towards oxidation was only small, typical intensity profiles are displayed in the appendix of this chapter.

Sample B was prepared in the UHV preparation chamber in the home lab (cf. sec. 4.1.1 and sec. 4.5). The goal was to obtain a similar sample as sample A. From x-ray reflectivity, the effective thickness d·θ was determined 29 Å. To calibrate the Rh flux of the evaporator (Omicron EFM3, as for sample A), an auxiliary sample was grown in the preparation chamber, thereby the integrated flux monitor current of the evaporator was compared with effective thickness d·θ = 18 Å, as obtained from x-ray reflectivity. Finally, Rh was evaporated with a rate of 0.37 Å per minute and the evaporation time was adjusted to obtain an effective thickness of 29 Å for sample B as well. After the metal deposition, sample B was UHV-annealed for 10 minutes at a temperature of 900 K. By a load-lock-system, the sample was transferred under UHV-conditions into the mobile high pressure compatible UHV chamber as described in sec. 4.1.2. It was shipped with a running ion pump (in order to maintain UHV conditions) to the MPI-MF surface diffraction beamline at the synchrotron radiation facility ANKA, where the x-ray experiments were performed. Here, a photon energy of 10.5 keV was used, the critical angle of total external reflection for MgO is 0.21° at this energy.

5.2 Shape Sensitive X-ray Diffraction

The epitaxial relationship between Rh and the MgO substrate was determined from radial scans in high-symmetry directions and wide rocking scans through the in-plane reflections of Rh. The particles grow with (001)-orientation in cube-on-cube-epitaxy. As was pointed out in sec. (2.1.3), the shape of a Rhodium nanocrystal can be described as a truncated octahedron. It is limited by eight (111) equivalent surfaces and truncated by (100)-equivalent surfaces on the top, bottom and side of the particle. Fig. 3.6 shows the model shape of such a particle in combination with a reciprocal space map experimentally observed with x-ray diffraction. Fig. 5.1 shows the according reciprocal space map in the (H+K=2)-plane. It is centered at the Rh(111) Bragg reflection and contains a rod-like signal

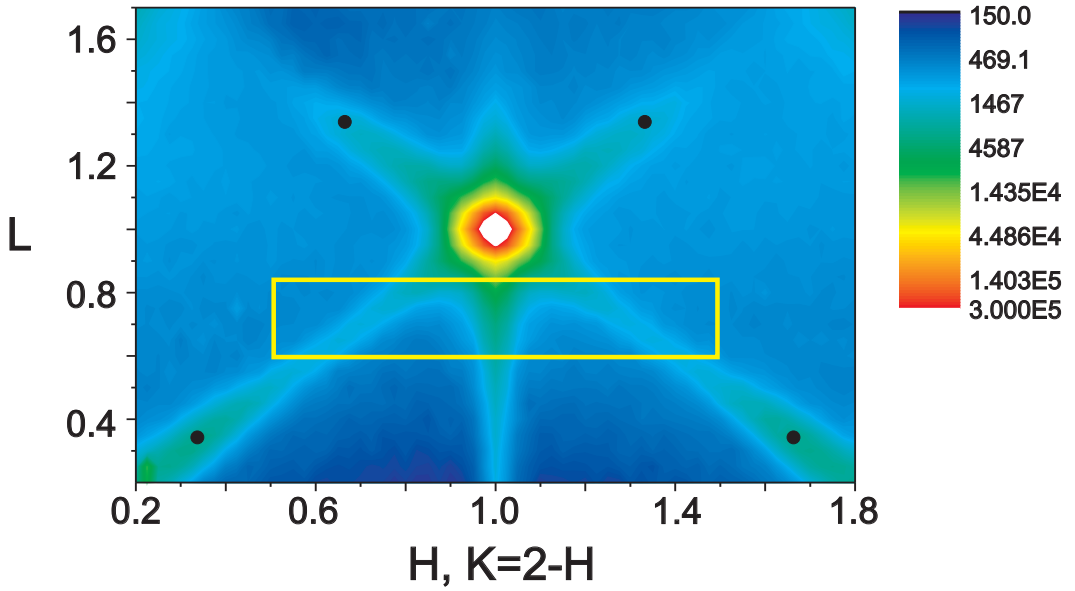

Fig. 5.1: Extended mesh scan for Rh/MgO particles with a diameter of 8 nm (sample A). The map is recorded in the (H+K=2)-plane and is centered at the Rh(111) reflection. It contains the scan directions $\langle 1\bar{1}1\rangle$, $\langle 1\bar{1}\bar{1}\rangle$ and $\langle 001\rangle$ and is therefore sensitive to the (111) equivalent facets and the top (001) facet of the nanoparticles. The yellow rectangle marks the q-range, where maps were recorded with a higher density of data points for the quantitative shape analysis. The black dots show the reflections due to internal twinning.

in (111)-equivalent and (001) directions interconnecting the surrounding Bragg reflections, as described in section 3.3. The observation of a CTR-like signal on the nanoparticles allows a direct conclusion of the existence of limiting surfaces and therefore a qualitative estimation of the particle shape. The displayed reciprocal space map does not contain the rod signal of the (100)-equivalent surfaces on the side of the particles, which point into other directions. As will be shown from the results of the quantitative analysis, one can still infer the size of the (100) side facets from the quantitative analysis. The direct experimental observation of a (100)-side rod will be demonstrated in section (5.4). As was described in section 3.3.5, identical particles which are well-aligned with the substrate would lead to characteristic interference fringes. The fact that the intensity distribution does not contain such features can be attributed to a size-distribution and the mosaicity of the particles, which leads to smearing out of interference fringes. To obtain detailed information on the shape and oxygen-induced changes on the shape, high resolution reciprocal space maps were recorded from (H, K)=(0.5, 1.5) to (1.5, 0.5) and L = 0.6-0.84, with a total amount of 1515 data points. This region is marked with a yellow rectangle in fig. 5.1. The q-range of the high resolution mesh scans was chosen in such a way that no contribution of twinned particles (cf. appendix B in this chapter) is included.

5.3 Shape and Shape Change of the FCC Core

After Rh deposition and an initial oxidation/reduction cycle ($p_{O2} = 1 \cdot 10^{-6}$ mbar, $p_{CO} = 10^{-5}$ mbar) at 570 K, the sample was annealed at 970 K for 5 minutes and subsequently cooled down to 600 K, in order to achieve equilibrium shape of the particles. Subsequently, extended mesh scans and high resolution mesh scans for the sample under UHV conditions and during exposure to an oxygen pressure of $3 \cdot 10^{-5}$ mbar were recorded.

Fig. 5.2 (a) shows the experimentally observed and the fitted intensity distribution of the high resolution reciprocal space map. The obtained shape of the fcc-core is displayed in fig. 5.2 (d) The result of the analysis is a shape described by the parameters $\{N_P = 31 \pm 1, N_E = 3 \pm 1, N_T = 20 \pm 1, N_B = 5 \pm 1\}$[1].

The ideal Wulff construction claims that $\frac{\gamma_i}{h_i} = const.$, where γ_i is the surface energy of facet plane i with distance h_i from the center of the unsupported particle. This implies that the (100) facets on the side of the particle are expected to have the same size as the (001) facet on top of the particle, or equivalently, $N_E = N_P - N_T$ shall be fulfilled. This is neither the case for the oxidized nor for the clean particles. The obtained parameters for the nanoparticle shape can be used to estimate the ratios of the surface energies of the facets. For the top facets, one obtains $\frac{\gamma_{001}}{\gamma_{111}} = \frac{h_{001}}{h_{111}} = \sqrt{3} \cdot \frac{N_T}{N_P} = 1.12 \pm 0.09$ and $\frac{\gamma_{100}}{\gamma_{111}} = \frac{h_{100}}{h_{111}} = \sqrt{3} \cdot \frac{N_P - N_E}{N_P} =$

[1]For accuracy of the fit results of the particle shape, cf. appendix A.2 in this chapter.

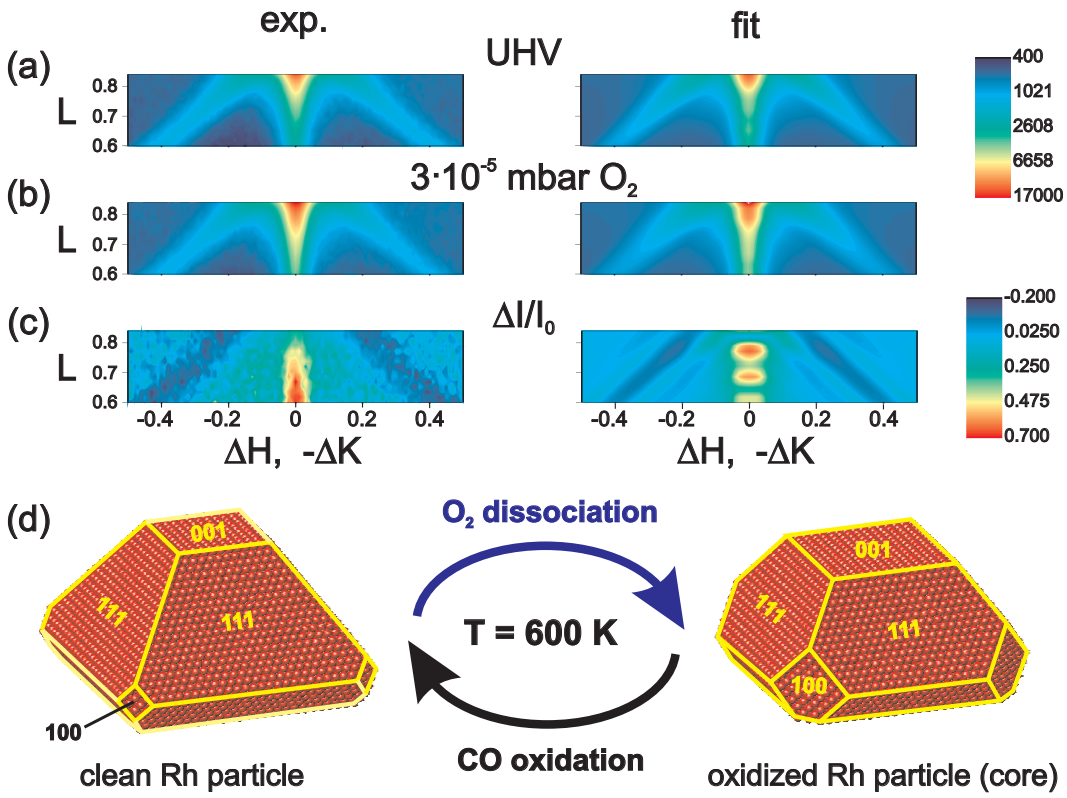

Fig. 5.2: High resolution mesh scans for the particles under UHV conditions and in an oxygen atmosphere of $3{\cdot}10^{-5}$ mbar. The difference map $\Delta I/I_0$ shows a decrease of the signal along the $\langle 111\rangle$-directions, whereas there is an increase along $\langle 001\rangle$. The lower part shows the fitted intensity profile, which is related to a particle shape described by $\{N_P = 31 \pm 1, N_E = 3 \pm 1, N_T = 20 \pm 1, N_B = 5 \pm 1\}$ for the particles under UHV conditions and $\{N_P = 31 \pm 1, N_E = 7 \pm 1, N_T = 16 \pm 1, N_B = 5 \pm 1\}$ for the particles under oxidizing conditions.

1.56 ± 0.06 for the side facets. The theoretical value [25] is $\frac{\gamma_{001}}{\gamma_{111}} = 1.16$. Thus, the top facets have a size which is in approximate agrement with the Wulff construction, but the side facets are smaller. This is can be assigned to a confinement effect mediated by strain and/or nanoparticle edge effects (line tensions) which are neglected in the Wulff construction. The Rh adhesion energy E_{ad} can be calculated from ref. [95] as $E_{ad} = \gamma_{100} \cdot \frac{N_T - N_B}{N_T} = 108 \pm 10$ meV/Å^2, which is below the theoretical value of 130 meV/Å^2 that was determined for a monolayer of Rh on Mg(100) support [96].

In the next step, the Rh nanoparticles were exposed to an oxygen atmosphere of $3{\cdot}10^{-5}$ mbar. The diffraction map is displayed in figure 5.2 (b), together with the fit. For a better visibility, the difference map $\Delta I/I_0$ is displayed in fig. 5.2 (c). It shows an increase of intensity along the $\langle 001 \rangle$ direction, and a decrease of intensity along the $\langle 111 \rangle$-equivalent directions. This result implies qualitatively, that the shape of the particle must change in such a way that the surface area of the (111)-equivalent facets decreases, and the area of the (001) top or bottom facet increases. Indeed, the fit of the intensity distribution leads to a particle shape which is characterized by $\{N_P = 31 \pm 1, N_E = 7 \pm 1, N_T = 16 \pm 1, N_B = 5 \pm 1\}$, which implies that the (001) facet on top and on the side of the particles increase[2]. The strong increase of (110) facet area as predicted by theory for the applied conditions [25], was not observed for the 8 nm particles (cf. fig. 5.7 (b) in section 5.4). Furthermore, no additional higher indexed facets are formed in between the (111) and the top (001) facet, which would readily be observable via additional diffraction intensities.

A further observation is that the shape change of the particles is reversible upon CO exposure at 10^{-5} mbar. This can directly be verified by inspection of the line scans given in fig. 5.3 (a), which shows a line-scan at L = 0.8 before oxidation and after inlet of oxygen. The feature is the intensity increase on the (001) rod position and the decrease on the (111) facet signal. Fig. 5.3 (b) shows the corresponding line scan after CO reduction, and as a comparison, the line scan before oxidation, which is nearly identical. The slight increase of intensity is due to an increase of the background, related to a slightly higher incident angle, probably related to a slight variation of the beam due to the refill of the electron storage ring.

Note, that the line scan in fig. 5.3 (a) that was performed in the oxygen atmosphere shows a peak at $H_{top} = -\frac{1}{3}$. This peak had not been present under UHV conditions, but is also missing, when the same scan is performed later on in the oxygen atmosphere. This suggests that there exists a transient structure during the shape change of the particle. In order to decelerate its decay, the

[2]It will be shown in the following sections that under the applied oxidation conditions, the nanoparticle is covered with an ultra thin oxide shell. The influence of the oxide on the signal on the (001) top facet was included in the calculations, as described in sec. 3.4.2. The oxide layer on the Rh(111) facets does not contribute to the recorded reciprocal space map.

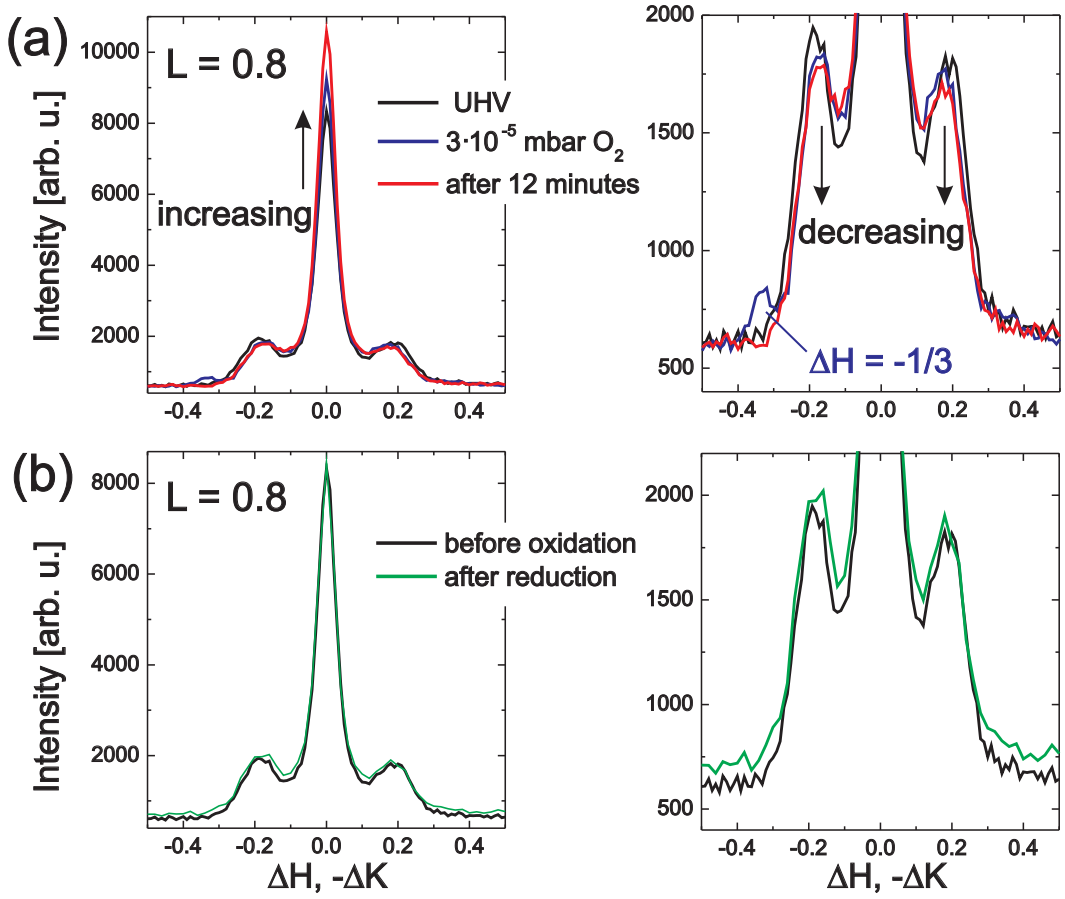

Fig. 5.3: Line scans at (H+K=2) for L=0.8 which is contain in their center the (001) rod signal, and at $(\Delta H, -\Delta K = \pm\ 0.2)$, the signal of the (111) facets. (a): During oxidation, the signal of the (001) rod increases and along the (111) facets decreases. In the beginning of the oxidation, an additional reflection is visible at $(\Delta H, -\Delta K) = \pm\frac{1}{3}$. (b): Under reducing conditions with CO, the original line profile can be recovered. The slight increase of intensity is due to increased background.

sample was cooled down to a temperature of 530 K after reduction with $1{\cdot}10^{-5}$ mbar of CO.

5.3.1 Observation of a p(3×1) Superstructure

At this lower temperature, oxygen with a pressure of $2 \cdot 10^{-5}$ mbar was dosed. As can be seen from fig. 5.4 (a), peaks occur at positions $H_{top} = \pm\frac{1}{3}$, simultaneously, an intensity decrease of the (001) facet signal can be monitored. Thus, the occurrence of the structure must happen prior to the flattening of the particles, otherwise an intensity increase of the (001) rod signal should be observable, as observed at 600 K. Further scans in selected directions show that the signal can be assigned to a p(3×1)-structure. The positions where the reflections of a p(3×1) structure are anticipated are sketched in fig. 5.4 (b). The p(3×1)-structure was observable on a timescale of ≈ 30 minutes. It could be recovered after reducing with CO and re-applying of oxygen. Six further cycles of reduction and oxidation were applied at this temperature. Another oxidation/reduction cycle was performed at a temperature of 570 K. In all cases the signal of the (3×1) structure could be reproduced. For a stabilization of the structure, the temperature was further decreased to 500 K, where again oxidation/reduction cycles were applied. A mesh scan in the (H+K=2)-plane under UHV conditions and in an atmosphere of $2{\cdot}10^{-5}$ mbar is displayed in fig. 5.4 (d). The rod-like signal appearing in the oxygen atmosphere evidences the two-dimensional structure of the layer. In the end of this synchrotron x-ray diffraction study, about 1.5 hours after the last oxidation inlet, the sample was cooled down without a reduction and transferred out of the vacuum chamber.

As was pointed out in section (2.3.2), a reconstruction for the oxidation of the Rh(100) single crystal surface was reported in refs. [48, 49] with a possible (3×1) structure. Even though there is no dedicated structure analysis for this reconstruction, there exists also a p(3×1) structure on the $Pt_{25}Rh_{75}(001)$ surface. It is believed [50] that this reconstruction has a similar structure to that on Rh(100). This model suggests that every third metal row is shifted by half a surface unit cell, together with relaxations of the top Rh atoms perpendicular to the surface. This model, adapted to Rh(100), is displayed in fig. 5.4 (c). The oxygen atoms are arranged in such a way that they are threefold coordinated by Rhodium atoms.

5.3.2 High-resolution TEM study

The same sample, in the oxidized state and after exposure to ambient conditions, was subject of a high-resolution cross section transmission electron microscopy study and spatially-resolved electron energy-loss spectroscopy (performed by Dr. N.Y. Jin-Phillipp, MPI MF). For some of the particles, it could be shown that the (111) and (001) facets are covered with a one monolayer thin oxide with a

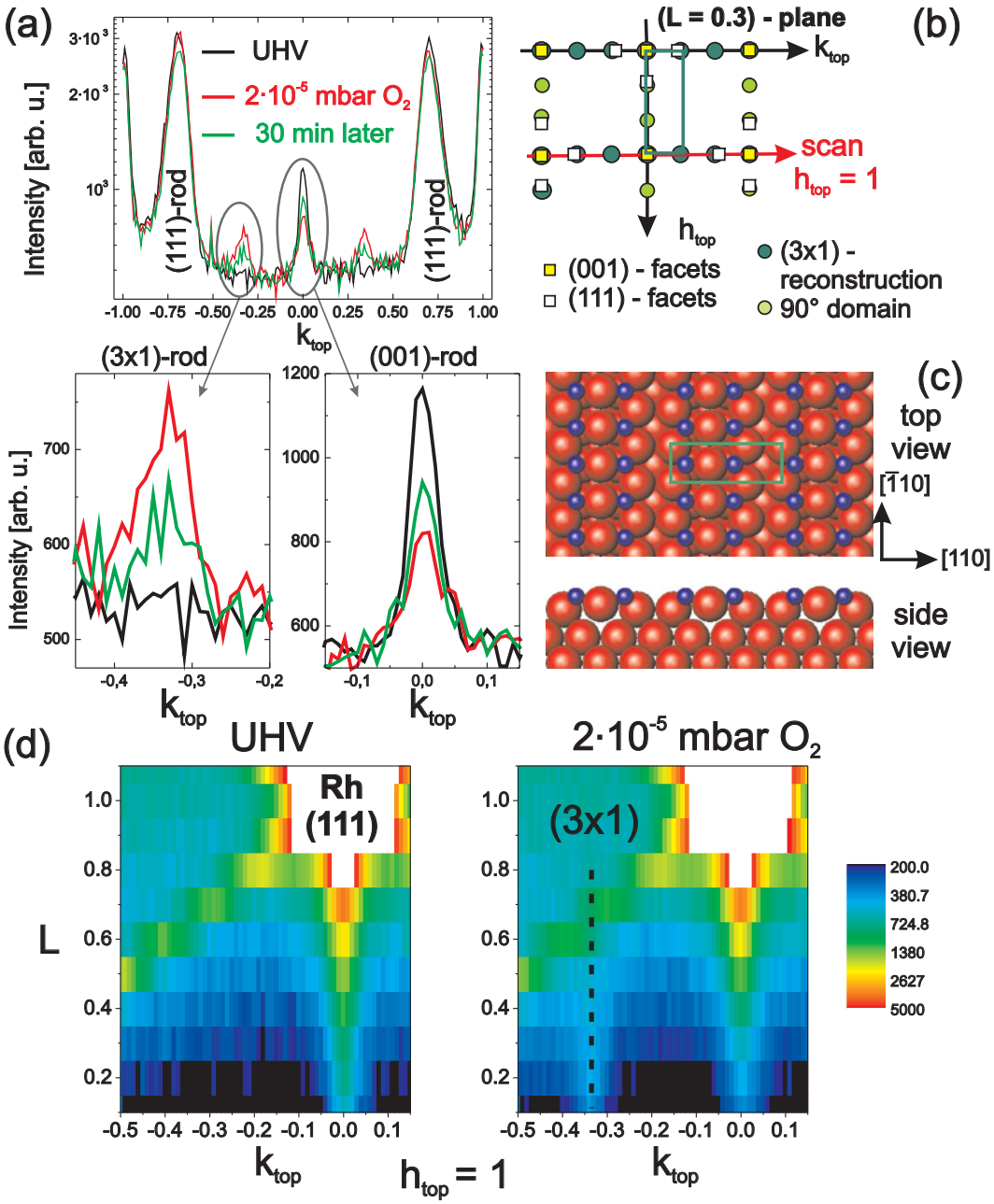

Fig. 5.4: p(3×1) structure observed on the top facet of the Rh nanoparticles. (a) line scans at T=530 K under UHV and oxidizing conditions, showing that the formed structure is transient. (b) Sketch of the scan direction and positions of the reflections of a p(3×1) structure together with the positions of the facets-rods of Rh. (c) A shifted row model according to [50] of the p(3×1)-reconstruction. (d) To demonstrate the two-dimensional structure, line scans at different l-values were performed and show a rod-like intensity distribution along q_z. To delay the decay of the structure during the scans, a lower temperature of 500 K was applied.

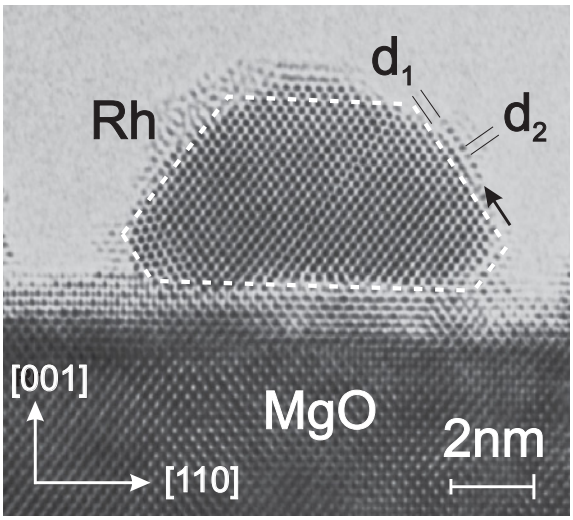

Fig. 5.5: High resolution TEM micrograph of a Rh/MgO particle. The layer marked with the arrows has a distance d_1 from the (111) facet and a lateral periodicity d_2 that corresponds well with the O-Rh-O trilayer surface oxide on Rh(111). (Courtesy of Dr. N. Y. Jin-Phillipp, MPI MF). The dashed hexagon nearly describes the particle shape and has the same aspect ratio as the average particle shape obtained from quantitative analysis under oxidizing conditions.

lateral periodicity d_2 and a lattice spacing d_1. As concluded from TEM image simulations, the observed structure corresponds to the O-Rh-O surface oxide trilayer structure as the Rh surface oxides that have been known from the Rh(111) and Rh(001) single crystal surfaces (refs. [11, 12] and section 2.3.2). The results of this TEM study will be described in detail in reference [13]. The observation of the surface oxide, even though the sample was exposed to ambient conditions and the rather destructive TEM specimen preparation gives first evidence of kinetic barriers toward bulk oxide formation one the surface oxide has formed. More details on the role of the surface oxide as a kinetic barrier can be found in section 5.5.

5.4 In situ Observation of Surface Oxides on Rh Nanoparticles

The results of the TEM study, combined with the results of the surface x-ray diffraction experiment suggests that the surface oxide phases are the final state of oxidation in the pressure range of 10^{-5} mbar and the observed p(3×1) structure is a precursor of the surface oxide phase. This explains why after vanishing of the p(3×1) structure, a CO reduction was necessary to recover the p(3×1) structure in a following oxidation step. For a more detailed study of the formation and decomposition of these surface oxides, a further in situ x-ray diffraction experiment of the oxidation of Rh/MgO(100) was performed[3]. Moreover, the bulk oxide formation could not be studied on the 8 nm particles, as the used vacuum chamber did not allow gas pressures far above the 10^{-5} mbar pressure

[3]Already for the 8 nm particles, reflections were observed that could be explained only by the formation of the surface oxides on the (001) and (111) facets. However, the focus was set on the unexpected formation of the p(3×1)-structure in this synchrotron experiment.

range. For this reason, the surface x-ray diffraction experiments of the oxidation of sample B was performed in the high-pressure compatible chamber (sec. 4.1.2). As concluded from the Bragg peak FWHMs, the mean size of the Rh particles is 9 nm diameter and 5 nm in height, thus about 10% larger than the average particle size of sample A. In order to investigate the formation of the surface oxides, line scans in high symmetrical direction with respect to the surface lattices of the (001) and the (111)-equivalent facets were performed. The upper left part of fig. 5.6 shows the reciprocal lattice of the Rh(001) surface. As was described in section (3.1.2) for the c(2×8) surface oxide structure model [11], due to the hexagonal arrangement of the atoms, not at all positions $(H_{top}, K_{top}) = \left(\frac{m}{2}, \frac{n}{8}\right)$ does exists a structure factor contribution, especially not in radial high symmetry directions with respect to the underlying metal lattice. The green dots show the positions of reflections where a signal of this surface oxide is anticipated, and the position of the line-scan that was performed experimentally. A scan of K_{top} at $H_{top} = \frac{7}{8}$ was used for the detection of the c(2×8) reconstruction.

The upper right part of fig. 5.6 shows the positions of the surface oxide on the (111)-equivalent facets with respect to the (111) surface lattice. This signal can be detected along radial scans in high symmetry directions[4].

The diagrams in the bottom of fig. 5.6 show the reference scans for the sample under UHV-conditions, during oxidation with a pressure of $1 \cdot 10^{-5}$mbar of oxygen and after subsequent reduction with carbon monoxide. The experiment was performed at a temperature of T = 600 K. Under oxidation conditions, a new peak appears at $\mathrm{K}_{top} = 1/2$ and $\mathrm{K}_{top} = 3/2$ for the top (001) facet, and for the (111) facet, a peak at $\mathrm{H}_{\overline{1}11} = 8/9$ appears. This signal disappears when a carbon monoxide atmosphere is applied. The p(3×1)-structure was not observed probably due to its fast decay at this temperature[5]. Two further oxidation/reduction cycles were performed at this temperature, and the superstructure reflections could be reproduced.

Direct Proof of the Enlargement of (100) Side Facets and Formation of (110) Facets

A result of the quantitative analysis of the the fcc core of sample A during oxidation was the enlargement of the (100) facets on the side of the particles. To obtain a direct support of this conclusion, scans containing the (100) rod were performed for the 9 nm particles before and after oxidation. As is shown in fig. 5.7 (a) for the 9 nm particles under UHV conditions, no rod signal is evident. However, when the sample was oxidized at $2.5 \cdot 10^{-5}$ mbar, a weak signal in two

[4] A h-scan with respect to a $(\overline{111})$-equivalent facet corresponds a radial scan in $\langle 4\overline{2}2\rangle_{fcc} = \langle 132\rangle_{top}$-direction.

[5] As was shown in fig. 5.3 (a) for the 8 nm particles, the decay of the structure is faster than the recording time of the line scan. A peak is observed at $\mathrm{H}_{top} = -\frac{1}{3}$, but the structure has already vanished when the scan position at $\mathrm{H}_{top} = +\frac{1}{3}$ was reached.

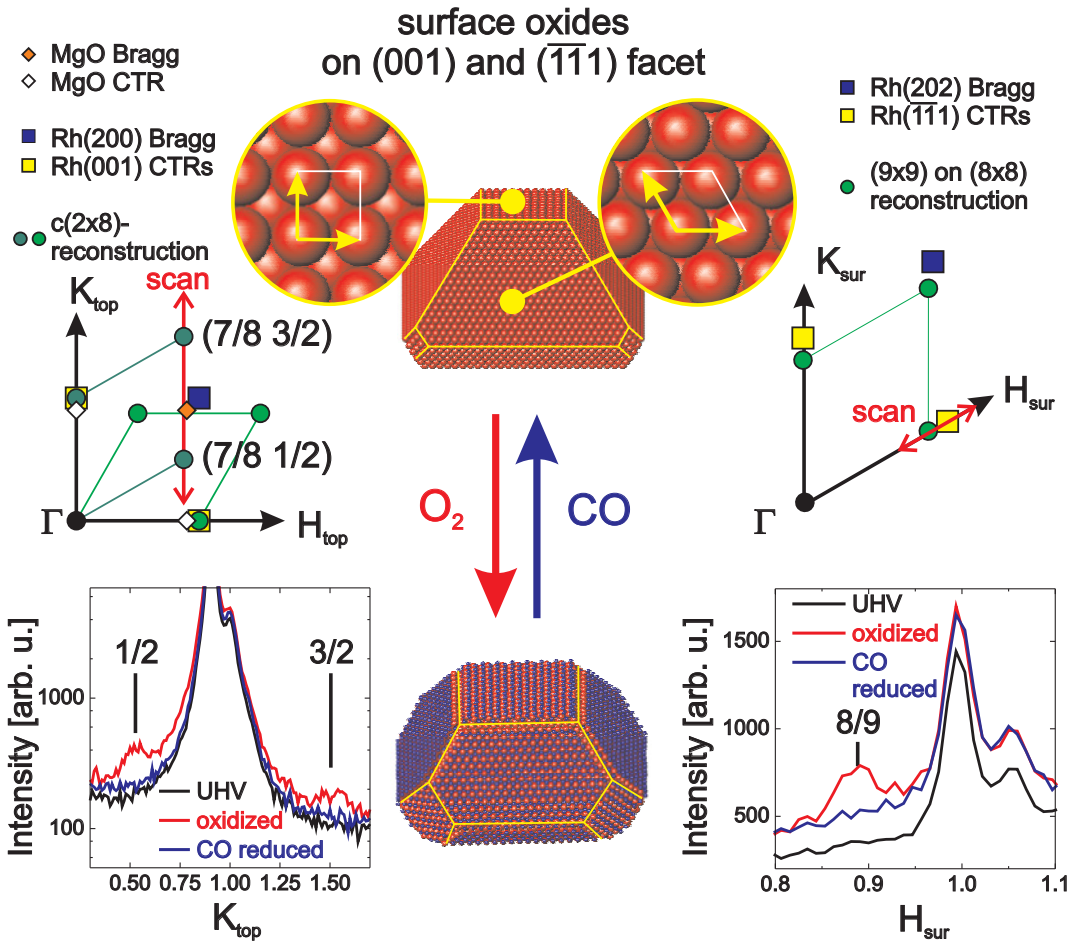

Fig. 5.6: Observation of surface oxide phase on the nanoparticles (111) and (001) facet. Top: real space and reciprocal space sketches of the surface lattice. Bottom: scans demonstrating the growth of the surface oxides under oxidizing conditions and their decay after applying carbon monoxide. Center: sketch of the shape change of the particle, mediated by the formation of the surface oxide shell.

Rh_2O_3 on (111)	H_{top} K_{top} L	Rh_2O_3 on (110)	H_{top} K_{top} L
$(10\bar{2})$	(0.49 0.52 0.03)	$(10\bar{2})$	(0.387 0.605 0))
$(01\bar{4})$	(0.98 0 0.07)	$(1\bar{1}4)$	(0.776 .0.605 0)
$(11\bar{6})$	(1.5 0.5 0.10)	(030)	(0 1.816 0)
$(2\bar{1}0)$	(0 1.05 0)		

Table 5.1: Calculated positions of Rh_2O_3 Bragg reflections on (111) and (110) equivalent facets, which can be detected at $q_z \approx 0$ and assuming the same epitaxy as for the single crystal surfaces.

⟨100⟩-equivalent directions can be found, but also a streak in a ⟨110⟩-equivalent direction. Thus, not only the (100)-side facets increase, as deduced from the quantitative analysis for the 8 nm particles, but there exist also (110) facets on the side of the 9 nm particles, as predicted by theory [25]. This is sketched in the center of fig. 5.7.

One may wonder if also on the 8 nm particles, (110)-facets may have formed. For this purpose, it is sketched in fig. 5.7 (b) a large map measured in an oxygen atmosphere of $3 \cdot 10^{-5}$ mbar, together with a difference map comparing with the signal from oxidized sample A with that under UHV-conditions. These maps include a ⟨110⟩-equivalent direction, which is marked with the red arrow. No evidence for a signal along this directions is given by the map under oxidizing conditions nor in the difference map. Thus, on the 8 nm particles, either the (110)-facets are too small to be observed or do not exist.

5.5 Bulk Oxide Formation

The oxidation experiments with the 9 nm particles were continued at a more elevated sample temperature of 670 K. The oxygen pressure was increased stepwise starting in the 10^{-5} mbar range up to the mbar range. Apart from the reference line scans for the surface oxide, also in-plane rocking scans were performed at all scattering angles corresponding to strong Bragg reflections according to ref. [41]. The rocking scans and the position of the reflections in q-space are plotted in figs. 5.10 - 5.13. The scans were recorded under UHV conditions, at an oxygen pressure of 10^{-5} mbar (formation of surface oxide), and at 1 mbar. At 10^{-5} mbar the formation of the c(2×8) and the (8×8)/(9×9) structure could be observed. No changes occur at a pressure of 10^{-3} mbar. At the following oxidation step at 1 mbar, the formation of Rh_2O_3 was initiated and Rh_2O_3 reflections became observable. Simultaneously, the signal of the surface oxide was still present. Two of appearing peaks in fig. 5.8 (b) can be related to Rh_2O_3 bulk oxide reflections: (116) and (113). Further reflections are present at $K_{top} = 0.4$ (d = 2.79 Å) and $K_{top} = 1.5$ (1.55 Å) in figs. 5.8 (b) and 5.9, at the position of the surface oxide. As the surface oxide peak at $K_{top} = 0.5$ vanished, the peak at 1.5 must stem from

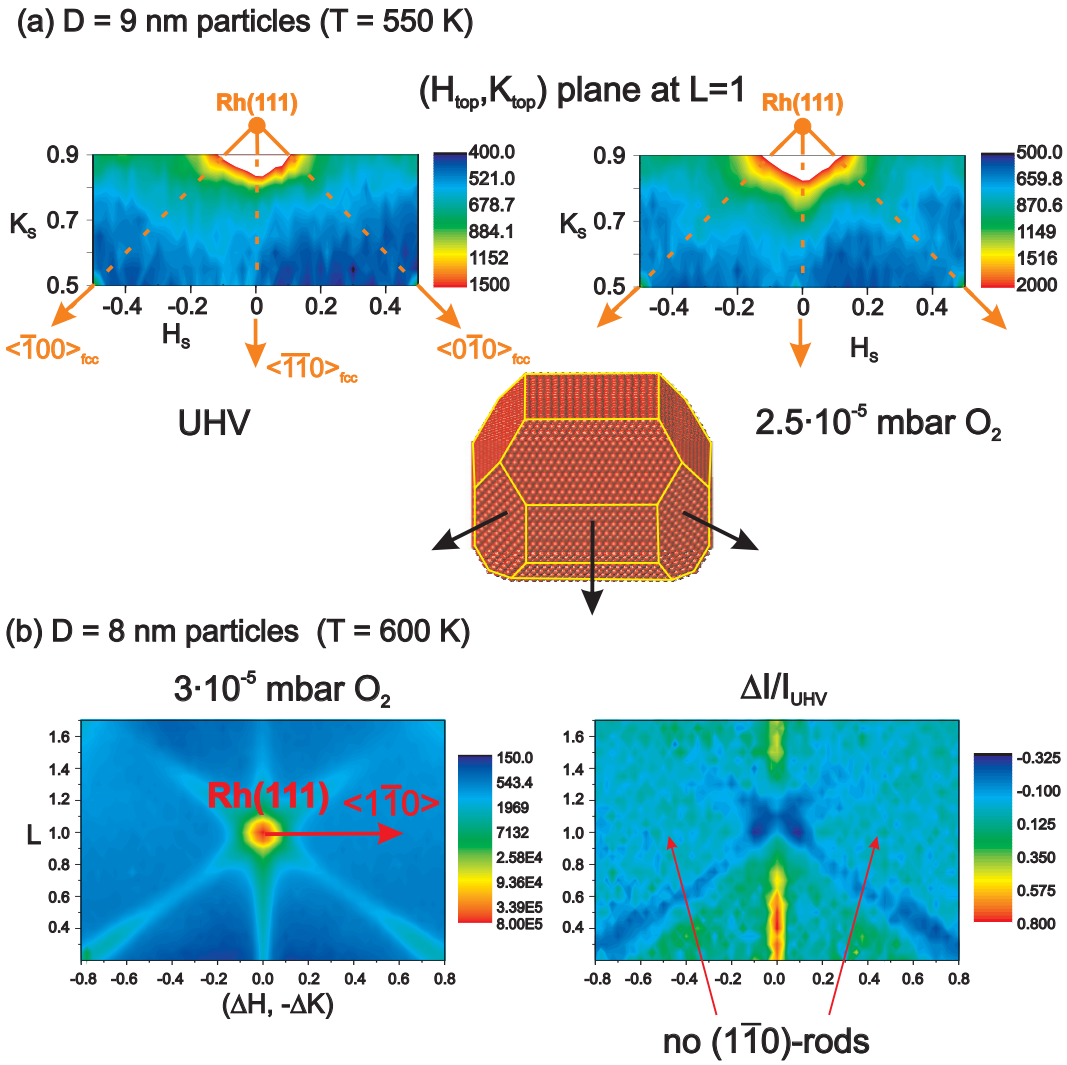

Fig. 5.7: (a) To prove directly the suspected increase of (100) facets, a map in the L=1 plane was measured for sample B. A weak increase of intensity along the $\langle\bar{1}00\rangle$ and $\langle\bar{1}00\rangle$-directions is detected, together with signal along $\langle\bar{1}\bar{1}0\rangle$. The orientation of the mapped (100) and (110) facets is sketched with the particle in the center. (b) In contrast, there exists no hint for (110) facets on sample A. The extended mesh scan contains an equivalent direction as for sample B, which is marked by the right arrow. Neither under UHV conditions, nor in the difference map under oxidizing conditions, a streak along $\langle 1\bar{1}0\rangle$ can be detected.

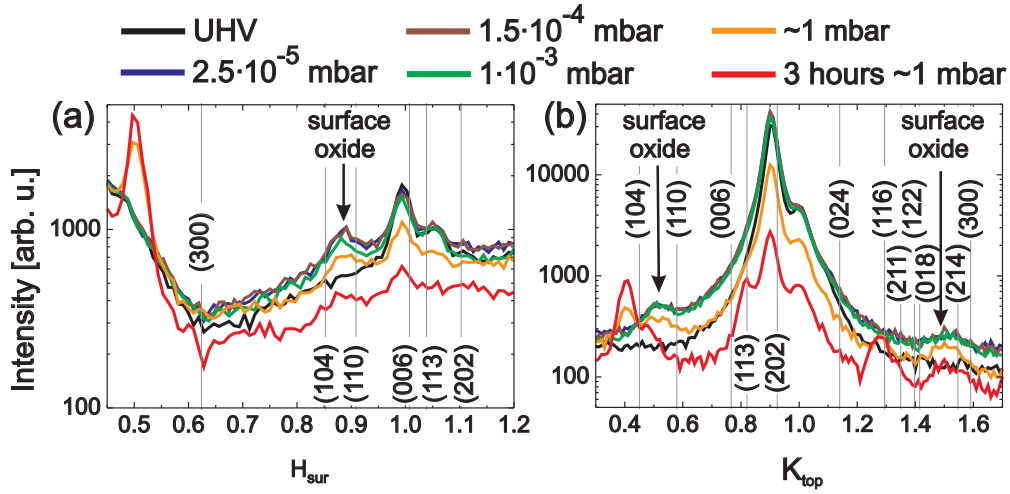

Fig. 5.8: Oxidation at T = 670 K starting from ultrahigh vacuum. In the pressure range from 2.5×10^{-5} mbar up to $1 \cdot 10^{-3}$ mbar, the surface oxide reflections were observed. For the oxidation in the millibar range, Rh_2O_3 was found first in coexistence with the surface oxide.

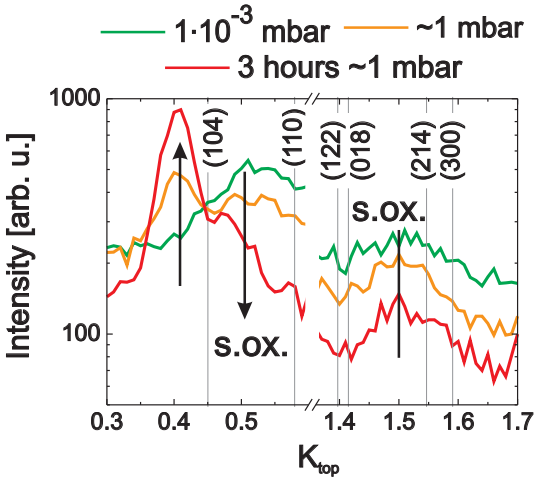

Fig. 5.9: The detailed view shows that the surface oxide peak at $K_{top} = 0.5$ vanishes at high oxygen pressures. This is why the remaining peak at $K_{top} = 1.5$ does not stem from the surface oxide at high pressure, but from a structure with a coincident lattice spacing (d = 1.55 Å), possibly RhO_2(002). The peak at $K_{top} = 0.4$ (d = 2.79 Å) can neither be assigned Rh_2O_3 nor RhO_2.

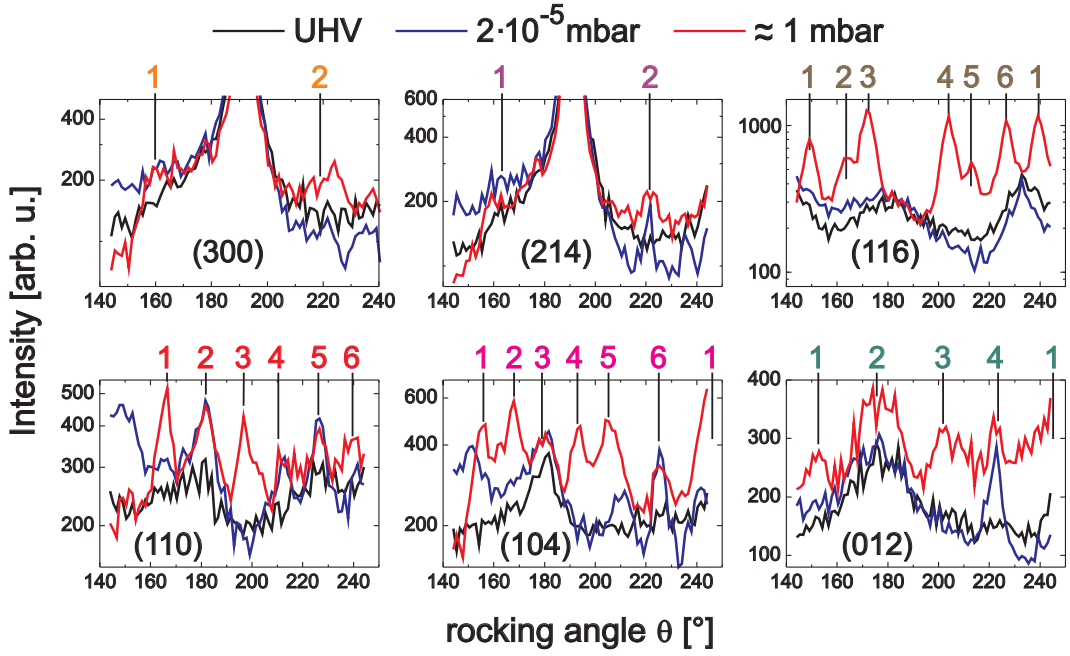

Fig. 5.10: In-plane rocking scans at q-positions that correspond to strong reflections of Rh_2O_3. The scans were recorded under UHV conditions, at an oxygen pressure of $2{\cdot}10^{-5}$ mbar where the surface oxide is stable and at 1 mbar, after formation of the bulk oxide phase.

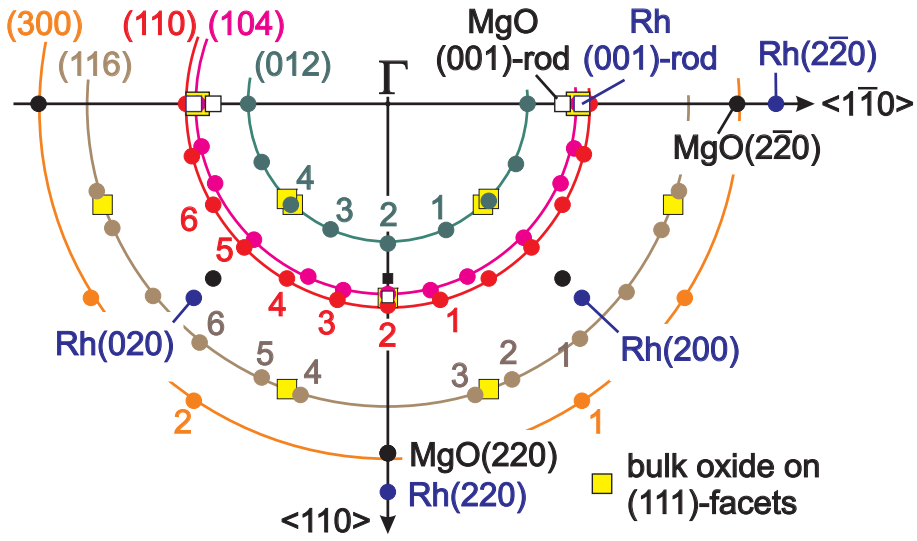

Fig. 5.11: The measured reflections are plotted in the surface coordinate system of the top facet. Open circles denote either weak intensity or when the reflections may overlap with a Rh or substrate Bragg reflection or truncation rod. The reflections that can be related with epitaxial (0001) oriented bulk oxide on the (111) facets are marked with yellow squares.

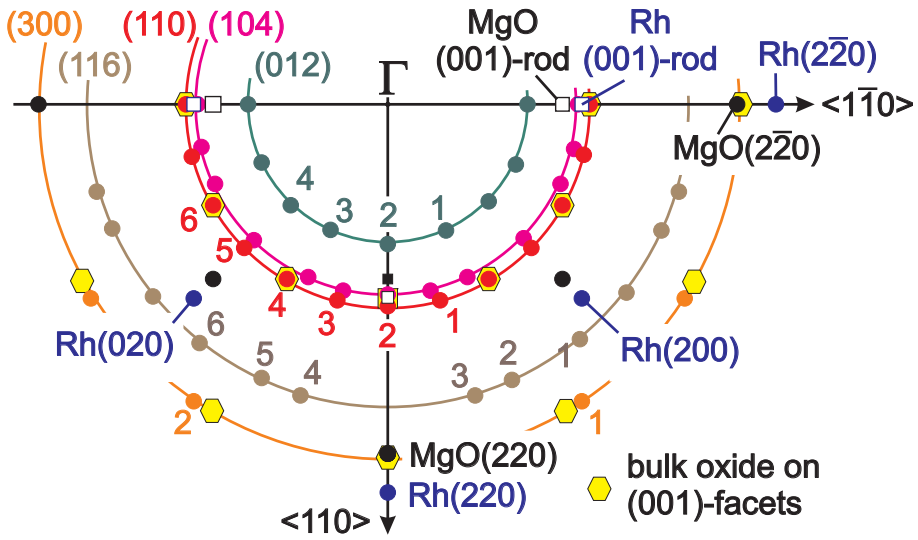

Fig. 5.12: The reflections that can be related with epitaxial (0001) oriented bulk oxide on the top (001) facet are marked with yellow hexagons.

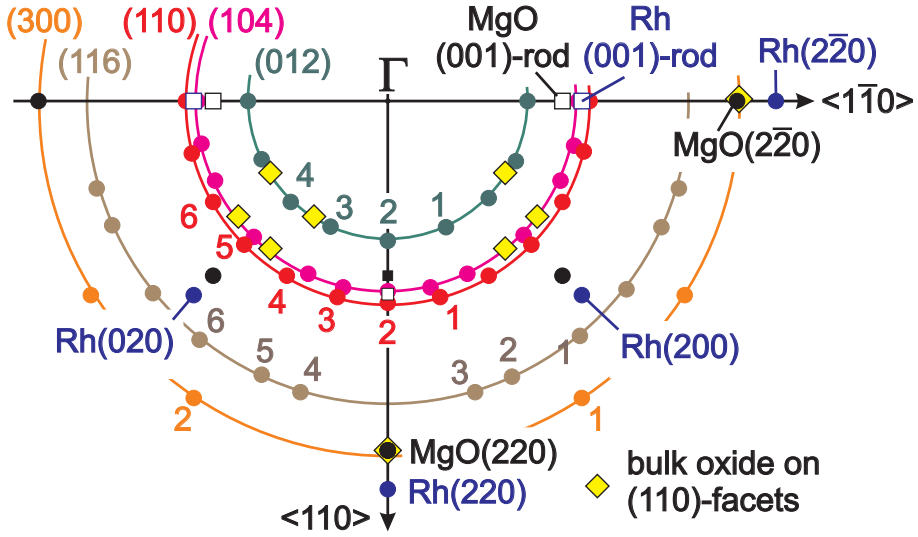

Fig. 5.13: The yellow diamonds show the positions to be expected for bulk oxide growth on (110) facets. The positions do not match with the experimental observation.

another phase stable under these pressure conditions. However, the lattice spacing 2.79 Å can neither be assigned to Rh_2O_3 nor to RhO_2 with a rutile structure [42], nor to the spinel compound Rh_2MgO_4. The lattice spacing 1.55 Å, however, can be assigned to the RhO_2(002) reflection.

The rocking scans (fig. 5.10) show a distinct distribution of the oxide Rh_2O_3 reflections, which indicates an epitaxial growth of the oxide islands. However, the high amount of different reflections indicates that several orientations of the oxide exist. It is interesting to analyze, if the reflections can be explained with an orientation of the Rh_2O_3 on the facets on the nanoparticles in the same orientation as the single crystal surfaces. Rh_2O_3 grows with (0001)-orientation on on Rh(111), Rh(110) and Rh(100). The azimuthal orientation is given in such a way that the [100] and [010] direction of Rh_2O_3 point into the same direction as the hexagonally arranged Rh atoms within the surface oxide [97]. For the Rh (001)-top facet, it follows that the Rh_2O_3(110) and Rh_2O_3(300) are oriented parallel to H_{top} and in azimuthal domains every 30° (yellow hexagons in fig. 5.12). If the same orientations of the bulk oxide exists also on the (100)-side facets, only the Rh_2O_3(006) reflection would be observable with an in-plane scan, which was beyond the observable q-range in the experiment. The Rh_2O_3 reflections on the (111) and (110) facets, of which the coordinates with respect to the sample surface occur at a value $q_z \approx 0$ are listed in table 5.1. For the oxide on the (001) and (111) facets, there is a good agreement between calculated and experimental positions. The deviations can be explained, as in the position of the plots, the maximum values of the rocking scans were used, however the peaks have a rocking width of several degrees. No agreement was found for the (110) facets. Anyway, there exists a number of bulk oxide reflections which cannot be explained by the (0001) oriented particles on the facets with the single-crystal like epitaxy. Note that RhO_2(101) has a similar lattice spacing (d = 2.544 Å) as Rh_2O_3(110) (d = 2.567 Å), and some of the reflections in the rocking scans can also stem from RhO_2.

To sum up, besides the Rh_2O_3 growth on the (111) and (001) facets of the Rh nanoparticles, the Rh_2O_3 epitaxy may also be driven by the MgO support. In addition, reflections occur, of which one lattice spacing (1.55 Å) can be explained by RhO_2, the reflections with a lattice spacing of 4.65 Å and 2.79 Å can neither be explained by RhO_2 nor by the $RhMg_2O_4$ spinel compound.

5.6 Summary

It could be shown that on Rh/MgO(001) particles with average diameters of 8 nm and 9 nm, the surface oxide that was reported for the Rh(111) and Rh(100) single crystal surfaces can be grown by exposing the particles to molecular oxygen in the pressure range of 10^{-5} mbar. The growth of these structures was found under in situ conditions with x-ray diffraction and ex situ with high resolution

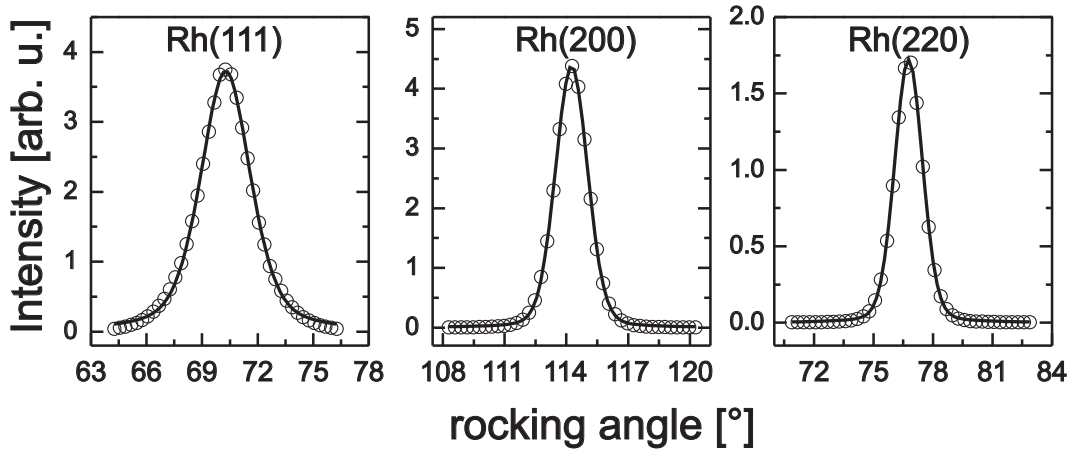

Fig. 5.14: Angular distribution $A(\omega)$ of the particles. The rocking profiles of the Bragg reflections were fitted with Pseudo-Voigt Functions. Rh(111): $\Delta\omega = 3.2°,\ \mu = 0.53$, Rh(200): $\Delta\omega = 1.8°,\ \mu = 0.22$, Rh(220): $\Delta\omega = 1.7°,\ \mu = 0.23$.

transmission electron microscopy. A precursor of this surface oxide is a p(3×1) structure on top of the (001) facet of the particles. Its decay kinetics depends on the sample temperature. The growth of the surface oxide is accompanied by a slight shape change of the fcc-core of the particle. The increase of the (100) side facet area was deduced from the quantitative analysis of the reciprocal space maps of the 8 nm particles. On these particles, the formation of (110) facets as anticipated from theory was not observed. On the 9 nm particles, the increase of the (100) facets on the side of the particles could be directly evidenced with the appearance of a rod signal in (100) equivalent directions. In addition, the occurrence of (110) facets could be demonstrated. It has been known that the surface oxides on the single crystal surfaces are thermodynamically instable and form kinetic barriers for the bulk oxide formation. No bulk oxide formation was observed at 10^{-3} mbar of oxygen at 670 K. This is in contrast to the results obtained for 4 nm particles on Rh/α-Al_2O_3 that will be presented in section 8.3. Even though the same temperature was applied, bulk oxide formation already occurred below this pressure.

Appendix A: Details on the Shape Analysis

A.1 Determination of $\{N_P, N_E, N_T, N_B\}$

Diffraction maps were simulated in a wide range of the average particle parameters $\{N_P, N_E, N_T, N_B\}$. It turned out that the sensitivity of the fits on the parameter N_P was not very decisive. However, for a precise determination of the shape parameters, further arguments than merely a good fit of the reciprocal space maps need to be considered. Firstly, the result must be compatible with

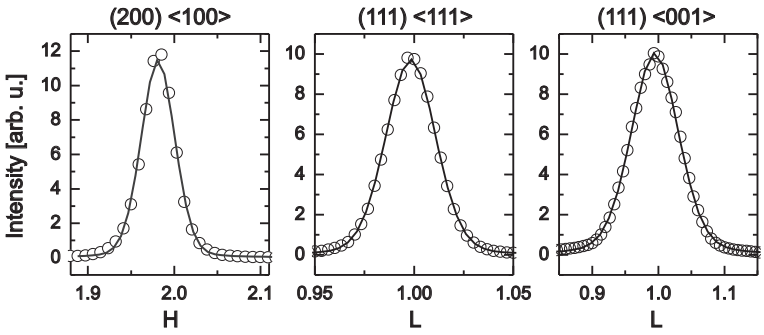

Fig. 5.15: The Rh Bragg reflections (O_2 atmosphere) scanned in different directions and fitted with Pseudo-Voigt functions. FWHMS (rec. lat. units of Rh-fcc): $\Delta q_{\langle 100\rangle}$=0.4612, $\Delta q_{\langle 111\rangle}$=0.5166 and $\Delta q_{\langle 001\rangle}$=0.8498.

N_P	N_E	N_T	N_B	χ^2	$\Delta q_{\langle 100\rangle}$ 0.0461	$\Delta q_{\langle 111\rangle}$ 0.517	$\Delta q_{\langle 001\rangle}$ 0.0850	# fcc	# s.ox.
30	8	16	5	9832	0.0478	0.0540	0.0841	12531	$\approx$ 1570
31	**7**	**16**	**5**	**10237**	**0.0455**	**0.0516**	**0.0843**	13859	$\approx$ 1710
32	7	17	5	11161	0.0442	0.0500	0.0813	15243	$\approx$ 1830
33	7	17	5	10748	0.0425	0.0482	0.0803	16448	$\approx$ 1930

Table 5.2: Best fits of the oxidized particles for varying N_P and experimentally and calculated FWHMS of the Bragg reflections. The right two columns show how many atoms the particle with the average shape contains and how many atoms are necessary to form a surface oxide shell.

the shape analysis via the FWHMs of the Bragg reflections (as far as can be assumed that there are no particles with a completely different shape, which would not contribute to the recorded reciprocal space map). Secondly, if the set of parameters $\{N_P, N_E, N_T, N_B\}$ changes from UHV to oxidizing conditions, also the number of atoms changes within the fcc-core of the particles. This difference of atoms should be as high as the number of atoms that is necessary to cover the fcc core of the particle with a surface oxide shell, assuming there is no interparticle mass transport.

For the different values of the parameter N_P, the χ^2-value was plotted against each of the values N_E, N_T and N_B, as shown in fig. 5.16 for $N_P = 31$. The global minimum of χ^2 for a fixed N_P can be achieved from the plot. This procedure was performed for several values of N_P.

First, the parameter determination for the oxidized particles is discussed. Table (5.2) shows the parameters of the best fits obtained for $N_P = 30$–33, and the values of χ^2 do not suggest a systematic tendency with N_P. For this reason, the FWHMs of the Bragg reflection into $\langle 100\rangle$, $\langle 111\rangle$ and $\langle 001\rangle$ directions was calculated, which are the entries in the following columns in the table. The experimental scans through the Bragg reflection are displayed in fig. 5.15. The FWHM was obtained by fits of Pseudo-Voigt functions. A comparison between

N_P	N_E	N_T	N_B	χ^2	$\Delta q_{\langle 100\rangle}$ 0.04552	$\Delta q_{\langle 111\rangle}$ 0.0499	$\Delta q_{\langle 001\rangle}$ 0.0823	# fcc
30	3	20	5	16805	0.0466	0.0516	0.0769	13905
31	**2**	**20**	**5**	**17428**	**0.0451**	**0.0501**	**0.0763**	15093
32	2	20	5	18185	0.0436	0.0494	0.0755	16369
33	2	20	5	19149	0.0420	0.0470	0.0746	17661

Table 5.3: Particles under UHV-conditions: best fits for varying N_P, calculated FWHMS of the Bragg reflections and experimental values under reducing conditions. The right column is the number of atoms within a particle which is described by the four parameters.

the calculated and the experimental value shows the best agreement for $N_P = 31$. Note, that the scans in $\langle 100\rangle$ and in $\langle 111\rangle$ were performed in radial directions and their widths do not depend on the mosaicity of the particles. Due to geometric constraints in the diffraction experiment with a fixed incident angle, the $\langle 001\rangle$ direction cannot be measured radially, e. g. through the (002) reflection. It was determined experimentally by the scan in $\langle 001\rangle$ direction through the (111) reflection. Even though the experimental value (0.0850) is in excellent agreement with the calculated value (0.0843), one must keep in mind that the intrinsic experimental peak width should be smaller. An uncertainty of only one atomic layer in the particle height would already lead to a distinct sharper line width (0.0819 for one additional layer on top of the particle). A particle that is described by $\{N_P = 31, N_E = 7, N_T = 16, N_E = 5\}$ consists of 13859 atoms. If its covered completely by a surface oxide shell, another 1710 Rh atoms would be necessary, so that before oxidation, the average particle should have consisted of approximately 15600 atoms.

The χ^2-maps of the particles under UHV conditions for varying N_P lead to the values listed in table (5.3). As the χ^2 values decrease monotonically with decreasing N_P, the fit of the reciprocal space map on its own would suggest that the value of N_P should be even smaller than 30. Now, similar arguments as for the oxidized particles can be applied. The first is the analysis of the Bragg FWHMs. A set of line scans was only available after CO reduction of the particles, which, however can be expected to be reliable as the shape sensitive scans in fig. 5.3 (a) showed the reversibility of the particle shape. As discussed for the oxidized particles, attention should be paid to the scans in $\langle 100\rangle$ and $\langle 111\rangle$ direction, as these could be scanned radially. The best agreement is obtained for a value of $N_P = 31$. The next argument to be applied is the number of Rhodium atoms. A particle described by $\{N_P = 31, N_E = 2, N_T = 20, N_E = 5\}$ consists of 15093 atoms. As was estimated from the oxidized particle, the particle under UHV condition should contain around 15600 atoms. This means, there is a lack of around 500 Rh atoms to cover the particle with a closed oxide skin. However, if the parameter N_P was 32, the particle would consist of 16369 atoms, so there

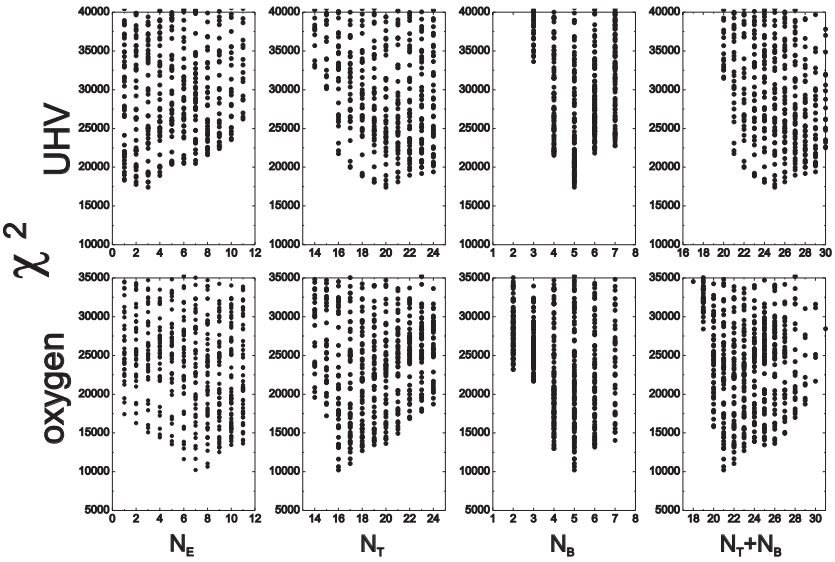

Fig. 5.16: The value of χ^2 for $N_P = 31$.

would be a surplus of almost 800 atoms. An even larger value for N_P should be excluded, as the descrepancy of the Bragg line scan FWHMS and the surplus would be even larger. Note, that only integer numbers were considered to describe the average shape of the particles. Of course, each single particle within the size distribution needs to be described by integer values, however the average value within a size distribution can take non-integer values, which is an explanation for a slight lack or a slight surplus of atoms.

A.2 Sensitivity on Parameters

Fig. 5.16 shows the topology of χ^2, which was obtained from the fits of the high resolution reciprocal space maps. In fig. 5.17 it is displayed the intensity profile, if the particle parameters are varied by ± 2. The fits for the clean particles vary only slightly, when N_E and N_T are changed, whereas there are strong variations with respect to the parameter N_B. One may argue, that the sensitivity of the parameters N_E, N_T of the particles under UHV conditions is poor. There are however, two arguments, that the determination is reliable. As table (5.3) shows for the different values of the parameter N_P, the value N_T is constant at 20 and N_E varies only from 2 to 3. If the values were not reliable, a higher variance of the values should be expected. Secondly, if the parameter N_E for the side facet is that small, a very small variation of its value cannot have a big influence on the diffraction map, as the corresponding size changes of the (111) facets are only marginal (e.g. if N_E increases from two to three, only 36 atoms are removed from the particle). For the oxidized particles, the shape variations are more obvious for all the three parameters, if their values are changed, so their uncertainty can be estimated to be $\pm$ 1.

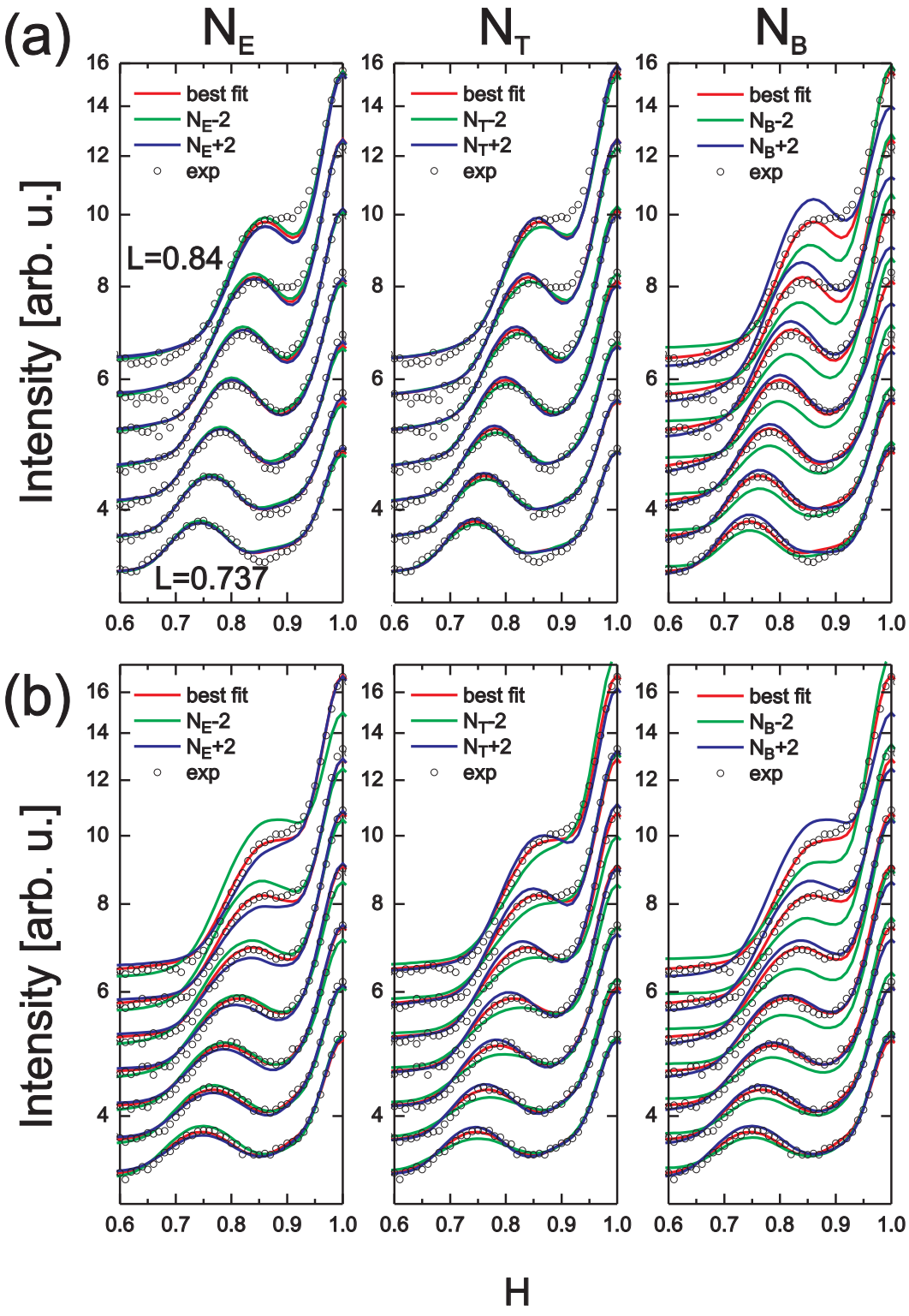

Fig. 5.17: It is plotted, when the parameters $\{N_E, N_T, N_B\}$ of the best fit are varied by ± 2.

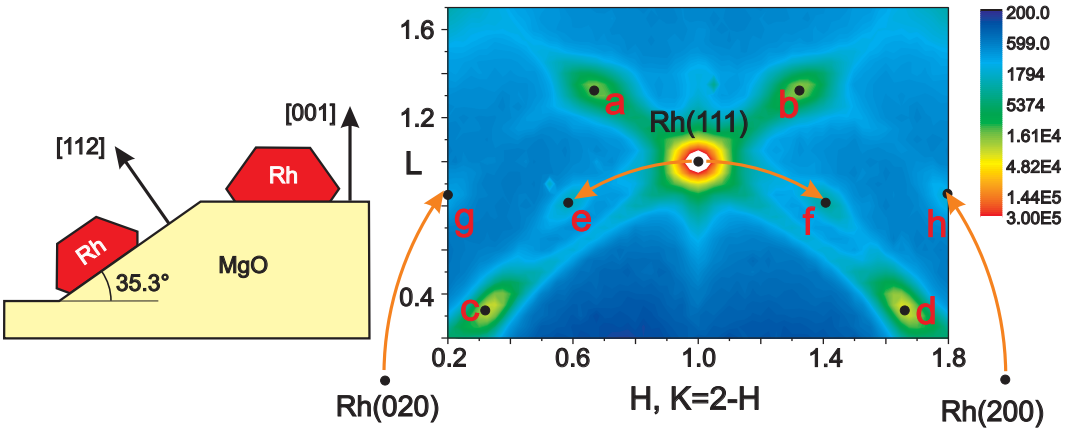

Fig. 5.18: Extended mesh scan of the (H+K=2)-plane for the 9 nm particles. The points labeled a, b, c, d are caused from internal twinning. The peaks labeled e, f, g, h stem from Rh particles sitting on (112) faceted MgO.

Appendix B: Internal Twinning and Misoriented Particles

Fig. 5.18 shows an extended reciprocal space map from the 9 nm particles which shows additional features in comparison with the map for 8 nm particles (fig. 5.1). Firstly, a remarkable intensity distribution occurs at the dots marked with a,b,c,d. The positions are at $\frac{1}{3}(244)$, $\frac{1}{3}(424)$ $\frac{1}{3}(151)$ $\frac{1}{3}(511)$. These positions are caused from internal twinning of the particle, i.e. if the stacking sequence ABCABC... along a (111)-equivalent direction gets inverted (see also App. B). There exist additional weak reflections (marked with e-h). These points cannot be explained by internal twinning. However, one can calculate that these points are at positions that correspond to the position of the Rh(111), Rh(200) and Rh(020) peak, but rotated by an angle of $\pm 35°$ around the $\langle 110 \rangle$-direction. As during manufacturing of this sample, a higher energy for the argon ion sputtering was applied, it is reasonable to assume that a faceting of the MgO signal may have occurred. The tilt angle of 35° of the Bragg reflections fits well to the formation of (112) facets on MgO, of which the surface is tilted by 35.3° in comparison with the (001) surface. From the intensity ratio of the Rh(111) reflection with the intensity of these misoriented particles, it can be estimated that not more than 1-2% of the particles are affected.

Appendix C: GISAXS Line Scans

Fig. 5.19 shows the GISAXS patterns that were recorded parallel to the wide angle diffraction reciprocal space maps under UHV conditions and with oxygen exposure at 600 K. The patterns were recorded for two different azimuths. The

changes of the line scans upon oxidation are are very small, indicating that oxygen exposure does not result in strong size and shape changes.

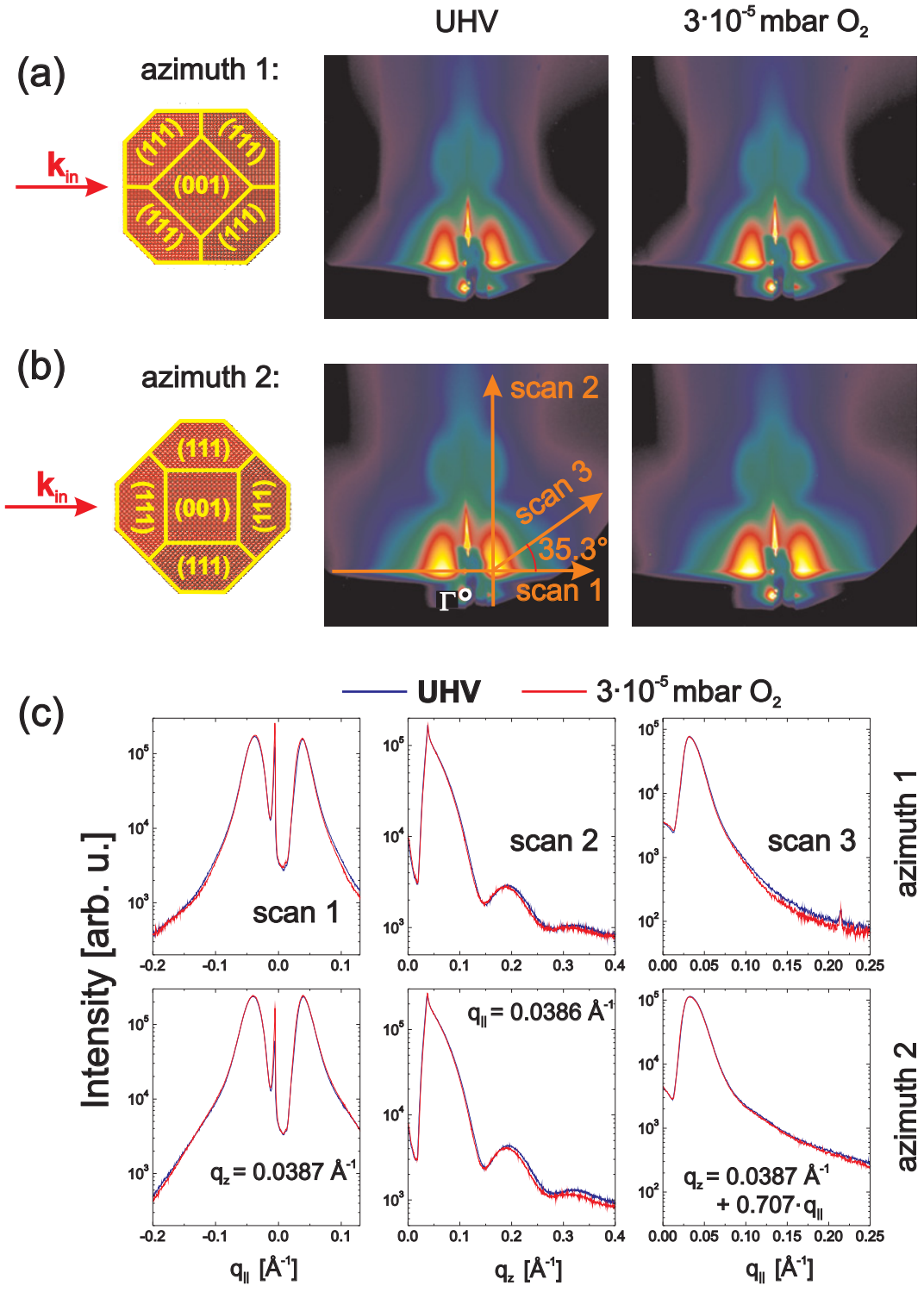

Fig. 5.19: (a, b) GISAXS patterns for the particles under UHV conditions and oxidation at $3{\cdot}10^{-5}$ mbar for two different azimuthal orientations. (c) The line scans were taken from the CCD images along the directions as marked in (b).

Chapter 6

Oxygen-induced Shape Changes of Pd/MgO(100) Nanoparticles

The shape of 6 nm Pd nanoparticles under oxidation conditions was previously studied by the analysis of the FWHM anisotropy of the Bragg reflections (cf. [18] and sec. 3.3.4). Above an oxygen pressure of 0.1 mbar at a temperature of 500 K, the bulk oxide PdO started to form, which was accompanied by a shrinking of the fcc core of the metal nanoparticle. At oxygen pressures below 10^{-3} mbar, the mean shape of the fcc core only changed slightly by a height decrease from 23 to 21 atomic layers, but with the other particle parameters constant. Remarkable shape changes occurred at more elevated pressures when the bulk oxide started to form.

A recent DFT study on the oxidation of Pd crystals suggests that on the other hand, due to the formation of surface oxides on the particles, shape changes should also occur at much lower pressures. In this chapter, it will be described the shape changes of 8 nm Pd/MgO(100) particles under the influence of oxygen pressures in the range of 10^{-5} mbar. As was shown for Rh/MgO(100) particles in the previous chapter, slight shape changes can be monitored with the analysis of reciprocal space maps. This kind of analysis will be applied and extended for the Pd/MgO particles under UHV and oxidizing conditions.

6.1 Growth of the Pd Particles

The experiment was performed at beamline BM 32 of the European Synchrotron Radiation Facility with the same sample growth chamber and the same beam energy as for the Rh/MgO particles as described in the previous chapter. The preparation of the MgO substrate crystal was performed in a uniform way, and the growth of Pd was also conducted with an Omicron EFM3 electron beam evaporator at a substrate temperature of 670 K. The deposition of Pd was followed with SXRD by extended radial scans through the MgO(200) peak which monitors

the occurring signal of the Pd(200) peak (fig. 6.1 a).

Fig. 6.1 (b) shows a wide rocking scan through the Pd(220) reflection which confirms the cube-on-cube epitaxy of (001) oriented Pd particles on MgO(100). The extended diffraction map (fig. 6.1 c) was taken after the metal deposition, annealing at T $\approx$ 900 K and subsequent cooling down to 600 K. As was explained in the previous chapters, such a map contains information about the shape of the particles. It is centered at the Pd(111) reflection and maps the (H+K=2)-plane at different L-values. The Pd(111)-peak is interconnected to the surrounding Bragg peaks by broad diffraction rods along the $\langle 001 \rangle$, $\langle \bar{1}11 \rangle$, $\langle 1\bar{1}1 \rangle$ directions. These diffraction rods give direct evidence for the truncated pyramidal shape of the Pd nanoparticles. Apart from the signal of the rods associated with the particle facets, the map contains the same additional features, with a high similarity to fig. 5.18 as obtained for the Rh/MgO(100) particles. The peaks at $\frac{1}{3}(511)$ and $\frac{1}{3}(424)$ can be assigned to internal twinning (Appendix B.3). The peaks marked with red squares in fig. 6.1 (c) can be explained by a slight fraction of (112)-faceted MgO mediating the tilt angle of the surface by an angle of 35.4° on the particles.

Fig. 6.2 (a) shows a high resolution TEM micrograph of Pd/MgO particles[1]. It shows very smooth (111)-equivalent facet and a top (001) facet. The bottom side is less smooth. The substrate is rough, and the roughness is mediated on the bottom side of the Pd particle. Fig. 6.2 (b) is an example of a particle with internal twinning. The plane along which the stacking inversion occurs is marked with arrows. Even though the particle is twinned, its main part on the right side of the arrows shows a well-defined shape.

In order to check for the sensitivity of the particles towards oxygen, a reference line scan was performed under UHV conditions, at an atmosphere of $5 \cdot 10^{-6}$ mbar of oxygen and after subsequent reduction with 10^{-5} mbar of CO. After the susceptibility towards the applied gas atmosphere was confirmed with the reference scans, the sample was again annealed to 900 K, and finally cooled down to 570 K.

6.2 Shape Changes of the Particles during Oxidation

After this reference cycle of oxidation, reduction and annealing, a high resolution mesh scan was recorded under UHV conditions. It ranges from (H, K) = (0.5, 1.5)-(1.5, 0.5) and L from 0.6 to 0.84 with a total amount of 1414 data points. It shows the clear surface rod signal the (111)-equivalent facets and the (001)

[1]The TEM specimen was prepared from the same sample after the x-ray experiments. The high-resolution TEM was performed on a JEOL 1250 atomic-resolution microscope operated at 1250 keV.

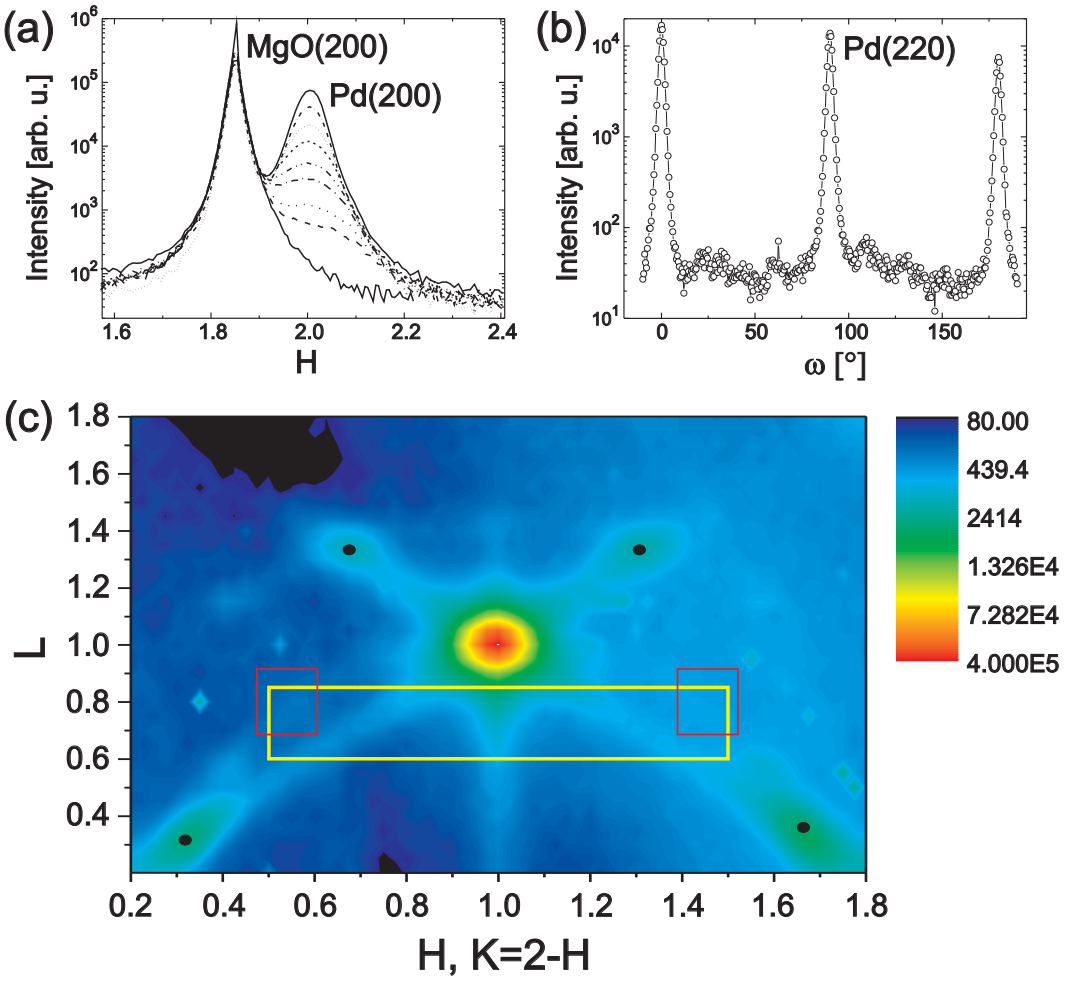

Fig. 6.1: (a) Monitoring of the Pd(200) reflection during particle growth. (b) The broad rocking scan through Pd(220) shows the cube-on-cube epitaxy of Pd with MgO. (c) The extended reciprocal space map contains a clear signal of internal twinning, marked with black circles. The red squares indicate misoriented Pd particles due to a small fraction of (112) facets of the MgO support. The yellow rectangle marks the region at which high resolution maps were recorded for the quantitative shape analysis.

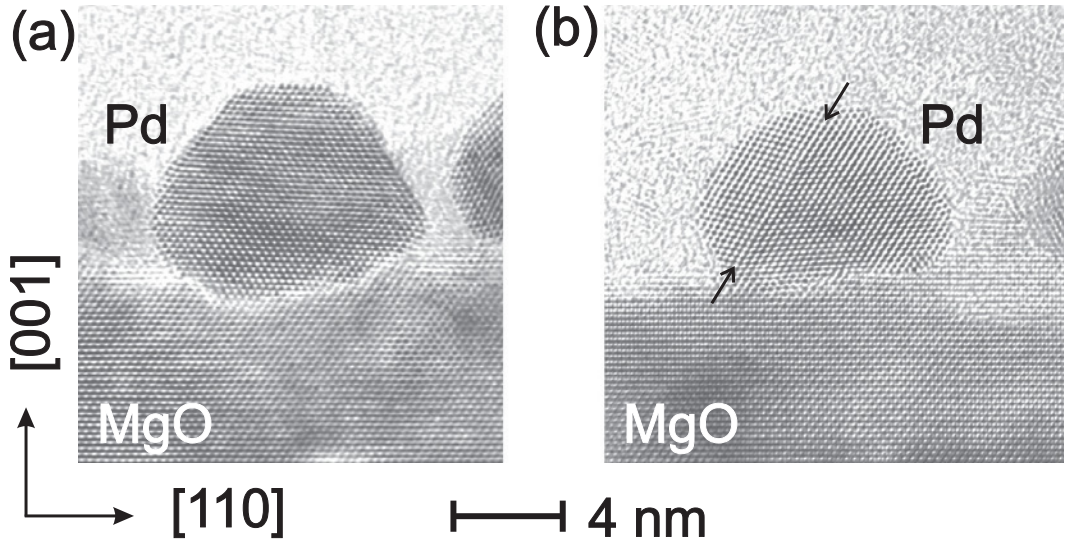

Fig. 6.2: High resolution TEM image of Pd particles without (a) and with (b) internal twinning. The plane where stacking inversion occurs is marked with arrows. (Courtesy of Dr. N. Y. Jin-Phillipp, MPI MF.)

facets. The small amount of intensity at the left and right edge of the reciprocal space maps (marked with red rectangles in fig. 6.3 (a)) for L > 0.7 is related to the misoriented Pd particles due to the suspected (112) faceting of the MgO(100) support and is not related to the particle shape.

When the sample was exposed to an oxygen atmosphere of 10^{-5} mbar, a change of the intensity distribution appeared. Fig. 6.3 (b) shows the relative change of intensity $\Delta I/I_0$ in comparison with the reciprocal space map prior to oxidation. The intensities of the (111)- and the (001)- rods decrease by a value of around 20% (this equals to an intensity increase of 30% above the background level). Interestingly, an intensity increase of around 20% can be observed simultaneously between these rods. As it was reported in a DFT study on the particle shape of Pd particles [25] and will be discussed in the last part of this chapter, apart from the low-index (111) and (100) surfaces, also higher indexed facets such as (110), (331), (112) and (113) facets may be present on the particle depending on the oxygen chemical potential. As it is indicated with the red lines in the figure, the direction of intensity increase matches well with ⟨112⟩-equivalent directions. The recorded high resolution reciprocal space map should also be sensitive to the formation of (113) facets. The according rod directions are marked with blue lines in fig. 6.3 (b). These directions, however, describe the directions of intensity increase less well than (112) facets. Evaluating this observation qualitatively, it can be concluded that (112) facets form under the influence of the oxygen atmosphere, or even that (112) facets might exist prior to oxidation and their size increases in the oxidizing atmosphere. Thereby, the

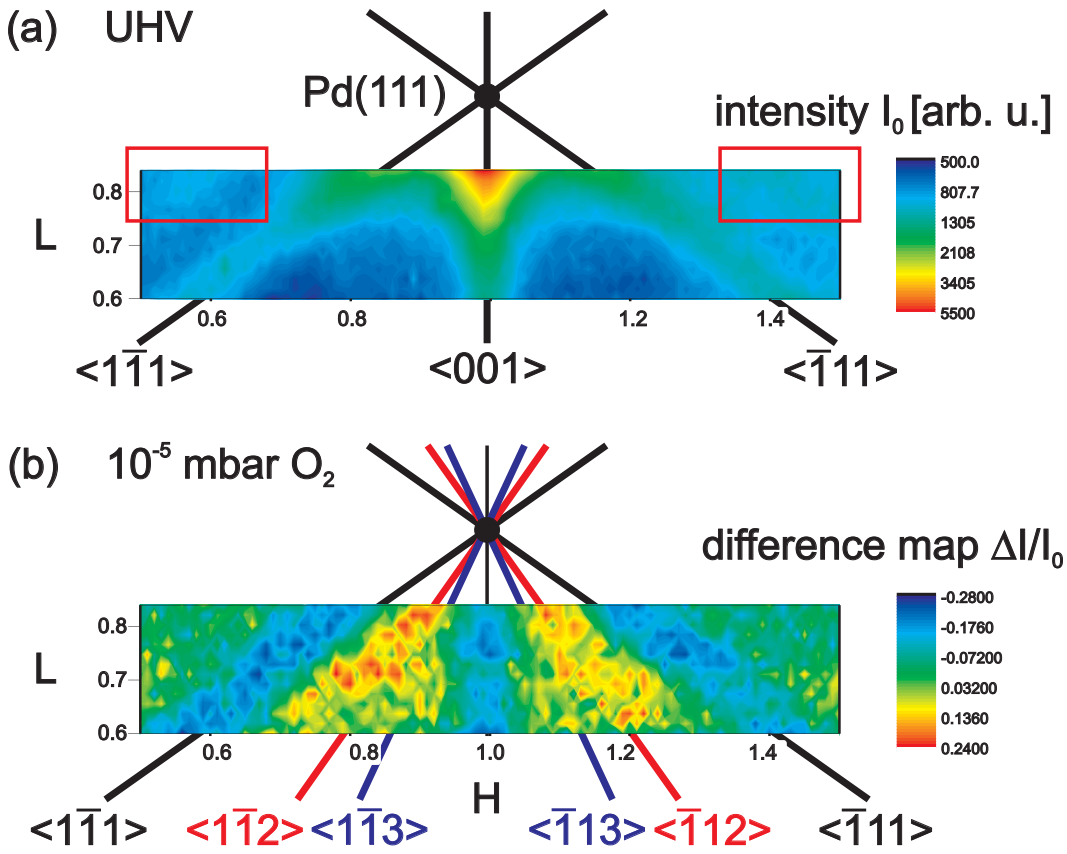

Fig. 6.3: High resolution reciprocal space maps of UHV (a) and oxygen-exposed particles (b). Upon oxidation, the intensity of the (111) and (001) signal decreases, whereas there is a signal increase between these directions. The ⟨112⟩-equivalent directions are marked with red lines. They match the region of intensity increase better than the blue lines that correspond to ⟨113⟩ directions.

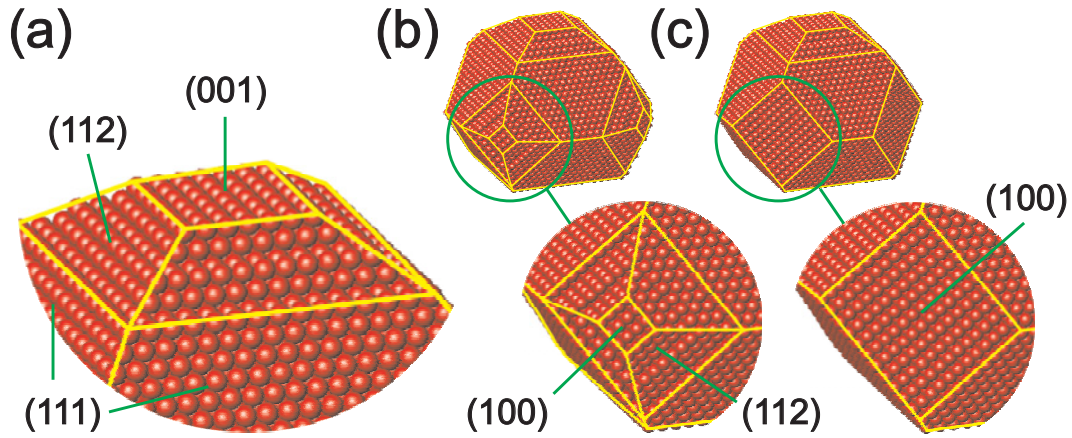

Fig. 6.4: In general, (112) facets are located at subtending (111) and (100) facets on top of the particles (a) and on the side of the particles (b). For the quantitative description, only the (112) facet on top of the particles will be considered and the particle is modeled as displayed in (c).

area of the (111) and (001) facets must decrease accordingly.

6.3 Quantitative Analysis of the Particle Shape

6.3.1 Modeling of the Additional Facets

Detailed information of the shape change can be extracted from the reciprocal space maps only by quantitative analysis. The shape model that was applied for the Rh nanoparticles in the previous chapter only considered the (111)-equivalent and (100)-equivalent facets, and the average shape of the particles was described by four natural numbers $\{N_P, N_E, N_T, N_B\}$. The observation of an intensity increase along the (112) facets shows that the applied model shape is not sufficient to describe the Pd particles under oxidizing conditions and require an enhanced model. The (112)-equivalent facets can in principle be expected to occur at all edges of the particles, which are defined by subtending (111)- and (100)- facets.

Fig. 6.4 (a) sketches the top area of a particle, with (112) facets between the top (001) facet and the neighboring (111) facets. In principle, the (112) facets should also occur neighboring to the side (100) facets as sketched in fig. 6.4 (b). The rod signal of these facets was not directly recorded in the (H+K=2)-plane, as their rod signal is located in different planes. In the previous chapter for the Rh/MgO particles it was shown that the quantitative analysis of this map is still sensitive to the parameter N_E describing the size of the (100) side facets. This sensitivity, however, does not mean that the side facet contributes a dedicated signal into the (H+K=2)-plane, but rather that the (100)-side facets cause a decrease the size of the (111) facets and therefore only contribute indirectly to

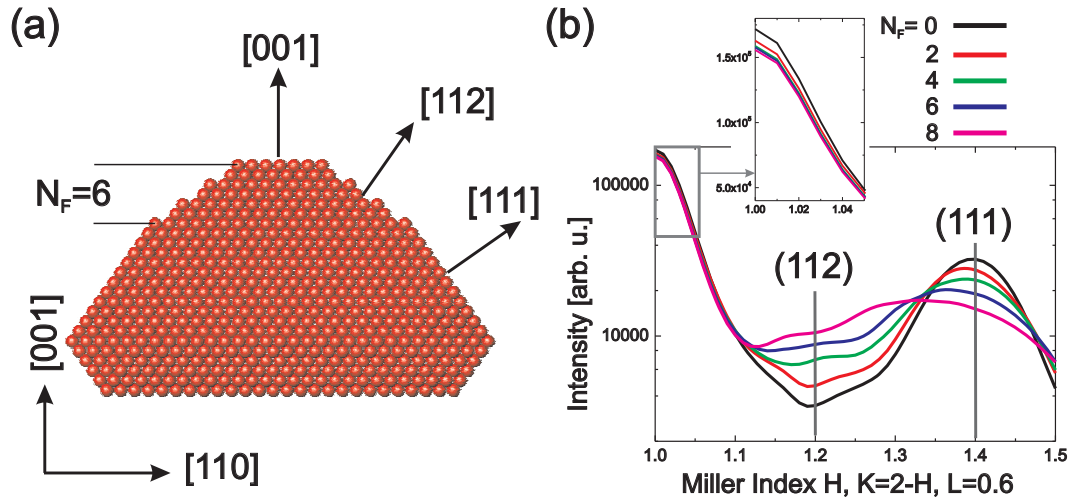

Fig. 6.5: An additional parameter N_F describes the numbers of atomic layers starting from top of the particle which are affected by the (112)-faceting. (a) The drawn particles has the parameters $N_P = 30$, $N_E = 5$, $N_F = 18$, $N_F = 5$, $N_F = 6$. (b) Line scans at L = 0.6 for different values of N_F.

the recorded reciprocal space map. If the sides of the particle are composited of (100) and (112) facets as sketched in fig. 6.4 (b), the (111) facets still have the same size as the particle sketched in fig. 6.4 (c) without the contribution of (112) facets on the side of the particles. For this reason, one cannot expect a high sensitivity of the intensity distribution in the (H+K=2)-plane in order to clarify to which extend the side of the particle is composited of (100) or (112) facets. This is why the shape of the particles is modeled as sketched in fig. 6.4 (c), with the (112) facets only on the top of the particles.

A side view of a particle with the extended shape model is drawn in fig. 6.5 (a). As holds generally for an fcc (112)-surface, its atomic structure is given by the alternation of a (111)-terrace with a (001)-terrace. For the modeling of the additional type of facet one additional parameter N_F is introduced. It describes the number of atomic layers which are affected by this faceting counted from the top of the particle. The effect of this parameter on the intensity distribution can be seen in fig. 6.5 (b). The diagram shows a simulated line scan for a particle with $\{N_P = 30, N_E = 5, N_T = 18, N_B = 6\}$ and several values of N_F. In the calculation, a size dispersion $\sigma = 30\%$ and a Gaussian mosaicity of 4° was considered. It shows a remarkable decrease at the position of the (111) facets, and a strong increase at the position of the (112) rod. For the given parameters, the decrease of the signal on the (001)-facet is only slight. Note, that the signal of the (112) facet is so broad that its scattering signal does not appear as a distinct peak in the intensity distribution. This also explains why in the intensity difference

map (fig. 6.3) the direction of intensity increase is smeared out on a larger area than the rods of the (111) and (001) facets.

6.3.2 Estimation of the Parameter Range

A fifth parameter N_F was introduced to describe the particles under oxidizing conditions. This leads to a high number of parameter combinations which would not have allowed a full factorial simulation for all the five parameters in small steps. On the other hand, as was shown in the previous chapter for the shape analysis of Rh/MgO particles, the sensitivity of the fits of the reciprocal space maps with respect to the particle parameters N_E, N_T, N_B depend only very weakly on the diameter parameter N_P. For this reason, the reciprocal space maps were simulated in fine steps for the parameters N_E, N_T, N_B, N_F while using only two different values for N_P. To estimate a meaningful range for the average particle parameters for the simulations of reciprocal space maps, the Bragg peak anisotropy simulation was applied for the as-grown particles. Fig. 6.6 shows the line scans through several Bragg reflections in high symmetry directions. For a huge range of average particle parameters $\{N_P = 25 - 31; N_E = 0 - 10; N_T = 12 - 30; N_B = 1 - 9\}$ in steps of ± 1 for each parameter, the FWHM along the same directions was calculated and compared with the experimental values. Fig. 6.7 shows the projection of the relative deviation on each parameter. The fit suggests a parameter shape with $N_P = 27$ and N_T+$N_B \approx$ 21-27. The fit further shows that the sensitivity on the values for N_T, N_B and N_E is small. Still, the calculated FWHM along $\langle 111 \rangle$ direction (0.059 r.l.u. of Pd) is 6% broader than the experimental value (0.055). Thus, the parameter value N_P must be correspondingly larger, and the reciprocal space maps were calculated for a value $N_P = 28$. In order to take into account possible effects of particle size increasing due to interparticle mass transport during the annealing cycles, reciprocal space maps were additionally calculated for the same parameter range with $N_P = 30$.

As an auxiliary measurement to evaluate a meaningful particle height, an x-ray reflectivity curve was recorded after the synchrotron x-ray diffraction study under ex situ conditions on the rotating anode. The data are plotted in fig. 6.8, together with the fit for a one-layer box model. The curve was fitted with a layer thickness h = 4.0 nm, a coverage $\theta = 40\%$, a roughness of $\sigma = 1.6$ nm for the layer and a substrate roughness of 0.55 nm. It is reasonable to assume that the actual average particle height is between the 21 and 29 atomic layers, corresponding to a layer thickness between h and h+σ, which is compatible (though the high error bars) with the FWHM results for the as-grown Pd particles.

6.3.3 Fit of the Reciprocal Space Maps

According to the size estimations from the FWHMs and x-ray reflectivity, a database of diffraction maps was calculated in the parameter range $N_E = 0 -$

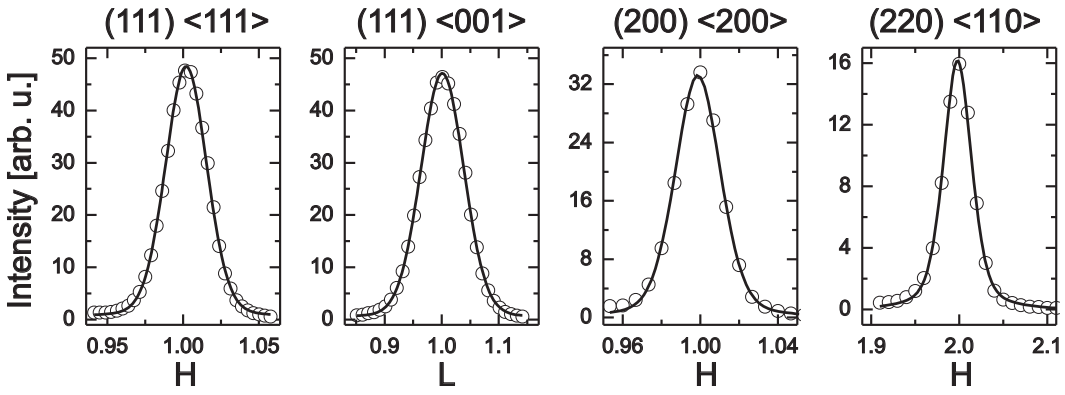

Fig. 6.6: Line scans through the Bragg reflections, fitted with Pseudo-Voigt-Functions. FWHMS (reciprocal lattice units fcc): ⟨111⟩: 0.0558, ⟨001⟩: 0.893, ⟨100⟩: 0.055, ⟨110⟩: 0.054.

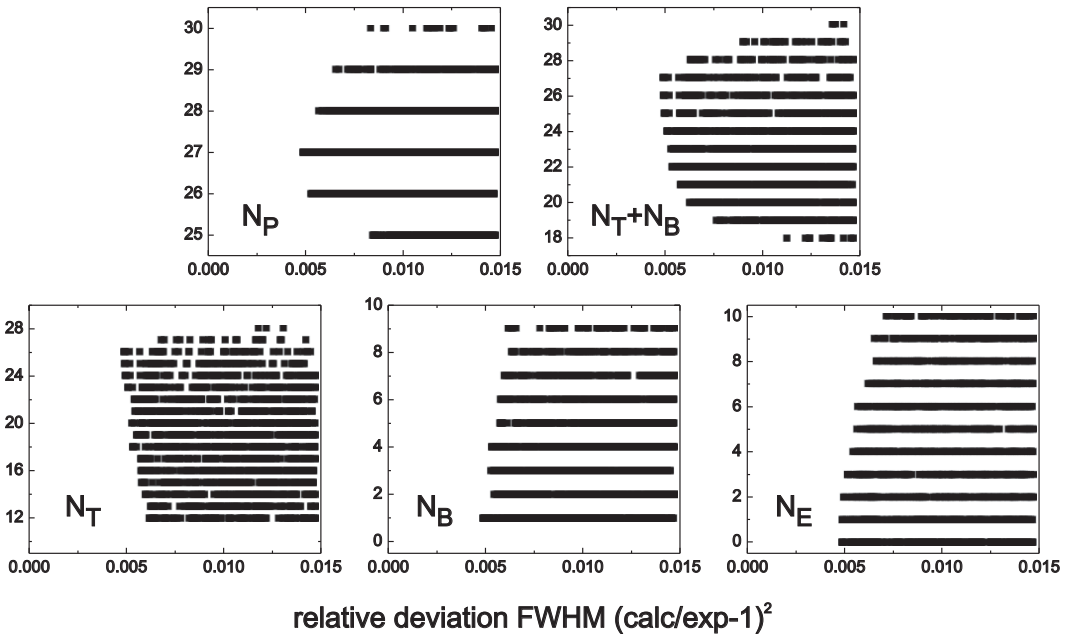

Fig. 6.7: Shape analysis with the Bragg FWHM anisotropy. For each set of average particle parameters $\{N_P, N_T, N_B, N_E\}$, the FWHMS were calculated. As a comparison with the experimental value, the relative deviation between experimental and calculated FWHMs was calculated $\sum_i (FWHM(calc.)_i/FWHM(exp.)_i - 1)^2$. This deviation is projected on each shape parameter.

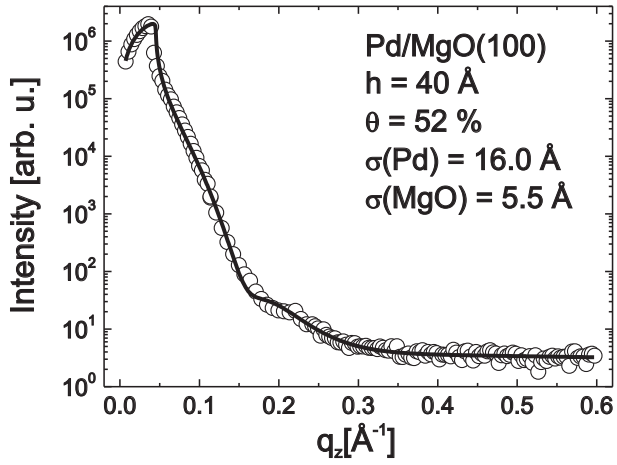

Fig. 6.8: Ex situ reflectivity curve of the sample after the oxidation experiment. The fit was performed with a one-layer box model suggesting a coverage $\Theta = 52\%$ and a particle height of 4 nm. This height corresponds to average parameters $N_T + N_B = 21$, the roughness 1.6 nm corresponds to 8 atomic layers. Thus, the particle height should not exceed 29 atomic layers.

	UHV		O_2	
N_P	28	30	28	30
N_E	11	10	11	10
N_T	19	18	18	17
N_B	12	12	12*	12*
N_F	0	0	4	4

Table 6.1: Fit results for the clean and in 10^{-5} mbar O_2 at 570 K. For the oxidized particles, the parameter N_B diverges and was therefore fixed to the value of the particles under UHV conditions.

$14, N_T = 13 - 29, N_B = 3 - 12, N_F = 0 - 8$ (each with ΔN_i=1) for $N_P \in \{28, 30\}$. A Gaussian size dispersion of 30 % was used and the q_z-dependent mosaicity function composited of two Pseudo-Voigt-Functions, obtained from the rocking profile of the Pd(111) and Pd(220) reflections as plotted in fig. 6.9. These calculated diffraction maps were fitted to the experimental data with a scaling factor plus a background. The region in the q-map that was affected by misoriented particles (marked with quadrangles in fig. 6.3) was ignored for the fit.

Particle Shape under UHV Conditions

The average particle parameters which reproduce at their best the experimental intensity distribution are summed up in the left part of table 6.1 for $N_P = 28$

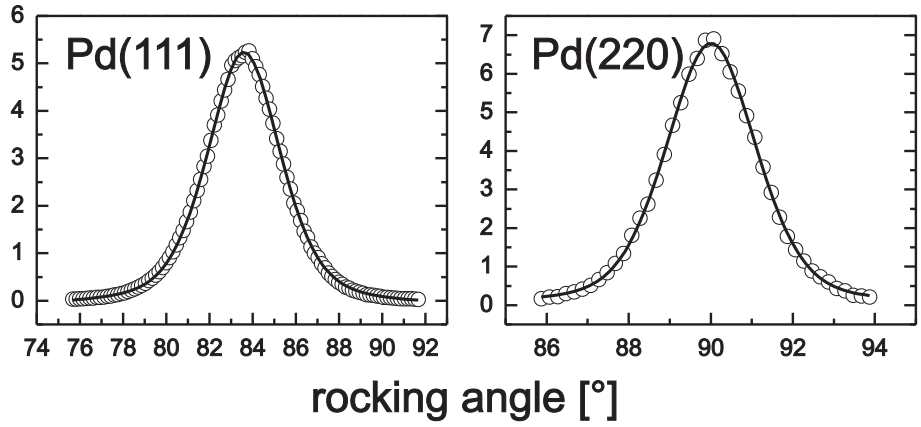

Fig. 6.9: Angular distribution $A(\omega)$ of the particles. The rocking profiles of the Bragg reflections were fitted with Pseudo-Voigt Functions. Pd(111): $w = 4.1°$, $\mu = 0.55$, Pd(220): $w = 2.6°$, $\mu = 0.43$.

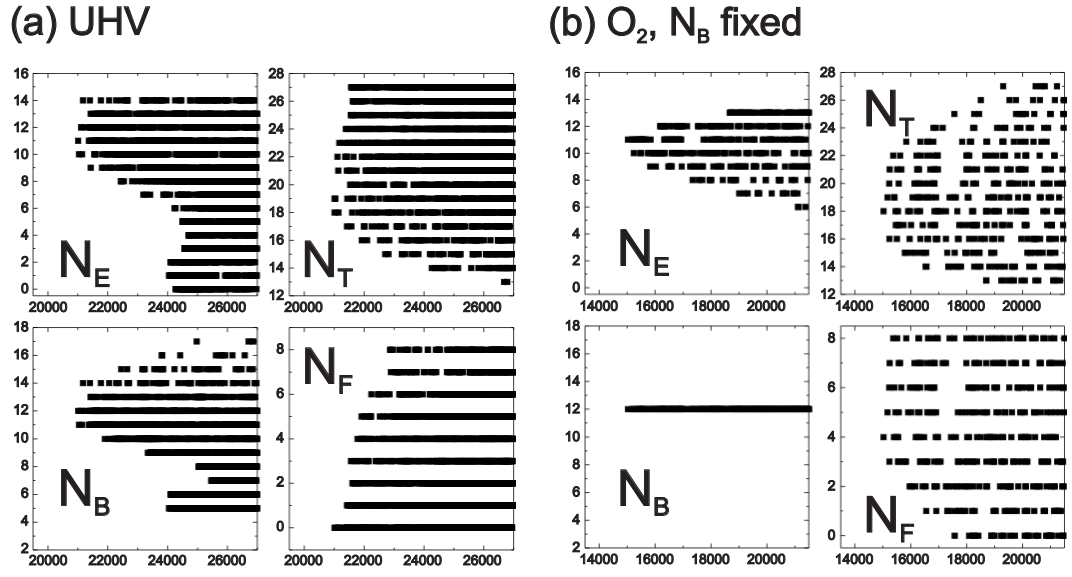

Fig. 6.10: χ^2-Maps of the fits for $N_P = 28$ under UHV conditions and under oxidizing conditions. Under oxygen, N_E and N_B diverge out of the parameter range and leads to unphysical values (a). Subfigure (b) shows the constrained fit if N_B is fixed at the value for UHV conditions.

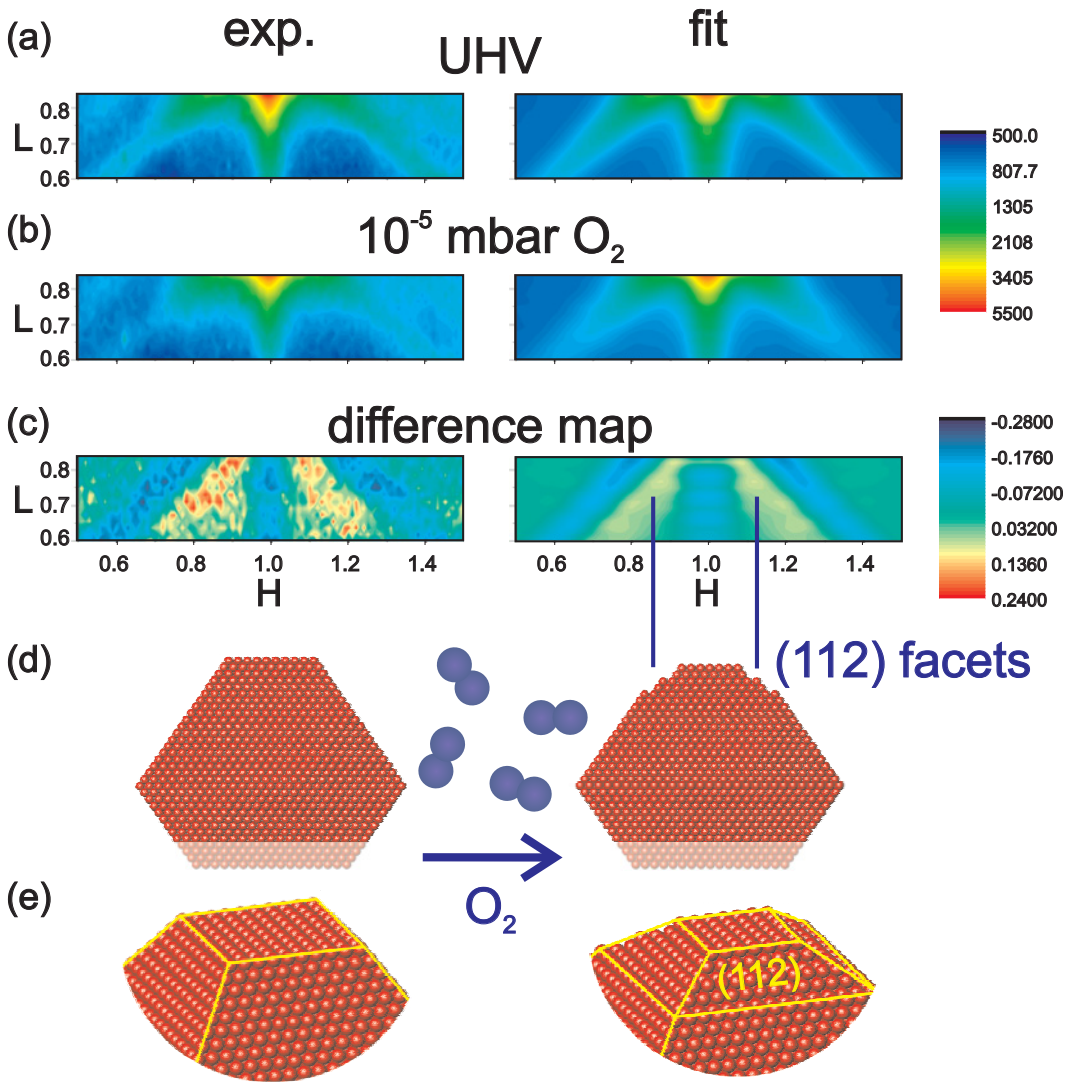

Fig. 6.11: Experimental and fitted intensity distribution under UHV conditions (a) and in 10^{-5} mbar O_2 at 570 K (b). Resulting particle shape under UHV and oxidizing conditions (d). The marked four layers on the bottom side of the particles (d) underline the deviation between the experimental parameter $N_B = 12$ (obtained 12 under UHV conditions and had to be fixed under oxidizing conditions) and the expected value according to the adhesion energy ($N_B = 10 \pm 2$). As is explained in the text, from XRR an even smaller height is expected. The oxygen leads to a (112) facet formation in the topmost ≈ 4 atomic layers (e).

and $N_P = 30$. Fig. 6.10 (a) shows the χ^2-distribution for the fitted average particle parameters. The according average particle shape under UHV conditions is plotted in the bottom left part of fig. 6.11. It is remarkable that the parameter N_F characterizing the (112) facets has a value of zero. This means, that this facet is not at all present and the particle has a well-defined edge between the (111) and (001) equivalent facets. For the following quantitative discussion, the averaged values $\{N_P = 29 \pm 1, N_E = 11.5 \pm 1, N_T = 18.5 \pm 1, N_B = 12 \pm 1, N_F = 0\}$ will be used. The obtained particle shape can be used for a comparison with a previous GISAXS study of Pd/MgO(100) particles [80]. In that study, for particles with an average diameter up to ≈ 12 nm a constant ratio between diameter and height was observed, this is why an equilibrium shape was assumed. For the particles shape obtained from the XRD-mapping, the ratio of the height of the top part of the particle and its diameter $h_{001}/h_{111} = \frac{N_T}{\sqrt{2}N_P} = 0.45 \pm 0.04$ is in good agreement with the value of 0.46 as given in ref. [80] and expected for a ratio of surface energies $\gamma_{111}/\gamma_{001} = \sqrt{3}/2$, as mentioned in sec. (2.1.2). The parameter N_E matches well with the anticipated value $N_P - N_T$ for a non-supported fcc-particle. However, the total height of the particle of 6 nm ($N_T + N_B = 31$) appears too high in comparison with the height obtained for the Bragg reflection analysis for as-grown particles and the x-ray reflectivity after the oxidation experiment as described in section 6.3.2. This value of the average particle height is also too high in comparison with the values obtained in ref. [80]. According to ref. [80] and the geometrical meaning of the particle parameters N_i, the adhesion energy β is given as:

$$\beta = 2\gamma_{100}\left(1 - \frac{N_T + N_B}{\sqrt{2}N_P}\frac{\gamma_{111}}{\gamma_{100}}\right) \tag{6.1}$$

Using the fact that $\gamma_{111}/\gamma_{001} = \sqrt{3}/2$ and the surface energy $\gamma_{100} = 1.64$ J/m^2 and $\beta = 0.91$ J/m^2 as obtained from a TEM study [24], it follows $N_B = 10.6 \pm 2$. Even though the value of $N_B = 12$ is within the error bar, there needs to be an explanation for the poor agreement between the reciprocal space maps and the Bragg/XRR analysis. This can be found in the relatively high substrate roughness of the MgO support, which was found 0.55 nm (cf. fig. 6.8). If the roughness of the substrate is mediated on the particles, as can be seen in the TEM micrograph (fig. 6.2), the bottom (001) facet of the particle is badly defined. This should lead to a decrease of the intensity along the $\langle 001 \rangle$ rod in comparison with a particle with a smooth bottom facet. In the quantitative analysis, no interfacial roughness was included. The fit results suggests a too large parameter for N_B, as an increase of N_B leads to a decrease of the (001) bottom surface area and therefore to a decrease of the rod signal along $\langle 001 \rangle$.

Particle Shape during Oxidation

For the particles in an oxygen atmosphere of 10^{-5} mbar at 570 K, the parameters describing the average particle shape are summed up in the right part of table

6.1 for $N_P = 28$ and $N_P = 30$. For a free parameter of N_B no convergence of the fit could be achieved. This is why N_B was fixed at 12, which is the value for the particles under UHV conditions. The accordingly constrained χ^2-map is displayed in fig. 6.10 (d) and shows a minimum at $\{N_P = 28, N_E = 11, N_T = 18, N_B = 12, N_F = 4\}$. The resulting simulated reciprocal space maps under UHV and oxidation conditions are plotted together with the experimental reciprocal space maps and the particle shape (fig. 6.11).

The results of the quantitative shape analysis of the reciprocal space maps can be compared with the recent DFT study [25] about the shape of mesoscopic Pd particles. In these calculations, a range of the chemical potentials of oxygen μ_0 between -2 and -0.5 eV was considered. The oxygen pressure of 10^{-5} mbar at a temperature of 570 K corresponds to μ_0 = -1.02 eV. At this chemical potential, the values of the surface energies for the different facets are: $\gamma_{111} = 0.067$ eV/Å^2, $\gamma_{100} = 0.070$ eV/Å^2, $\gamma_{110} = 0.074$ eV/Å^2, $\gamma_{112} = 0.081$ eV/Å^2, $\gamma_{113} = 0.081$ eV/Å^2 and $\gamma_{331} = 0.072$ eV/Å^2

The ratios of the surface energies can be used for a comparison with the experimental values of the distances d_i of the facets from the center of the particle[2] via the Wulff theorem: $\frac{\gamma_i}{d_i} = const.$ The top (001) and (112) facets, described by the particle parameters $\{N_P, N_T, N_F\}$ are suited for a comparison with the theoretical values[3], which are $\frac{\gamma_{001}}{\gamma_{111}} = 1.04$ and $\frac{\gamma_{112}}{\gamma_{111}} = 1.21$.

With $N_P = 29 \pm 1$, $N_T = 17.5 \pm 1$ and $N_F = 3.5 \pm 1$, which is averaged over the fit minima for N_P=28 and 30, one obtains the following values for the ratios of the facet distances from the center of the particle: $\frac{d_{001}}{d_{111}} = \frac{\sqrt{3}N_T}{N_P} = 0.99 \pm 0.19$ and $\frac{d_{112}}{d_{111}} = 0.89 \pm 0.06$.

While the ratio $\gamma_{001}/\gamma_{111}$ is compatible with the experimentally obtained value d_{001}/d_{111} (though the error bar is quite high), there is a remarkable discrepancy between the theoretical value for $\gamma_{112}/\gamma_{111}$ and the experimental ratio h_{112}/h_{111}. Or, equivalently, the (112) facets are larger than anticipated from theory. Interestingly, as was observed for the Pd(112) single crystal surface [97], the (112) surface is not stable at μ = -1 eV. This shows that the particles properties are different from the single crystal surface. However, in the x-ray experiment it was not retrieved if ultrathin surface oxides are present on the (001) and (111) facets which are expected to form on Pd nanoparticles above a chemical potential of -1.2 eV [25].

[2]While h_{111} and h_{001} result straightforwardly from the particle parameters, one obtains for the (112) facets: $\left(\frac{h_{112}}{a_0}\right)^2 = \frac{1}{24}\left(N_P^2 + N_T^2 + N_F^2\right) + \frac{1}{36}\left(N_P N_T - N_T N_F - N_P N_F\right)$

[3]The bottom and side facets cannot be used. N_B is be overestimated due to the roughness. As only the projected shape is recorded in the reciprocal space map, an uncertainty exists to which extend the side of the particles is composited of (100) facets or (112) facets.

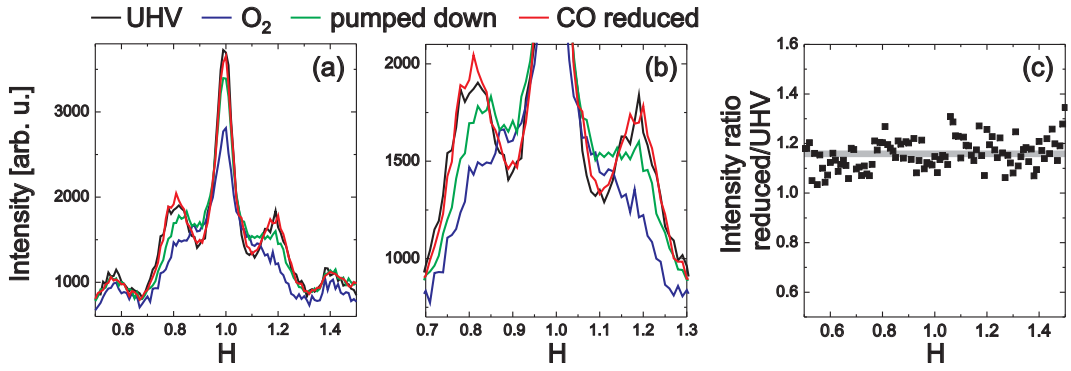

Fig. 6.12: (a) Line scan at (H, K = 2-H, L = 0.8) under UHV conditions (black line) and under oxidizing conditions at 10^{-5} mbar (blue line) which leads to an intensity decrease of the (001) and (111) facets and an increase in between. When the oxygen is pumped down (green line), the intensity distribution starts to revert and the line shape is reproduced after reduction with 10^{-5} mbar CO (red line). A detailed perspective is given in (b). Due to a jump in the beam monitor signal during oxidation process (probably due to a change of the beam position after storage ring injection), the intensity under UHV conditions was corrected by a factor 1.16. As can be concluded from the constant ratio of the intensities under UHV conditions and after reduction (c), the UHV line shape is fully reverted after reduction.

6.4 Reversibility

In the next step of the experiment, the oxygen was pumped down and the sample was annealed at a temperature of 900 K and subsequently cooled down again to the previous temperature of 570 K. Again, a high resolution mesh-scan was recorded for the sample under vacuum conditions and after dosing oxygen with a pressure of 10^{-5} mbar. Also in the latter oxidation, an intensity decrease of the (111) and (001) peaks was observed, and the intensity increase along (112)-direction could be reproduced. Subsequently, the oxygen was pumped down and a reduction with CO was performed (fig. 6.12). The line shape recovery demonstrates that the shape change is reversible. It is worth noting that the initial recovery of the UHV-like signal is observed in the absence of O_2, prior to dosing the carbon monoxide. This clearly shows that the oxygen atmosphere is required to stabilize the (112) facets.

6.5 Summary

It was shown that (112) facets form upon oxidation of Pd nanoparticles with a diameter of 8 nm at T = 570 K and an oxygen pressure of 10^{-5} mbar. The particle shape under UHV conditions is in agreement with a previous GISAXS study [80], except for the the bottom part of the particle described by N_B which

is too high. This parameter is larger than anticipated from the study of 6 nm particles [18] and from TEM (cf. fig. 6.2). It is suspected that this is a fit artifact, which occurs if the roughness of the substrate is mediated onto the bottom part of the particles. The roughness at the interface should lead to a decrease of the diffraction signal along $\langle 001 \rangle$, this decrease is generated in the fits with a too large value for the bottom facet which also leads to a decrease of the diffraction signal. Under oxidizing conditions, the formation of (112) facets can be observed. It can be estimated that the topmost 4 atomic layers contribute to the (112) faceting. The (112) facets can be degenerated just by removing the oxygen atmosphere and accelerated by the application of CO.

The formation of the (112) facets upon oxidation is not in agreement with the theoretical results for mesoscopic particles [25]. In that study, (112) facets should be rather present under UHV conditions and vanish upon oxidation while simultaneously forming (311), (331) and (110) facets. One key point in the DFT study is that the particles should not expose sharp edges between the low-index surfaces, but rather high-index surfaces should arise between the dominating low-index facets [25]. The quantitative analysis, however, suggests a parameter for the top (112) facet $N_F = 0$ under UHV conditions. Thus, (112) type facets should not be present at all and the particle is well-described only by (111) and (100) equivalent facets.

Chapter 7

Size-dependent Oxidation of Pd Nanoparticles on MgO(100)

This chapter describes a combinatorial high energy x-ray microbeam study of the oxidation of Pd/MgO(100) nanoparticles in a size range from 4 nm to 24 nm in diameter at a temperature of 570 K and near atmospheric pressures. The applied experimental scheme using high energy x-rays allows studying the oxidation for different particle sizes under identical experimental conditions. Three size regimes with a different oxidation behavior can be identified. For particles smaller than 5 nm in diameter, complete transformation to PdO takes place, which is aligned epitaxially with the MgO substrate. Particles with a diameter between 5 nm and 9 nm shrink during oxidation accompanied by the formation of epitaxial PdO. Larger particles with D > 9 nm are covered by polycrystalline PdO which forms a passivating layer preventing the metal core from further oxidation.

7.1 Introduction

In a previous TEM study [24], Pd nanoparticles with a diameter of 10 nm were investigated after exposure to oxygen. The formation of PdO was observed at the edges of the (111) facets, after applying an oxygen pressure of around 10^{-3} mbar at T = 823 K. Pd/MgO(100) nanoparticles with a diameter of 6 nm were studied more recently by x-ray diffraction and atomic force microscopy [18]. The formation of PdO was observed at 500 K when an oxygen pressure above 0.1 mbar was applied. Five epitaxial orientations of PdO on MgO were observed, which are sketched in fig. 7.1.

The epitaxial relationship found for PdO on the Pd(100) single crystal surface (cf. ref. [66] and fig. 7.2) has not been observed. Therefore, it was concluded that the PdO phase does not grow on the 6 nm particles themselves, but directly on the MgO support. It was suggested, that due to the influence of oxygen, the metal particles release Pd atoms or PdO groups which subsequently diffuse on

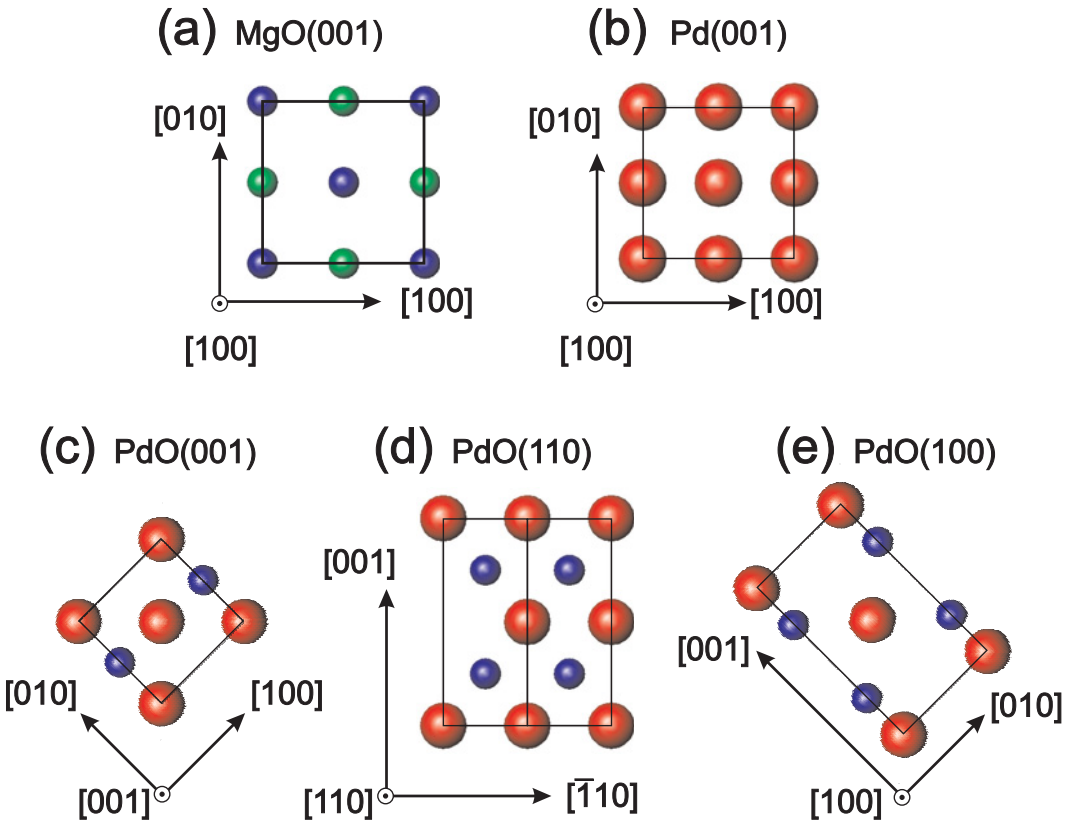

Fig. 7.1: Epitaxial relationship of Pd and PdO with respect to MgO(100). The images (a)-(e) show a top view on the unit cells, which are plotted true to scale and in the azimuthal alignment as determined in ref. [18]. (a), (b) Pd grows with cube-on cube epitaxy on MgO(100). PdO grows in (001)-orientation (c), (110)-orientation (d), and (100)-orientation (e). For the (110) and (100) oriented oxide, also 90° domains exist.

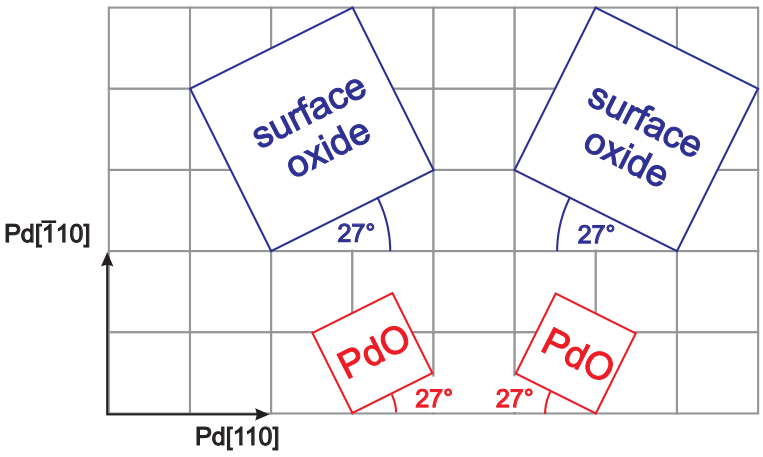

Fig. 7.2: As a comparison, the orientation of PdO and the $(\sqrt{5} \times \sqrt{5})$surface oxide with respect to the surface lattice of Pd(100) is displayed. The bulk oxide grows in (001) orientation, but its azimuthal alignment is different from the PdO stemming from Pd/MgO particles (fig. 7.1 c).

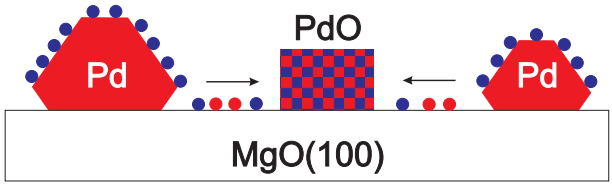

Fig. 7.3: Oxidation mechanism suggested for 6 nm Pd nanoparticles [18]: due to the influence of oxygen, the particles release metal atoms; the PdO formation occurs on the substrate.

the MgO surface, which in turn causes the nucleation of PdO in direct contact with the substrate (fig. 7.3).

A strong size dependence of the activity of nanoparticles towards chemical reactions has been observed for different metal/support combinations [14, 15, 17], which motivates to shed new light on the size-dependent oxidation mechanism of Pd nanoparticles on MgO(100). To obtain information about the influence of the particle size on the oxidation mechanism, an in situ x-ray diffraction study at a photon energy of 85 keV was performed on a specimen on which the particles were deposited with a size gradient between 4 nm and 24 nm in diameter. The high energy microbeam served to investigate the nanoparticles with different sizes under identical temperature and gas pressure conditions. Such a scheme allows a reliable investigation of the particle size effects, as for conventional photon energies in the 10 keV range, a dedicated sample preparation would be necessary due to geometrical constraints of the relatively high diffraction angles. With the high-energy setup and the use of an area detector, a large area in reciprocal space nearly without curvature can be mapped, which allows a fast data acquisition.

7.2 Sample Preparation and Experimental Details

Two edge-oriented MgO(100)- single crystals with a size of 5 × 10 mm were annealed in air at 1670 K. One crystal had been cut in a way that the the [100]- and the [010]-axes respectively were parallel to its edges (denoted as "sample *a*" in the following). At the other crystal, the [110]- and the $[1\bar{1}0]$-direction respectively were parallel to its edges (labeled as "sample *b*" in the following discussion). They were mounted on an inconel sample holder with a parallel orientation of their long edges, as is sketched in fig. 7.4 (a).

The preparation of the MgO crystals was performed as explained in section 4.5. The Pd was deposited with an electron beam evaporator (Omicron EFM 3) at a substrate temperature of 670 K. On the tip of the evaporator, a special mask had been mounted that enabled deposition with a defined cut-off line. By a stepwise translation of the sample relative to the evaporator, six 1.6 mm wide stripes of Pd with increasing Pd deposition were produced along both substrates (fig. 7.4 a). In the following, the different deposition areas which are related with

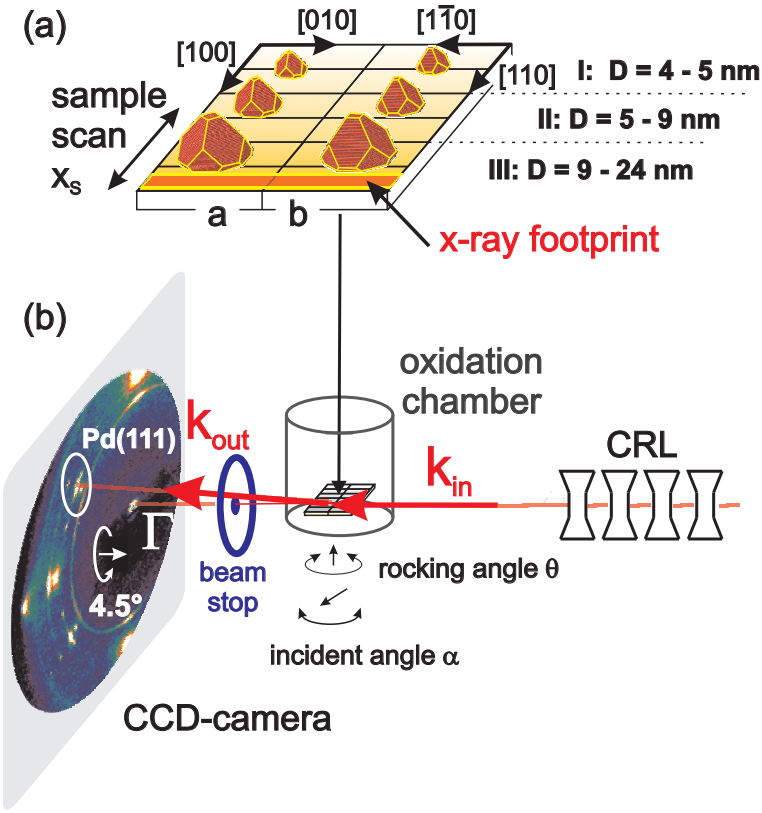

Fig. 7.4: (a): Six stripes with varying nominal thickness were evaporated on both MgO crystals. The regions labeled with I, II and III turned out to have distinct oxidation properties. (b): Set-up of the x-ray experiment.

the nanoparticle diameters D will be denoted as (I) for D = 4-5 nm, (II) for D = 5-9 nm, and (III) for D = 9-24 nm. The sample was transfered under in situ conditions into the mobile oxidation chamber (sec. 4.1.2) that was used for the x-ray diffraction experiments. These were performed at the instrument HEMD (*h*igh *e*nergy *m*icro *d*iffraction) at beamline ID 15A at the European Synchrotron Radiation Facility in Grenoble, France (sec. 4.3.2). The high energy microbeam (E = 85 keV, $\Delta E/E = 2{\cdot}10^{-3}$) is focussed on the sample with the compound refractive lens, resulting in an x-ray spot size of 24.5 × 4 μm^2 (horizontal × vertical, FWHM). A sketch of the experimental set-up is shown in fig. 7.4 (b). The incident angle was set close to the critical angle of total external reflection of MgO, which is 0.025° at this energy, in order to limit the scattering from the substrate. For these settings, a slab-like footprint of the x-ray beam is produced on the sample surface with a width of 24.5 μm and a length of 9 mm, which enables simultaneous diffraction from both substrate crystals as can be seen from fig. 7.5. This allows a simultaneous mapping of the Pd(111) and Pd(200) reflections, which can be used for a determination of the FWHMs along ⟨111⟩ and ⟨100⟩ direction with *radial* scans, which means without a line broadening due to mosaicity. Obtaining the information of FWHMs along different high symmetry directions was motivated to use the data for a Bragg peak anisotropy analysis of the particle shape as described in section 3.3.4 and reference [18]. However, the

presence of a slight height difference or tilt of the substrates gave rise to attenuation of the signal from substrate A, this is why for the quantitative analysis, only the Pd(111) reflection from substrate B was used.

The diffraction data were collected with a CCD camera, which was placed 1.07 m downstream of the sample. A special circular mask and a beam stop were applied to suppress the direct beam and unwanted powder rings from the beryllium window on the detector. The different surface areas (I-III) with varying nanoparticle sizes could be interrogated with the x-ray beam by translating the sample along x_s. The camera was tilted by an angle of 4.5° around its surface normal (figs. 7.4 (b) and 7.11 (b)), in order to distinguish surface scattering signal from undesirable artifacts sometimes present in the CCD readout.

7.3 Experimental Results

A typical CCD image is shown in fig. 7.5. It was obtained from the largest particles on substrate *b* in area III by an x-ray exposure of 9 seconds. The image contains several characteristic diffraction spots: the Pd(111) reflection from the nanoparticles and the MgO(220) reflections both from sample *b*. The additional spots can be associated with parasitic (111)-oriented Pd nanoparticles and internal twinning of (001)-oriented particles, and a tail of the Pd(200) reflections from Pd particles on substrate *a*. Due to the low absorption of the high energy x-rays, a diffraction signal is obtained for a negative momentum transfer perpendicular to the sample surface. The diffraction rods along the $\langle 111 \rangle$, $\langle 1\overline{1}1 \rangle$ and $\langle 001 \rangle$ direction emanating from the Pd(111) reflection are clearly visible and give evidence for particles with a well defined shape. In the following, the focus will be on the reciprocal space region close to Pd(111) that carries the information of the size and shape change of the nanoparticles during oxidation.

Fig. 7.6 shows an overview of the typical diffraction maps which have been observed at different sample areas (nanoparticle diameter D = 4.8 nm, 5.6 nm, 11 nm and 24 nm) for different conditions. Prior to the oxidation, the as grown sample has been subject to a 920 K annealing program under x-ray control. From the changes of the Pd(111) Bragg reflection, it can be concluded that the average nanoparticle size increases and bigger Pd particles coalesce (as inferred from the disappearance of the CTR scattering signal).

To obtain size-dependent information on the Pd particles for the different conditions in the experiment, the sample was translated perpendicular to the beam in steps of 0.25 mm. At every position, diffraction images were recorded. To determine the particle diameter D and the height H, line scans were performed on the CCD-images along $\langle 111 \rangle$ and $\langle 001 \rangle$ direction through the Pd(111) reflection. The scans along $\langle 111 \rangle$ are displayed in fig. 7.7. A transformation between the position on the CCD image and the corresponding reciprocal lattice was applied which is described in more detail in the appendix of this chapter. A simulation of

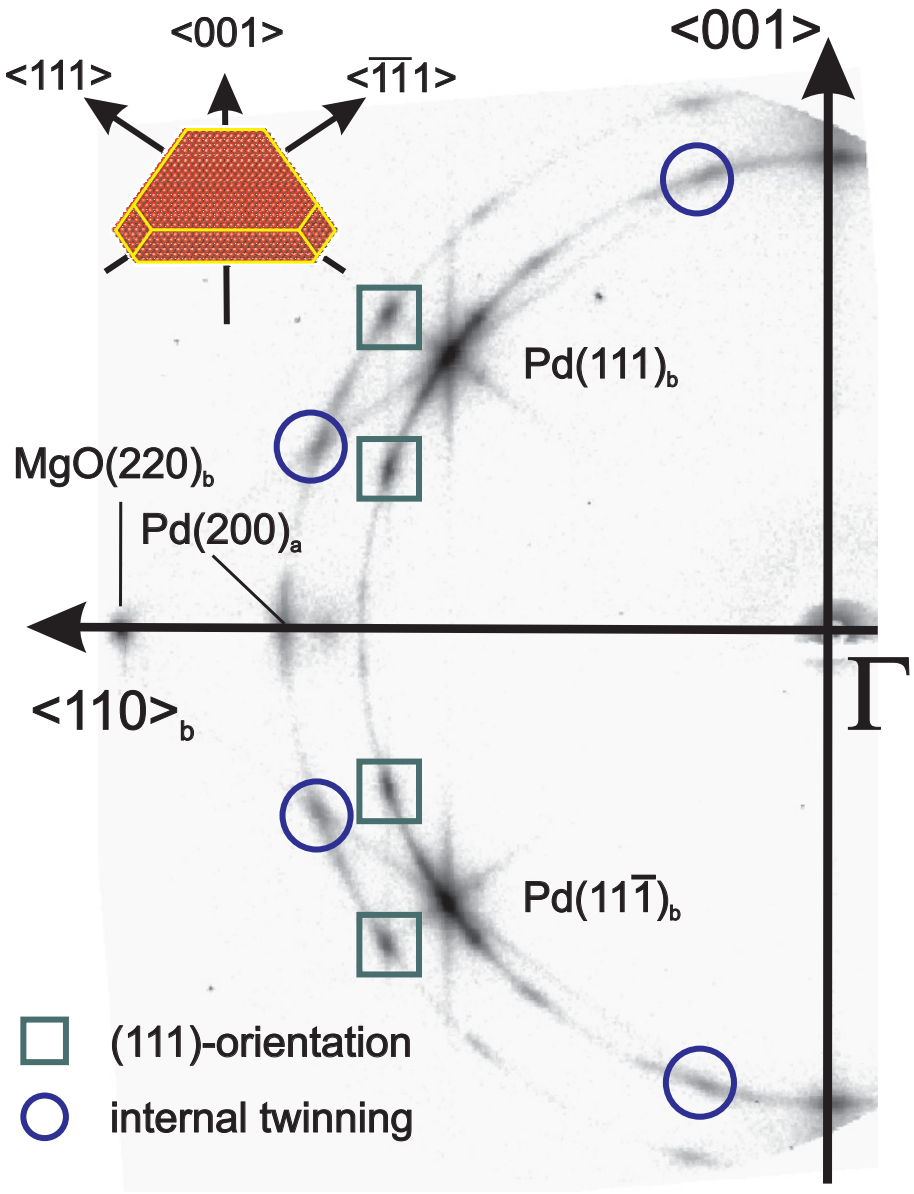

Fig. 7.5: CCD image of the largest as-grown particles. The indices a,b refer to the substrate crystals with different edge-orientation. The reflections marked with circles stem from internal twinning of the epitaxial (001) oriented particles from substrate b, those marked with squares are caused from (111) oriented particles.

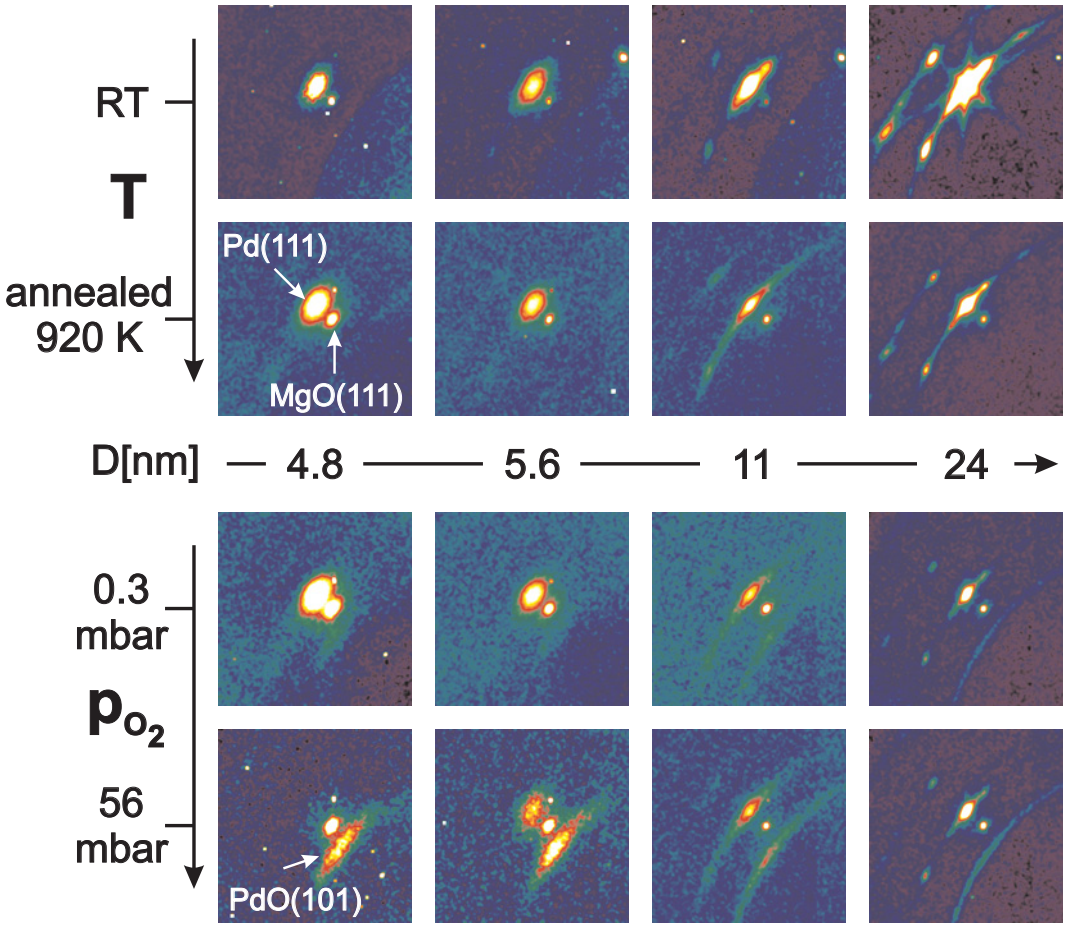

Fig. 7.6: Vicinity of the Pd(111) reflection for selected positions on the sample. The upper part shows the spots for the as-grown sample and after annealing, the lower part for the sample exposed to oxygen.

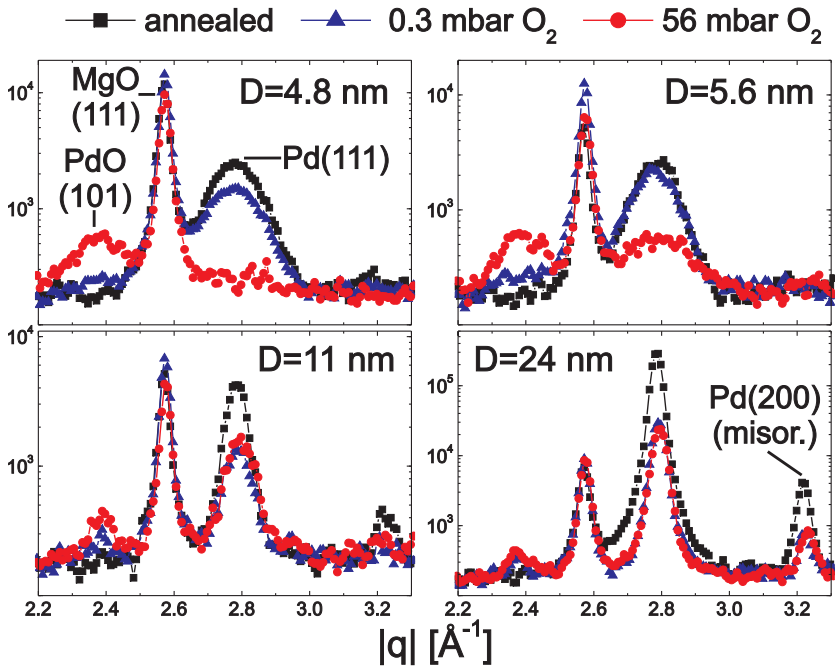

Fig. 7.7: Radial scans through Pd(111) evidencing the formation of PdO and the decrease of the Pd nanoparticle signal.

the peak anisotropy as a function of the particle shape according to the formalism described in [18] leads to $D = 1.2\frac{2\pi}{\Delta q_{111}}$ and $H = 1.14\frac{2\pi}{\Delta q_{001}}$ as a good approximation to extract average values for the diameter D and the height H, if no further directions of the FWHM anisotropy are useable. Note, that the typical value for the size distribution is about 30%, as concluded in ref. [18] from auxiliary plan view TEM and AFM measurements. In the next section, the size and pressure dependence of the nanoparticle oxidation will be described.

7.3.1 Size and Pressure Dependence of the Pd Nanoparticle Oxidation

The sizes of the particles after annealing the sample are plotted in fig. 7.8. The diameters of the Pd particles are in a range from 4 nm to 24 nm and the heights from 3 nm to 18 nm. In the plots for the height and the diameter, distinct steps and terraces of about 1.6 nanometers can be recognized. They correspond to the translation of the sample during Pd deposition. The oxidation study was carried out at a temperature of 570 K in two steps. First, an exposure of the sample to O_2 at a pressure of 0.15-0.3 mbar was applied for several hours. After the x-ray characterization, a further exposure to 56 mbar of O_2 was performed, the data discussed in the following was recorded after an exposure time of 1.5 hours. The lower part of fig. 7.6 shows the evolution of the Bragg reflections at selected positions of the sample during the oxygen exposure. Correspondingly, for these positions of the sample, line scans in $\langle 111 \rangle$ direction are shown in fig. 7.7 for the annealed case and for both oxidation stages. Fig. 7.6 exhibits the following

features: the MgO(111) reflection at q = 2.6 Å^{-1} and the Pd(111) reflection from the nanoparticles at q = 2.8 Å^{-1} which shows different widths associated with the different sizes queried with the x-ray microbeam. When the particles are oxidized, a third diffraction peak emerges at at q = 2.4 Å^{-1} which can be identified as the PdO(101) bulk oxide Bragg reflection. The most remarkable observations are: (i) the decrease of the Pd(111) intensities, and the simultaneous increase in the peak width (the small Pd nanoparticles in fig. 7.7 show drastic changes at 56 mbar) and (ii) the appearance of a PdO(101) Debye-Scherrer ring for large particles and a well-defined PdO(101)diffraction spot for the small particles.

For all particle sizes, a decrease of the Pd(111) signal and a broadening of the peak can be observed at 0.3 mbar, which is a direct hint of a reduction of the particle size. Simultaneously, a diffraction signal starts growing at the position at the PdO(101) reflection at 2.4 Å^{-1}. The change in the signal after the second oxidation step (56 mbar) is rather dramatic for the 4.8 nm and the 5.6 nm particles, and is less significant for the large particles with D = 11 nm and 24 nm. The Pd(111) signal disappears completely for particles with D = 4.8 nm, whereas the PdO(101) diffraction signal gets more pronounced. For the 5.6 nm particles, the Pd(111) peak weakens remarkably and broadens, while the PdO(101) diffraction signal grows. For the large particles, the change in the Pd(111) signal is very small at 56 mbar, indicating a passivation of the particles. A rather ringlike PdO(101) diffraction signal can be observed (fig. 7.6).

Fig. 7.8 shows the size of the particles during oxidation. After the first oxidation at 0.3 mbar, all particles undergo shrinkage in height and diameter, which is especially pronounced for the large particles from region III. The second oxidation step at 56 mbar has a radical effect on particles with D < 5 nm (I), of which the signal vanishes completely. The particles with diameters D between 5 nm and 9 nm (II) undergo shrinkage, whereas the large particles with D > 9 nm (III) keep their average size. As can bee seen from the PdO signal in the lower part of fig. 7.6, also the PdO formation is influenced by the particle size, which is discussed in more detail in the following section.

7.3.2 PdO Formation

The size reduction of the Pd particles is accompanied by the formation of the bulk oxide phase PdO. Fig. 7.9 (c) shows the diffraction patterns for D = 4.8, 5.6, 11 and 24 nm recorded by the CCD after oxidation at 56 mbar. Fig. 7.9 (a, b) focus onto the PdO(101) diffraction lines as a function of the momentum transfer $|\boldsymbol{q}|$ and of the angle ψ.

A well-defined diffraction spot is present for the small particles at the PdO(101) position, which corresponds to (001) oriented PdO particles in epitaxy to the MgO(100) substrate (the domain plotted in fig. 7.1 (c). Additionally, a tail from the PdO(002) reflection is visible along the $\boldsymbol{q}_{\mathbf{001}}$-direction perpendicular to the sample surface. The well-defined PdO(101) spot gets more and more smeared

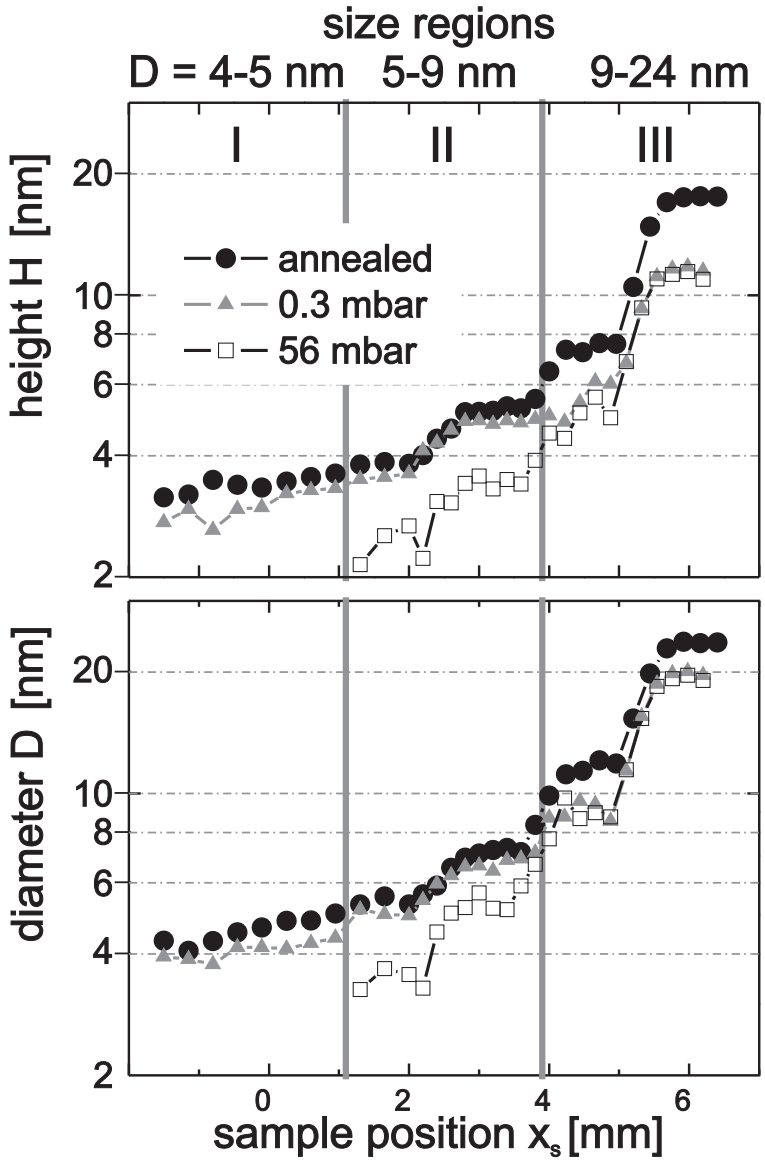

Fig. 7.8: Particle size as a function of sample position in the different stages of the experiment: after annealing, oxygen atmosphere of 0.3 mbar and oxygen atmosphere of 56 mbar. Size regimes with different oxidation behavior are marked with Roman numbers (I, II, III).

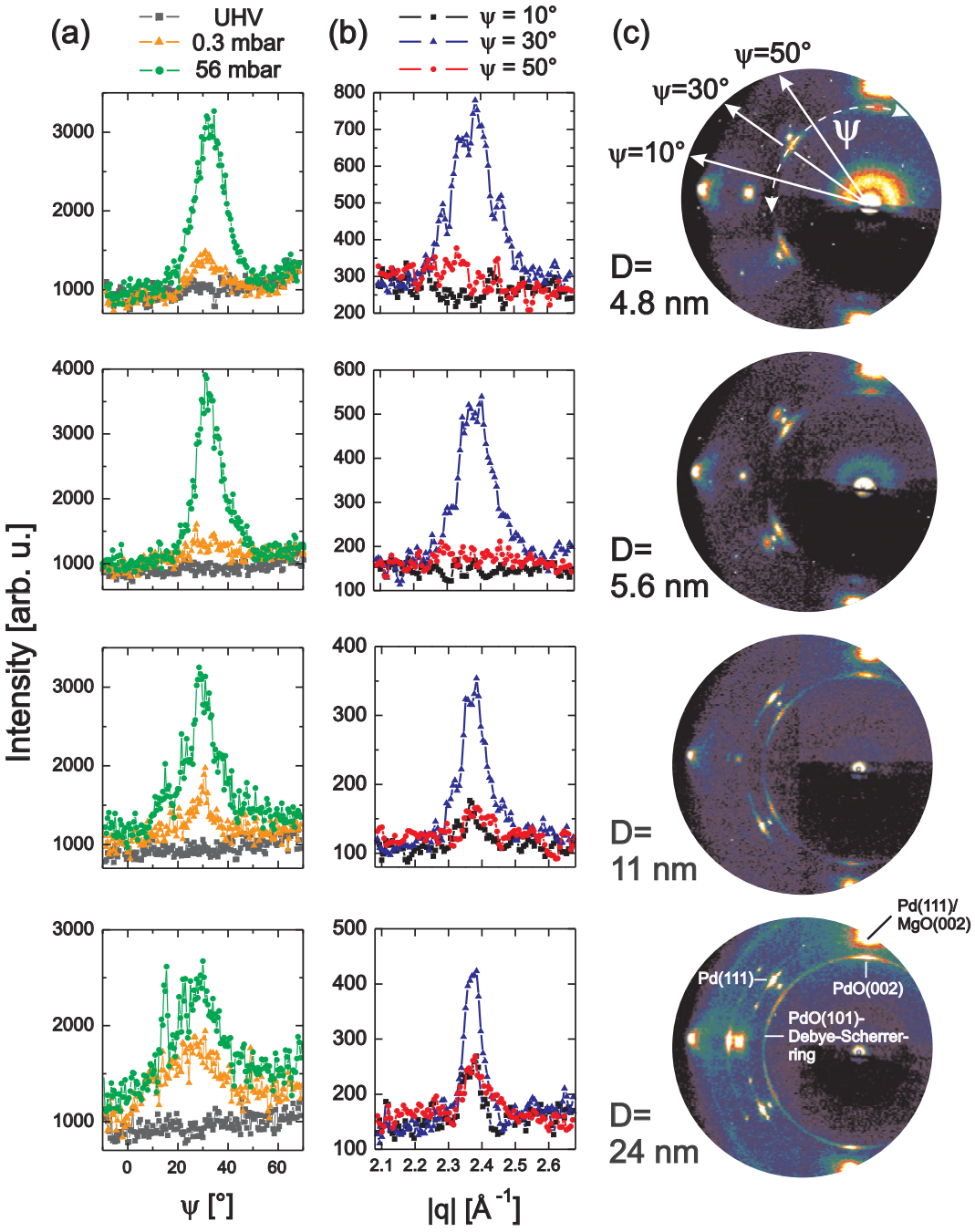

Fig. 7.9: (a) Evolution of the PdO(101) signal along ψ. (b) Radial scans at 56 mbar for different values of ψ to check for polycrystallinity. (c) CCD images at an oxygen pressure of 56 mbar.

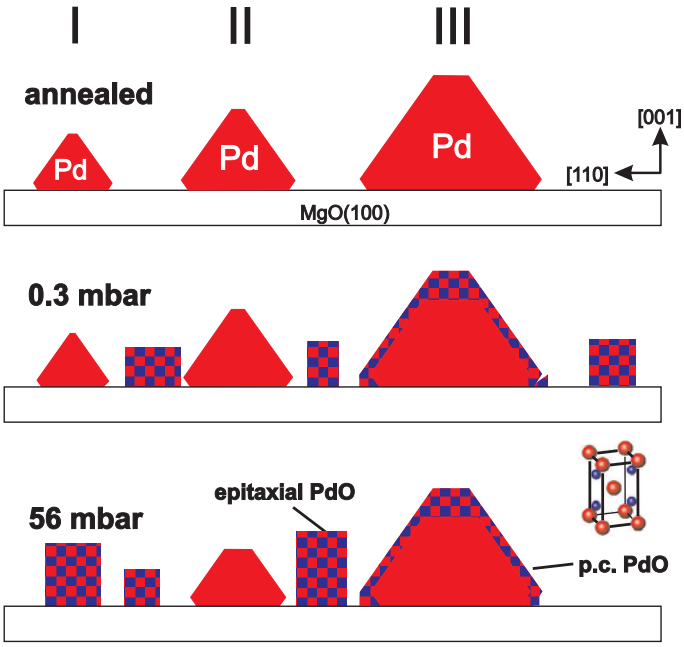

Fig. 7.10: Scenario of the oxidation for different particle sizes sketching the decreasing Pd metal core and the complete transformation of the particles respectively. It is shown the substrate-determined growth of epitaxial PdO as well as the formation of a polycrystalline passivating layer.

out on a ring-like diffraction pattern for the larger particles. Still, the tail of the PdO(002) reflection is present, which evidences an additional preferential (001) texture of the oxide for the bigger Pd particles. The orientation order of PdO can be demonstrated with ψ-scans at q = 23.8 $\AA^{-1}$, corresponding to the PdO(101) reflection[1]. These scans give information about orientation and texture of PdO grains relative to the incident beam direction. They are plotted in fig. 7.9 (a) for the different stages of the experiment. A maximum is detected at the position of epitaxial PdO(101) for all particle sizes and for both oxygen pressures, which gets washed out in ψ for the large particles. The degree of polycrystallinity can be checked with radial scans at $\psi = 10°$, $\psi = 30°$ and $\psi = 50°$, which are shown in fig. 7.9 (b). No remarkable peaks are present at $\psi = 10°$ and $\psi = 50°$ for the smaller particles in size regime I and II, but a reflection in the high symmetry direction $\psi = 30°$. This is inline with an epitaxial growth of PdO directly on the MgO(100) substrate as reported in ref. [18]. For the particles with D > 9 nm (size regime III), also the scans at $\psi = 10°$ and $\psi = 50°$ show distinct reflections, which attests a polycrystalline, powder-like growth of PdO.

7.4 Discussion and Conclusion

Basically three size regimes of Pd/MgO(100) nanoparticles can be identified with a different oxidation behavior, either particles with diameters from 4 to 5 nm (I), from 5 nm to 9 nm (II) and particles between 9 nm and 24 nm (III). For

[1]The PdO(002) reflection has practically the same lattice spacing, which means that for polycrystalline PdO there is an overlap of PdO(101) and PdO(002).

all size regimes a decrease of the particle size can be observed, especially of the height, during PdO formation. The scenario of the size-dependent oxidation mechanism is sketched in fig. 7.10. The decrease of the size of the particles in range I and II is small in the first oxidation step at 0.3 mbar, but is more distinct at an oxygen pressure of 56 mbar. At this oxidation step, the smallest particles (I) transform completely into the bulk oxide PdO. This points to a lower kinetic barrier for PdO formation as compared to the corresponding single crystal surfaces of Pd(111) and Pd(100), which can be passivated by the growth of the surface oxide layers or chemisorbed oxygen at 570 K and atmospheric oxygen pressures [29, 58]. The PdO islands formed by complete oxidation of the small Pd nanoparticles (I) are epitaxial to the MgO(100) substrate which is different from that found for epitaxial PdO forming on Pd(100) single crystal surfaces (ref. [66], fig. 7.2).

In size regime II, the metal core of the Pd particles shrinks with increasing oxygen pressure, while PdO is formed. The PdO is epitaxial to MgO, as for size regime I. The observation is compatible with the oxidation mechanism suggested in ref. [18] for 6 nm particles. Because of the size distribution of about 30%, it is likely that small particles are completely oxidized first and then act as nucleation centers for epitaxial PdO growth on MgO(100). As the particles turn out still to be reactive after the first oxidation at 0.3 mbar, one can conclude that they are not covered by a passivation PdO shell with a thickness in the nm range. This implies that the Pd particle facets are either covered by chemisorbed oxygen or an ultra thin surface oxide layer, similar to the $\left(\sqrt{6} \times \sqrt{6}\right)$ structure on Pd(111) or the $\left(\sqrt{5} \times \sqrt{5}\right)$ surface oxide on Pd(100) (refs. [29, 65] and sec. 2.4)[2]. Pd particles may serve as dissociation centers for O_2 molecules, as well as possibly PdO islands do. Pd atoms from the particle corners and Pd-O complexes may diffuse on the MgO surface, where they are incorporated into the growing PdO particles [98].

The largest particles (size regime III) show different properties during oxidation: their size changes mainly in the first oxidation step, but the further decrease in the second oxidation step is very small. It can be concluded that at an O_2 pressure of 0.3 mar, a polycrystalline PdO layer forms on the surface of the Pd particles. This oxide shell forms a kinetic barrier for further oxidation of the particles. The observation of PdO growing on the particles in this size regime and not only directly on the substrate is supported by the TEM study [24], which reports on the formation of PdO on the edge of a Pd particle with a diameter of around 10 nm. The epitaxial fraction of PdO in size range III can either be caused purely from the smaller particles within the size distribution, or the large particles themselves release in addition Pd atoms for PdO formation on the substrate, in concurrence with the growth of PdO on the Pd particles. Note, however, that for supported particles, the size of the particles and the coverage of

[2]No diffraction data was retrieved from these structures.

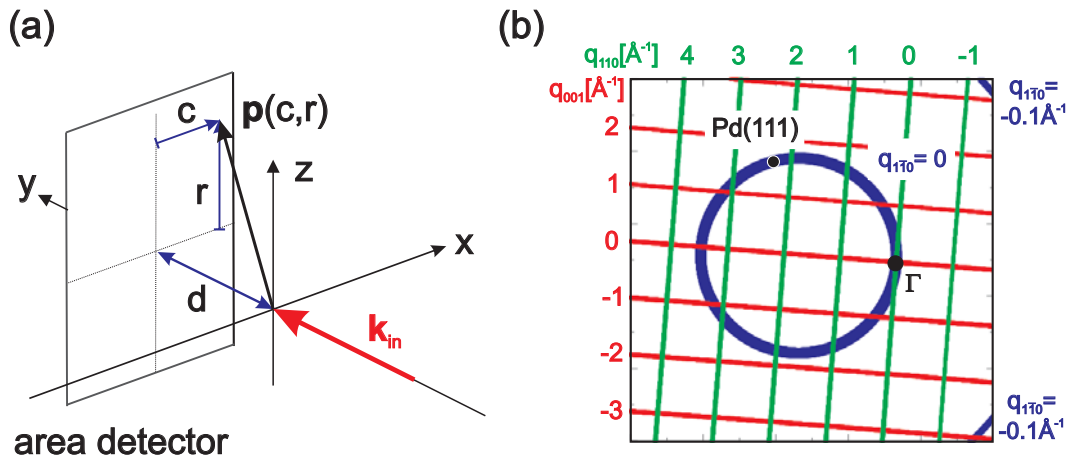

Fig. 7.11: (a) Initial position of the area detector in a Cartesian right hand laboratory frame, (b) Momentum transfer in coordinates of the reciprocal lattice of Pd.

the support must not be seen independently. It is also possible that the growth of the PdO on the large Pd nanoparticles occurs not only as an intrinsic size property, but also as the fraction of the bare MgO surface is lower than for small particles, which may limit the amount of PdO growing in direct contact with MgO.

To conclude, it could be shown that a size dependent oxidation mechanism exists for the oxidation of epitaxial Pd/MgO(100) nanoparticles. For small particles, the formation of PdO may be facilitated by lowering kinetic barriers down to the thermodynamic stability limit for bulk oxide. This in turn makes it more likely that the bulk oxide itself can take part in a chemical reaction.

Appendix: Reciprocal Space Mapping with 2d Detector

The transformation between detector coordinates and the momentum transfer in the reciprocal lattice is described in the following. Let the laboratory frame be defined by a right hand Cartesian coordinate frame $\{x, y, z\}$. A notation is used where the direct beam points in the y-direction, the x-direction points horizontally and the z-direction vertically. For an initial position, a reference point of the detector is hit by the direct beam, the rows and columns of the detector pixel array show into x- and z-direction respectively, whereas the normal of the detector surface shows into y-direction. The position of a detector pixel in the laboratory frame can be expressed by $\boldsymbol{p}\,(c, r) = \begin{pmatrix} c \\ d \\ r \end{pmatrix}$. Thereby, r and c denote the row and column of the pixel with respect to the reference point and d

is the distance between the sample and the detector. The rotation of the detector via the motors of the diffractometer is described by a rotation matrix $\boldsymbol{D}$. With the wavelength λ, the scattering vector in the laboratory frame is:

$$\boldsymbol{q} = \frac{2\pi}{\lambda}\left\{\frac{1}{\sqrt{r^2+c^2+d^2}}\boldsymbol{D}\begin{pmatrix}c\\d\\r\end{pmatrix} - \begin{pmatrix}0\\1\\0\end{pmatrix}\right\}$$

This vector must be expressed in the basis of the considered reciprocal lattice. The reciprocal lattice vectors $\boldsymbol{b_j}\,(j=1,2,3)$ are defined via the lattice vectors of the crystal $\boldsymbol{a_i}\,(i=1,2,3)$ and the relationship $\boldsymbol{a_i}\cdot\boldsymbol{b_j} = 2\pi\delta_{ij}$. The vectors $\boldsymbol{b_i}$ are listed in the (3×3)-Matrix $\boldsymbol{B} = (\boldsymbol{b_1}, \boldsymbol{b_2}, \boldsymbol{b_3})$. The orientation matrix $\boldsymbol{U}$ describes the initial orientation of the crystal lattice with respect to the laboratory frame, in practice after alignment of the optical surface. In the experiment, the sample may be rotated via the motors of the used diffractometer, in case of the experiment presented here, these are the rocking angle θ and the incident angle α. The entire rotation is described by a rotation matrix $\boldsymbol{S}$. The scattering vector can be expressed via the Miller indices h, k, l by $\boldsymbol{q} = \boldsymbol{SUB}\begin{pmatrix}h\\k\\l\end{pmatrix}$. The rotation matrices $\boldsymbol{D}$ and $\boldsymbol{S}$ for the rotation of the sample and the detector must be expressed as a function of the angles of the diffractometer. It is very convenient to use the following rotation matrices describing the rotation round the x, y and z axis by an angle ϵ:

$$\boldsymbol{R_x}(\epsilon) = \begin{pmatrix}1 & 0 & 0\\ 0 & \cos\epsilon & -\sin\epsilon\\ 0 & \sin\epsilon & \cos\epsilon\end{pmatrix}$$

$$\boldsymbol{R_y}(\epsilon) = \begin{pmatrix}\cos\epsilon & 0 & \sin\epsilon\\ 0 & 1 & 0\\ -\sin\epsilon & 0 & \cos\epsilon\end{pmatrix}$$

$$\boldsymbol{R_z}(\epsilon) = \begin{pmatrix}\cos\epsilon & -\sin\epsilon & 0\\ \sin\epsilon & \cos\epsilon & 0\\ 0 & 0 & 1\end{pmatrix}$$

In case of the diffractometer used in the experiment described here, the detector is rotated by a fixed angle $-4.5°$ around the y-Axis: $\boldsymbol{D} = \boldsymbol{R_y}(-4.5°)$. The sample rotation by the rocking angle θ and the incident angle α are expressed by $\boldsymbol{S} = \boldsymbol{R_x}(\alpha)\boldsymbol{R_z}(\theta)$. For the orientation matrix $\boldsymbol{U}$, a miscut of the sample was neglected, so that formally $\boldsymbol{U} = \boldsymbol{R_z}(\theta_0)$. This means, for $\alpha = 0°$, $\theta = -\theta_0$, the [110], [1$\bar{1}$0], and [001]-axes of substrate b (fig. 7.4 a) are parallel to the x, y and z axes of the laboratory frame. After setting the incident angle α in the experiment, the rocking angle θ is moved to a position $\theta = -\theta_0 + \theta_c$ to center the Pd(111) peak. In the calculation of the q-Map, this centering is taken into

account by varying θ_c in such a way that the momentum transfer component in $\boldsymbol{q}_{\mathbf{1\bar{1}0}}$-direction becomes zero for $|\boldsymbol{q}_{\mathbf{110}}| = \frac{2\pi\sqrt{2}}{3.89\mathring{A}}$ and $|\boldsymbol{q}_{\mathbf{001}}| = \frac{2\pi}{3.89\mathring{A}}$.

No approximation exploiting the small curvature of the Ewald sphere is applied, therefore the transformation holds for any energy. In addition, this calculation can be easily adapted to any kind of diffractometer, just the matrices $\boldsymbol{D}$ and $\boldsymbol{S}$ must be given as a function of the diffractometer angles in the same way as for a point detector. For example, on a six-circle diffractometer in z-axis mode as described in ref. [85], $\boldsymbol{D} = \boldsymbol{R_x}(\alpha)\boldsymbol{R_z}(-\delta)\boldsymbol{R_x}(\gamma)$ and $\boldsymbol{S} = \boldsymbol{R_x}(\alpha)\boldsymbol{R_z}(-\omega)$.

Chapter 8

Oxidation Studies of Pd and Rh Particles on α-Al_2O_3(0001)

In the previous chapters, the oxidation properties of Rh and Pd nanoparticles on MgO(100) supports were discussed and this support leads essentially to (001)-oriented particles in a cube-on-cube epitaxy. Further orientations of the particles can be achieved by using other support surfaces. The growth and oxidation of (111)-oriented Pd clusters was previously performed on oxide thin film supports for STM, e.g. Fe_3O_4 on Pt(111) [99] or the O-Rh-O surface oxide on Rh(111) [100]. To conduct oxidation studies at near atmospheric pressures, the stability of the support surface is crucial, which is typically not the case for ultra thin oxide films on metal single crystal supports. For this reason, it is preferable to use oxide single crystals. The α-Al_2O_3(0001) single crystal surface was previously used for growth and sintering studies [101] and oxidation studies [102]. The use of α-Al_2O_3 single crystals as support may be seen of special interest, as in technical catalysis, typically the transition metal particles are dispersed over powders of aluminum oxide. For example, Pd supported on alumina is a catalyst for methane combustion, the hydrochlorination of chlorobenzene [103] or reduction of NO by CO [104, 105].

8.1 Experimental Details

Pd particles were grown in the stationary UHV chamber (sec. 4.1.1), and the support crystal was prepared as explained in section 4.5. A substrate temperature of 570 K was applied for the metal deposition. After deposition, the sample was studied under ambient conditions with x-ray reflectivity at the rotating anode (sec. 4.3). From reflectivity it follows a thickness of 1.6 nm with a roughness of 0.6 nm, and an electron density of 11% in comparison with bulk palladium. This reduced electron density implies that the morphology of Pd is given as particles and not as a wetting film. A chromel/alumel K-type thermocouple was

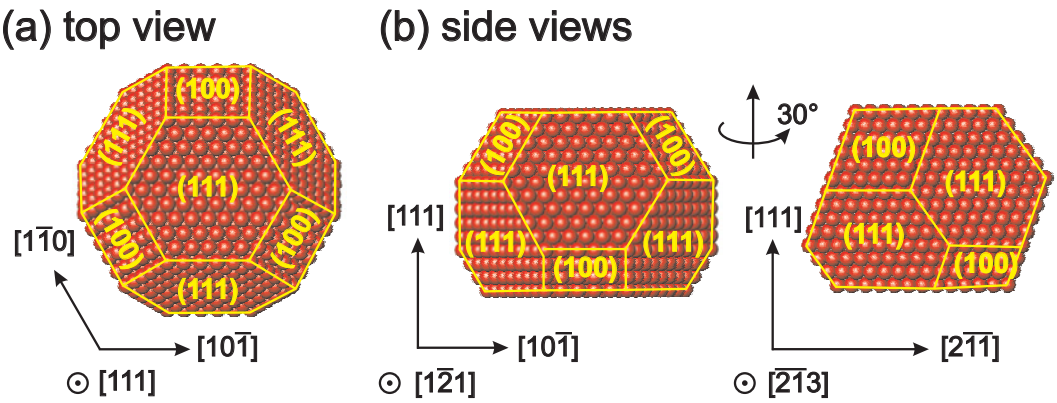

Fig. 8.1: Model shape of a supported (111)-oriented fcc particle terminated by (111) and (100) facets.

attached to the crystal prior to transfer into the mobile oxidation chamber. UHV conditions were obtained after the bake out of the system. The x-ray studies were performed at the MPI-MF beamline at ANKA with a photon energy of 10 keV. Due to the air exposure of the sample, an annealing program under x-ray control was applied. Several cycles of CO exposure with pressures between 10^{-5} mbar up to 1 mbar and oxygen with pressures between 10^{-5} and 10^{-2} mbar were applied in a temperature range between 570 K and 920 K.

In the following, all XRD line scans and reciprocal space maps will be indexed in reciprocal lattice units of sapphire[1] with a = b = 4.75 Å c = 12.99 Å, $\alpha = \beta = 90°$, $\gamma = 120°$. Particular reflections of Rh and Pd particles in (111)-orientation will be indexed with the surface lattice of (111)-oriented particles with $a = b = \frac{a_0}{\sqrt{2}}$, $c = a_0\sqrt{3}$, $\alpha = \beta = 90°$, $\gamma = 120°$, as explained in appendix B.2. Bragg reflections of particles occurring in different orientations and Debye-Scherrer-Rings will be indexed in reciprocal lattice units of fcc-coordinates.

8.2 Oxidation of Pd/α-Al_2O_3(0001) Nanoparticles

8.2.1 Epitaxial Orientation of the Particles

A reciprocal space map at L = 0.15 is displayed in fig. 8.2[2]. It was recorded at T = 670 K and under oxidizing conditions at p = $4{\cdot}10^{-3}$ mbar. It contains

[1]For simplicity the Miller indices with three components instead of the four component Bravais coordinates are used.

[2]It was recorded at this relatively large L value and not at L = 0.08, according to the incident and exit angle $\alpha_{i/f}$ at the critical angle for total external reflection 0.23° for the substrate, in order to move from the center of the sharp and intense substrate reflections that are partially overlapping with the relatively broad Pd reflections.

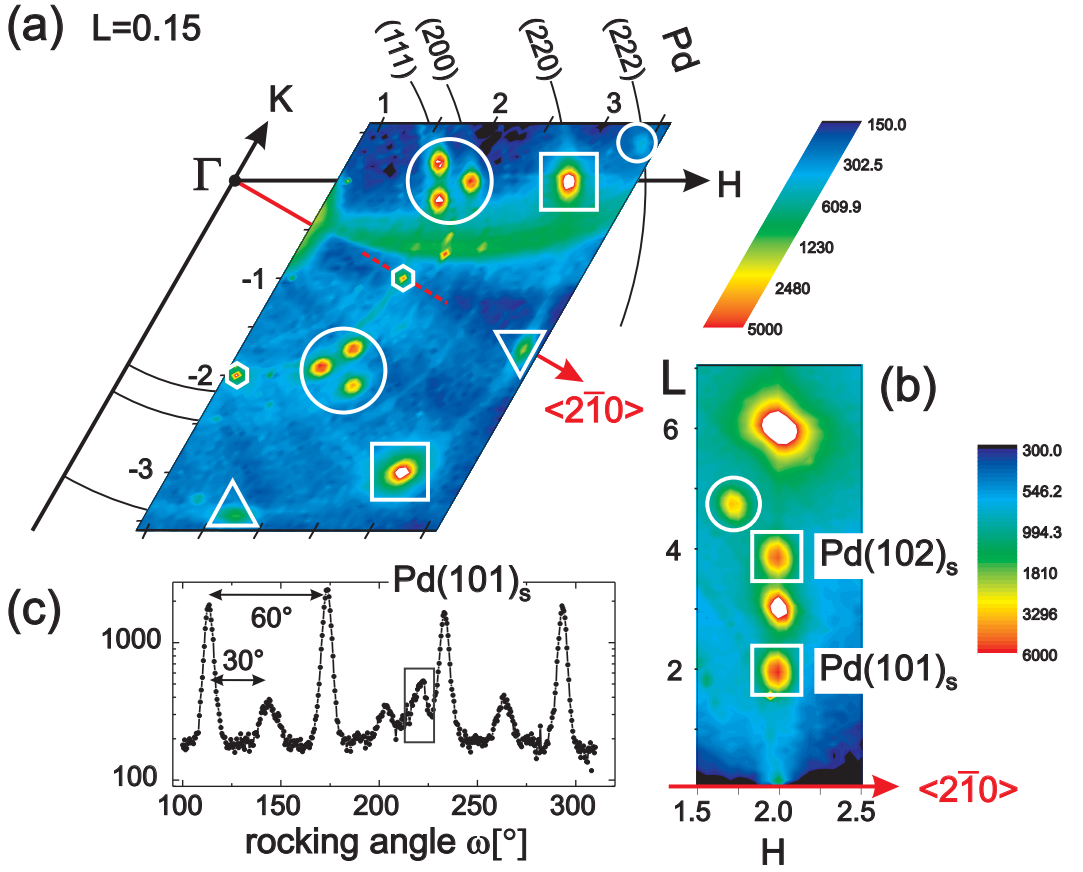

Fig. 8.2: XRD scans revealing epitaxial Pd. Reflections marked with circles belong to (110)-oriented Pd. The reflections marked with squares can be assigned to (111)-oriented Pd in a $\left(\sqrt{3} \times \sqrt{3}\right)$R30° relation with respect to the sapphire (0001) surface. Triangles are the superposition of (110)-oriented Pd with (111)-oriented Pd. This (111)-oriented Pd has an azimuthal shift of 30° with respect to the reflections marked with squares. The small hexagons mark the $(2\bar{1}0)$ and the $(1\bar{2}0)$ reflections of α-Al_2O_3, which are not overlapping with Pd reflections. The in-plane mesh scan is not sufficient for a full retrieval of all domains and was complemented by out-of plane scans (b) and the broad rocking scan through Pd$(101)_S$ (c). The smeared-out intensity at k ≈ -0.5 in (a) and within the gray rectangle in (c) is caused from undesired scattering of the direct beam at the thermocouple, but does not affect the analysis of the relevant Bragg peaks.

reflections that can be assigned to Pd(111), Pd(200), Pd(220) and Pd(222). It is conspicuous that (111) and (200) types of reflections arrange in triplets which are marked with large circles. Secondly, there are Pd(220) type reflections that overlap with Al_2O_3(300). These are marked with squares. All peaks can also be observed at an azimuthal shift of 60°. Pd(220)-type peaks are also present at an azimuthal shift of 30° marked with triangles. One Pd(222) reflection is located within the map and is highlighted with a small circle. Furthermore, there is a weak contribution of Debye Scherrer rings of Pd and sapphire. The arc-lice intensity distribution around K = -0.5 is situated in a ω = const. range, i.e. with a fixed angular relation between the incident beam and the sample. This indicates that the x-ray is scattered at a particular position of the sample, probably the thermocouple attached on the side of the support crystal. However, the relevant peaks used for the diffraction analysis are not affected from that signal.

The diffraction pattern can be explained with a coexistence of epitaxial Pd particles in (111) and in (110) orientations. The according real space arrangement of the metal domains are displayed in the left part of figs. 8.3 (a, b) and the corresponding positions of the Bragg reflections are sketched in the right part of the figure. The yellow quadrangle is the experimentally interrogated **q**-range. The Pd(220) reflections overlapping with Al_2O_3(300) and $(3\bar{3}0)$ stem from the domains labeled with Roman numbers I and II in the figure, where the surface unit cells are tilted by an angle of 30° with respect to the sapphire surface unit cell. Closer inspection of the lattice constant shows that this is a $\left(\sqrt{3}\times\sqrt{3}\right)$R30° relation. This epitaxy can be explained with the good match of the atom rows $d_1 = \sqrt{\frac{3}{8}}\cdot 3.89$ Å of Pd and the distance $\frac{1}{2}\cdot$ 4.75 Å of rows of Al atoms in sapphire. The mismatch is only 0.3%.

The triplet of Pd(111) and Pd(220) peaks arises from particles in (110)-orientation, with three azimuthal orientations as sketched in fig. 8.3 (b). Also this orientation can be ascribed to the distances of atomic rows within Pd and of the support. The distance $d_2 = \sqrt{\frac{3}{2}}\cdot 4.75$ Å fits to the lattice constant of Pd with a lattice mismatch of 6%, this larger value explains why the 30° domains are less favored.

The Pd reflections marked with triangles in figs. 8.2 a 8.3 (a, b) can be explained with the (110)-oriented particles, but also with additional domains of (111) oriented particles, that are labeled as domain III and IV. As holds generally for (111)-oriented fcc structures, their azimuthal alignment cannot fully be retrieved only from the in-plane reciprocal space map, as at $q_z = 0$, it cannot be distinguished if only a single domain is present or if in addition, a second domain with an azimuthal shift of 60° exists (cf. appendix B.2). The existence of both domains I and II can be deduced from the reciprocal space map in fig. 8.2 (b), which contains the $Pd(101)_s$ and $Pd(102)_s$ reflections and can only occur if two domains azimuthally shifted by 60° are present. A broad rocking scan through $Pd(101)_S$ shows distinct peaks in steps of 30° (fig. 8.3 (c)). These reflections

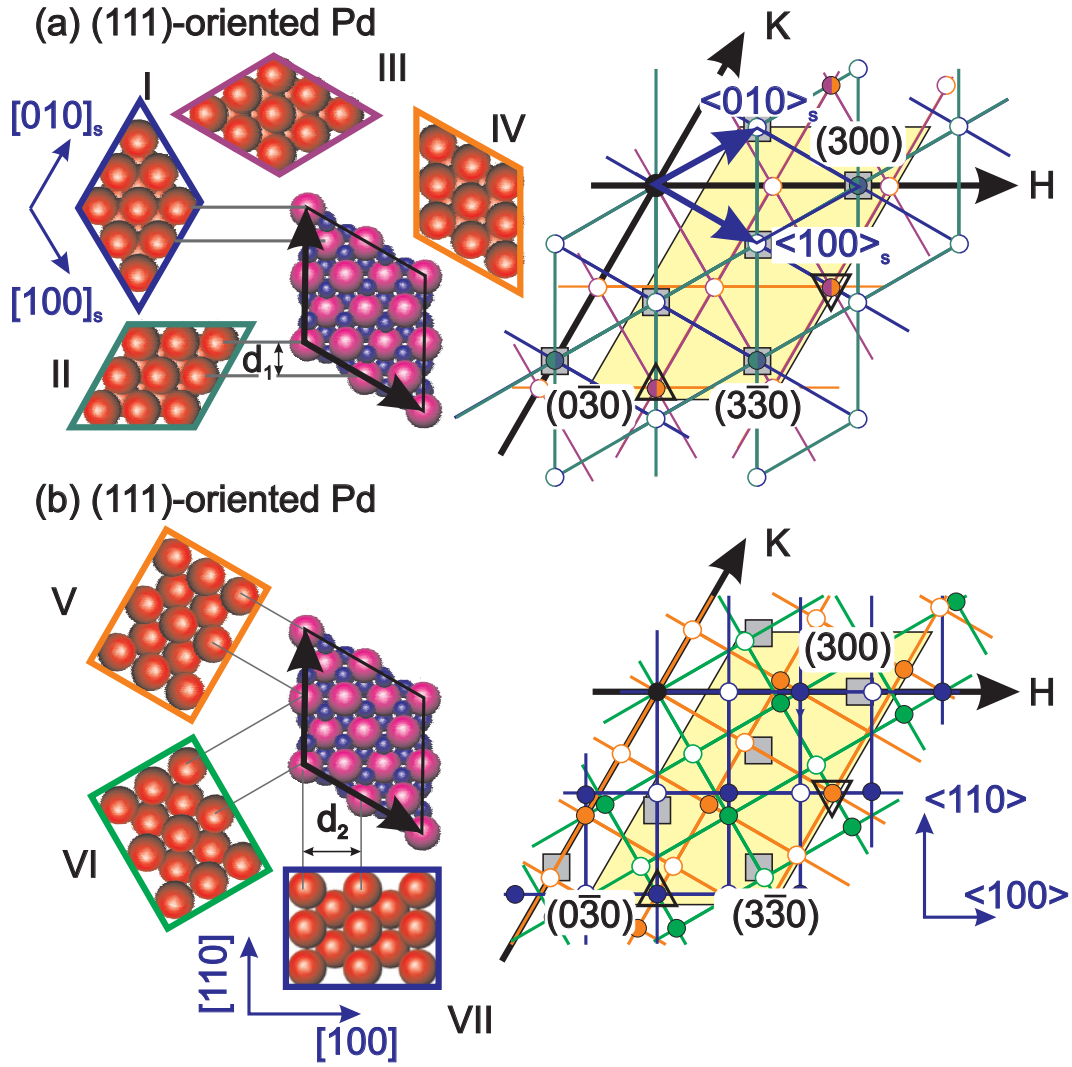

Fig. 8.3: Epitaxial relationship for (111) and (110) oriented Pd domains on α-Al_2O_3(0001). The gray lines indicate the good match of Pd rows to the Al rows of sapphire. Right: Positions of Bragg reflections for $q_z = 0$. The filled circles represent allowed reflections of Pd, the open circles represent forbidden reflections. For the transformation from fcc to (111)-surface coordinates, see appendix B.2. The yellow quadrangle is the **q**-range interrogated in the experimental reciprocal space map and the grey squares are the positions of the substrate Bragg reflections.

can only be explained by domains III and IV of (111)-oriented Pd and cannot be caused from (110)-oriented Pd.

To sum up, seven epitaxial domains exist on the sapphire surface, three of them are (110)-oriented, two of them are (111) oriented with $R(\sqrt{3} \times \sqrt{3})30°$ relation with respect to the support lattice and two of them are azimuthally shifted by $\pm$ 30°. From the FWHMs of the Bragg reflections[3], it is estimated that the (111) particles have a height of 3 nm and a diameter of 4 nm, the (110)-oriented particles have a height of 2.5 nm and a diameter of 4 nm. From the integrated intensities obtained by rocking scans, it is estimated that the relative occurrence is 3.5% for each of the (110) oriented domains (V-VII), 7 % of Pd is contained in each of the 30° domains (III, IV) of (111)-oriented Pd and 38% in domain I and II, respectively, for (111) oriented Pd in $R(\sqrt{3} \times \sqrt{3})30°$ epitaxy. The following oxidation experiments will be focussed on the (111)-oriented particles from domain I. Assuming that these particles are limited by (111) and (001) facets, and their distance ratio h_{001}/h_{111} is ≈ 1.16, the average particle size and shape corresponds to that displayed in fig. 8.1.

8.2.2 Oxidation of the Particles at Moderate Pressures

At a substrate temperature of 570 K, oxygen was dosed stepwise starting with a pressure of 10^{-7} mbar up to 10^{-2} mbar. Simultaneously, a time scan of the intensity of (1.98 -1.99 2.2) was recorded, which is on the shoulder of $Pd(101)_s$. A shoulder position can be expected to be sensitive for changes either of the maximum Bragg intensity as well as for changes of the line width. In between, the FWHM of the Bragg reflections was characterized by scans in high-symmetry directions through $Pd(101)_S$. The according scans are displayed in fig. 8.4. As can be seen in fig. 8.4 (a), the intensity decreases by around 20% on a timescale of two hours and seems to saturate after four hours at an oxygen pressure of 10^{-2} mbar. The FWHM of the Bragg reflections, however, did not change remarkably. When the oxygen was pumped down and carbon monoxide was ingested, the intensity increased to the initial value.

The oxygen exposure at moderate pressures was also performed at an elevated temperature of 620 K. Also here, a decrease of the Pd intensity can be observed. A slight increase of the FWHM along $\langle 2\bar{1}0 \rangle$ and $\langle 001 \rangle$ by 3% can be observed, which means that the fcc-core of the particles decreases slightly, possibly because of a displacement of the outermost Pd atoms. The original intensity can be retrieved by pumping down the oxygen (without dosing carbon monoxide), and switched back by redosing oxygen, as displayed in fig. 8.4 (b).

[3]Here, diameter and height means $\frac{2\pi}{\Delta q}$ along $\langle 2\bar{1}0 \rangle$ and $\langle 001 \rangle$. A detailed FWHM anisotropy simulation as for the (001) oriented particles was not conducted.

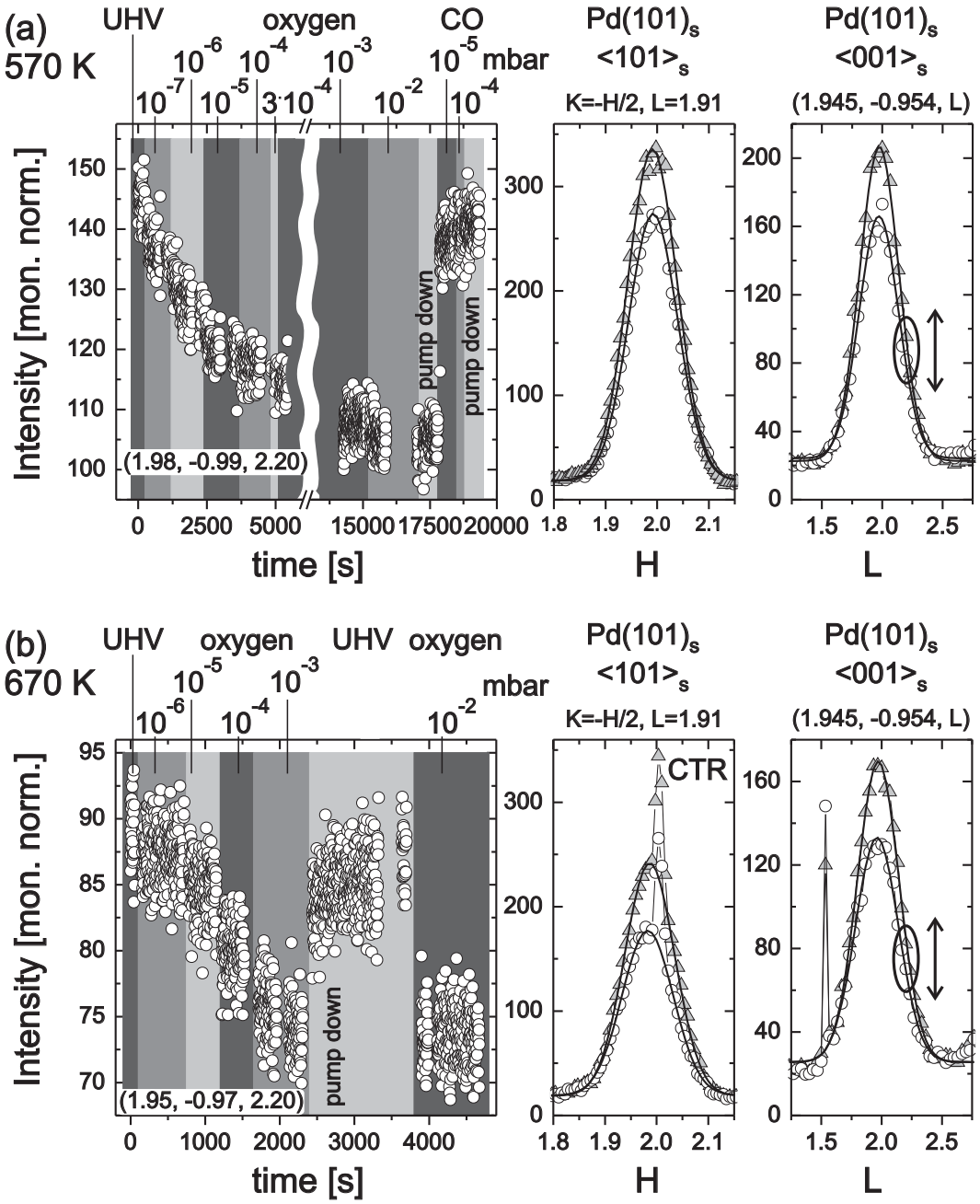

Fig. 8.4: (a) Time dependent scans on the shoulder of the $Pd(101)_S$ reflection at 570 K. The scans through the Bragg reflection were performed under UHV conditions (triangles) and in an oxygen atmosphere of 10^{-2} mbar (circles). (b) Time scans and Bragg characterization at T = 670 K and UHV and 10^{-3} mbar.

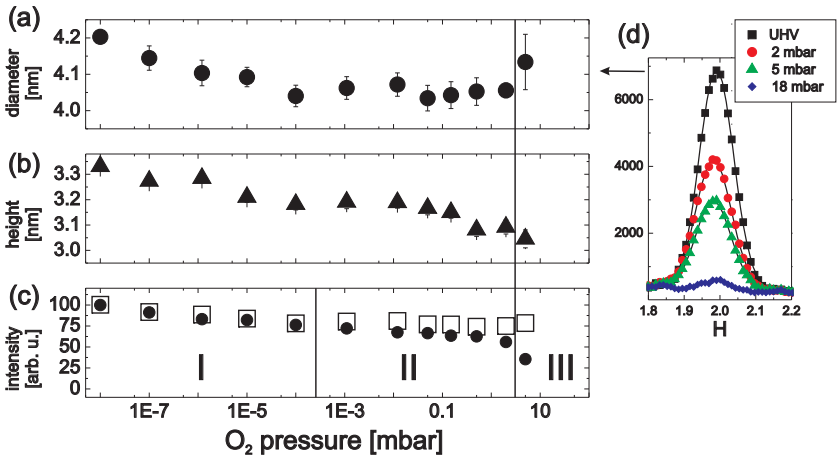

Fig. 8.5: Particle size as a function of oxygen pressure at T = 620 K starting from UHV. The corresponding shape under UHV conditions is given in fig. 8.1. (a) Height $h = 2\pi/\Delta q(001)$, (b) diameter $d = 2\pi/\Delta q(2\bar{1}0)$, (c) circles: maximum intensity, open squares:$\left(d^2 \cdot h\right)^2$ (proportional to the squared number of atoms of an average particle), both normalized to UHV values. Circles and dots match very well in region I, which indicates that the island density does not change in the process of oxygen adsorption. In region II, there is a deviation, possibly because of an oxygen-induced mass transport. In region III, PdO formation is observed. (d) Line scans at (H, K = -H/2, L = 1.97), corresponding to a scan through $(101)_S$ along $\langle 100 \rangle_S$-direction.

8.2.3 PdO Formation

At a sample temperature of 620 K, the oxidation was studied in a pressure range starting from 10^{-7} mbar up to the mbar range. At each oxygen pressure, scans in high symmetry directions through $Pd(101)_S$ were performed in order to obtain the particle size. The values are displayed in fig. 8.5. Up to a pressure of 1 mbar, a systematic decrease of intensity as well as of the particle height and diameter can be observed. The diameter changes from 4.2 nm to about 4.0 nm, the height from 3.3 nm to 3.0 nm. The systematic decrease of the particle size with increasing oxygen pressure corroborates that the change is related to the oxygen exposure and not merely to a statistical error of the FWHM determination. Apart from the maximum intensity (normalized to 100% under UHV conditions), fig. 8.5 (c) also contains the values $\left(d^2 \cdot h\right)^2$ (normalized to 100%) and plotted as open squares. The latter value is proportional to the squared number of atoms within an average particle. Both plots should be identical, as long as the island density does not change and as long as all particles within the size distribution show a uniform behavior of their shrinkage of the fcc core. Indeed, below 10^{-3} mbar (region I in fig. 8.5) both plots show rather good agreement. This gets different between 10^{-3} mbar and 1 mbar (region II). The intensity drops stronger than the squared number of atoms of an average particle. This is an indication that

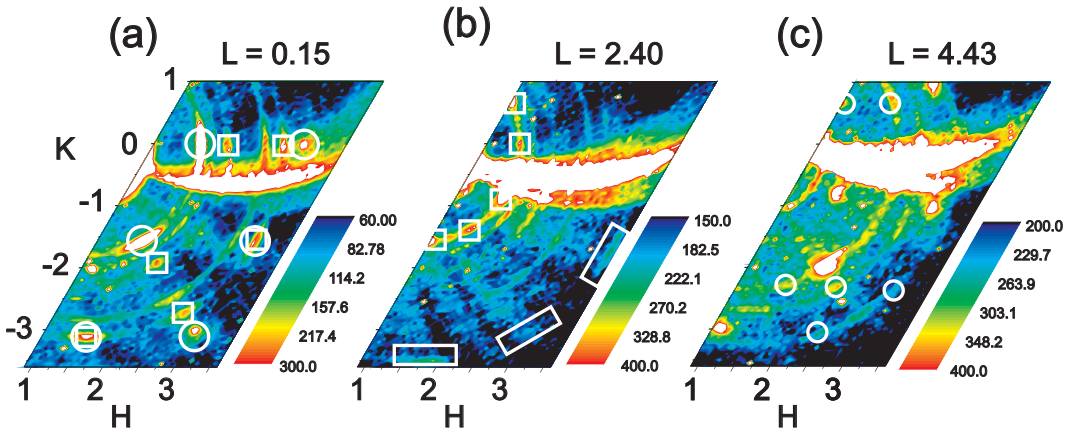

Fig. 8.6: Mesh scans at different L-values. Bragg reflections that can be assigned to (001)-oriented PdO are marked with squares (a) and quadrangles (b), respectively. The reflections of (100)-oriented PdO are marked with circles (a), (c).

the size dispersion function changes, probably because small particles within the size distribution undergo strong structural changes. In region III, at a pressure of 5 mbar, there is a remarkable intensity decrease and the Pd Bragg reflections vanish completely at a pressure of 18 mbar. This is accompanied by the formation of the bulk oxide phase PdO.

The growth of PdO was characterized by reciprocal space maps at different L-values. As can be inferred from figs. 8.6 and 8.7 (a, b), PdO grows in (100) and (001) orientation, each with three domains rotated by 120°. Apart from additional Debye-Scherrer rings of PdO, there exist further reflections at distinct positions that cannot be assigned to a low-index-orientation of PdO with respect to the sapphire surface. The orientations of epitaxial PdO with respect to the sapphire surface unit cell is displayed in the left part of fig. 8.7 (a, b). The right part of the same figure shows the position of reflections at $q_z = 0$. Reflections with filled circles are strong reflections, those marked with white circles are symmetry forbidden or only contribute less than 10% of the Pd(101) reflection according to [53]. For $q_z = \frac{2\pi}{c}$, where one is sensitive to the (001)-oriented PdO, the pattern of allowed and forbidden Bragg reflections is the inverse from the displayed $q_z = 0$ map, and accordingly at $q_z = \frac{2\pi}{a}$ for (100) oriented particles.

The epitaxial orientations can be explained with the good match of atomic rows of PdO with those of the sapphire (0001) surface. The distance of three metal rows along PdO[100] ($d_1 = \frac{3}{2} \cdot 3.03$ Å) fits to the sapphire lattice with a mismatch of 4.5%. For the (100)-oriented particles, the distance of three metal rows along PdO[001] ($d_2 = \frac{3}{2} \cdot 3.03$ Å) is approximately the distance of four aluminum rows $\sqrt{3} \cdot 4.75\mathring{A}$, with a mismatch of 3%.

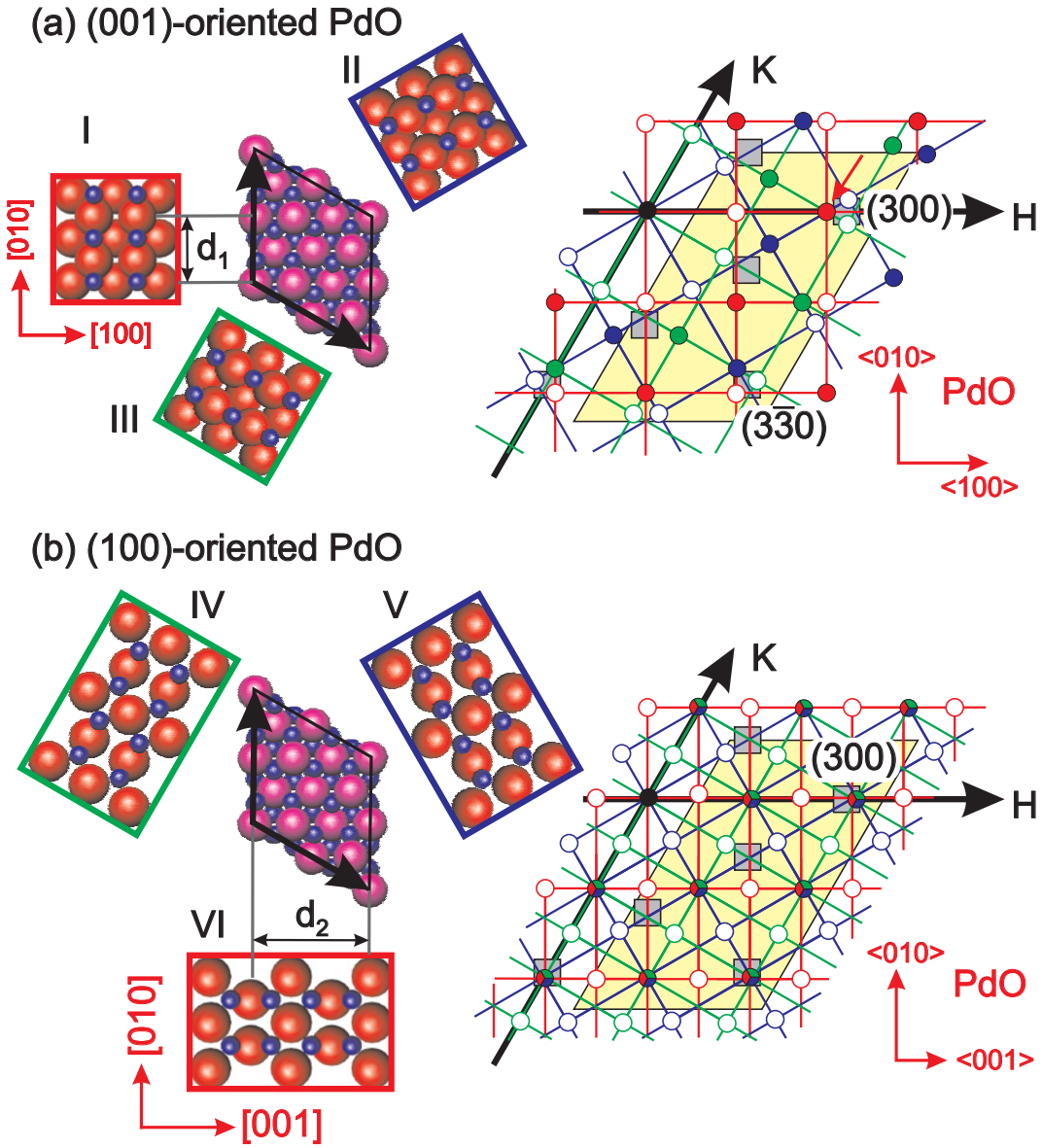

Fig. 8.7: Orientation of the PdO domains with respect to the substrate lattice. For reasons of lucidity, all structures are plotted on an area of 2×2 unit cells. The right figures show the positions of Bragg reflections. Colored circles are strong Bragg reflections, those with a white filling are forbidden/weak reflections. The distance $d_1 = \frac{3}{2} \cdot 3.03$ Å fits to the sapphire lattice constant with a mismatch of 4.5%. For the (100)-oriented particles, the distance $d_2 = \frac{3}{2} \cdot 5.33$ Å is approximately $\sqrt{3} \cdot 4.75$ Å, with a mismatch of 3%.

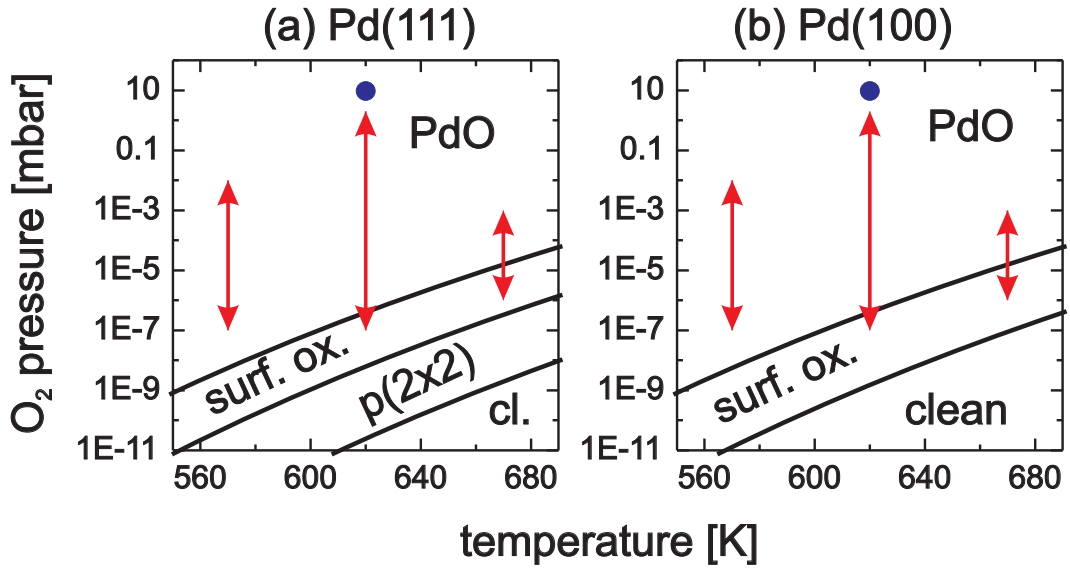

Fig. 8.8: Phase diagram of the interaction of molecular oxygen with Pd(111) (a) and Pd(100) (b). The red arrows indicate the applied pressure range at each temperature where the intensity decrease and peak broadening was observed. The blue dot shows the conditions of PdO formation.

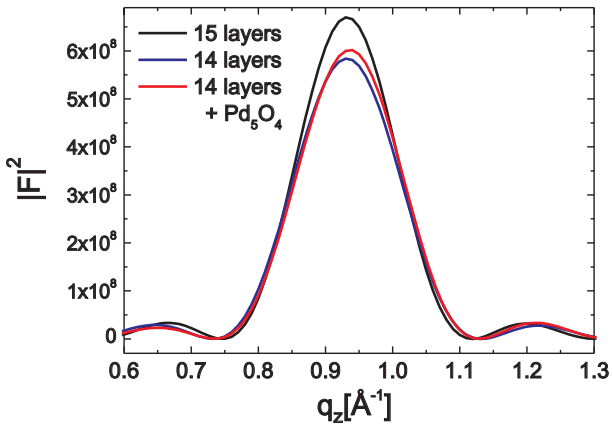

Fig. 8.9: Calculated intensity of a q_z scan through $Pd(101)_{sur}$ for a slab of 15 layers of Pd(111) (black line), 14 layers of Pd (blue line) and 14 layers of Pd, covered with the Pd_5O_4 surface oxide film (for the structure, cf. fig. 2.10). To take into account the registry, an area of 7 replicated Pd_5O_4 unit cells was used with each Pd(111) layer containing 48 Pd atoms in the simulation, according to ref. [56].

8.2.4 Discussion

One key observation is the reversible decrease of the Pd Bragg intensity in the temperature range from 570 K to 670 K and oxygen pressures below 10^{-2} mbar. The original intensity could be retrieved either by pumping down the oxygen and accelerated by applying carbon monoxide. At 570 K and 670 K, only a negligible broadening of the Bragg reflections was observed, possibly because of a slightly miscentered Bragg reflection. At T = 620 K, a systematic decrease of the particle diameter from 4.2 to 4.0 nm was observed, and a height decrease from 3.3 to 3.1 nm, which corresponds to one monolayer. This indicates, that only the outermost atomic layer is displaced from its fcc-position as is to be expected for chemisorbed oxygen or the ultra thin surface oxides. The applied temperature and pressure range can be compared with the phase diagrams for the Pd(111) and Pd(100) single crystal surface (fig. 8.8). The arrows show the lowest and highest applied oxygen pressure for each temperature, where the intensity decrease was observed. Under these conditions, the phase diagram suggests the growth of PdO. The actual PdO growth occurred at a pressure which is about seven orders of magnitude higher than expected from the phase diagram for the transition between the ultra thin surface oxide to the bulk oxide phase, which indicates the presence of a remarkable kinetic barrier. From experimental studies of the Pd single crystal surfaces [29, 56] the formation of surface oxides can be anticipated under the applied conditions and must be seen as the kinetic barrier for the bulk oxide formation. Also for Pd/MgO particles, a kinetic barrier is present and PdO grows at higher chemical potentials than -1.2 eV (cf. ref. [18], chapter 9). For the Pd/α-Al_2O_3(0001) discussed here, there is no direct evidence from the x-ray data for the formation of ordered structures of the limiting top (111) facets. As not even a signal of the Pd top facets was observed, one cannot expect a diffraction signal of a chemisorbed superstructure on the facets. Still, the presence of chemisorbed oxygen on the particles is supported from the oxidation study of Pd/α-Al_2O_3(0001) with particle diameters of 2-10 nm [102]. From the measurements with thermal desorption spectroscopy, low-energy ion scattering and XPS, it was suspected that oxygen is chemisorbed on the particle surface and moves to subsurface positions.

In a recent STM study [100], the oxidation of Pd particles supported by a thin O-Rh-O-Film on Rh(111) was investigated. At T = 380 K and $2.5 \cdot 10^{-5}$ mbar of oxygen, oxidized and metallic Pd(111) surfaces could be distinguished and suggested the growth of a Pd_5O_4 like layer, with the tendency that larger particles (diameter up to $\approx$ 50 nm) get oxidized more easily.

The x-ray study presented here allows the estimation that the outermost atomic layer of small particles with a diameter of 4 nm, the particle is involved in the formation of a kinetic barrier for bulk oxide formation. Fig. 8.9 shows a calculated intensity profile, how the Pd_5O_4 surface oxide would affect the Pd(111) reflection profile. According to a particle height of 3.3 nm that decreases to 3.1

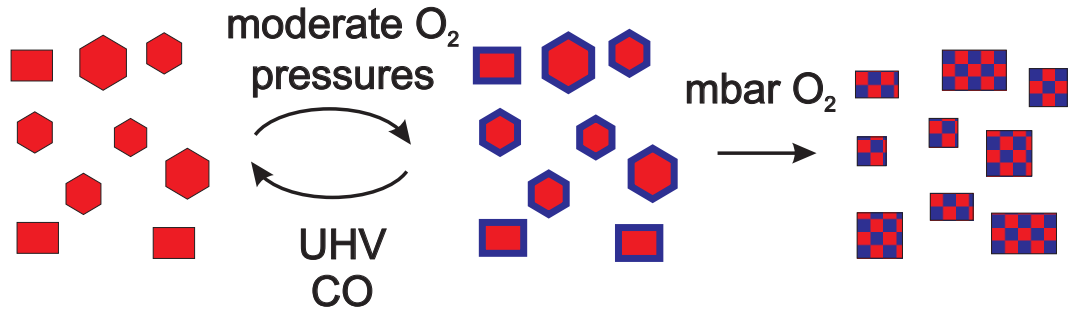

Fig. 8.10: Suggested morphology of the particles: at moderate pressures, O_2 adsorbs on the particle surface and the island density remains unaffected. This adsorption is reversible. The growth of bulk PdO occurs at high pressures in the mbar range.

nm during oxidation, a stack of 15 layers of Pd, 14 layers of Pd and 14 layers of Pd covered with Pd_5O_4 was used for the calculation. It shows that the effect of the surface oxide leads to a slight increase of intensity compared with the uncovered slab. This underlines that the experimentally observed intensity decrease must stem from a shrinking of the fcc core of the particles and not from destructive interference of the Pd_5O_4 diffraction signal with the Pd(111) reflection.

From the retrieval of the original intensity after pumping down the oxygen or applying CO, it can be concluded that the morphology of the islands does not change during oxygen exposure at moderate pressures as sketched in fig. 8.10. This is further supported from the good agreement of the maximum intensities and the values estimated from the particle diameter and height (cf. region I in fig. 8.5 (c)). Thus, the average density of the Pd islands does not change at moderate pressures and the intensity decrease must be assigned to a shrinking of the fcc core. This is an indication of a process taking place on the surface of the particles.

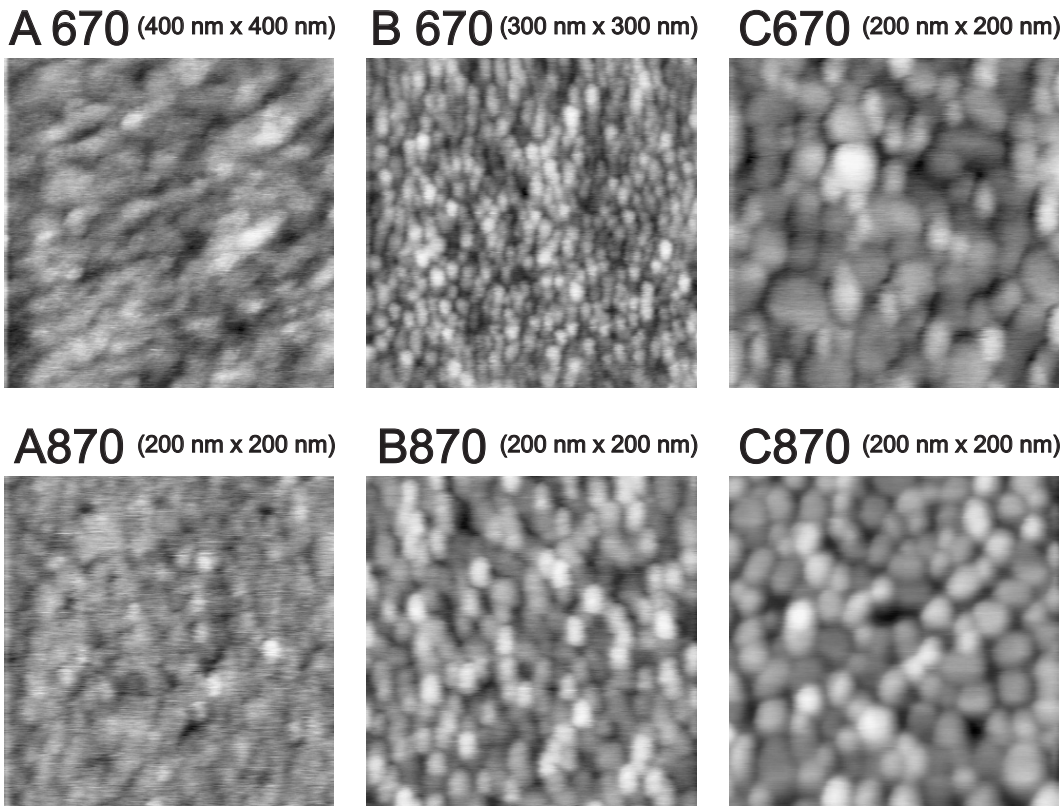

Fig. 8.11: AFM images of the Rh particles deposited on sapphire studied ex situ in contact mode (Courtesy of Dr. D. Garcia de Oteyza Feldermann). From left to right: increasing effective film thickness, growth temperatures 670 K (top) and 870 K (bottom).

8.3 Oxidation of Rh/α-Al_2O_3(0001) Nanoparticles

8.3.1 Growth Prestudies

Samples of Rh on Al_2O_3(0001) with different thicknesses were grown at T=670 and 870 K[4]. They were characterized by x-ray reflectivity at the rotating anode, with synchrotron x-ray diffraction (BW2 at HASYLAB) and AFM. The reflectivity data could be fitted with a simple one-layer model (tab. 8.1). For all samples, the obtained electron density was lower than the value for bulk Rh, this is why it can be assumed island growth, inline with the results observed with AFM (cf. fig. 8.11). However, for the samples with the lowest material deposition (A670 and A870), it is unclear to which extend Rh islands or surface roughness of the

[4]Performed by Dr. G. Richter and M. Pudleiner, Central Scientific Facility *Thin Film Growth*, MPI MF.

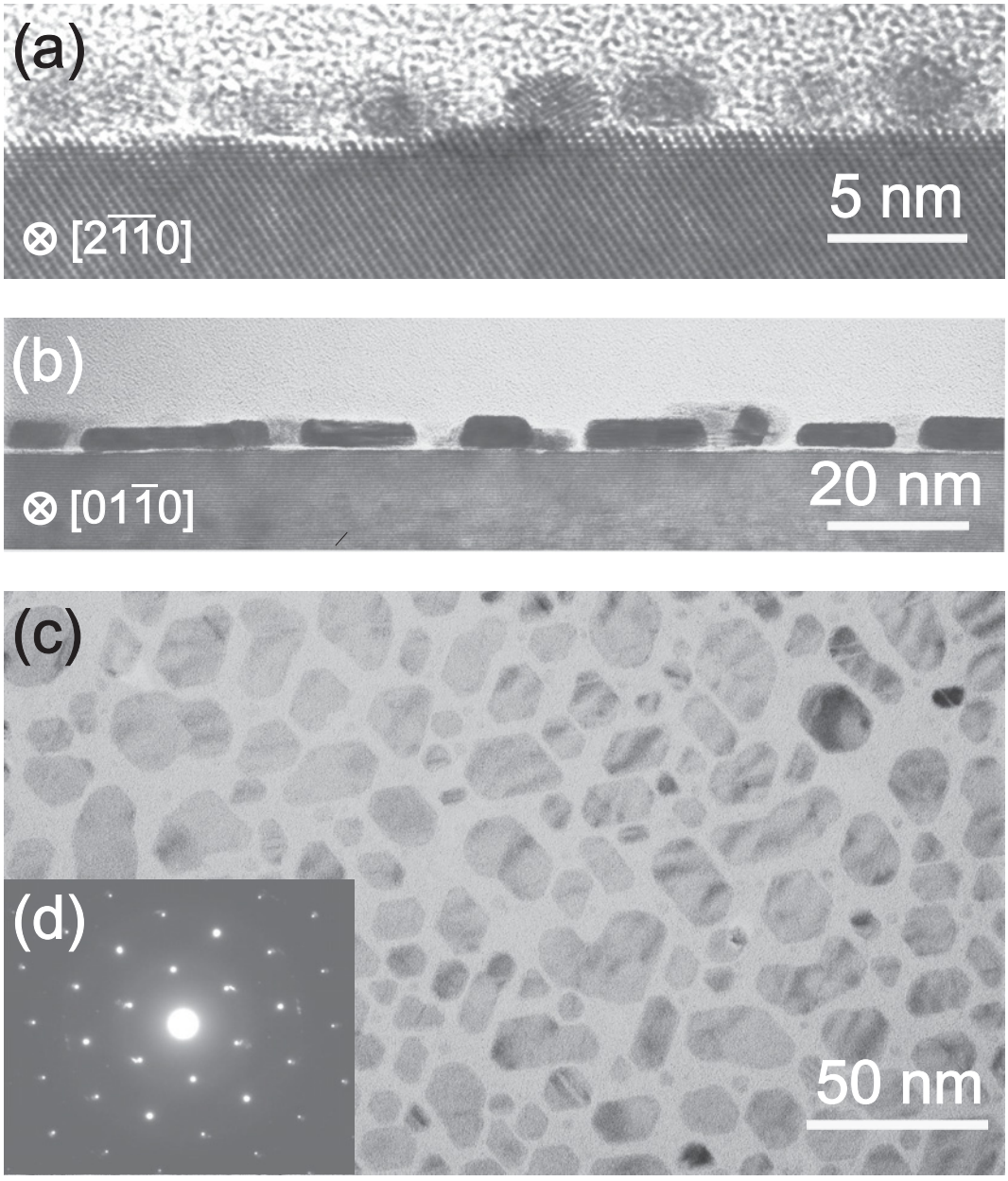

Fig. 8.12: High resolution TEM micrographs of Rh/α-Al_2O_3(0001) samples grown at T_S = 670 K. For sample A670 (a) the particles have a diameter of 3.5 nm and a height of 2 nm. For sample C670 (b, c), the particles have a flat shape and well-defined (111) surfaces on top. The plan view image (c) shows that only a few particles have the ideal shape of truncated regular pyramids but are rather coalesced. (d) Electron diffraction image. (Courtesy of N.Y. Jin-Phillipp, MPI MF.)

sample	h [Å]	δ/δ_{Rh}	σ_{film} [Å]	$\sigma_{subst.}$[Å]
A670	13	17 %	4.7	7.5
B670	29	46 %	8.1	5.7
C670	34	64 %	6.3	1.8
A870	12	21 %	8.6	6.4
B870	12	23 %	5.4	2.2
C870	39	46 %	12	0

Table 8.1: Results from the x-ray reflectivity for the various Rh/α-Al_2O_3(0001) samples and application of the box model as explained in sec. 3.2.

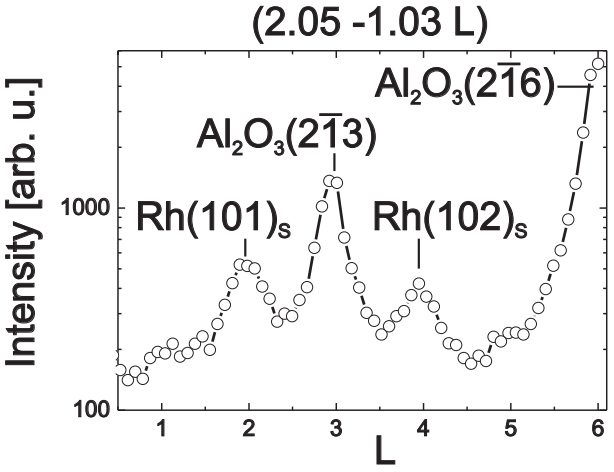

Fig. 8.13: The scan along the $(10L)_S$ reveals the existence of domains with an azimuthal shift of 60°, in the same way as the Pd domains I and II in fig. 8.3 (a) could be concluded from fig. 8.2 (b).

substrate contribute to the AFM signal. In order to obtain detailed information on the particle shape, TEM studies were performed of the samples A670 and C670, with the lowest and highest amount of deposited metal grown at 670 K. The high-resolution images are displayed in fig. 8.12. It can be seen from the cross section images that the aspect ratio (i.e. the ratio of diameter and height) of the smallest particles is around 1-1.5. The large particles have a rather flat shape with large very well-defined (111) facets on top. The plan view image shows that some of the particles have a hexagonal base area, as displayed in fig. 8.1 for the model shape of a (111)-oriented particle terminated by (100) and (111) equivalent facets. Quite a high fraction of the particles has an irregular shape, which indicates coalescence of the islands during metal deposition. The electron diffraction pattern indicates that particles are oriented in (111)-direction, as for domain I and II in fig. 8.3 for Pd on sapphire. Unlike for the Pd particles, there are neither reflections that can be assigned to particles in (110) orientation nor to the 30° domains of particles in (111) epitaxy.

8.3.2 In situ Oxidation

The Rh/α-Al_2O_3(0001) particles used for oxidation studies were grown under in situ conditions in the mobile oxidation chamber under x-ray control. For this purpose, an α-Al_2O_3(0001) crystal was mounted on a sample holder together

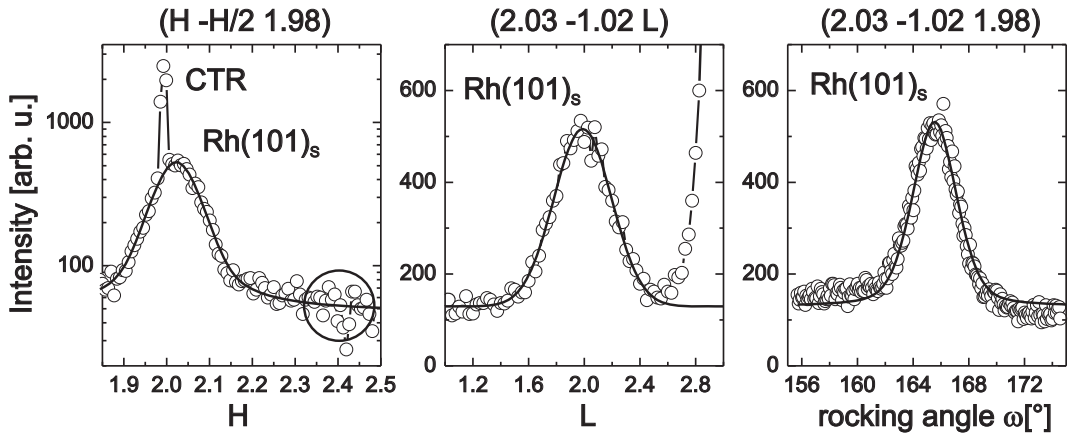

Fig. 8.14: Characterization of the as-grown particles. (a), (b) High symmetry line scans through $Rh(101)_S$. From the line width the size is determined as d = 4.8 nm and h = 2.6 nm. The circle in (a) is the position where a Rh(200) powder ring would occur, as might be expected due to the Rh Debye-Scherrer Rings observed in-plane, cf. fig. 8.15. No signal is present, which shows that the Rh grains are not isotropically distributed. The FWHM of the rocking scan (c) is 3.7°.

with a K-type thermocouple attached on the side of the crystal and was inserted into the mobile oxidation chamber. The electron beam evaporator was finally installed on the mobile chamber. The x-ray diffraction studies were performed at the MPI MF surface diffraction beamline at a photon energy of 10 keV. The setup of the x-ray chamber with the electron beam evaporator is shown in fig. 4.2. Prior to metal deposition, the crystal was heated in an oxygen atmosphere of $5{\cdot}10^{-5}$ mbar at T = 820 K for one hour. Rh was evaporated at a substrate temperature of 670 K and the growth was monitored by x-ray diffraction.

Fig. 8.14 shows scans through $Rh(101)_S$ in high symmetry directions along $\langle 100\rangle_S$ and $\langle 001\rangle$ as well as rocking scans after final deposition[5]. From the line widths of the Bragg reflections, the particle size is obtained as 2.6 nm in height and 4.8 nm in diameter. The FWHM of the rocking scan is 3.7°. As can be seen from the line scan in fig. 8.13, two domains in (111) orientation are present, azimuthally rotated by 60°.

As this particle size is roughly in agreement with those of the small Rh particles displayed in fig. 8.12 (a), it can be assumed that the shape is also similar.

Fig. 8.15 is an in-plane scan and gives rise to a signal of Rh(111) and Rh(200) Debye Scherrer Ring with reflections with distinct maxima at the same positions

[5]As for Pd, there is an overlap of $Rh(110)_S$ with $Al_2O_3(300)$, this is why no radial scan along $\langle 100\rangle_S$ was performed to study the Bragg FWHM. The distance of atomic rows of (111)-oriented Rh $\sqrt{\frac{3}{8}}{\cdot}3.80$ Å fits to the distance of Al rows of sapphire $\frac{1}{2}{\cdot}4.75$ Å with a mismatch of 2.1%.

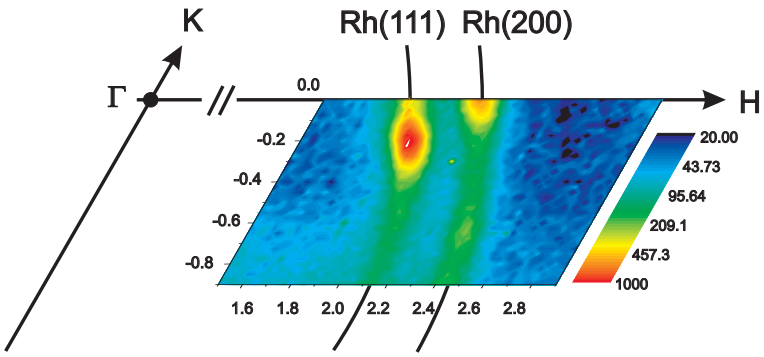

Fig. 8.15: The mesh scan at L = 0.08 reveals (110) oriented epitaxial Rh besides a textured fraction. For real space sketches of the domain orientation, cf. figs. 8.2 and 8.3 (b) for Pd on alumina.

as for (110)-oriented epitaxial Pd particles described in the previous sections for Pd. This is rather surprising, as the electron diffraction patterns for the samples studied with TEM did not show any diffraction peaks of (110)-oriented Rh. This means that the (110) orientation may be caused by differences of the substrate preparation[6]. As in fig. 8.14 (a) no reflection is present at the Rh(200) position, it can be concluded that the Debye Scherrer rings are not caused by isotropically distributed Rh grains, but rather that there are Rh particles with (110) texture.

8.3.3 Bulk Oxide Formation

The bulk oxide formation of the Rh particles was studied at T = 670 K. The evolution of the peak maximum of the Bragg $Rh(101)_S$ reflection for different pressures is displayed in fig. 8.16 (a). The time scan was interrupted consecutively and line scans were recorded in order to monitor the growing oxide. The oxygen dosage was started with a pressure of 10^{-7} mbar, whereby the Rh Bragg intensity remains unchanged. Already at a pressure of 10^{-6} mbar, a slight intensity decrease is observable. In the line scans displayed in fig. 8.16 (c), at a pressure of 10^{-5} mbar, a very slight intensity increase occurs at H = 1.6 and 2.8, which becomes more pronounced at 10^{-4} mbar. These occurring reflections can be assigned to Rh_2O_3 (110) and Rh_2O_3 (300) respectively. When the oxygen pressure was increased to 10^{-3} mbar, the Rh signal of the (111)-oriented Rh particles vanished completely, and so did the particles in (110)-orientation. The oxide growth was characterized by a radial scan through Rh_2O_3 $(2\bar{1}0)$ and a broad rocking scan through this reflection (fig. 8.17). These scans show that the rhodium oxide grows in (0001)-epitaxy on sapphire, mainly with a hexagon-on-hexagon alignment and a smaller fraction with an azimuthal shift of 30°. The Rh_2O_3 (110) reflection in fig. 8.16 (d) can be explained by a Debye-Scherrer ring of polycrystalline Rh_2O_3 growing in concurrence with the epitaxially aligned oxide.

[6]Possibly this is related to carbon contamination, as this substrate had not been subject of ultrasonic cleaning in ultrapure acetone / ethanol which later turned out to be a decisive pretreatment to remove carbon from the surface.

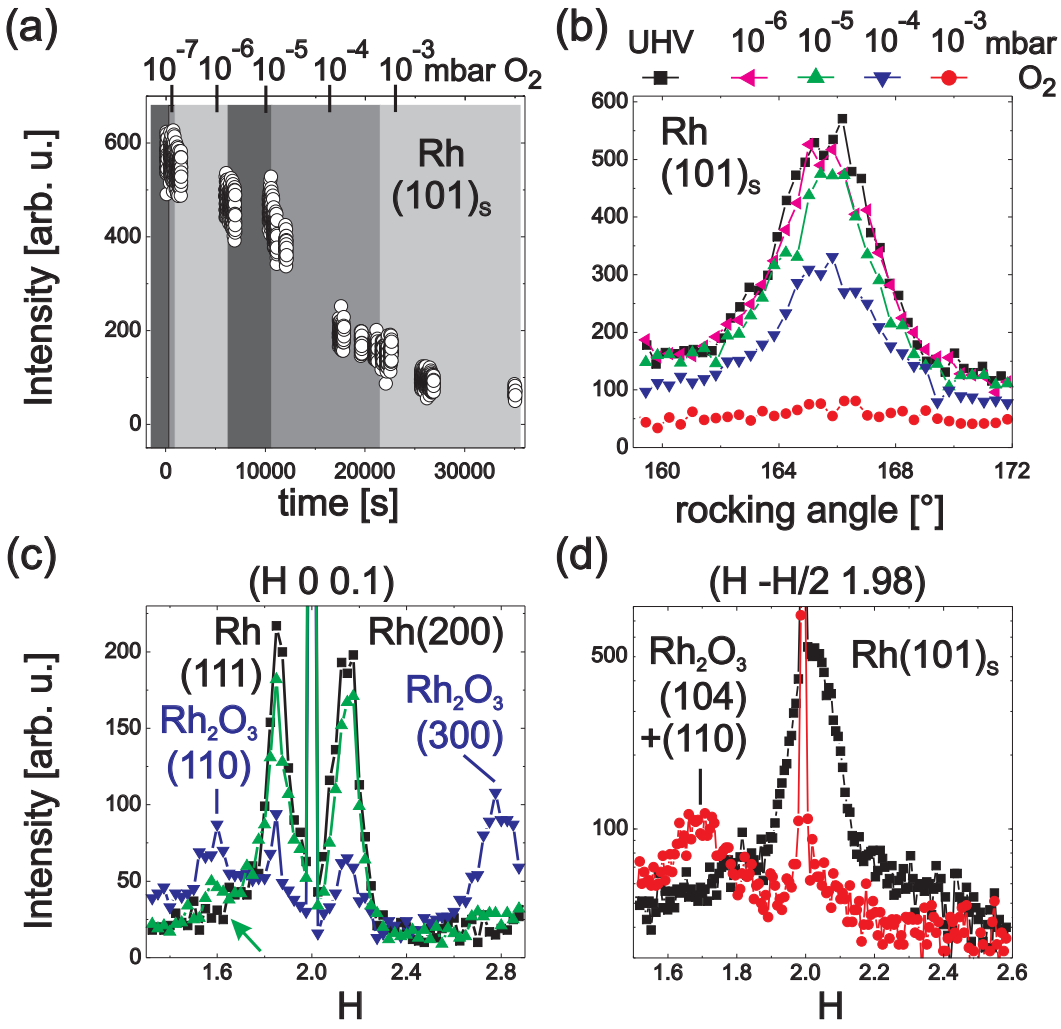

Fig. 8.16: (a) Evolution of the Rh(101)$_S$ Bragg reflection with increasing oxygen pressure at 670 K. (b) The rocking scans show the intensity decrease and the complete vanishing of the reflection. (c) At 10^{-5} mbar, slight reflections of oxygen Rh_2O_3 reflections emerge which become clearly visible at 10^{-4} mbar. The Rh reflections in this scan belong to the (110)-oriented particles. (d) Signal of polycrystalline Rh_2O_3.

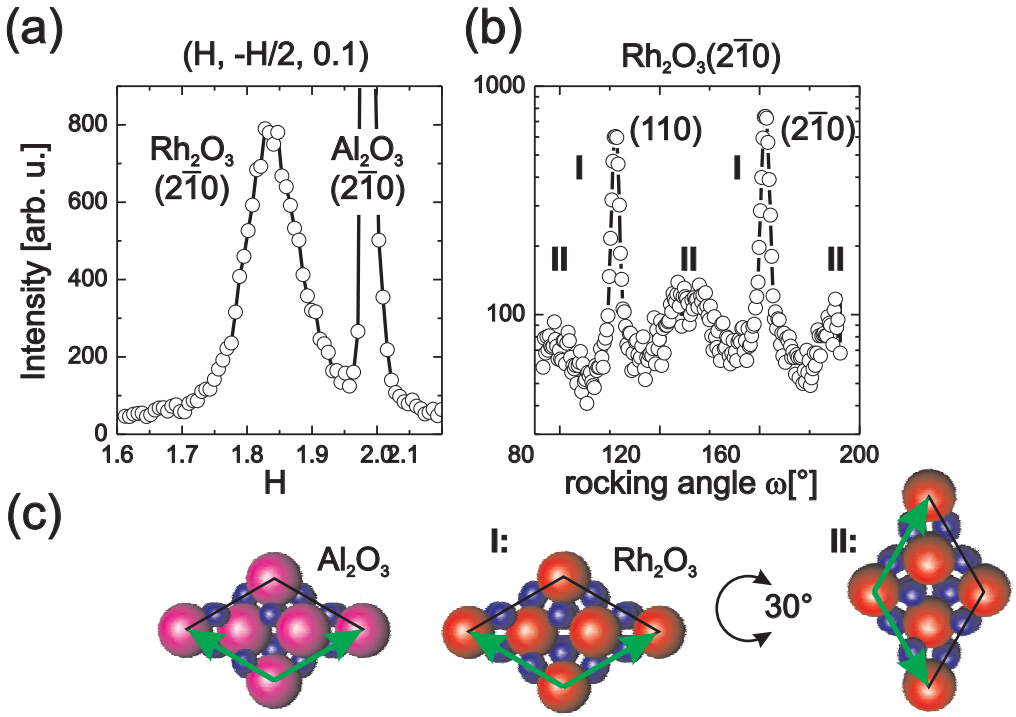

Fig. 8.17: (a) Radial scan and (b) rocking scan through Rh_2O_3 (2$\bar{1}$0). The reflections marked with I can be assigned to (0001)-oriented Rh_2O_3 with an hexagon-on-hexagon epitaxy with α-Al_2O_3, those marked with II belong to domains with an azimuthal shift of 30°.

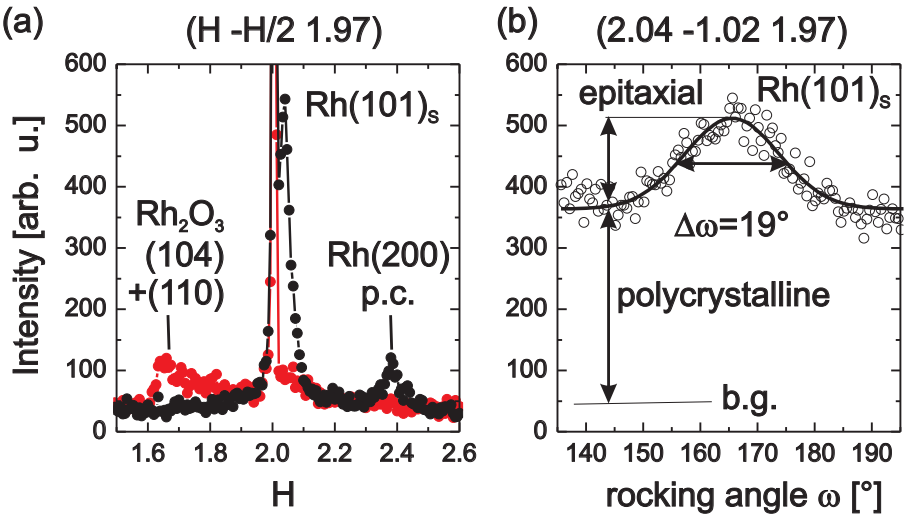

Fig. 8.18: (a) Scans through $Rh(101)_s$. Red dots: completely oxidized Rh, black circles: after reduction with 10^{-5} mbar CO. The Rh(200) reflection and (b) the broad rocking scan show mainly polycrystalline Rh and only poorly ordered epitaxial Rh.

8.3.4 Reduction and Reoxidation of the Particles

If Rh particles are used as catalysts for the CO oxidation, they undergo oxidation and reduction cycles. For this reason, the reduction of Rh_2O_3 with CO and the reoxidation was subsequently studied.

Fig. 8.18 shows selected scans for the completely oxidized sample, and after reduction with 10^{-5} mbar CO. After reduction, the Rh_2O_3 signal vanished completely. A remarkable observation is the occurrence of the Rh(200) Bragg reflection in fig. 8.18 (b), which was not observed for the particles prior to oxidation (fig. 8.14). Before oxidation, the particles were epitaxially (111) oriented or (110)-textured. After CO reduction, polycrystalline Rh is present. Still, a weak epitaxial order of the (111)-oriented particles can be inferred from fig. 8.18 (d), which is an extended rocking scan through the $Rh(101)_S$ reflection with a FWHM of 19°.

The scans displayed in fig. 8.19 were recorded through $Rh(101)_s$ along $\langle 100\rangle_S$ and $\langle 001\rangle_S$. The line widths correspond to a diameter of 8.9 nm and a height of 3.4 nm, which is by a factor of two larger in diameter than the as-grown epitaxial Rh particles. Note, however, that this reflection is now the superposition of a Debye Scherrer ring and of (badly ordered) epitaxial Rh and the scans do not go radially through the Debye Scherrer ring. This means that the actual size of Rh particles may be even larger.

The second oxidation was performed in steps starting from $2{\cdot}10^{-4}$ mbar up to a pressure of 1 mbar at a more elevated temperature of 770 K. The in-plane line scan in fig. 8.20 (b) shows different features from the first oxidation. A new peak appears at (1.64, -0.82, 0.1), which can be identified as $Rh_2O_3(104)$. Thus,

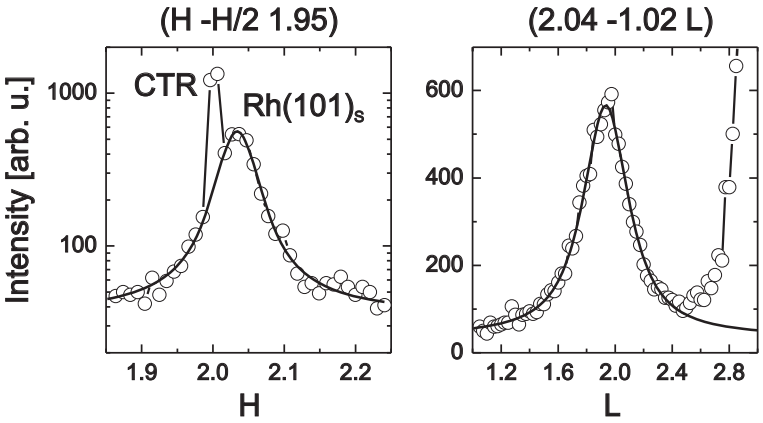

Fig. 8.19: Scans in high symmetry direction through $Rh(101)_S$ after reduction and fits of the FWHM with Pseudo-Voigt functions.

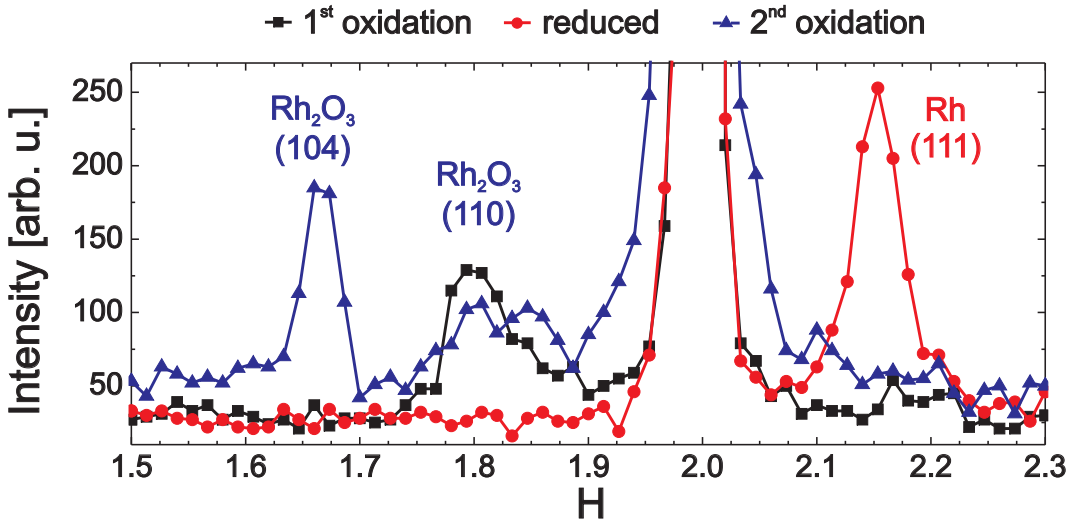

Fig. 8.20: In-plane scan along (H, -H/2, 0.1) to compare the bulk oxide formation of the 1^{st} and the 2^{nd} oxidation.

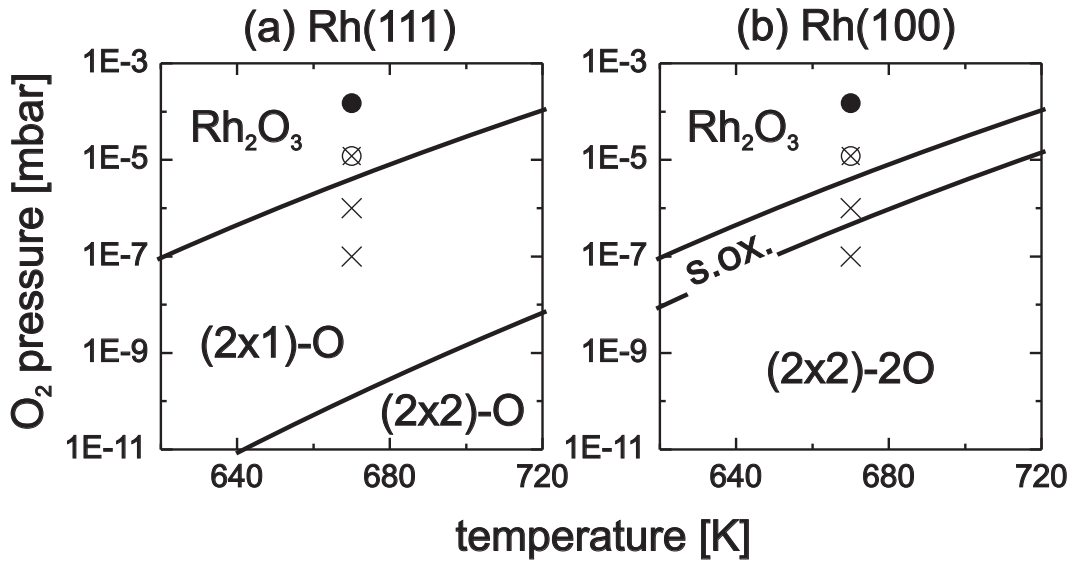

Fig. 8.21: Comparison of the experimental results with the theoretical phase diagram of the Rh(111) and Rh(100) single crystal surfaces. At the crosses, no oxide was detected. At the position of the crossed circle an intensity decrease of $Rh(101)_S$ could be detected and a very slight intensity increase of Rh_2O_3 occurred that became more remarkable at the position of the filled circle.

Rh_2O_3 now grows polycrystalline.

8.3.5 Discussion

Fig. 8.21 shows the theoretical phase diagram for the Rh(111) and Rh(100) single crystal surfaces, together with the experimentally observed formation of the bulk oxide. The starting Rh_2O_3 formation at 10^{-5} mbar at 670 K and its definite proof at 10^{-4} mbar is in good agreement with the phase diagram. This means, that there are no remarkable kinetic barriers towards bulk oxide formation. Note, that for the Rh/MgO particles with a diameter of 9 nm (sec. 5.5), the O-Rh-O trilayer surface oxide was stable at 10^{-3} mbar at the same temperature, and no bulk oxide was observed under these conditions. This is clearly a size effect, which shows that for sufficiently small particles, kinetic barriers can be lowered to the thermodynamic limit.

Fig. 8.22 sketches the island morphology during the oxidation-reduction cycle. The as-grown particles were mainly oriented epitaxially, and after complete oxidation, the oxide was also mainly epitaxial. After reduction, the Rh was rather polycrystalline, and the epitaxial fraction was poorly ordered. Simultaneously, the Rh grain size increased by at least a factor of two in comparison with the as-grown particles. During an oxidation-reduction cycle, a remarkable material transport must occur between the islands.

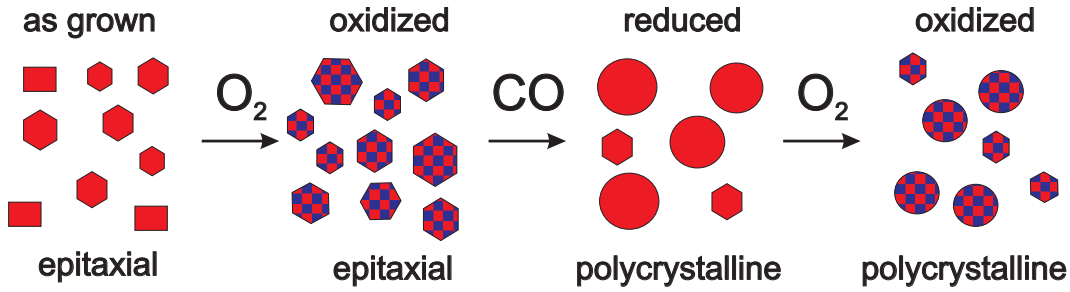

Fig. 8.22: Proposed morphology of the Rh nanoparticles. The as grown particles grow mainly epitaxially, and after the first oxidation, the oxide is predominantly epitaxial as well. After reduction, a remarkable polycrystalline fraction is present, with islands that are significantly larger than for the as-grown particles. The reoxidation leads to polycrystalline oxide.

Epitaxial Rh leads to epitaxial Rh_2O_3 in the first oxidation procedure at 670 K, and polycrystalline Rh_2O_3 results from polycrystalline Rh in the second oxidation step. It can be concluded that the oxide nucleation takes place directly on the metal particles and not on the support, as was discussed for PdO growth of Pd/MgO particles with diameters below and above 9 nm in chapter 7.

8.4 Summary

This chapter shows the results of in situ oxidation studies of Rh and Pd nanoparticles on α-Al_2O_3(0001) supports, with similar particle sizes of 4 nm and 5 nm in diameter and 3 nm in height. Even though the Rh and Pd particles had similar sizes, it could be found large differences with respect to the presence of kinetic barriers for bulk oxide formation.

It was found that the Pd particles on grow epitaxially in (111) and (110) orientation with seven differently oriented domains. The particles were exposed to oxygen at moderate pressures at different temperatures, at 620 K also in the mbar range. An intensity decrease of the Pd Bragg signal was observed in a wide pressure range and temperatures from 570 K to 670 K. It could be shown at 620 K that this is accompanied by a slight shrinking of the fcc core. It can be estimated that the height and diameter of the particle decreases by around one atomic layer. The original intensity can be reverted by pumping down the oxygen and accelerated by applying CO atmospheres. At a temperature of 620 K, a transition to bulk oxide was found at an oxygen pressure of 5 mbar. The formation of surface oxide is an explanation for the slight broadening of the Pd Bragg reflection due to the reduced size of the fcc metal core. A comparison with the calculated phase diagrams for the oxidation of the Pd (111) and (100) single crystal surface shows that under the applied conditions the bulk oxide phases should have formed. PdO actually occurred between 5-18 mbar at 620

K. This is seven orders of magnitude higher than expected from the calculated phase diagrams. This shows that oxygen adsorbs on the surface and acts as a kinetic barrier towards bulk oxide formation. The PdO is epitaxially oriented on sapphire, consisting of three domains in (001) orientation and three domains in (100) orientation.

Alumina-supported Rh particles with a diameter of 5 nm were grown and studied under in situ conditions with x-ray diffraction. Apart from (111)-oriented epitaxial particles (which are favored as inferred from the prestudies), there existed in addition (110)-oriented epitaxial and textured Rh. At T = 670 K and an oxygen pressure of 10^{-5} mbar, the bulk oxide started to form. The Rh_2O_3 forms with a hexagon-on hexagon epitaxy with respect to the support. In addition, there exists a small fraction of oxide islands azimuthally shifted by 30° and polycrystalline Rh. The growth conditions are in good agreement with the theoretical phase diagram. This result shows a difference with the 9 nm Rh/MgO(100) particles (chapter 5.5), where the bulk oxide formation was studied at the same temperature. For those particle, no bulk oxide was observed even at 10^{-3} mbar, but instead the surface oxide phase was present on the facets. This means, for the 5 nm alumina-supported particles, there exists no remarkable kinetic barrier to form the bulk oxide. After reduction of the particles, the Rh islands had an increased diameter and were polycrystalline. The reoxidation lead to polycrystalline Rh_2O_3. Thus, the oxide nucleation takes place directly on the rhodium particles. Furthermore, inter-particle mass transport takes place, which shows that the particle size and shape is not reversible during an oxidation-reduction cycle.

Chapter 9

Deactivation of Pd/MgO(100) Particles during CO Oxidation

The experiments described in the previous chapters were focussed on the oxidation properties of nanoparticles in pure oxygen atmosphere, and the application of CO served to reduce the oxidized particles. The next step to obtain an atomistic understanding of the role of nanoparticles during a technologically relevant chemical reaction is to observe the structural evolution of the particles under reaction conditions.

Previously, the oxidation of CO was studied on well-defined model systems ranging from Pd single crystal surfaces, vicinal surfaces and Pd nanoparticles on ultra thin oxide film supports, both by theory and experimental studies. With STM, it was found that Pd(100) undergoes roughening at 480 K when the CO production rate is high [26, 106]. It was shown with surface x-ray diffraction during CO oxidation of Pd(100) that a thin PdO layer is formed during high catalytic activity [107]. Ab-initio kinetic Monte-Carlo simulations suggest that under reaction conditions an ultra-thin surface oxide layer is thermodynamically favored. In contrast, low pressure molecular beam experiments on Fe_3O_4 thin film supported Pd particles showed that a partial oxidation of the Pd nanoparticles above 500 K leads to a reduced activity of CO oxidation [108, 109].

This chapter deals with Pd/MgO(100) nanoparticles with a diameter of 9 nm during CO oxidation. The structure and composition during oxidation, CO reduction and oxidation in CO/O_2 mixtures was investigated with a combination of in situ x-ray diffraction, ex situ transmission electron microscopy and ex situ spectroscopy techniques. During oxidation with mixtures of 50% CO and 50% CO a new phase is forming with a lattice constant close to the value of the MgO support that can be assigned to carbon incorporation into the Pd nanoparticles leading to an expanded lattice. During the CO oxidation experiments, a deactivation of the system could be observed. The electron microscopy and spectroscopy techniques shows that this can be attributed to the growth of a ≈ 100 nm capping layer that contains C, O and Mg.

These results demonstrate that under high pressure conditions, new reaction pathways may be opened that cannot be anticipated from an extrapolation of the Pd nanoparticle properties under UHV conditions.

9.1 Experimental Details

The preparation of the MgO substrate was performed as explained in section 4.5. Pd was deposited with electron beam evaporation at a substrate temperature of 670 K. After deposition, the sample was transferred out of the preparation chamber. A chromel / alumel K-type thermocouple was mounted with its tip on the edge of the sample in order to allow a control of the substrate temperature in the following oxidation experiments. The sample was subsequently inserted into the mobile high pressure compatible x-ray vacuum chamber that was baked out prior to the x-ray experiments to obtain UHV conditions.

The x-ray experiments were performed at beamline ID 03 at the European Synchrotron Radiation Facility in Grenoble, France[1]. The photon energy was 14 keV, thereby the critical angle of MgO for total external reflection is 0.11° and the critical angle for Pd is 0.19°. The incident angle was set to 0.16-0.17°. All XRD scans in this chapter are given in reciprocal lattice coordinates of bulk Pd in cube-on-cube epitaxy on MgO(100).

The chamber was connected to a gas manifold that was equipped with gas bottles of oxygen and carbon monoxide with high purity. The carbon monoxide was cleaned in a Cu trap at 570 K in order to remove carbonyls. For the application of CO and O_2 mixtures, the x-ray chamber was used as a batch reactor, this means by disconnecting the vessel from the vacuum pumps and filling it with the reactants.

Due to the fact that the sample was exposed to air during transfer from the preparation chamber into the x-ray oxidation chamber, an annealing program under x-ray control was applied. Thereby, several cycles of O_2 exposure at T = 570 K and subsequent annealing at T = 920 K were performed. Finally, the sample was exposed to $3{\cdot}10^{-5}$ mbar of pure CO and annealed to 920 K.

After the x-ray experiment, XPS, AES sputter depth profiling, TEM and EELS/EDX were performed.

The chemical composition of the sample surface was investigated by XPS using a Thermo VG Thetaprobe system. A description of the instrument is given in reference [110]. Monochromatic Al K_α radiation was used (E = 1486 eV). The x-ray spot on the sample had a size of 400 μm. A broad spectrum was recorded in steps of 0.2 eV at a constant pass energy of 200 eV. Detailed spectra of C 1s, Mg 1s, Pd 3d and the overlapping O 1s and Pd 3p cores were measured in steps of 0.01 eV at a constant pass energy of 25 eV. The sample was irradiated with

[1]The beamline is described in sec. 4.3.2.

a diffuse beam of low-energy electrons (E = 0.5 eV) combined with low energy Ar^+-ions that were generated in a combined flood gun (Thermo Electron Type 822-06) filled with $5{\cdot}10^{-4}$ mbar, in order to achieve charge neutralization of the insulating sample. The analysis of the spectra was performed by the subtraction of a Shirley-type inelastic background and fitting of the resulting spectrum with mixed Gaussian-Lorentzian peak components under the constraint that similar components in the resulting spectra had the same Gaussian-Lorentzian Fraction and FWHMs.

Depth-resolved information about the distribution of C, Pd, O and Mg was obtained with sputter-depth profiling using Auger electron spectroscopy [111]. A JEOL Jamp 7830F scanning Auger microscope was used with a beam voltage of 3 keV and a spot diameter $\approx$ 20 nm while sputtering with 1 keV ions at an incident angle of 55° with respect to the sample normal. The sputtered area had a size of 300×300 μm^2, the analyzed area had a size of 10×10 μm^2. The sample was covered by a mask with a circular hole with a diameter of 3 mm, in order to protect the rest of the sample from possible sputter defects. An approximate sputter depth was obtained from the sputter time and adopting the known sputter rate of a Ta_2O_5 reference sample. The quantification was obtained by weighting the peak heights from the differentiated spectra with the instrumental elemental sensitivity factors provided by the manufacturer. The C-contribution was obtained in a two-step procedure due to the overlap of the C-KLL and Pd-MNN spectral lines in the vicinity of 272 eV. A reference spectrum of pure Pd was fitted to the measured Pd-MNN spectral line in the energy range of 300-350 eV by adopting a scaling factor and allowing slight energy shifts. In the next step, the scaled Pd contribution of C-KLL in the vicinity of 272 eV was subtracted from the measured C-KLL spectrum. The difference signal was assigned the C-KLL-line.

Finally, two cross-section TEM specimens were prepared from part of the sample. The specimen manufacturing and TEM analysis was performed at the StEM at the MPI MF. The specimens were sliced, grounded, polished and thinned by Ar-ion milling. For one of the specimens, epoxy was used. Images were recorded with a JEOL JEM 4000 FX and a JEOL JEM 2000 FX transmission electron microscope. Analytical TEM was performed with a VG HB501UX scanning transmission electron microscope that was equipped with an energy-dispersive x-ray spectrometer (EDX) and an electron energy-loss spectrometer (EELS). An accelerating voltage of 100 keV was applied and the beam diameter (FWHM) was 0.7 nm.

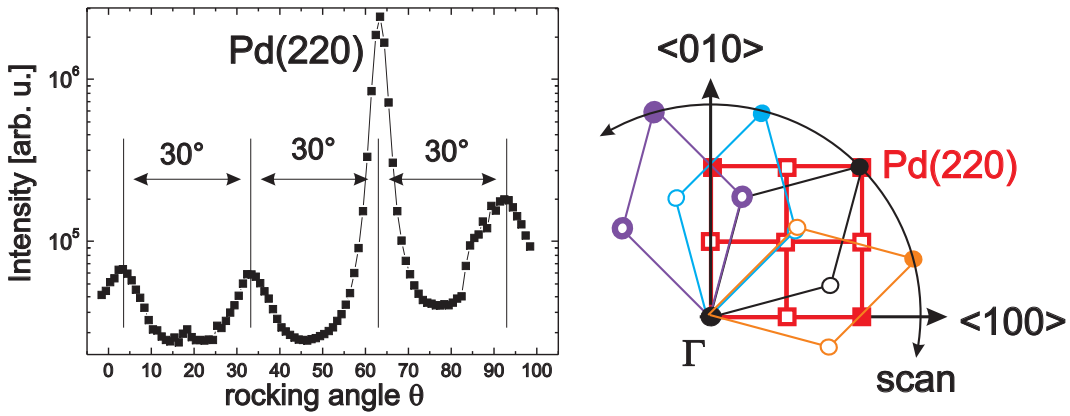

Fig. 9.1: Rocking-scan through Pd(220) in-plane Bragg reflection. The reflections can be assigned to epitaxial (001) oriented particles and epitaxial (111) oriented particles.

9.2 In situ Oxidation Study with Synchrotron X-ray Diffraction

As was explained in the previous chapters, Pd grows with cube-on-cube epitaxy on MgO(100). Such epitaxial growth can be inferred from a rocking scan through the in-plane Pd(220) Bragg reflection, which is shown in fig. 9.1. In addition to the reflection that is associated with particles in cube-on-cube epitaxy, additional reflections exist at azimuthal shifts of multiples of 30°. These can be assigned to parasitic (111)-oriented epitaxial particles as mentioned in sec. 7.3. As concluded from the FWHM of the Bragg reflections, the size of the particles in cube-on-cube epitaxy is 9 nm in diameter and 6 nm in height.

The evolution of the sample structure in the different gaseous environments was monitored by different reciprocal space scans. Structural changes of the epitaxial Pd particles were recorded with radial scans through the Pd and MgO Bragg reflections. As has been known from ref. [18] and was described in chapter 7, epitaxially oriented PdO on MgO(100) grows with five different domains. Two of the domains have their c-axis in the surface plane and the a-axis perpendicular to the surface, as is sketched in fig. 9.2 (a). To follow the formation of PdO, extended rocking scans were performed at fixed momentum transfer at the PdO(103)/PdO(020) Bragg reflection, $q_{\|} = 4.09$ Å^{-1} and $q_z = 0.042$ Å^{-1}. As is displayed in fig. 9.2 (b), there is an overlap of the PdO(020) reflection with MgO(220) from the oxide domain marked green in fig. 9.2 (a). At an azimuthal shift of 30° and 60°, PdO reflections can be observed. The reflection shifted by 60° is the $(01\bar{3})$-peak from the same PdO-domain. The reflection shifted by 30° can be assigned to the PdO(013) reflection of the PdO domain rotated by 90° and marked blue in fig. 9.2 (a).

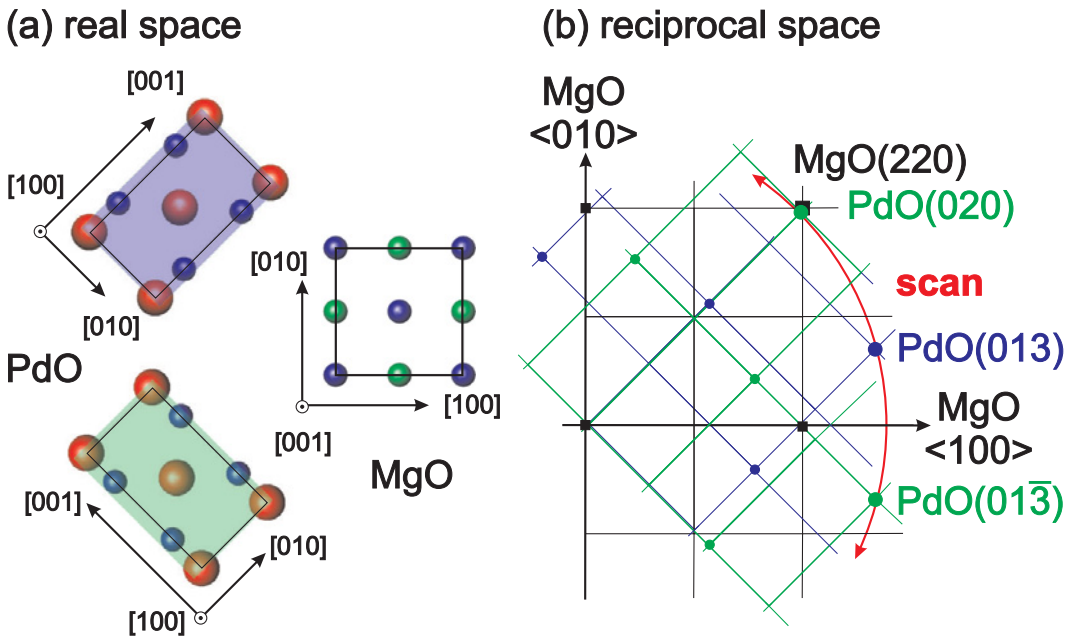

Fig. 9.2: (a) The orientations of both (100)-oriented epitaxial PdO domains are drawn with respect to MgO(001). (b) The green and the blue grids are the reciprocal lattices of both oxide domains in the frame of the MgO reciprocal lattice. The red curve shows the position of the rocking scan in fig. 9.3. The filled dots mark strong reflections of PdO.

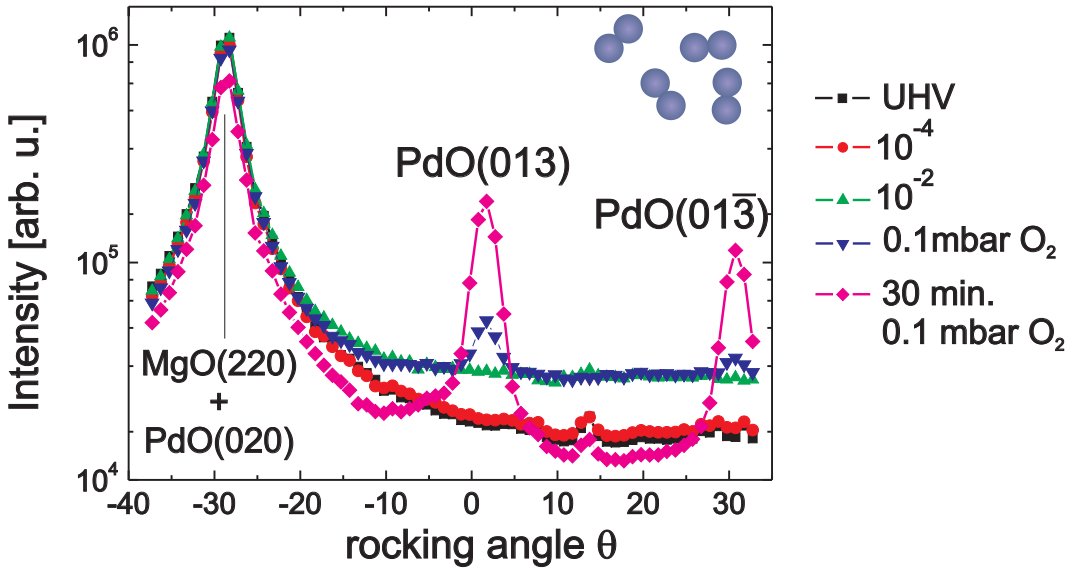

Fig. 9.3: Pressure dependent signal of epitaxially grown PdO-islands in (100)-orientation forming in a pure oxygen atmosphere.

9.2.1 Oxidation in a Pure Oxygen Atmosphere

Before the sample was exposed to mixtures of carbon monoxide and oxygen, it was first checked the susceptibility of the particles towards pure oxygen at a temperature of 570 K.

Oxygen was dosed stepwise starting with a pressure of 10^{-6} mbar. Up to a pressure of $1.5{\cdot}10^{-2}$ mbar, no signal of epitaxial PdO was obtained. When a pressure of 0.1 mbar was applied, epitaxial PdO started to form. After 30 minutes of oxygen exposure at the same pressure, a strong increase of the PdO signal was recorded. Besides the monitoring of PdO formation, Bragg reflections of the Pd particles with cube-on-cube epitaxy were scanned during oxygen exposure.

9.2.2 Exposure to CO/O_2 Mixtures

The oxide was reduced by a 10 minutes exposure to 48 mbar of carbon monoxide, without changing the sample temperature. This lead to a removal of the oxide reflections (green dots in fig. 9.4). In the following step, the sample was exposed to a mixture of carbon monoxide and oxygen. Thereby, 50 mbar of carbon monoxide were first ingested, subsequently oxygen was added until a total pressure of 100 mbar was reached. The total pressure decreased to a value of 84 mbar, indicating the conversion of carbon monoxide to carbon dioxide. Note, that the total pressure is higher than the expected 75 mbar for a complete conversion of a 100 mbar 1:1 mixture of carbon and oxygen, as during the inlet of the oxygen, already a conversion into CO_2 took place. This reaction is accompanied by the formation

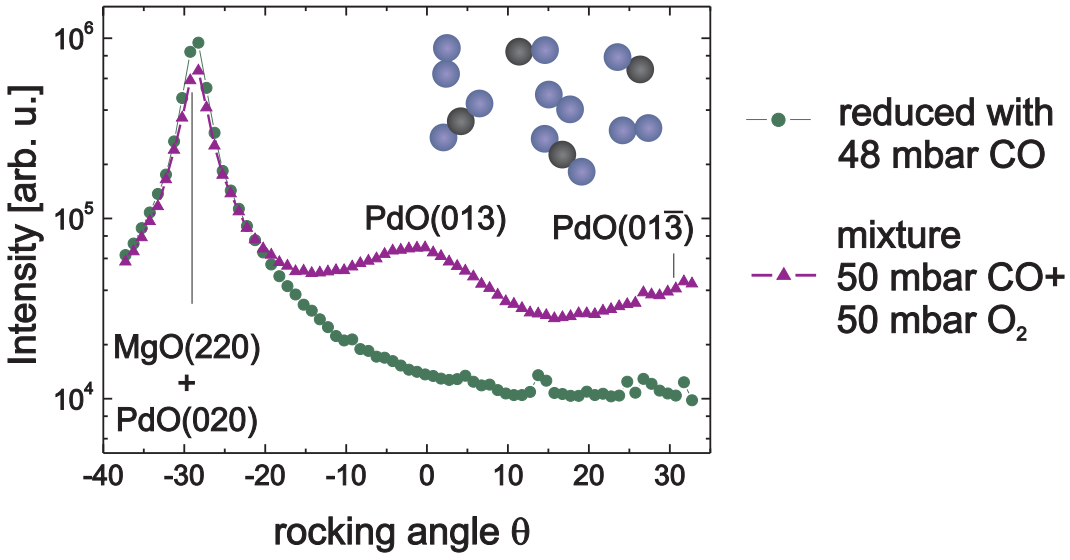

Fig. 9.4: In the 1:1 mixture of 50 mbar CO and 50 mbar of O_2 the PdO islands are poorly ordered.

of PdO, which is displayed in fig. 9.4. The rocking profile of PdO(020)/PdO(013) shows a much broader azimuthal distribution than in the previous oxidation with pure oxygen. In three further steps, the O_2 partial pressure was increased stepwise until a total pressure of 330 mbar was reached. Afterwards, the gas mixture was pumped down, and to decompose the PdO, the sample was annealed at 940 K for 10 minutes.

An interesting feature can be observed in the radial line scan through (2 0 0.026) after the subsequent cooling of the sample back to 570 K (black squares in figure 9.5 (a). In the region of the MgO(200) reflection, a broad shoulder is observed which has a higher intensity than the Pd(200) reflection. A first obvious explanation may be given that either MgO crystallites may have formed, or that Pd may have arranged commensurately on the substrate, or that another phase with a coincident lattice constant may have formed. In order to find out how the formation of this peak is related with the previous sample preparation, the exposure to pure oxygen, pure carbon monoxide and a mixture of CO/O_2 was repeated. The oxidation with pure oxygen leads basically to the same results as the very first oxygen exposure: Up to a pressure of 10^{-2} mbar, no PdO is observed, but at a pressure of 0.1 mbar, the epitaxial PdO starts to form (figure 9.5 a). Simultaneously, the intensity of the Pd(200) reflection decreases remarkably, also in agreement with the previous oxidation in pure oxygen atmosphere. The intensity of the shoulder around MgO(200) changes only slightly during this oxygen exposure.

Subsequently, a pure atmosphere of carbon monoxide was applied (fig. 9.4). At 10^{-2} mbar, the PdO signal vanished completely, simultaneously, the Pd(200)

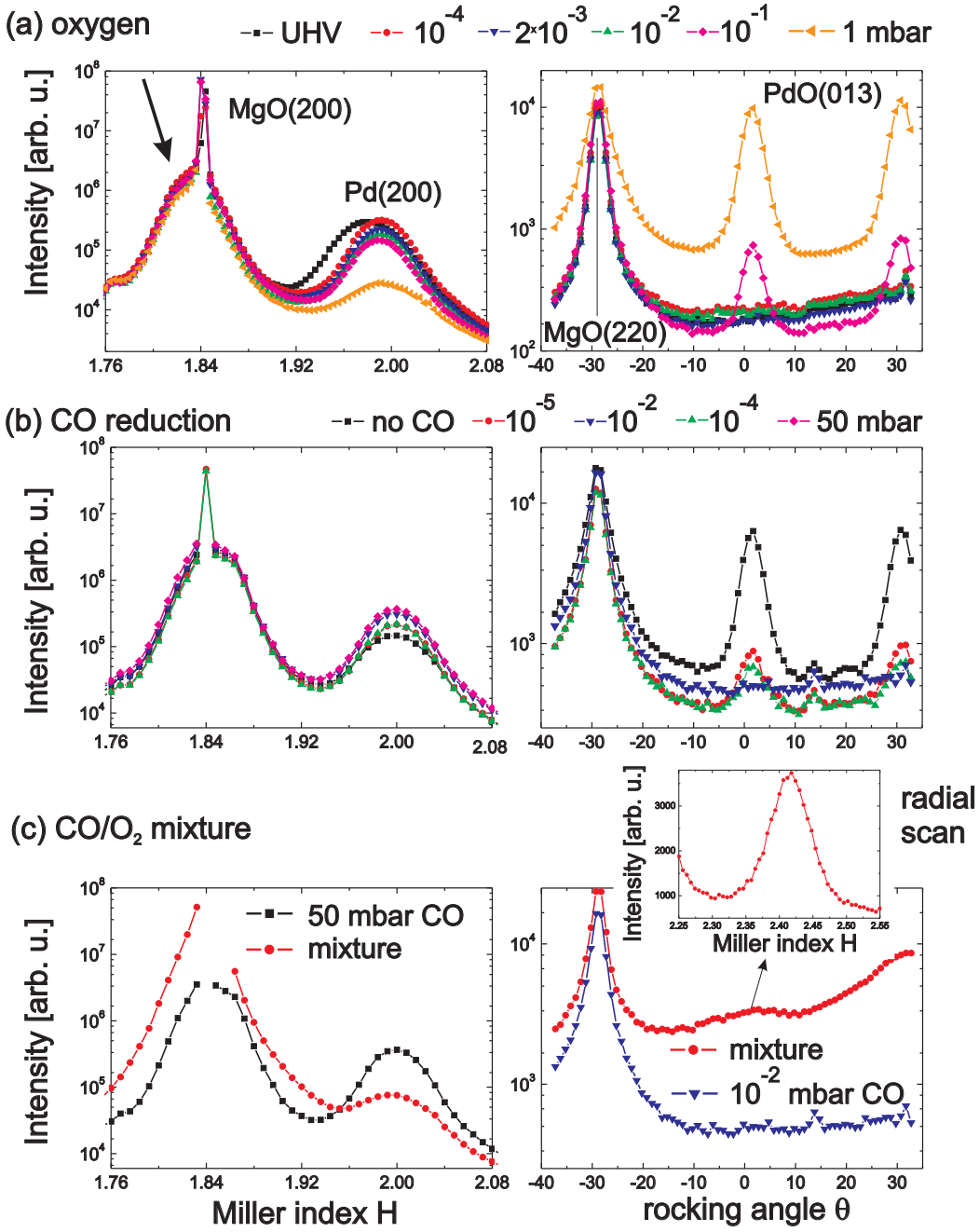

Fig. 9.5: A broad shoulder was found in the vicinity of the MgO(200) reflection (a). It is only weakly affected by exposure to oxygen and shows no susceptibility towards a CO atmosphere (b). Applying a CO/O_2-mixture lead to a significant signal increase and the formation of poorly ordered PdO (c). The inset is a radial scan through PdO(013).

signal increased. However, the signal of the MgO(200) shoulder remains unaffected during this CO treatment, even at a pressure of 50 mbar.

The black line in fig. 9.5 (c) shows the intensity after the last CO reduction at 50 mbar, the blue line is the PdO reference scan that was obtained after CO exposure at 10^{-2} mbar, which both serve as reference scans of the reduced sample. Starting from vacuum, 50 mbar of CO was ingested and oxygen was added until a total pressure of 100 mbar was reached. Again, the intensity of Pd dropped, whereas the intensity of the MgO(200) shoulder increased remarkably.[2] Again the formation of PdO was observed, with the broad azimuthal orientation as it was the case for the first exposure of the sample to the 100 mar CO/O_2 mixture. To demonstrate the intensity distribution in the rocking scan is not merely caused by an increased background, a radial scan through the PdO(013) peak is plotted in the inset of fig. 9.5 (c). From its line width a PdO particle size of 3 nm is estimated.

One further cycle consisting of CO reduction and oxidation with a 100 mbar 1:1 mixture of CO and O_2 was performed. Thereby, the conversion from CO and O_2 into CO_2 was measured with a quadrupole mass analyzer that was connected to the chamber via a leak valve. Further scans showed that the new phase is epitaxial, has a lattice parameter close to MgO and a fcc-structure. To obtain more insight into the reactivity and structure of the new phase, the sample was annealed at 940 K for 10 minutes and finally oxidized at 700 K and an oxygen pressure of 500 mbar. Within the annealing process the PdO was decomposed, but the new phase survived the heat treatment (fig. 9.6). The final oxidation lead to a complete conversion of the Pd particles into PdO, while the new phase also persisted these oxidation conditions.

9.3 Ex situ Characterization of Chemical Composition and Structure

After this final oxidation, different parts of the sample were studied ex situ with a combination of TEM imaging and different spectroscopy techniques, in order to obtain detailed information about the chemical composition and morphology of the sample surface.

9.3.1 TEM Analysis

Cross-sectional TEM specimens were prepared for imaging and analytical studies with TEM. Figures 9.7 (a, b) display different regions of the sample. Fig. 9.7 (a)

[2] In the experimental setup, the detector was protected with attenuation foils in the beam that were automatically set if the intensity was sufficiently high. Sometimes, this automatic setting was too slow and the detector was saturated, as in this case for the MgO(200) reflection.

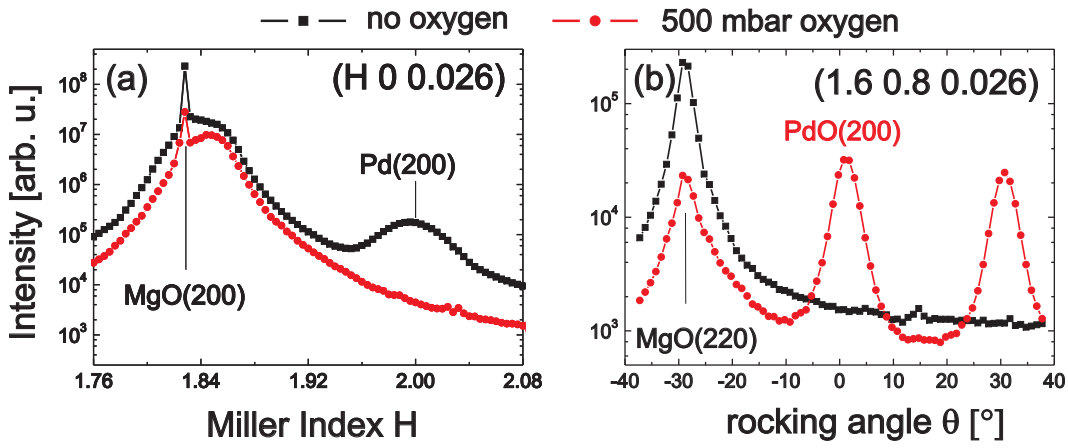

Fig. 9.6: (a), (b) After annealing at 940 K, no PdO signal is left (black squares). The final oxidation at 500 mbar (red dots) and T = 770 K leads to a complete vanishing of the Pd Bragg signal and the formation of PdO. The new phase (reflection in the vicinity of MgO(200))persists both the harsh treatments of annealing and the oxidation.

shows uncovered oxidized Pd particles on the MgO substrate. From additional TEM images recorded on varying positions of the specimen, there are also areas which are covered by a ≈ 100 nm thick layer (fig. 9.7 b). Between this layer and the MgO support, nanoparticles are visible. Both images show a disturbed zone of the MgO substrate in its topmost ≈ 15 nm. It consists of small crystallites with diameters of 1-10 nm and heights of 1-2 nm. The electron diffraction pattern from the sample, including covering layer, nanoparticles and MgO substrate is shown in fig. 9.8. It shows diffraction spots arising from MgO in the (010) azimuth and powder rings that also correspond to lattice spacing close to the MgO values. The diffraction pattern from the overlayer region shows powder rings only. No distinct diffraction signal of metallic Pd or PdO is detected. This shows that the particles at the interface must have lattice spacings close to those of the MgO substrate.

The inhomogeneity of the surface, either being covered with the ≈ 100 nm thick layer or consisting of uncovered parts is confirmed by scanning electron microscopy (fig. 9.9) which shows a groove-like pattern.

9.3.2 EELS and EDX Analysis

Electron energy loss spectroscopy (EELS) and energy dispersive x-ray spectroscopy (EDX) were performed to profile the elemental composition on a region of the specimen covered by the layer. Fig. 9.10 (c) shows a high-angle annular dark field (HAADF) STEM image of the investigated sample regions. A strong material contrast is observed for the nanoparticles. Four regions of the sample, namely the MgO bulk (I), the disturbed zone (II), the nanoparticles (III) and the

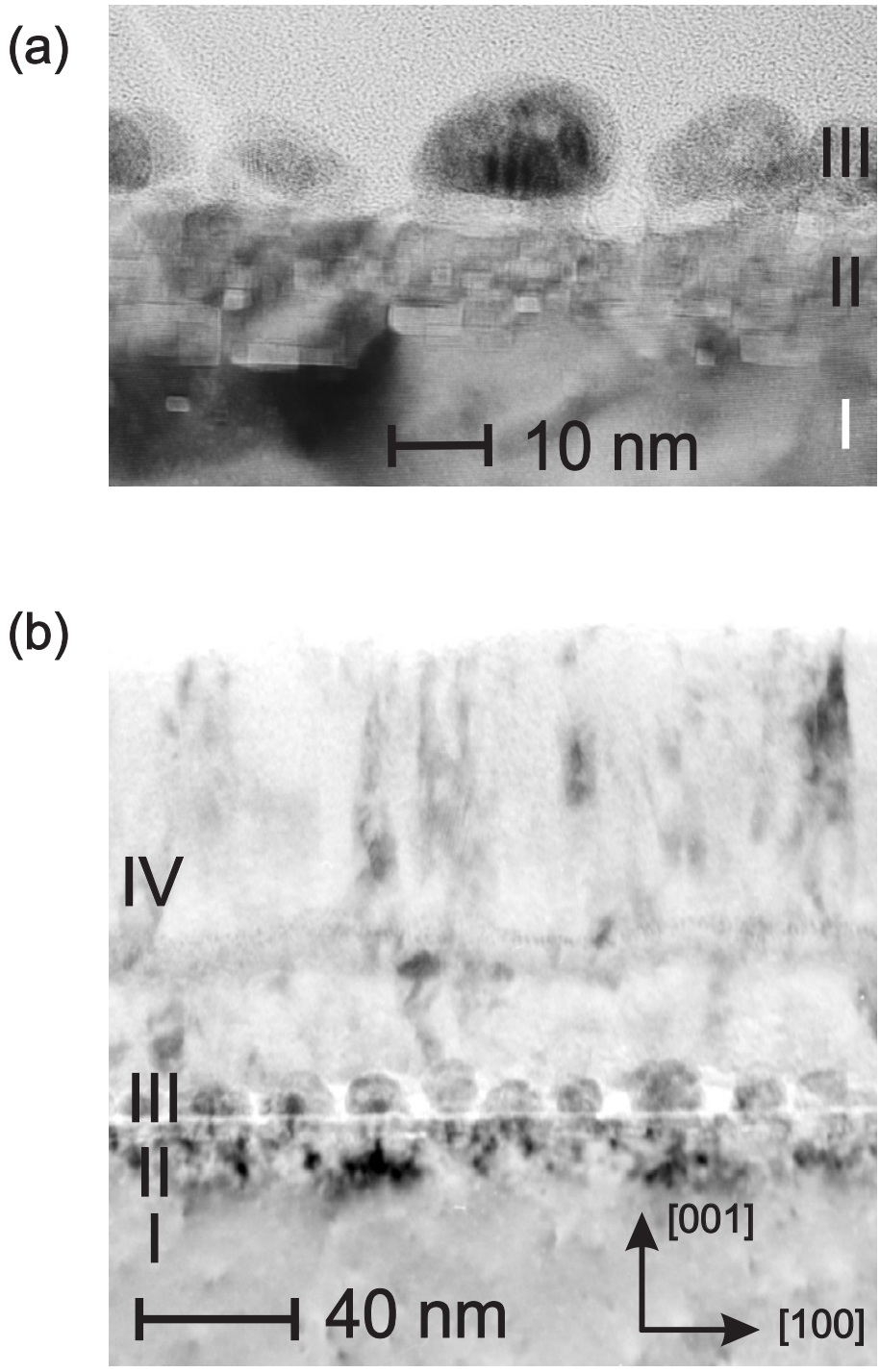

Fig. 9.7: Bright field images of cross-sectional TEM specimens without (a) and with (b) the capping layer. The regions I-IV mark the MgO substrate, the disturbed substrate zone close to the interface, the nanoparticles and the capping layer. (Courtesy of P. Kopold, MPI MF.)

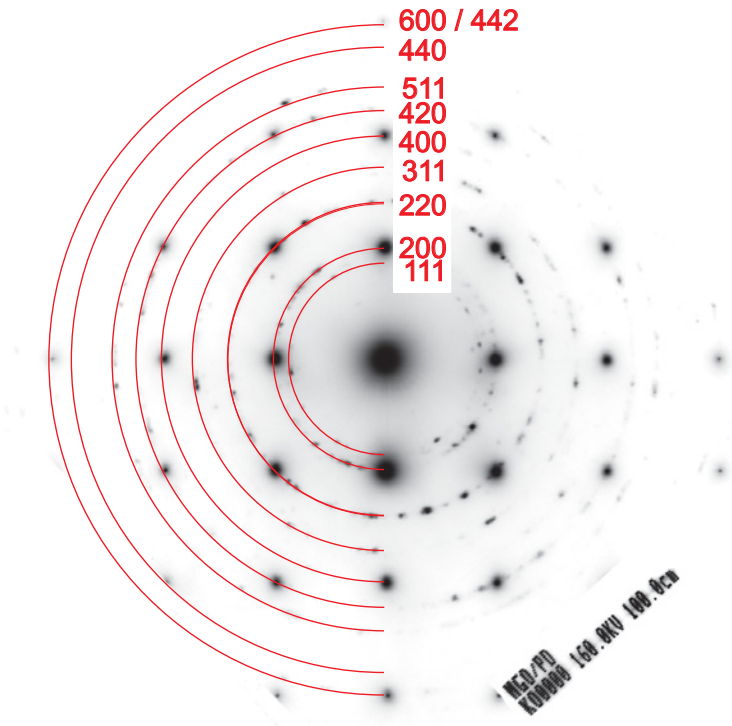

Fig. 9.8: Transmission electron diffraction pattern of the cross-section sample shown in fig. 9.7 (b). (Courtesy of P. Kopold, MPI MF.) The drawn semi-circles on the left correspond to the lattice spacings of MgO and match well with the observed diffraction pattern.

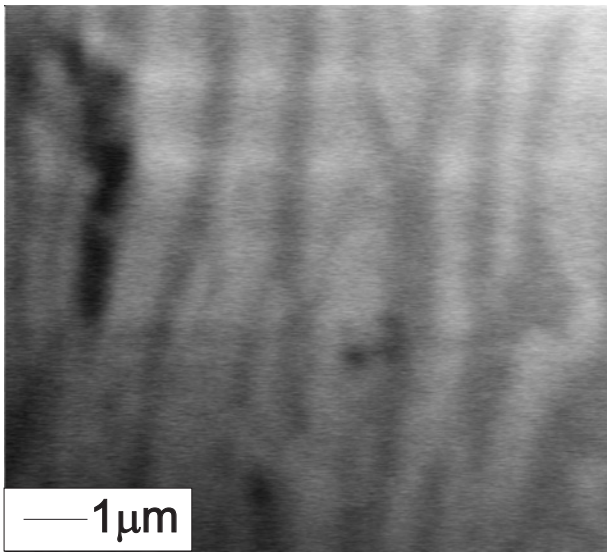

Fig. 9.9: Top view on the sample surface imaged with SEM. It shows a groove-like pattern that confirms the TEM results of the inhomogeneous thickness of the covering layer. (Courtesy of B. Siegle, MPI MF.)

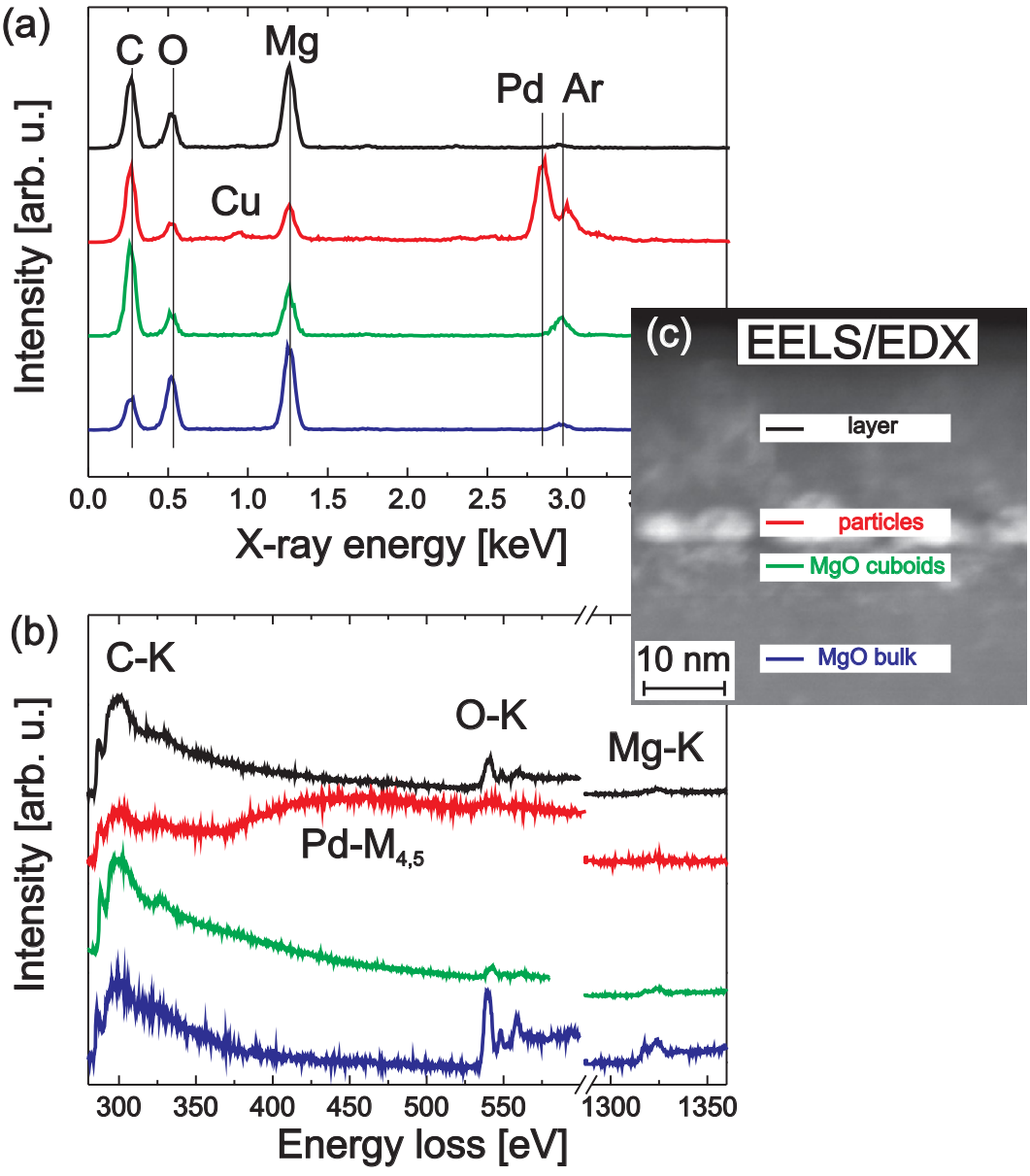

Fig. 9.10: EDX (a) and EELS spectra (b) for the different regions of interest on the sample as marked in the HAADF STEM cross section image (c). Blue line: MgO bulk, green line: disturbed zone, red: Pd nanoparticles, black: capping layer. (Courtesy of Dr. V. Srot, MPI MF.)

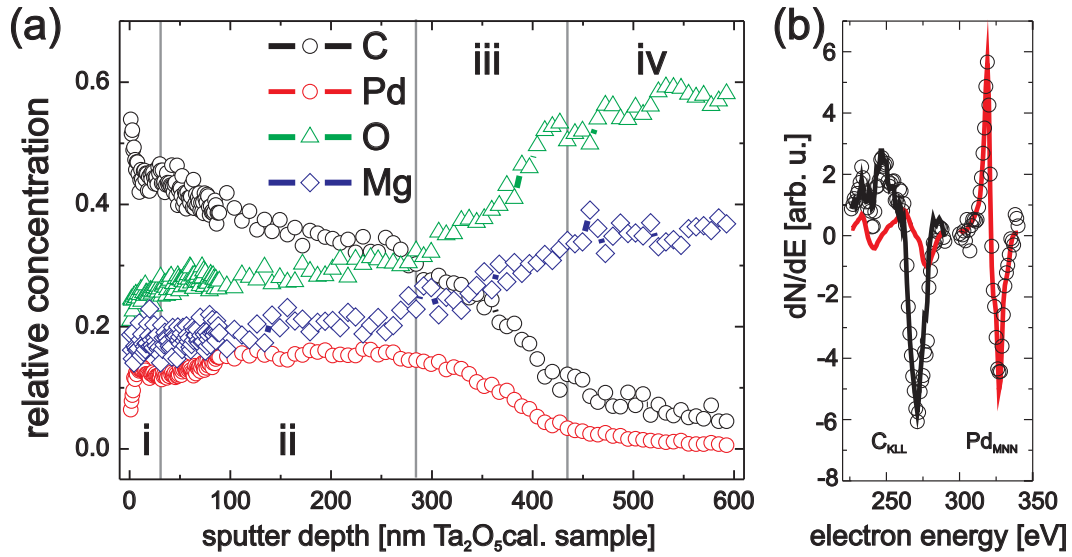

Fig. 9.11: (a) Relative concentrations of C, Pd, Mg, O as obtained from Auger sputter profiling. Dots: experimental values, red line: fitted Pd reference spectrum, black line: difference spectrum assigned to carbon. Up to a sputter depth of 100 nm, an energy of 500 eV for Ar^+ was used, then it was increased to 1000 eV which lead to a three times higher sputter rate on a [Ta_2O_5] reference. (b) To separate the C from Pd signal, an auxiliary spectrum from a pure Pd surface was subtracted in the vicinity of 272 eV. (Spectra recorded by B. Siegle, MPI MF.)

covering layer (IV) were used for spectroscopy. The EDX spectra displayed in fig. 9.10 (a) show significant contributions of carbon, oxygen, magnesium, palladium and argon. A remarkable magnesium and oxygen signal can be detected in the covering layer (IV), but no Pd. The carbon signal observed at all positions cannot be used for the analysis, as the TEM specimen was carbon coated to avoid charging effects. The argon signal is caused from the Ar ion-milling process during TEM specimen preparation. A signal of Pd can be found only at the position of the particles (III). The signals of oxygen and magnesium are much weaker in the region of the particles, but their ratio is similar to region (IV) in the overlayer. This is compatible with an overgrowth of the particles by the material of which the capping layer (IV) exists. Regions (I) and (III) show the signal of magnesium and oxygen as anticipated for pure MgO. The composition of the different sample regions was also obtained by EELS measurements performed in the same apparatus, as plotted in fig. 9.10 (b).

9.3.3 Depth-resolved Auger Electron Spectroscopy

To clarify the role of carbon in the capping layer, AES sputter-depth profiling was performed. Figure 9.11 (a) shows the depth-resolved concentration profiles of C, Pd, O and Mg up to an effective sputter depth of $\approx$ 100 nm. The depth

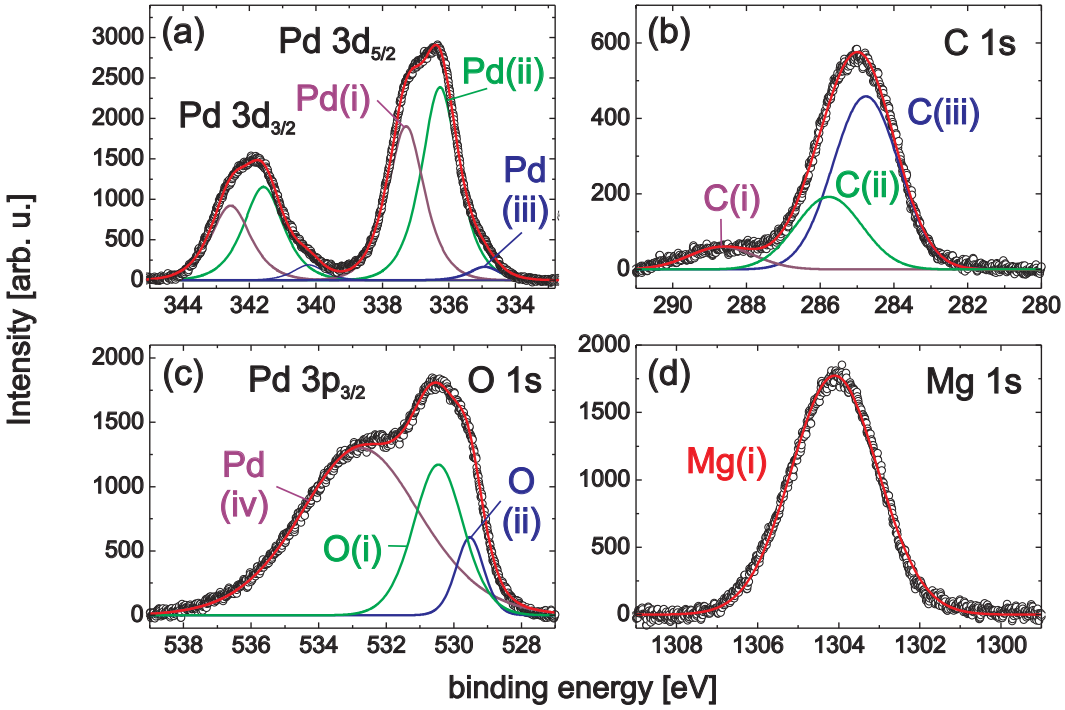

Fig. 9.12: XPS-spectra, after subtraction of Shirley-type background. (a): Metallic and oxidic Pd $3d_{3/2}$ and Pd $3d_{5/2}$ main peaks, (b): the C 1s main peak, (c): the combined Pd 3 $p_{3/2}$ and O 1s main peaks, (d): the oxidic Mg 1s main peak. (Courtesy of Dr. L. Jeurgens, MPI MF.)

profile (fig 9.11 a) can be roughly divided into four regions, labeled with Roman numbers i-iv. The signal of all elements can be detected before sputtering. In region i, the carbon signal decreases rapidly and can be associated with a very thin layer on the surfaces enriched in C. In region ii, the signal of carbon decreases slowly, while the signals of Pd, O and Mg slightly increase. These results give evidence that the capping layer contains a remarkable amount of C apart from Mg and O as identified by EELS and EDX. The detection of Pd in region i and ii can be explained by the inhomogeneous coverage of the surface with the Mg-O-C-layer, as in the AES spectra, the surface composition is probed laterally averaged. In region iii, both the C and the Pd signal show a remarkable decrease, which indicates that the Mg-O-C layer and the uncovered Pd particles get sputtered away. In the transition from region iii to iv, the Mg and O concentrations increase strongly while C and Pd decrease. In region iv, the Mg and O concentrations gradually approach constant values which marks the interface to the MgO substrate.

Core-level	Main peak	Binding energy [eV]	Chemical assignment
Pd $3d_{5/2}$	Pd(i)	337.3	PdO_2
	Pd(ii)	336.3	PdO
	Pd(iii)	334.9	metallic Pd
Pd $3p_{3/2}$	Pd(iv)	532.8	PdO / PdO_2
O 1s	O(i)	530.5	$MgCO_3$-like
	O(ii)	529.5	PdO
Mg 1s	Mg(i)	1304.1	$MgCO_3$-like
C 1s	C(i)	288.7	$MgCO_3$-like
	C(ii)	285.8	CO
	C(iii)	284.8	adventitious C

Table 9.1: Binding energies and chemical assignment of the main peaks from fig. 9.12.

9.3.4 XPS Study

The XPS analysis shows that the sample surface is composited of Mg, C, O and Pd, in agreement with the electron spectroscopy results. The different local chemical states were identified from an analysis of the measured C 1s, Pd $3d_{3/2}$, Pd $3d_{5/2}$, O 1s, Pd 3p and Mg 1s spectra as displayed in fig. 9.12. The resulting binding energies are listed in (tab. 9.3.4) which also contains their chemical assignment.

The Pd $3d_{5/2-3/2}$ spectrum could be fitted with three different chemical species labeled with Pd(i), Pd(ii) and Pd(iii), thereby maintaining the spin-orbit splitting of 5.3 eV. The weak peak of Pd(iii) at 334.9 eV can be assigned to residual metallic Pd [58] that was not completely oxidized in the final oxidation step of the sample and did not give any evidence of a Bragg diffraction signal after the final oxidation (see fig. 9.6). The Pd(iii) peak at 336.3 eV corresponds to bulk PdO [58]. The third main peak Pd(iii) at 337.3 eV is attributed to Pd oxide in a higher oxidation state, e.g. PdO_2. The formation of this phase was proposed in a recent DFT study [112] which is compatible with the conditions applied in the oxidation experiment in sec. 9.2. Pd-C compounds accessed with XPS can be excluded, as they would cause a Pd 3d5/2 component shifted by about 0.6 eV to the higher binding energy side of the Pd(i) peak [113] and is not observed here. The C 1s spectrum in fig. 9.12 consists of three spectral components. The main peaks at 285.8 eV and 284.8 eV, C(I) and C(ii), can be assigned to CO and adventitious carbon, in agreement with the observation of a carbon rich layer at the outer sample surface in the first part of the AES sputter depth profile. The weak peak C(i) at a binding energy of 288.7 eV indicates the formation of a carbonate species, such as magnesite $MgCO_3$ [114, 115]. Note that the C(i) intensity is weakened due to the enrichment of C at the outer sample surface. For a comparison with the values of the C 1s, O 1s and Mg 1s peaks, all binding energy values in ref. [114] were shifted by 4.88 eV to correct for the overcompensation

of differential charging by the employed floodgun in that reference. Fig. 9.12 (c) shows the region of Pd $3p_{3/2}$ and O 1s. The Pd $3p_{3/2}$ peak at 532.8 eV and the O 1s peak at 529 eV (O(ii)) are characteristic for PdO [58]. The peak O(i) at 530.5 eV agrees well with O 1s arising from the Mg-C-O surface layer as formed after CO_2 attack on MgO powder [114], denoted as $MgCO_3$. Accordingly, the Mg 1s peak at 1304.1 eV (fig. 9.12 (d)) matches with the Mg 1s peak for the CO_2 attacked MgO powder in ref. [114]. To sum up, the XPS study confirms the involvement of Mg, O and C at the sample surface as concluded from the electron spectroscopy studies. In addition, Pd was found in an oxidized state as PdO, in a higher oxidation state and with a small amount in its metallic phase.

9.4 Discussion

The ex situ structural and chemical analysis described in the last section show that after the CO oxidation experiment and the high-pressure oxidation the system Pd/MgO(100) transformed into PdO and a layer containing Mg, C and O. The presence of $MgCO_3$ at the surface is revealed with XPS. The carbonate is reported to be stable up to 1000 K [115] and explains why it was not removed during the in situ x-ray experiment with a maximum heating temperature of 940 K. The observation of Mg carbonate is compatible with a recently reported FTIR study on Pd/MgO particles under CO oxidation conditions [116]. It needs to be discussed how the ex situ results can be associated with the in situ x-ray experiments and what are the detailed mechanisms occurring during the deactivation of the model catalyst.

The most striking observation from the in situ x-ray experiments during the oxidation of CO was the decrease of the Pd signal from epitaxial nanoparticles with the lattice spacing of bulk Pd. Simultaneously, an new broad reflection was observed below the MgO(200) substrate reflection with increasing intensity during the reaction. From the electron microscopy study it is clear that Pd-containing nanoparticles are present below the Mg-C-O layer at the interface to the MgO substrate. These are deactivated due to the growth of the layer. Furthermore, the electron diffraction in an area containing the capping layer, the nanoparticles below that layer and the MgO substrate show diffraction spots and Debye-Scherrer rings that can all be assigned to MgO lattice spacings. Thereby, the diffraction rings are caused from the covering layer. It can therefore be concluded that the capping layer consists of polycrystalline MgO which is embedded in a carbon matrix. This inference is also in agreement with the EELS and EDX intensity ratios of O and Mg, which are similar for the overlayer and the MgO substrate. Crystalline magnesite has a corundum structure with d-spacings different from MgO [117] and should give rise to additional diffraction rings, which are not observed.

Furthermore, the combination of the x-ray and TEM results are compatible

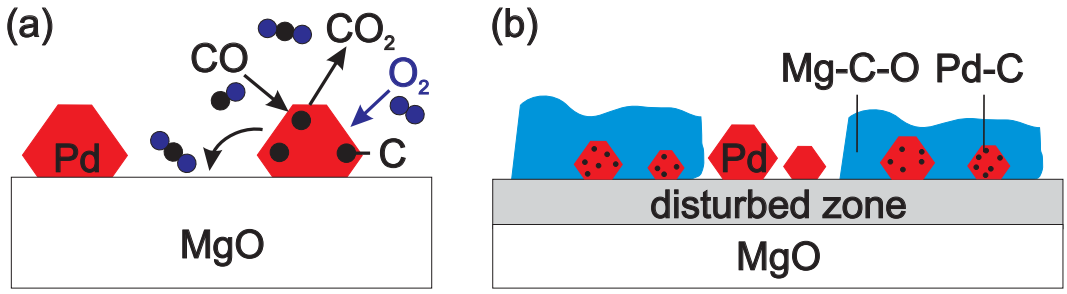

Fig. 9.13: Proposed scenario of CO oxidation and deactivation over Pd/MgO(100) nanoparticles. (a) O_2 and CO dissociate on the Pd particle surface. Remaining carbon dissolves into the Pd lattice while produced CO_2 spills over onto the substrate where it reacts with MgO. (b) Continuous deactivation of the Pd particles by the growth of the capping layer.

with the formation of Pd nanoparticles with a lattice constant close to the value of MgO. The expansion of the lattice spacing of the nanoparticles can be assigned to the incorporation of carbon which occupy interstitial octahedral sites [2, 118]. During CO oxidation on the Pd particles, the disproportionation reaction 2 CO $\rightarrow$ CO_2 + C may take place [116, 119] which leads to formation of atomic carbon. Even though molecular beam experiments showed that the surface of Pd nanoparticles should be in an oxygen-rich state at 570 K [120] for a 1:1 CO/O_2 mixture, apparently CO adsorbs under high pressure conditions. The CO molecules undergo dissociation and provide atomic carbon which is dissolved into the Pd nanoparticles. This scenario is sketched in fig. 9.13. Molecular oxygen and CO adsorb dissociatively on the particles. CO_2 can either be produced by direct reaction with adsorbed oxygen species or by CO disproportionation. The CO_2 molecules will either desorb or spill-over onto the MgO support. This leads to the reaction where the Mg-O-C capping layer is formed. This reaction may also bee seen as the reason for the disturbed zone at the interface with the small MgO cuboids as observed in the cross-section TEM images.

9.5 Summary

In conclusion, it could be shown that the model catalyst Pd/MgO(100) can be cycled between metallic Pd and the bulk oxide phase PdO by oxidation and CO reduction at 570 K. During CO exposure and CO oxidation in mixtures of 50% CO/O_2 at a total pressure of 100 mbar, Pd nanoparticles incorporate carbon atoms. This allows the particles to expand and to accommodate to the lattice spacing of the MgO substrate. During CO oxidation, the formation of poorly ordered PdO is observed. It might be located either on the MgO support or on the nanoparticle facets. From the experimental data, it cannot be concluded whether the disordered PdO or the metallic Pd nanoparticles are involved in the

CO oxidation. A deactivation of the model catalyst system takes place via the formation of a layer that consists of MgO crystallites in a carbon matrix and a surface carbonate layer. These results underline the need to study the model catalysts at ambient conditions, as new reaction pathways may occur at elevated pressures.

Chapter 10

Summary and Outlook

Project Context

The research for this thesis was performed within the project $NanO_2$ which was promoted within the Sixth Framework program by the European Union. The aim of the project is to understand the oxidation of nanomaterials under industrially relevant conditions and thereby to overcome the pressure and materials gap from single crystal oxidation studies at UHV-near conditions to the ambient pressure oxidation of nanoparticles.

Results

In this thesis, the oxidation properties of oxide-supported Rh and Pd nanoparticles in the size range from 4 nm to 24 nm were studied. The most important experimental method was synchrotron x-ray diffraction, which allowed in situ studies of oxidation in a wide pressure range up to near-atmospheric pressures. Reciprocal space mapping was applied as a shape sensitive tool. Together with the development of simulations using kinematic diffraction theory, a quantitative analysis of the particle shape could be achieved. The modeling of intensity distributions with reciprocal space maps was applied for the shape changes of MgO-supported Rh and Pd particles. A prerequisite was the epitaxial growth of the particles.

For the system Rh/MgO(001), surface oxides were found on the (111) and the top (001) facets. In addition, a p(3×1) reconstruction was found as a transient structure during formation of the surface oxide on the top facet. The surface oxide growth is associated with a shape change of the fcc-core of the particle, that become flatter thereby increasing the top (001) and side (100) facets. For particles with a diameter of 9 nm, in addition the formation of (110) facets was found which is predicted by theory. As for the single crystal surfaces Rh(100) and Rh(111), the surface oxide acts as a kinetic barrier for bulk oxide formation.

For the Pd nanoparticles on MgO(100) with a diameter of 8 nm it was shown that (112) facets form upon oxidation in the 10^{-5} mbar range. About four atomic layers are involved in this faceting process. This observation is in contrast to theoretical predictions for mesoscopic unsupported particles (the growing surface oxides should stabilize the (001) and (111) facets) and the Pd(112) single crystal surface which is instable upon oxidation at similar chemical potentials. The (112) facets on the Pd/MgO(100) particles vanish completely when the oxygen is pumped down or the particles are exposed to a reducing CO atmosphere.

At more elevated pressures, the bulk oxide PdO can be formed. The bulk oxide formation was studied as a function of the particle size. A high-energy microbeam x-ray diffraction scheme was applied that allowed a combined study of several particles in the size range from 4 to 24 nm in diameter under identical preparation conditions. Pd particles that are smaller than 9 nm in diameter shrink in size with increasing oxygen pressure in the mbar while epitaxial PdO is formed growing on the MgO surface. Even smaller particles with a diameter of less than 5 nm transformed completely into PdO. In contrast, if the particles are larger than 9 nm, polycrystalline PdO is formed on the particles. This oxide forms a passivating shell that prevents the covered metallic Pd core from further oxidation.

The bulk oxide formation was studied for α-Al_2O_3(0001) supported epitaxial Pd and Rh nanoparticles in (111) orientation with average diameters of 4 and 5 nm respectively and heights of 3 nm. The formation of chemisorbed oxygen on the Pd nanoparticles was deduced from an intensity decrease of the Pd Bragg reflections, which could be reverted upon removing the oxygen atmosphere. At elevated oxygen pressures in the mbar range, the growth of epitaxial PdO was achieved. This pressure is several orders of magnitude higher than anticipated from the theoretical phase diagrams of the PdO formation. The suspected chemisorbed oxygen seems to act as a kinetic barrier. In contrast, the oxidation of the Rh particles was achieved at an oxygen chemical potential close to the anticipated value of the phase diagram which shows that no remarkable kinetic barriers are present. This seems to be a size effect, as for the 9 nm Rh particles on MgO, under the same conditions no bulk oxide was observed but instead the ultra thin O-Rh-O trilayer surface oxide. During reduction of the oxidized particles, the morphology changes strongly as the Rh islands become polycrystalline and larger in size which shows that a remarkable inter-particle mass transport takes place.

The oxidation of CO was studied in the presence of Pd/MgO particles at near-atmospheric pressures. An inhomogeneous capping layer consisting of MgO crystallites embedded into carbon grows in the presence of CO/O_2 mixtures. The mass transport from the support into this capping layer leads to a disturbed zone at the MgO-particle interface consisting of small MgO cuboids in the size range of a few nanometers. Simultaneously, due to CO_2 disproportionation, carbon is incorporated into the Pd particles which leads to an expansion of their surface lattice and accommodation to the MgO substrate. These results underline the

necessity to study model catalyst systems at ambient conditions as new reaction pathways can be opened at elevated pressures that cannot be anticipated from an extrapolation of the UHV-near reaction properties.

Outlook

It has been known that *There's Plenty of Room at the Bottom*[1], and this phrase is frequently used to highlight the progress and opportunities of nanotechnology. By regarding the opportunities of diffraction at nanostructures one may be inclined to append that there's also *Plenty of Reciprocal Space* at the Bottom.

The reciprocal space mapping allowed a quantitative analysis of the change of the shape of the nanoparticles in the gas atmosphere. With advances in detector technology, further improvements of shape recording of a particle during a reaction can be expected. The shape change of the nanoparticles happens on the timescale of not more than a few minutes. On the other hand, recording a reciprocal space map with a point detector as performed in this work may take several hours. For the analysis, only the information of the (H+K=2)-plane was applied, which however contains the information of the (100)-side facets only indirectly. This is why diffraction maps in several distinct directions would increase the reliability and sensitivity of the shape analysis. A suitable approach would be using an area detector and recording the signal in the vicinity of the Bragg reflection by rocking the sample. This would allow a full three-dimensional mapping of the intensity distribution in reciprocal space, and could in principle be performed on the timescale of a few minutes. The reason why this has not been done in this study was the lack of dynamic range of the existing area detector for the scans, which would be necessary for a simultaneous mapping of the weak rod signal and the strong Bragg signal. This could meanwhile be solved by using the Pilatus detector [121], which is an area detector that has a very high dynamic range and can even record Bragg data.

A further goal to work on is a advanced development of the simulations of the intensity maps, where additional parameters could be included like variation of the size distribution, strained layers at the particle-support interface, relaxations at the particle surface or inclusion of internal twinning.

In this context, further improvement can be made in the synthesis of the particles. If both the azimuthal distribution of the particles could be reduced and the particles could be made monodisperse, the reciprocal space map should contain Laue oscillations, from which an enhanced sensitivity of slight shape changes can be expected.

It seems obvious that apart from Rh and Pd studied in this work, similar studies on catalytically active nanoparticles of further transition and noble metals

[1]Title of the lecture given by Richard Feynman at the Meeting of the American Physical Society in 1959.

like Pt, Ru, Ag or Au or the uncountable amount of their alloys can lead to valuable new insight in the structure during oxidation.

As was pointed out in ref. [122], the understanding of a lot of factors like size, shape and surface structure is important for the development of improved catalysts, and many improvements have been achieved to experimentally access the properties of catalysts. The research began with single-crystal surfaces under controlled conditions and now moved to the study of real catalysts under reaction conditions. Apart from this understanding of the processes on an atomic scale, also a controlled synthesis has to be achieved. This will lead to the goal *Catalysis by Design*, this means the targeted development and synthesis of a catalyst to promote a desired chemical reaction.

Appendix A

Acronyms and Symbols

Acronyms

AES	Auger electron spectroscopy
AFM	atomic force microscopy
ANKA	Angströmquelle Karlsruhe
BM	bending magnet
CCD	charged couple device
CTR	crystal truncation rod
DFT	Density Functional Theory
EDX	energy dispersive x-ray spectroscopy
EELS	electron energy loss spectroscopy
ESRF	European Synchrotron Radiation Facility
fcc	face centered cubic
FWHM	full width half maximum
GISAXS	grazing incidence small angle x-ray scattering
HASYLAB	Hamburg Synchrotron Radiation Laboratory
HEMD	high energy x-ray micro diffraction setup
HRCLS	high resolution corel level spectroscopy
ID	insertion device
LEED	low energy electron diffraction
MBE	molecular beam epitaxy
MPI MF	Max Planck Institute for Metals Research
SEM	scanning electron microscopy
StEM	Stuttgart Center for Electron Microscopy
STM	scanning tunneling microscopy
(S)XRD	(surface) x-ray diffraction
TEM	transmission electron microscopy
XPS	x-ray photoelectron spectroscopy
XRR	x-ray reflectivity
UHV	ultra high vacuum

Symbols

α_c	critical angle for total external reflection
$\alpha_{i/f}$	incident/exit angle
β	imaginary part of refraction index
$1-\delta$	real part of refraction index
E	energy
F($\mathbf{q}$)	structure factor
Γ	momentum transfer zero
$\boldsymbol{k_{i/f}}$	wave vector of the incoming/diffracted beam
λ	wave length
Λ	information depth
$\mu(T,p)$	chemical potential
p	pressure
$\mathbf{q}$	scattering vector
t	time
T	temperature
2θ	scattering angle
Z	atomic number

Appendix B

Transformation of Coordinates

In this thesis, reconstructions with respect to the (111)- and (001)- surfaces of Rh and Pd were discussed. The notations in literature, e.g. c(2×8) on Rh(100), refer to the surface unit cells which are different from the standard fcc unit cell. Within the whole thesis, when surface coordinates are applied, those on the (001) surface are denoted as (h, k, l)$_{top}$, as they were of special importance to discuss reconstructions on (001) facets on the *top* of the particles. The surface coordinates of the fcc (111)-surface are labeled as (h, k, l)$_{sur}$. In the following, the transformation between the fcc and surface coordinate systems is described.

B.1 Coordinates of the FCC(100) Surface

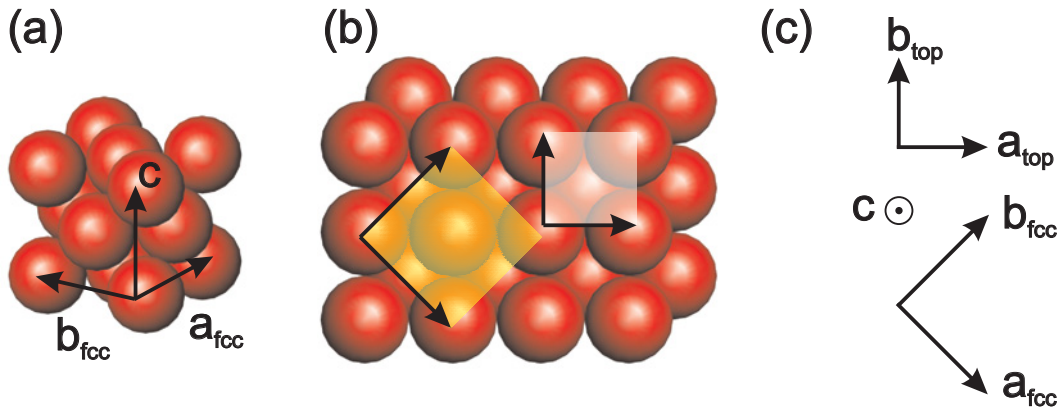

Fig. B.1: Standard fcc unit cell (a), top view on a fcc (100) surface (b) together with the orientations of the fcc- and surface lattice (c).

Fig. B.1 (a) shows the fcc unit cell of Rh and Pd. A view on the (100) surface is given in fig. B.1, and the projection of the fcc-unit cell is indicated with the yellow square. The white square represents the surface unit cell. The surface coordinate

$(hkl)_{sur}$	$(hkl)_{fcc}$
(003)	(111)
(110)	$(02\bar{2})$
(101)	$(11\bar{1})$
(012)	(020)

Table B.1: Transformation table for the Bragg reflections in (111) surface coordinates and fcc coordinates.

has the lattice parameters $a = b = \frac{a_0}{\sqrt{2}}$, $c = a_0 \cdot \sqrt{3}$, $\alpha = \beta = \gamma = 90°$. The lattice vectors of the surface unit cell with respect to the fcc-lattice are described by $\boldsymbol{a_{top}} = \frac{a_0}{2}\begin{pmatrix}1\\\bar{1}\\0\end{pmatrix}$, $\boldsymbol{b_{top}} = \frac{a_0}{2}\begin{pmatrix}1\\1\\0\end{pmatrix}$, $\boldsymbol{c} = a_0\begin{pmatrix}0\\0\\1\end{pmatrix}$. The resulting unit cell is body centered. The transformation between the Bragg reflections is straightforward and is given by: $h_{top} = \frac{1}{2}(h-k)$, $k_{top} = \frac{1}{2}(h+k)$, $l_{top} = l$.

B.2 Coordinates of the FCC(111) Surface

An (111)-surface of an fcc-crystal is described in a hexagonal coordinate system with $a = b = \frac{a_0}{\sqrt{2}}$, $c = a_0 \cdot \sqrt{3}$ and $\alpha = \beta = 90°$, $\gamma = 120°$. The lattice vectors can be described as $\boldsymbol{a} = \frac{a_0}{2}\begin{pmatrix}1\\0\\\bar{1}\end{pmatrix}$, $\boldsymbol{b} = \frac{a_0}{2}\begin{pmatrix}\bar{1}\\1\\0\end{pmatrix}$ and $\boldsymbol{c} = a_0 \cdot \begin{pmatrix}1\\1\\1\end{pmatrix}$ with respect to the surface unit cell. The hexagonal surface unit cell contains three atoms at positions $(0,0,0)$, $\frac{1}{3}(2,1,1)$ and $\frac{1}{3}(1,2,2)$, as displayed in fig. B.2 (a). The resulting Bragg reflections with the associated reciprocal lattice are given as follows:

$$\begin{pmatrix}h\\k\\l\end{pmatrix}_{fcc} = \frac{1}{3}\begin{pmatrix}2 & -2 & 1\\2 & 4 & 1\\-4 & -2 & 1\end{pmatrix}\begin{pmatrix}h\\k\\l\end{pmatrix}_{sur}$$

The Bragg reflections in the reciprocal lattice of the surface coordinates are marked with black dots in fig. B.2. If the momentum transfer L $= 3n, n \in \mathbb{N}$, symmetry related reflections occur at multiples of 60°, if L $\neq 3n$, reflections occur only in multiples of 120°. If there are additional metal domains which are rotated azimuthally by 60°, (fig. B.2 (c)), the Bragg reflections are located at correspondingly rotated positions, which are marked with orange dots in fig. B.2 (d). If L $= 3n$, the Bragg signal of both domains overlap, but if If L $\neq 3n$, both domains can be probed separately with diffraction.

B.3 Internal Twinning

The effect of 60°-domains along (111)-equivalent directions does not only occur for distinct particles, but can also occur within one particle, which is denoted as internal twinning. In the experimental sections of this work, this could be observed for some of the samples with Rh and Pd/Mg0(100) particles. If the

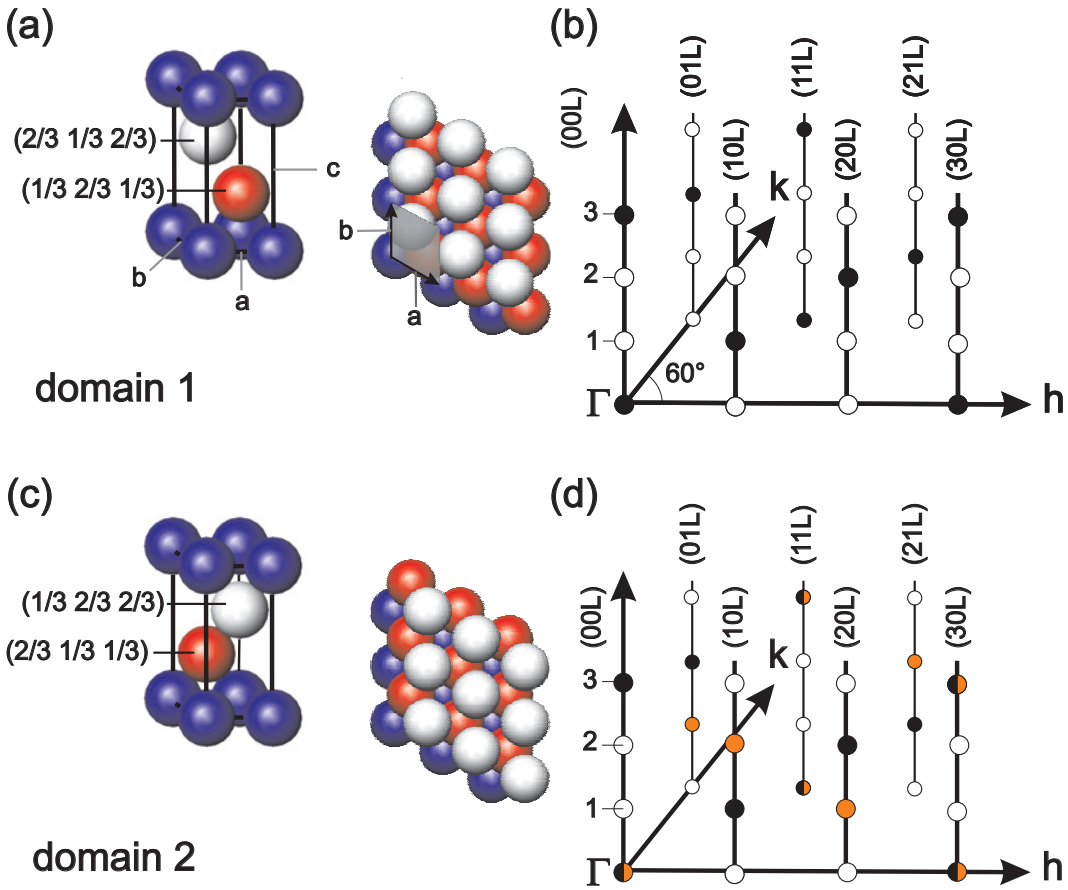

Fig. B.2: Sketch of the Bragg reflections for a (111) oriented fcc surface with respect to its surface unit cell (a, b). If 60° domains exist (c), some of the reflections are superimposed (d), e.g. (110), others are located at distinct positions, e.g. (101).

particle is twinned internally, the sequence of ABCABC-stacking gets inverted along a (111)-equivalent direction. The position calculation of the Bragg reflection is equivalent to that performed in the previous section. The positions of the reflections of the twin can be expressed in fcc-coordinates. The (111)-equivalent reflections of the twin are located at $\frac{1}{3}(\pm 1, \pm 1, \pm 5)$ and all possible permuted coordinates, the (200) reflection is located at $\frac{1}{3}(\pm 4, \pm 4, \pm 2)$. The peaks $\frac{1}{3}(2, 4, 4)$, $\frac{1}{3}(4, 2, 4)$, $\frac{1}{3}(5, 1, 1)$ and $\frac{1}{3}(1, 5, 1)$ are located in the (H+K=2)-plane which was used for the shape sensitive intensity distribution maps.

Bibliography

[1] F. Schüth. Schlüsseltechnologie der Chemischen Industrie – Heterogene Katalyse. *Chemie in unserer Zeit*, 40:92–103, 2006.

[2] D. Teschner, J. Borsodi, A. Wootsch, Z. Revay, M. Hävecker, A. Knop-Gericke, S. D. Jackson, and R. Schlögl. The Roles of Subsurface Carbon and Hydrogen in Palladium-Catalyzed Alkyne Hydrogenation. *Science*, 320:86–89, 2008.

[3] A. K. Datye, J. Bravoa, T. R. Nelson, P. Atanasova, M. Lyuborvskyb, and L. Pfefferle. Catalyst microstructure and methane oxidation reactivity during the Pd↔PdO transformation on alumnia supports. *Applied Catalysis A*, 198:179, 2000.

[4] H. S. Gandhi, G. W. Graham, and R. W. McCabe. Automotive exhaust catalysis. *Journal of Catalysis*, 216:433–444, 2003.

[5] C. H. F. Peden, D. W. Goodman, D. S. Blair, P. J. Berloowith, G. B. Fisher, and S. H. Oh. Kinetics of CO Oxidation by O_2 or NO on Rh(111) and Rh(100) Single Crystals. *J. Phys. Chem.*, 92:1563, 1988.

[6] P. Mars and D. W. Van Krevelen. Oxidations carried out by means of vanadium oxide catalysts. *Chemical Engineering Science*, 3:41–59, 1954.

[7] M. S. Chen, Y. Cai, Z. Yan, K. K. Gath, S. Axnanda, and D. Wayne Goodman. Highly active surfaces for CO oxidation of Rh, Pd and Pt. *Surface Science*, 601:5326–5331, 2007.

[8] G. Ertl. Primary steps in catalytic synthesis of ammonia. *J. Vac. Sci. Technol. A.*, 1:1247–1253, 1982.

[9] G. Ertl. Temporal and spatial self-organisation in catalysis at single crystal surfaces. *Catalysis Letters*, 9:219–230, 1991.

[10] C. Mohr, H. Hofmeister, J. Radnik, and P. Claus. Identification of Active Sites in Gold-Catalyzed Hydrogenation of Acrolein. *J. Am. Chem. Soc.*, 125:1905–1911, 2003.

[11] J. Gustafson, A. Mikkelsen, M. Borg, E. Lundgren, L. Köhler, G. Kresse, M. Schmid, P. Varga, J. Yuhara, X. Torelles, C. Quiros, and J. N. Anderson. Self-Limited Growth of a Thin Oxide Layer on Rh(111). *Physical Review Letters*, 92(12):126102, 2004.

[12] J. Gustafson, A. Mikkelsen, M. Borg, J. N. Andersen, E. Lundgren, C. Klein, W. Hofer, M. Schmid, P. Varga, L. Köhler, G. Kresse, N. Kasper, A. Stierle, and H. Dosch. Structure of a thin oxide film on Rh(100). *Physical Review B*, 71:115442, 2005.

[13] N. Y. Jin-Phillipp, P. Nolte, A. Stierle, and H. Dosch. Surface oxidation of Rh nanoparticles on (001) MgO. *Submitted*.

[14] M. Valden, X. Lai, and D. W. Goodman. The Structure of Catalytically Active Gold on Titania. *Science*, 281:1647, 1998.

[15] C. Becker and C. R. Henry. Cluster size dependent kinetics for the oxidation of CO on a Pd/MgO(100) model catalyst. *Surface Science*, 352–354:457–462, 1996.

[16] T. Schalow, B. Brandt, D. E. Starr, M. Laurin, S. Schauermann, Sh. K. Shaikhutdinov, J. Libuda, and H.-J. Freund. Oxygen-induced restructuring of a Pd/Fe_3O_4 model catalyst. *Catalysis Letters*, 107(3–4):189–196, 2005.

[17] T. Schalow, B. Brandt, D. E. Starr, M. Laurin, S. K. Shaikhutdinov, S. Schauermann, J. Libuda, and H.-J. Freund. Size-Dependent Oxidation Mechanism of Supported Pd Nanoparticles. *Angew. Chem. Int. Ed.*, 45:3693–3697, 2006.

[18] N. Kasper, A. Stierle, P. Nolte, Y. Jin-Phillipp, T. Wagner, D. G. de Oteyza, and H. Dosch. In situ oxidation study of MgO(100) supported Pd nanoparticles. *Surface Science*, 600:2860–2867, 2006.

[19] G. Ertl, H. Knötzinger, F. Schüth, and J. Weitkamp. *Handbook of Heterogenous Catalysis*. Viley-VCH, Weinheim, 2008.

[20] M. D. Ackermann, T. M. Pedersen, B. L. M. Hendriksen, O. Robach, S. C. Bobaru, I. Popa, C. Quiros, H. Kim, B. Hammer, S. Ferrer, and J. W. M. Frenken. Structure and Reactivity of Surface Oxides on Pt(110) during Catalytic CO Oxidation. *Physical Review Letters*, 95:255505, 2005.

[21] J. G. Wang, W. X. Li, M. Borg, J. Gustafson, A. Mikkelsen, T. M. Pedersen, E. Lundgren, J. Weissenrieder, J. Klikovits, M. Schmid, B. Hammer, and J. N. Andersen. One-dimensional PtO_2 at Pt Steps: Formation and Reaction with CO. *Physical Review Letters*, 95:256102, 2005.

[22] G. Rupprechter, K. Hayek, and H. Hofmeister. Electron Microscopy of Thin-Film Model Catalysts: Activation of Alumina-Supported Rhodium Nanoparticles. *Journal of Catalysis*, 173:409–422, 1998.

[23] P. Hansen, J. B. Wagner, S. Helveg, J. R. Rostrup-Nielsen, B. S. Clausen, and H. Topsoe. Atom-Resolved Imaging of Dynamic Shape Changes in Supported Copper Nanocrystals. *Science*, 295:2053–2055, 2002.

[24] H. Graoui, S. Giorgio, and C. R. Henry. Shape variations of Pd particles under oxygen adsorption. *Surface Science*, 417:350–360, 1998.

[25] F. Mittendorfer, N. Seriani, O. Dubay, and G. Kresse. Morphology of mesoscopic Rh and Pd nanoparticles under oxidizing conditions. *Physical Review B*, 76:233413, 2007.

[26] B. L. M. Hendriksen, S. C. Bobaru, and J. W. M. Frenken. Oscillatory CO oxidation on Pd(100) studied with in situ scanning tunneling microscopy. *Surface Science*, 552:229–242, 2004.

[27] H. Over, Y. D. Kim, A. P. Seitsonen, S. Wendt, W. Lundgren, M. Schmid, P. Varga, A. Morgante, and G. Ertl. Atomic-Scale Structure and Catalytic Reactivity of the $RuO_2(110)$ Surface. *Science*, 287:1474, 2000.

[28] J. Rogal, K. Reuter, and M. Scheffler. First-Principles Statistical Mechanics Study of the Stability of a Subnanometer Thin Surface Oxide in Reactive Environments: CO Oxidation at Pd(100). *Physical Review Letters*, 98:046101, 2007.

[29] E. Lundgren, J. Gustafson, A. Mikkelsen, J. N. Andersen, A. Stierle, H. Dosch, M. Todorova, J. Rogal, K. Reuter, and M. Scheffler. Kinetic Hindrance during the Initial Oxidation of Pd(100) at Ambient Pressures. *Physical Review Letters*, 92(4):046101, 2004.

[30] C. R. Henry. Surface studies of supported model catalysts. *Surface Science Reports*, 31:231–325, 1998.

[31] M. Bäumer and H.-J. Freund. Metal deposits on well-ordered oxide films. *Progress in Surface Science*, 61:127–198, 1999.

[32] H.-J. Freund, M. Bäumer, J. Libuda, T. Risse, G. Rupprechter, and S. Shaikhutdinov. Preparation and characterization of model catalysts: from ultrahigh vacuum to in situ conditions at the atomic dimension. *Journal of Catalysis*, 216:223–235, 2003.

[33] C. R. Henry. Morphology of supported nanoparticles. *Prog. Surf. Sci*, 80:92–116, 2005.

[34] L.D. Marks. Particle Size Effects on Wulff Constructions. *Surface Science*, 150:358–366, 1985.

[35] C. Mottet, J. Goniakowski, F. Baletto, R. Ferrando, and G. Treglia. Modeling free and supported metallic nanoclusters: structure and dynamics. *Phase Transitions*, 77:101–113, 2004.

[36] A. L. Mackay. A dense non-crystallographic packing of equal spheres. *Acta Cryst.*, 15:916–918, 1962.

[37] L. D. Marks. Surface structure and energetics of multiply twinned particles. *Philosophical Magazine A*, 49:81–93, 1984.

[38] Jr. A. T. Fromhold. *Theory of Metal Oxidation*. North Holland, Amsterdam, 1976.

[39] R. Franchy. Growth of thin, crystalline oxide, nitride and oxynitride films on metal and metal alloy surfaces. *Surface Science Reports*, 38:195–294, 2000.

[40] G. S. Tripathi, N. E. Brenner, and J. Callaway. Electronic structure of rhodium. *Physical Review B*, 38(15):10454–10462, 1988.

[41] J. M. d. Coey. The crystal structure of Rh_2O_3. *Acta Cryst. B*, 26:1876–1877, 1970.

[42] R. D. Shannon. Synthesis and properties of two new members of the rutile family RhO_2 and PtO_2. *Solid State Communications*, 6:139–143, 1967.

[43] L. Köhler, G. Kresse, M. Schmid, E. Lundgren, J. Gustafson, A. Mikkelsen, M. Borg, J. Yujara, J. N. Andersen, M. Marsman, and P. Varga. High-Coverage Oxygen Structures on Rh(111): Adsorbate Repulsion and Site Preference is not enough. *Physical Review Letters*, 93:266103, 2004.

[44] A. Baraldi, V. R. Dhanak, G. Comelli, K. C. Prince, and R. Rosei. Order-disorder phase transitions of oxygen on Rh(100). *Physical Review B*, 56(16):10511–10517, 1997.

[45] A. Baraldi, J. Cerda, Martín-Gago, G. Comelli, S. Lizzit, G. Paolucci, and R. Rosei. Oxygen Induced Reconstruction of the Rh(100) Surface: General Tendency Towards Threefold Oxygen Adsorption Site on Rh Surfaces. *Physical Review Letters*, 82(24):4874–4877, 1999.

[46] Y. G. Shen, A. Qayyum, D. J. O'Connor, and B. V. King. Oxygen-induced surfade $(2 \times 2)\,p4g$ reconstruction of Rh(001). *Physical Review B*, 58(15):10025–10030, 1998.

[47] A. G. Norris, F. Schedin, G. Thornton, V. R. Dhanak, T. S. Turner, and R. McGrath. Surface x-ray diffraction study of the Rh(100) (2×2)-O reconstruction. *Physical Review B*, 62(3):2113–2117, 2000.

[48] C. W. Tucker Jr. Chemisorbed Coincidence Lattices on Rhodium. *Journal of Applied Physics*, 37(8):3013–3019, 1966.

[49] L. H. Dubois. Vibrational spectra of atomic adsorbates: Carbon, oxygen and sulphur on Rh(100). *J. Chem. Phys*, 77(10):5228–5233, 1982.

[50] M. Sporn, E. Platzgummer, E. L. D. Gruber, M. Schmid, W. Hofer, and P. Varga. A quantitative LEED analysis of the oxygen-induced $p\,(3 \times 1)$ reconstruction of $Pt_{25}Rh_{75}(100)$. *Surface Science*, 416:384–395, 1998.

[51] C. Dri, C. Africh, F. Esch, G. Comelli, O. Dubay, L. Köhler, F. Mittendorfer, G. Kresse, P. Dudin, and M. Kiskinova. Initial oxidation of the Rh(110) surface: Ordered adsorption and surface oxide structures. *The Journal of Chemical Physics*, 125:094701, 2006.

[52] G. Comelli, V. R. Dhanak, M. Kiskinova, K. C. Prince, and R. Rosei. Oxygen and nitrogen interaction with rhodium single crystal surfaces. *Surface Science Reports*, 32:165–231, 1998.

[53] J. Waser, H. A. Levy, and S. W. Peterson. The Structure of PdO. *Acta Cryst.*, 6:661–663, 1953.

[54] M. Todorova. *Oxidation of Palladium Surfaces*. PhD thesis, Technical University Berlin, 2004.

[55] J. Nell and H. St. C. O'Neill. Gibbs free energy of formation and heat capacity of PdO: A new calibration of the Pd-PdO bufer to high temperatures and pressures. *Geochimica at Cosmochimica Acta*, 60:2487–2493, 1996.

[56] E. Lundgren, G. Kresse, C. Klein, M. Borg, J. N. Andersen, M. De Santis, Y. Gauthier, C. Konvicka, M. Schmid, and P. Varga. Two-Dimensional Oxide on Pd(111). *Physical Review Leters*, 88(24):246103, 2002.

[57] M. Todorova, K. Reuter, and M. Scheffler. Density-functional theory study of the initial oxygen incorporation in Pd(111). *Physical Review B*, 71:195403, 2005.

[58] G. Ketteler, D. F. Ogletree, H. Bluhm, H. Liu, E. L. D. Hebenstreit, and M. Salmeron. In Situ Spectroscopic Study of the Oxidation and Reduction of Pd(111). *J. Am. Chem Soc.*, 127:18269–18273, 2005.

[59] H. Gabasch, W. Unterberger, K. Hayek, B. Klötzer, E. Kleimenov, D. Teschner, S. Zafeiratos, M. Hävecker, A. Knop-Gericke, R. Schlögl, J. Han, F. H. Ribeiro, B. Aszalos-Kiss, T. Curtin, and D. Zemlyanov. In situ XPS study of Pd(111) oxidation at elevated pressure, Part 2: Palladium oxidation in the 10^{-1} mbar range. *Surface Science*, 600:2980–2989, 2006.

[60] D. Zemlyanov, B. Aszalos-Kiss, E. Kleimenov, D. Teschner, S. Zafeiratos, M. Hävecker, A. Knop-Gericke, R. Schlgl, H. Gabasch, W. Unterberger, K. Hayek, and B. Klötzer. In situ XPS study of Pd(111) oxidation at elevated pressure, Part 1: 2D oxide formation in 10^{-3} mbar O_2. *Surface Science*, 600:983–994, 2006.

[61] H. Gabasch, W. Unterberger, K. Hayek, B. Klötzer, G. Kresse, C. Klein, M. Schmid, and P. Varga. Growth and decay of the Pd(111)-Pd_5O_4 surface oxide: Pressure-dependent kinetics and structural aspects. *Surface Science*, 600:205–218, 2006.

[62] J. Klikowits, E. Napetschnig, M. Schmid, N. Seriani, O. Dubay, G. Kresse, and P. Varga. Surface oxides on Pd(111): STM and density functional calculations. *Physical Review B*, 76:045405, 2007.

[63] P. Kostelník, N. Seriani, G. Kresse, A. Mikkelsen, E. Lundgren, V. Blum, T. Sikola, P. Varga, and M. Schmid. The Pd(100)-$\left(\sqrt{5}\times\sqrt{5}\right)$ R27°-O surface oxide: A LEED, DFT and STM study. *Surface Science*, 601:1574–1581, 2007.

[64] D. T. Vu, K. A. R. Mitchell, O. L. Warren, and P. A. Thiel. Tensor LEED analysis of the Pd(100)-$\left(\sqrt{5}\times\sqrt{5}\right)$ *R*27°-O surface structure . *Surface Science*, 318:129–138, 1994.

[65] M. Todorova, E. Lundgren, V. Blum, A. Mikkelsen, S. Gray, J. Gustafson, M. Borg, J. Rogal, K. Reuter, J. N. Andersen, and M. Scheffler. The Pd(100)-$\left(\sqrt{5}\times\sqrt{5}\right)$ R27°-O surface oxide revisited. *Surface Science*, 541:101–112, 2003.

[66] A. Stierle, N. Kasper, H. Dosch, E. Lundgren, J. Gustafson, A. Mikkelsen, and J. N. Andersen. A surface x-ray study of the structure and morphology of the oxidized Pd(001) surface. *The Journal of Chemical Physics*, 122:044706, 2005.

[67] P. Guenard, G. Renaud, A. Barbier, and M. Gautier-Soyer. Determination of the Al_2O_3(0001) Surface Relaxation and Termination by Measurements of Crystal Truncation Rods. *Surface Review and Letters*, 5:321–324, 1997.

[68] T. J. Godin and J. P. LaFemina. Atomic and electronic structure of the corundum (α-alumina)(0001) surface. *Physical Review B*, 49:7691, 1994.

[69] J. Guo, D. E. Ellis, and D. J. Lam. Electronic structure and energetics of sapphire (0001) and ($1\bar{1}02$) surfaces. *Physical Review B*, 45:13647, 1992.

[70] P. J. Eng, T. P. Trainor, G. E. Brown Jr., G. A. Waychunas, M. Newville, S. R. Sutton, and M. L. Rivers. Structure of the Hydrated α-Al_2O_3 (0001) Surface. *Science*, 288:1029, 2000.

[71] I. K. Robinson and D. J. Tweet. Surface x-ray diffraction. *Rep. Prog. Phys.*, 55:599–651, 1992.

[72] B. E. Warren. *X-ray diffraction*. Dover publications, Dover, 1990.

[73] H. Dosch. *Critical Phenomena at Surfaces and Interfaces*. Springer, Berlin Heidelberg, 1992.

[74] J. Als-Nielsen and D. McMorrow. *Elements of Modern X-ray Physics*. John Wiley & Sons, New York, Chichester, Weinheim, Brisbane, Singapore, Toronto, 2001.

[75] J. L. Billinge and I. Levin. The Problem with Determining Atomic Structure at the Nanoscale. *Science*, 316:561–565, 2007.

[76] C. Kumpf, R. B. Neder, F. Niederaenk, P. Luczak, A. Stahl, M. Scheuermann, S. Joshi, S. K. Kulkarni, C. Barglik-Chory, C. Heske, and E. Umbach. Structure determination of CdS and ZnS nanoparticles: Direct modeling of synchrotron-radiation diffraction data. *The Journal of Chemical Physics*, 123:224707, 2005.

[77] C. Kumpf. Structure determination of very small (1–5 nm) nano-particles. *Appl. Phys. A*, 85:337–343, 2006.

[78] C. Revenant, F. Leroy, R. Lazzari, G. Renaud, and C. R. Henry. Quantitative analysis of grazing incidence small-angle x-ray scattering: Pd/MgO(001) growth. *Physical Review B*, 69:035411, 2004.

[79] R. Lazzari. IsGISAXS: a program for Grazing-Incidence Small-Angle X-Ray Scattering analysis of supported islands. *Appl. Cryst*, 35:406–421, 2002.

[80] G. Renaud, R. Lazzari, C. Revenant, A. Barbier, M. Noblet, O. Ulrich, F. Leroy, J. Jupille, Y. Borensztein, C. R. Henry, J.-P. Deville, F. Scheurer, J. Mane-Mane, and O. Fruchart. Real-Time Monitoring of Growing Nanoparticles. *Science*, 300:1416–1419, 2003.

[81] I. K. Robinson and J. Miao. Three-Dimensional Coherent X-Ray Diffraction Microscopy. *MRS Bulltetin*, March 2004:1777–1781, 2004.

[82] G. J. Williams, M. A. Pfeifer, I. A. Vartanyants, and I. K. Robinson. Three-Dimensional Imaging of Microstructure in Au Nanocrystals. *Physical Review Letters*, 90:175501, 2002.

[83] M. A. Pfeifer, G. J. Williams, I. A. Vartanyants, R. Harder, and I. K. Robinson. Three-dimensional mapping of a deformation field inside a nanocrystal. *Appl. Phys. A*, 85:337–343, 2006.

[84] C. G. Schroer, P. Boye, J. M. Feldkamp, J. Patommel, A. Schropp, A. Schwab, S. Stephan, M. Burghamer, S. Schöder, and C. Riekel. Coherent X-Ray Diffraction Imaging with Nanofocused Illumination. *Physical Review Letters*, 101:090801, 2008.

[85] M. Lohmeier and E. Vlieg. Angle Calculations for a Six-Circle Surface X-ray Diffractometer. *Journal of Applied Crystallography*, 26:706–716, 1993.

[86] E. Vlieg. A (2+3)-Type Surface Diffractometer: Mergence of the z-Axis and (2+2)-Type Geometries. *Journal of Applied Crystallography*, 31:198–203, 1998.

[87] O. Bunk and M. M. Nielsen. Angle calculations for a z-axis/(2S+2D) hybrid diffractometer. *Journal of Applied Crystallography*, 37:216, 2004.

[88] A. Stierle, A. Steinhäuser, A. Rühm, F. U. Renner, R. Weigel, N. Kasper, and H. Dosch. Dedicated Max-Planck beamline for the in-situ investigation of interfaces and thin films. *Review of Scientific Instruments*, 75:5302–5307, 2004.

[89] M. Mezger. *X-Ray Studies of the Density Depletion at Hydrophobic Water-Solid Interfaces*. PhD thesis, University of Stuttgart, 2008.

[90] H. Reichert, V. Honkimäki, A. Snigirev, S. Engemann, and H. Dosch. A new x-ray transmission-reflection scheme for the study of deeply buried interfaces. *Physica B*, 336:46–55, 2003.

[91] W. Drube, H. Schulte-Schrepping, H.-G. Schmidt, R. Treusch, and G. Materlik. Design and performance of the high-flux/high-brightness x-ray wiggler beamline BW2 at HASYLAB. *Physica B*, 336:46–55, 1995.

[92] J. F. Watts and J. Wolstenholme. *An Introduction to SURFACE ANALYSYS by XPS and AES*. Wiley, Chichester, 2003.

[93] P. R. Buseck, J. M. Cowley, and L. Eyring. *High-resolution Transmission Electron Microscopy and Associated Techniques*. Oxford University Press, New York, Oxford, 1988.

[94] C. C. Ahn. *Transmission Electron Energy Loss Spectrometry in Materials Science and The EELS ATLAS*. Wiley-VCH, Weinheim, 2004.

[95] W. L. Winterbottom. Equilibrium shape of a small particle in contact with a foreign substrate. *Acta. Metall.*, 15:303, 1967.

[96] S. Nokbin, J. Limtrakul, and K. Hermansson. DFT plane-wave calculations of the Rh/MgO(001) interface. *Surface Science*, 556-568:977–982, 2004.

[97] A. Stierle. Personal communication.

[98] B. Huber, P. Koskinen, H. Häkkinen, and M. Moseler. Oxidation of magnesia-supported Pd-clusters leads to the ultimate limit of epitaxy with a catalytic function. *Nature Materials*, 5:44–47, 2006.

[99] T. Schalow, B. Brandt, D. E. Starr, M. Laurin, S. K. Shaikhutdinov, S. Schauermann, J. Libuda, and H.-J. Freund. Particle size dependent adsorption and reaction kinetics on reduced and partially oxidized Pd nanoparticles. *Physical Chemistry Chemical Physics*, 9:1347–1361, 2007.

[100] J. Klikovits. *Atomic-Scale Studies of Oxidized Pd and Rh Surfaces*. PhD thesis, Technische Universität Wien, 2008.

[101] S. L. Tait, L. T. Ngo, Q. Yu, S. C. Fain Jr., and C. T. Campbell. Growth and sintering of Pd clusters on α-Al_2O_3(0001). *The Journal of Chemical Physics*, 122:064712, 2005.

[102] S. Penner, P. Bera, S. Pedersen, L. T. Ngo, J. J. W. Harris, and C. T. Campbell. Interactions of O_2 with Pd Nanoparticles on α-Al_2O_3. *J. Phys. Chem. B*, 110:24577–24584, 2006.

[103] N. S. Babu, N. Lingaiah, R. Gopinath, P. Siva Sankar Reddy, and P. S. Sai Prasad. Characterization and Reactivity of Alumina-Supported Pd Catalysts for the Room-Temperature Hydrodechlorination of Chlorobenzene. *J. Phys. Chem C*, 111:6447–6453, 2007.

[104] J. Corts, E. Valencia, J. Herrera, and P. Araya. Mechanism and Kinetic Parameters of the Reduction Reaction of NO by CO on Pd/Al_2O_3 Catalyst. *J. Phys. Chem. C*, 111:7063–7070, 2007.

[105] T. R. Ward, P. Alemany, and R. Hoffmann. Adhesion of Rhodium, Palladium and Platinum to Alumina and the Reduction of NO on the Resulting surfaces: A Theroretical Analysis. *J. Phys. Chem.*, 97:7691–7699, 1993.

[106] B. L. M. Hendriksen, S. C. Bobaru, and J. W. M. Frenken. Bistability and oscillations in CO oxidation studied with scanning tunneling microscopy inside a reactor. *Catalysis Today*, 105:234, 2005.

[107] M. Ackermann. *Operando SXRD: A new view on catalysis*. PhD thesis, University of Leiden, 2007.

[108] T. Schalow, B. Brandt, M. Laurin, S. Schauermann, J. Libuda, and H.-J. Freund. CO oxidation on partially oxidized Pd nanoparticles. *Journal of Catalysis*, 58:242, 2006.

[109] B. Brandt, T. Schalow, M. Laurin, S. Schauermann, J. Libuda, and H.-J. Freund. Oxidation, reduction, and reactivity of supported Pd nanoparticles: mechanism and microkinetics. *Journal of Physical Chemistry C*, 111:938, 2007.

[110] M. S. Vinodh and L. P. H. Jeurgens. Quantitative analysis of angle-resolved XPS spectra recored in parallel data acquisition mode. *Surface and Interface Analysis*, 36:1629–1636, 2004.

[111] S. Hofmann. Advances in sputter depth profiling using AES. *Surface and Interface Analysis*, 35:556–563, 2003.

[112] A. Dianat, N. Seriani, M. Bobeth, W. Pompe, and L. C. Ciacchi. DFT Study of the Thermodynamic Stability of Pd-Pt Bulk Oxide Phase. *Journal of Physical Chemistry C*, 112:13623–13628, 2008.

[113] D. Teschner, E. Vass, M. Hävecker, S. Zafeiratos, P. Schnörch, H. Sauer, A. Knop-Gericke, R. Schlögl, M. Chamam, A. Wootsch, A. S. Canning, J. J. Gamman, S. D. Jackson, J. McGregor, and L. F. Gladden. Carbon incorporation during ethene oxidation on Pd(111) studied by in situ X-ray photoelectron spectroscopy at 2×10^{-3} mbar. *Journal of Catalysis*, 242:340–348, 2006.

[114] B. V. Crist. *Handbooks of Monochromatic XPS Spectra, Vol.1*. XPS International LLC, Mountain View, 2004.

[115] D. K. Aswal, K. P. Muthe, S. Tawde, S. Chodhury, N. Bagkar, A. Singh, S. K. Gupta, and J. V. Yakhmi. XPS and AFM investigations of annealing induced surface modificatons of MgO single crystals. *Journal of Crystal Growth*, 236:661–666, 2002.

[116] H. Borchert, B. Jürgens, V. Zielasek, G. Rupprechter, S. Giorgio, C. R. Henry, and M. Bäumer. Pd nanoparticles with highly defined structure on MgO as model catalysts: An FTIR study on the interaction with CO, O_2, and H_2 under ambient conditions. *Journal of Catalysis*, 247:145–154, 2007.

[117] H. Effenberger, K. Mereiter, and J. Zemann. Crystal structure refinements of magnesite, calcite, rhodochrosite, siderite, smithonite and dolomite, with discussion of some aspects of stereochemistry of calcite type carbonates. *Zeitschrift für Kristallographie*, 156:233–243, 1981.

[118] S. B. Ziemecki, G. A. Jones, D. G. Swartzfager, R. L. Harlow, and Jr. J. Faber. Formation of interstitial palladium-carbon phase by interaction of ethylene, acetylene, and carbon monoxide with palladium. *Journal of the American Chemical Society*, 107:4547, 1985.

[119] G. Rupprechter, V. V. Kaichev, H. Unterhalt, M. Morkel, and V. I. Bukhtiyarov. CO dissociation and CO hydrogenation on smooth and ion-bombarded Pd(111): SFG and XPS spectroscopy at mbar pressures. *Applied Surface Science*, 235:26–31, 2004.

[120] V. Johanek, M. Laurin, A. W. Grant, B. Kasemo, C. R. Henry, and J. Libuda. Fluctuations and Bistabilities on Catalyst Nanoparticles. *Science*, 304:1639, 2004.

[121] Ch. Broennimann, E. F. Eikenberry, B. Henrich, R. Horisberger, G. Huelsen, E. Pohl, B. Schnitt, C. Schulze-Briese, M. Suzuki, T. Tomizaki, H. Toyokawa, and A. Wagner. The PILATUS 1M detector. *Journal of Synchrotron Radiation*, 13:120–130, 2006.

[122] Editorial. Catalysis by Design. *Nature Nanotechnology*, 3:575, 2008.

List of Publications

Articles in Peer-Reviewed Journals

N. Kasper, A. Stierle, P. Nolte, Y. Jin-Phillipp, T. Wagner, D. G. de Oteyza, and H. Dosch. In situ oxidation study of MgO(100) supported Pd nanoparticles. *Surface Science* **600**, 2860-2867 (2006)

A. Stierle, R. Streitel, P. Nolte, A. Vlad, I. Costina, M. Marsman, G. Kresse, E. Lundgren, J. N. Andersen, R. Franchy, and H. Dosch. Real time observation of ultrathin epitaxial oxide growth during alloy oxidation. *New Journal of Physics* **9**, 331 (2007)

P. Nolte, A. Stierle, N. Kasper, N. Y. Jin-Phillipp, H. Reichert, A. Rühm, J. Okasinski, H. Dosch, and S. Schöder. Combinatorial high-energy x-ray microbeam study of the size-dependent oxidation of Pd nanoparticles on MgO(100). *Physical Review B* **77**, 115444 (2008)

P. Nolte, A. Stierle, N. Y. Jin-Phillipp, N. Kasper, T. U. Schulli, and H. Dosch. Shape Changes of Supported Rh Nanoparticles During Oxidation and Reduction Cycles. *Science* **321**, 1654-1658 (2008)

P. Nolte, A. Stierle, O. Balmes, V. Srot, P. A. van Aken, L. P. H. Jeurgens, and H. Dosch. Carbon Incorporation and Deactivation of MgO(001) supported Pd Nanoparticles during CO Oxidation. *Catalysis Today* (2009)
doi:10.1016/j.cattod.2008.12.002

Conference Proceeding

N. Y. Jin-Phillipp, P. Nolte, A. Stierle, P. A. van Aken, and H. Dosch. Direct Observation of Surface Oxidation of Rh Nanoparticles on (001)MgO, *EMC 2008, Proceedings of the 14th European Microscopy Congress, Vol. 2: Material Science.* S. Richter, A. Schwedt (Eds.), Springer, Berlin 2008, 225-226

Highlighted Results

Real time observation of ultrathin epitaxial oxide growth during alloy oxidation.
ESRF Highlights 2007, 82 (2007)

Nanoparticle Shape Shift.
Science, **321**, 1601 (2008)

X-ray Detection of Shape Changes of Catalytic Nanoparticles.
X-Ray Spectrometry, **37**, 652 (2008)

Catching Catalyst Particles In Action.
Chemical & Engineering News, **86**, 71 (2008)

Catalysis by design.
Nature Nanotechnology, **3**, 575 (2008)

Rhodiumkatalyse auf der Nanometerskala.
CHemie Plus, **2008** (11), 6 (2008)

X-ray diffraction: Catalysis live.
Nature Nanotechnology, doi:10.1038/nnano.2008.308
Nature Nanotechnology, **3**, 646 (2008)

Katalyse auf der Nanometerskala.
Max Planck Press Release, C/2008(203), see also:
http://www.chemieonline.de/bibliothek/details.php?id=2902/, 13 Oct 2008
http://www.analytica-world.com/news/d/88145/, 15 Oct 2008
http://www.chemie.de/news7d/88145/, 15 Oct 2008
http://www.internetchemie.info/news/2008/oct08/rhodium.htm., 15 Oct 2008

The Shape of Supported Rh Nanoparticles during Oxidation and Reduction.
ESRF Highlights 2008, 79 (2008)

Acknowledgements

Within this thesis project, I had the chance to study the oxidation properties of nanoparticle model catalysts with four metal-support combinations. When I reflect on what is the major result, the clear answer is the growth of the surface oxides on the Rh/MgO particles and the associated shape change of the fcc core. The quantitative analysis of the particle shape was not merely a sophisticated task, like the experimental parts of this work requiring a UHV environment. It turned out to be a real challenge and became the *kinetic barrier* for the completion of the thesis – in spite of all the other successful synchrotron beamtimes. Eventually, I was recompensed with these results published in Science Magazine. I consider this article as my biggest professional achievement hitherto, and I would like to acknowledge all those who contributed to the success of this thesis project.

I am thankful to **Prof. Dr. Helmut Dosch** for giving me the opportunity to conduct my PhD project at the Max Planck Institute for Metals Research. The unique experimental equipment of the institute and the access to beamtime at external synchrotron radiation facilities were definitely decisive for the results. What did not contribute less was the excellent working atmosphere in his department. I also want to acknowledge the opportunities to present the results at international conferences and workshops, such as the SXNS in Taiwan, the NIMS-Workshop in Kansai/Japan or the ECOSS in Liverpool/UK, which I regard as a big personal benefit.

I am deeply indebted to my supervisor **Dr. Andreas Stierle** for offering me this interesting research topic in the exciting field of nanoparticles. Especially his organization of the numerous beamtimes at synchrotron radiation facilities allowed these comprehensive studies of the nanoparticles with different metal / support combinations. I want to emphasize that he decisively supported the progress of the particle shape analysis by many discussions. I appreciate a lot his reading of the manuscript and the many hints of how to improve this thesis.

I thank **Prof. Dr. Peter Michler** from the Institute of Semiconductor Optics and Functional Interfaces of the University of Stuttgart for being the coreferee of this thesis. **Prof. Dr. Günther Mahler** from the 1^{st} Institute of Theoretical Physics of the University of Stuttgart is acknowledged for the chairmanship of the examination.

Transmission electron microscopy is an art, and its my great pleasure that a high number of samples were studied at the StEM at the MPI for Metals Research. I am indebted to **Dr. Neng Yun Jin-Phillipp** for the excellent quality of the high resolution transmission electron microscopy measurements and the discussions. **Marion Kelsch** and **Ute Salzberger** strongly contributed with their expertise for the TEM specimen preparation.

The last sub-project I started was the CO oxidation of the Pd/MgO particles. I thank **Peter Kopold**, **Dr. Vesna Srot** and **Dr. Peter van Aken** for their work in the TEM analysis. A decisive step was also the AES sputter depth profiling and the XPS analysis. I want to thank **Dr. Lars Jeurgens** and **Bernhard Siegle** for their work and the many discussions.

Even though the presented results in this thesis focus on the oxidation experiments, I want to mention that these only worked after the sufficient understanding of the metal particle growth. **Dr. Gunther Richter** and **Michael Pudleiner** from the central scientific facility *Thin Film Growth* at the MPI MF manufactured the first samples of Rh/Al_2O_3 and Rh/MgO(100). These samples provided very valuable information for the further oxidation experiments. I thank **Dr. Dimas Garcia de Oteyza Feldermann** and **Annette Weisshardt** for the AFM-measurements that delivered further insight of how the particles grow.

I appreciate a lot the access to HEMD at beamline ID 15 A at the ESRF in Grenoble, France. It was my first stay at this facility and my first publication as a main author resulted from this beamtime. For the success of the experiment I would like to thank **Dr. Harald Reichert**, **Dr. Adrian Rühm**, **Dr. John Okasinski** and **Dr. Sebastian Schöder**.

I am indebted to **Dr. Nicole Jeutter**, **Dr. Tobias Schülli**, **Dr. Olivier Balmes** and the other coworkers of the beamlines BM32 and ID03 at the ESRF for their contributions to the experiments during the remaining beamtimes at this facility, also at many night shifts.

I thank **Claus Ellinger** for the support during the beamtimes at HASYLAB and the oxidation of Rh/Al_2O_3 at ANKA. The nice sightseeing day in Hamburg made me forget about returning to Stuttgart without any relevant data after the breakdown of the storage ring.

Thanks to **Ralf Weigel** I could always rely on the performance of the MPI-MF surface diffraction beamline at ANKA. He also solved many small and many severe technical problems for the operation of the oxidation chamber at the beamline.

I thank **Frank Adams** for the x-ray support in the home lab, which especially in the beginning of my work allowed to perform valuable prestudies on my samples prior to the synchrotron beamtimes.

Dr. Ioan Costina advised me how to use the preparation chamber and I thank him for all his hints about UHV. With respect to questions about vacuum, I also would like to thank **Stephan Weber** and **Peter Schützendübe**.

The computer simulations for the analysis of the particle shape were per-

formed at the cluster *dxray33*. **Dr. Janos Major**, **Dr. Markus Mezger** and **Heiko Schröder** have always made a smooth run of the programs possible. **Taufan Zimmer** is acknowledged for the personal computer support.

Claudia Sussdorff is acknowledged for the excellent support with all kinds of administrative questions, especially during the last months of the completion of the thesis.

I thank **Arnold Weible** and **Thomas Meisner** from the central scientific facility *Specimen Manufacturing* for their support with annealing of the crystals. I also thank the transport service of the MPIs and **Ernst Günther** for their reliable transportation of the vacuum chambers and lots of other laboratory equipment between Stuttgart and the synchrotron radiation facilities. The members of the fine mechanical workshop and the low temperature service are acknowledged for their speedy technical realizations of the construction assignments.

I would like to thank my former office associates **Bernd Steinheil**, **Dr. Yi Zhang** and **Martino Saracino**.

Moritz Becker shared the office with me from the diploma thesis till the end of our PhDs and I thank him for the excellent working atmosphere and the many discussions. To sum up: La felicidad es *comer un pan* con carne de vaca, un cafe y el futbolín con des amig(j)os al chimenea ;-).

My special thanks goes to **Dr. Nikolai Kasper** who strongly minted the first 1.5 years of my work. During the two months of synchrotron beamtimes we had together I learned a lot from his experience and the many valuable hints about diffraction experiments. Furthermore, I benefited strongly from his previous research on the Pd/MgO(100) particles, and the calculation of the reciprocal space map intensities is based on his work of the Bragg width anisotropy.

I enjoyed working with my other colleagues from the nano-oxidation group: **Dr. Alexander Reicho**, **Dr. Alina Vlad**, **Dr. Melissa Delheusy**, **Dr. Vedran Vonk** and **Navid Khorshidi**.

I am deeply indebted to **my family** for their continuous support in all respects. I want to thank them for always making efforts facilitating me to concentrate on my education.

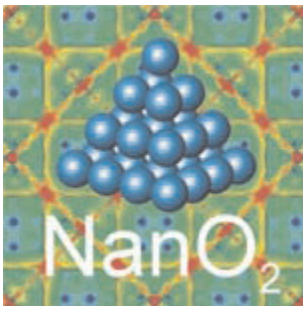

The European Union is acknowledged for support under contract NMP3-CT-2003-505670(NANO2).